Image-Derived Plasma Input Function for the Quantification of Positron Tomography Brain Studies with 6-[^{18}F]Fluoro-L-*meta*-Tyrosine

by

MARIE-CLAUDE ASSELIN , M.Sc., B.Sc.

A Thesis

Submitted to the School of Graduate Studies

in Partial Fulfilment of the Requirements

for the Degree

Doctor of Philosophy

McMaster University

Image-Derived Plasma Input Function for PET/FmT Brain Studies

DOCTOR OF PHILOSOPHY (2004) McMaster University

(Medical Physics) Hamilton, Ontario

TITLE: Image-Derived Plasma Input Function for the Quantification of Positron Emission Tomography Brain Studies with 6-[^{18}F]Fluoro-L-*meta*-Tyrosine

AUTHOR: Marie-Claude Asselin , M.Sc. (McMaster University)

SUPERVISOR: Dr Claude Nahmias

NUMBER OF PAGES: xx, 241

Acknowledgements

The PhD degree was a long time dream, but without the support of a number of people and institutions, this thesis would never have been completed. I take this opportunity to thank:

At **McMaster University** —

Claude Nahmias, for sharing his knowledge and enthusiasm about PET, and for his uninterrupted confidence in myself. Lindi Wahl, for being an inspiration. Colin Webber and John Mernagh, for guiding discussions.

Margo Thompson and Hilda Pope, for their help in collecting the clinical data. Raman Chirakal, Neil Vasdev, Shigeko Amano and Dr. Chen, for preparing the radiopharmaceuticals and for performing the blood analyses. Bev Kenyon, for his technical assistance, day and night, with image files and processing.

Geoffrey Hall, Anna Garnett, Shigeko Amano and Erin Niven, for making my days in the MindLab very enjoyable.

Wendy Malarek, for her personalized administrative assistance.

At **Hammersmith Hospital** —

Terry Jones (and Claude Nahmias), for giving me the opportunity to visit the Cyclotron Unit. Vin Cunningham, for sharing his modelling expertise and teaching me proper English.

Roger Gunn, Kris Thielemans, Peter Bloomfield and Ralph Meyers, for their technical advice. John Aston and Federico Türkheimer, for their statistical advice.

Sanida Mustafovic and Darren Hogg, for sharing good times and bad times.

John Thornback, Vin Cunningham and Sue Hume, for encouraging me to write up, even during working hours.

And wherever I was...

George Alexandrakis, for stimulating discussions about Science. Rainer Hinz, for his emotional support. And my parents, for teaching me not to give up.

Many more thanks to all those whose contribution, although not explicitly acknowledged here, is nevertheless appreciated.

Financially, this work was supported by the Natural Sciences and Engineering Research Council of Canada and the Fonds pour la Formation des Chercheurs et l'Aide à la Recherche du Québec, as well as by McMaster University (the Eugene G. Bolotkin and the Harvey Travel scholarships) and the Department of Nuclear Medicine of the McMaster University Medical Centre (the E.S. Garnett bursary).

Abstract

Positron emission tomography (PET) is an imaging technique that allows the *in vivo* measurement of tissue functions in humans using pharmaceuticals labelled with positron-emitting isotopes and a dedicated tomograph. Physiological parameters can be derived from the dynamic PET images by applying mathematical modelling techniques provided that an input function is available. In this thesis, a method that extracts the time course of radioactivity concentration in the blood from brain PET images is developed as a non-invasive alternative to arterial blood sampling. Even though the methodology is developed for 6-[^{18}F]fluoro-L-*m*-tyrosine (F*m*T), a presynaptic dopaminergic radiotracer, it is generalisable to other radiotracers.

The method is based on predefined regions of interest (ROI) drawn on the largest cerebral blood vessels, the venous sinuses, which are visible in the PET images. The time course of radioactivity in the cerebral blood was initially corrected for partial volume and spillover using a population value for the calibre of the blood vessel. The method was refined by parametrising the ROIs in order to extract the calibre of the blood vessel directly from PET images and to simultaneously correct the radioactivity concentration for partial volume and spillover. In a validation study, the radioactivity concentration was recovered to 100 $\pm$4% in syringes filled with an ^{11}C solution and inserted into a water-filled cylindrical phantom. Even though the diameter of syringes was estimated with an accuracy of half a pixel (1mm) in the phantom studies, the method systematically overestimated the blood vessel calibre by 2-3mm compared with measurements made in magnetic resonance venograms in human studies. The application of the parametric ROIs method to clinical studies awaits the development of more accurate scatter correction methods and the implementation of correction for head motion. The between-subject variations in the blood vessel calibre were measured to be comparable to the bias given by the parametric ROIs, thereby justifying the use of a population value over current subject-specific values.

A compartmental model relating the radiotracer F*m*T, its main radiolabelled

metabolite and their exchange between plasma and erythrocytes was also developed in order to transform the time course of total radioactivity measured in whole blood into the time course of the unmetabolised radiotracer in plasma. This blood model was found to be robust to measurement noise, and could be used to derive a population-based correction that allows the plasma input function to be determined non-invasively, thereby eliminating the need to draw and process blood. The blood model can be adapted for radiotracers other than F*m*T as long as the blood partition ratio of the parent radiotracer differs from that of its metabolites and/or the rate at which they equilibrate between plasma and erythrocytes is different.

Presynaptic dopamine function is severely disturbed in Parkinson's disease (PD) with a pattern of striatal involvement (posterior putamen dopamine levels decreased compared to that in caudate nucleus on the side opposite to the clinically impaired limbs) that distinguishes it from other movement disorders. Compared to arterial blood sampling, the image-derived plasma input function enabled the discrimination of normal and PD subjects as well as the identification of the affected and unaffected sides of the PD subject. The image-derived plasma input function also classified 20 of the 21 consecutive patients suspected of suffering from a variety of movement disorders into the same categories as determined using an indirect cerebellar input function. Using image-derived input functions, quantitative analyses of PET/F*m*T studies are feasible in a clinical setting and, in combination with striatal patterns of F*m*T uptake, the method provides useful diagnostic information in individual patients.

Contents

List of Figures

List of Tables

Chapter 1

Introduction

This thesis aims to develop a method that non-invasively generates a plasma input function for kinetic analyses of positron emission tomography (PET) data. PET is an imaging technique that allows the *in vivo* measurement of tissue functions in animals and humans. After the administration of tracer quantities of a radiolabelled pharmaceutical, the distribution of radioactivity is followed over time with a temporal resolution of seconds and a spatial resolution of millimetres. Mathematical modelling techniques, like compartmental or graphical analyses, can then be applied to the dynamic images in order to extract physiological parameters of interest such as the rates of transport, metabolism or binding of radiotracers. This requires the accurate characterization of the function that describes the time course of radiotracer delivery to tissue, the *input function.* The input function is usually derived from multiple blood samples drawn from an arterial cannula and processed to obtain the radiotracer concentration in plasma. Because this method is invasive, time consuming and prone to errors, it cannot always be implemented and practical alternatives are called for.

This thesis investigates the use of the largest cerebral blood vessels, the venous sinuses which are visible in the PET images, as input functions for the presynaptic dopaminergic radiotracer 6-[^{18}F]fluoro-L-*meta*-tyrosine (F*m*T). The venous blood concentration reasonably approximates the arterial blood concentration for radiotracers which, like F*m*T , are slowly extracted from the capillaries. Because the calibre of cerebral blood vessels is smaller than twice the spatial resolution of most tomographs, the radioactivity concentration extracted from PET images must be corrected for partial volume and spillover. Furthermore, these values are prone to statistical noise due to the small size of the regions of interest and to the short time frames required to capture the rapidly changing time

course of radioactivity concentration following a bolus injection of the radiotracer. F*m*T is a radiotracer which equilibrates slowly between plasma and erythrocytes and for which radiolabelled metabolites have been identified in plasma. A correction for the partitioning of radioactivity between plasma and eythrocytes as well as for peripheral metabolism of the radiotracer thus needs to be applied in order to extract the contribution of the injected radiotracer in plasma from the total radioactivity measured in the blood.

The structure of this thesis is illustrated in **Figure 1.1**. Chapter 2 gathers the general background information required to address the multi-faceted problem at hand. Section 2.1 explains how the radioactivity concentration in an object is measured using PET. Section 2.2 follows with an overview of mathematical modelling techniques most commonly applied to dynamic PET data. The interpretation of a PET study does not only rely on knowledge of the technical aspects of the data generation and processing, but as importantly, on the understanding of the biological aspects underlying the radiotracer used in the study. Because the method developed here is validated using mainly F*m*T but also 6-[^{18}F]fluoro-L-DOPA (6F-DOPA), section 2.3 reviews the biochemical data and the mathematical models developed for 6F-DOPA and F*m*T . More specific background information is also included in each of the results chapters. A non-invasive method to generate a plasma input function is developed in steps in the next three chapters. The feasibility of the method is first demonstrated in chapter 3 where a comparison is made with arterial sampling. Chapter 4 refines the method by extracting the anatomical information required for partial volume correction directly from the PET images. A compartmental model that allows for the time course of total radioactivity concentration in the blood to be transformed into the time course of the unmetabolised radiotracer concentration in plasma is developed in chapter 5. In chapter 6, the method is applied to PET/F*m*T images obtained from patients suffering from a variety of movement disorders and the discrimination power of the method is compared to that of a reference tissue approach. The thesis concludes with chapter 7 which comprises a summary of the preceding chapters and suggestions for future work derived from this thesis.

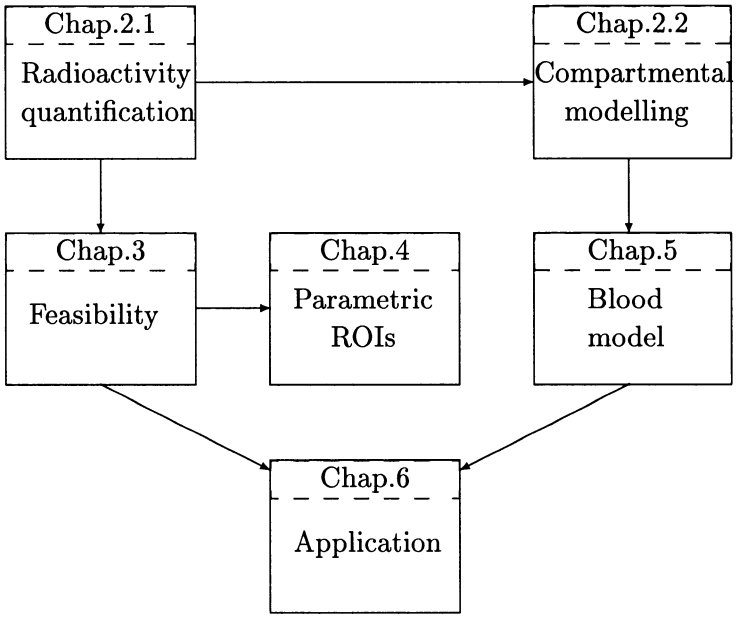

Figure 1.1: *Schematic structure of this thesis.*

Chapter 2

Physiological Quantification of PET Data

Positron emission tomography (PET) is a Nuclear Medicine imaging technique that measures with a dedicated tomograph the annihilation photons emitted following administration of a pharmaceutical labelled with a positron-emitting isotope. These molecules are designed such that they will accumulate in the tissue of interest, and this accumulation will ideally reflect specific physiological or biochemical processes. The acquired data are processed using reconstruction techniques to generate cross-sectional images of the spatio-temporal distribution of the radioactivity.

PET studies aim at quantifying regional and/or global changes in tissue functions, for example, between normal and disease states, or before and after treatment. The ability to detect these changes depends on the signal-to-noise characteristics of the PET data and the size of the changes. One of the motivations behind the development of mathematical models is to increase the power to detect changes in the physiological parameters of interest brought about by different conditions (Carson, 1991). This is accomplished by explicitly accounting for changes in extraneous factors (e.g. radiotracer delivery), thus reducing intersubject variations. On the other hand, inaccuracies in the model itself can increase intersubject variations either by introducing biases due to incorrect assumptions, or by propagating errors from additional measurements required by the model (e.g. input function). The application of a mathematical model to PET data is beneficial if the variations that it removes override those that it produces. When significant physiological changes are detected, however, the model facilitates the quantification and interpretation of these changes.

This thesis is concerned with the extraction of regional information from PET images and the use of these data in the determination of physiological parameters that will distinguish between normal and disease states. This task requires that each voxel value in the reconstructed image represents the absolute radioactivity concentration (in Bq/ml) in the corresponding tissue volume. The acquisition and reconstruction of PET images are explained in section 2.1. Section 2.2 presents the compartmental modelling approaches used in the analysis of the calibrated PET data. The last section focusses on the quantification of the kinetics of two radiotracers that probe the brain dopaminergic system. Models for 6-[^{18}F]fluoro-L-DOPA (6F-DOPA), the first dopaminergic radiotracer to be developed, are discussed in section 2.3.2. Section 2.3.3 proposes 6-[^{18}F]fluoro-L-*m*-tyrosine (F*m*T) as an alternative radiotracer that should overcome some of the modelling problems of 6F-DOPA.

2.1 Radioactivity Quantification Using 3D PET

2.1.1 Image Acquisition and Reconstruction

The PET signal is generated in several steps and captured by a sophisticated radiation detection system. The detected signal also undergoes several processing steps in its transformation into a volumetric image representing the distribution of radioactivity concentration in tissues.

2.1.1.1 Signal Generation: The Radiotracers

Radiopharmaceuticals

A radiopharmaceutical is a radioactive compound which can be administered safely to humans for diagnosis or treatment purposes. It is usually made up a of radioisotope bound to a pharmaceutical (a biomolecule or a drug). When used as an imaging agent, the decaying radioisotope emits the signal detected in PET, and the physico-chemical properties of the pharmaceutical determine the spatial distribution of the emitted signal. Ideally, the radioactive label would not perturb the physiological or biochemical pathways of the radiopharmaceutical. The lightest PET radioisotopes (^{11}C, ^{13}N, ^{15}O and ^{18}F, the latter as a substitute for hydrogen) can be used to label organic compounds isotopically. Furthermore, the radiopharmaceutical should not elicit a pharmacological response. These radioisotopes can be produced in high specific activities so that tracer amounts of the radiopharmaceuti-

cal can be administered. Their short half life allows for efficient use of the radiation dose for imaging. It remains that most often the magnitude of the signal is limited by the radiation dose given to the subject. On the other hand, the fast decay imposes restrictions on the production of the radioisotope — ideally on site using a dedicated particle accelerator or cyclotron — and on the speed and complexity of the chemical synthesis. PET radiochemistry has become very versatile, with the capacity to label a wide variety of biomolecules at many positions. However, the number of useful PET radiotracers is restricted since they must satisfy a number of criteria, the most important ones being selectivity to one or few pathways, delivery to the organ of interest, limited peripheral metabolism and suitable kinetics for the duration of a PET study (Pike, 1993).

Radioisotopes

Nuclei that contain an excess of protons decay either by electron capture or positron emission. In *positron emission*, a proton is converted to a neutron and a positive electron, called *positron* (β^+), is emitted along with an electronic neutrino (ν_e):

$$ {}^{A}_{Z}X \longrightarrow {}^{A}_{Z-1}Y + \beta^+ + \nu_e. \tag{2.1} $$

An orbital electron is also ejected so that the daughter nuclide remains neutral. Whereas any proton rich nucleus can decay by electron capture, only nuclei whose parent (${}^{A}_{Z}X$) mass exceeds the daughter (${}^{A}_{Z-1}Y$) mass by at least 1022 keV/c^2 — the combined mass of the positron and the ejected electron — can decay by positron emission, so that the two processes are in competition. The remainder of the mass difference is transformed into kinetic energy that is shared between the positron and the neutrino.

Positron interactions

In matter, the positron subsequently loses its kinetic energy by ionising and exciting the surrounding material. Most energy is transferred by inelastic collisions with atomic electrons. The positron hence travels a certain distance before reaching thermal energies. This distance, called *range*, increases with the energy of the positron and decreases with the density of the surrounding material. The probability of positron emission (or the positron branching ratio), the positron energy and range in water for the radioisotopes commonly used in human PET studies are gathered in **Table 2.1**. The range values indicate that the position of the radiolabeled molecule at the time of the positron emission can be inferred

Table 2.1: *Properties of positron emitting isotopes commonly used in human PET studies.*

Isotope	Half life [a]	β^+ branching ratio [a]	Average β^+ energy (MeV)[a]	β^+ range in water (mm)[b]
^{11}C	20.4 min	1	0.386	1.2
^{13}N	9.97 min	1	0.492	1.7
^{15}O	2.04 min	1	0.735	2.9
^{18}F	109.8 min	0.97	0.250	0.62
^{68}Ga	67.7 min	0.89	0.836	3.4
^{82}Rb	1.27 min	0.95	1.17, 1.54	5.2, 7.2

[a] Data extracted from *www.nndc.bnl.gov/nndc/formmird.html.*

[b] Values calculated from Pages *et al*(1972).

with at best a precision of about 1 mm.

Annihilation

Once the positron is thermalized, it combines with an electron in the surrounding material. In order to obey the principles of conservation of energy and momentum, the rest mass of the electron and positron is transformed into energy primarily in the form of two 511 keV photons, emitted opposite to each other and without any preferential direction. Any residual kinetic energy of the positron during annihilation causes the *annihilation photons* to deviate slightly from collinearity ($< 1°$).

Photon interactions

The annihilation photons further interact with the surrounding material, predominantly through the photoelectric effect or Compton scattering, pair production not being energetically possible. The *photoelectric effect* occurs when a photon interacts with an atomic electron, most often bound in the K-shell. The photon is completely absorbed and the photoelectron is ejected with a kinetic energy equal to the difference between the photon energy and the electron binding energy. The probability of photoelectric absorption τ increases with the atomic number Z of the surrounding material and decreases with the incident photon energy E_γ approximately as $\tau \sim Z^5/E_\gamma^{3.5}$ (Knoll, 1989). In *Compton scattering,* the photon interacts with a free or weakly bound electron. The photon is deflected

through an angle θ from its incident direction and transfers part of its initial energy to the recoil electron. The energy lost by the annihilation photon to the recoil electron in a single interaction varies between 0 at $\theta = 0°$ to 341 keV at $\theta = 180°$. For a wide range of materials, the probability of Compton scattering σ increases linearly with the atomic number of the surrounding material and falls gradually with the incident photon energy (Knoll, 1989). The scattered photon can undergo more interactions with the surrounding material, either another Compton scatter or a photoelectric absorption. The overall probability of interaction, called the *linear attenuation coefficient*, is the sum of the photoelectric absorption and Compton scattering probabilities, $\mu = \tau + \sigma$.

2.1.1.2 Signal Detection: The Tomograph

In a PET study, a subject to whom a radiolabelled pharmaceutical has been administered in tracer doses is positioned inside a tomograph consisting of multiple radiation detectors connected in coincidence to efficiently capture the annihilation photons emerging from the body.

Detectors

When an annihilation photon interacts with an inorganic scintillator, it transfers its energy to electrons which are elevated from the valence band to the conduction band of the crystalline lattice. These excited electrons later return to the valence band via intermediate metastable states created in the band gap by impurities in the crystal. During the transition, photons in the visible range of energy are emitted at a rate characteristic of the crystal. As other processes of energy transfer compete with luminescence, the fraction of incident energy converted into light, the *scintillation efficiency*, also depends on the crystal. On the face of the crystal opposite to the face of photon incidence, a photomultiplier tube (PMT) collects the visible light and generates an amplified electronic pulse.

The choice of a detector material for PET is based on an ideal combination of properties. In order to determine precisely the position of the annihilation event, the size of each crystal must be kept as small as possible. Because annihilation photons have a high probability of escaping from small detectors, the scintillator material must have a high stopping power if the *detection efficiency* is not to be compromised. Compton scattered photons have a lower energy than unscattered photons and discrimination between the two

types of events requires good *energy resolution* from the scintillator. At high count rates, the number of random coincidences and deadtime losses (see section **Corrections for High Count Rates** below) is limited with a scintillator that offers good *time resolution.*

Bismuth germanate ($Bi_4Ge_3O_{12}$ or BGO) has a high density (7.13 g/cm^3) and a large effective atomic number (Z=83 for Bi), resulting in the largest probability per unit volume for photoelectric absorption of commonly available scintillation materials (Knoll, 1989). The high stopping power of BGO overrides its other less desirable properties of a relatively low light yield (15% of that of thallium activated sodium iodide (NaI(Tl)) and a slow light decay (300 ns). The slower scintillation process of BGO combined with its lower scintillation efficiency results in an overall time resolution that is about a factor of two worse than that of NaI(Tl)(FWHM=6.8 ns for BGO vs. 3.8 ns for NaI(Tl)) (Cho and Farukhi, 1977). Because fewer visible light photons are being produced per unit of energy deposited in the BGO crystal, its energy resolution is about a factor of two worse than that of NaI(Tl) (11% for BGO and 6% for NaI(Tl) at 662 keV) (Ludziejewski *et al*, 1995). With a density of 7.4 g/cm^3 and an atomic number of Z=71 for Lu, cerium-doped lutetium oxyorthosilicate ($Lu_2(SiO_4)O$:Ce or LSO) has a detection efficiency for annihilation photons comparable to that of BGO. Its much higher scintillation efficiency (>50% of that of NaI(Tl)) and faster scintillation process (decay time constant of 47 ns) compared to that of BGO yield a superior time resolution of 0.400 ns (FWHM) (Ludziejewski *et al*, 1995). Inconsistencies in the production of LSO in both light output and decay time have to date hampered the improvement in energy resolution of LSO over that of BGO (Karp, 2002). Because of its favorable combination of properties, LSO is superseding BGO as a detector material for PET in 3D mode (see section **Detection Geometry** below) (Nutt, 2002).

The performance of a detector for PET does not depend only on the material properties, but also on the detector design. By grooving a scintillator block into, for example, an eight by eight matrix of crystal elements coupled to four PMTs (Casey and Nutt, 1986), the *block detector* improves both the sampling frequency and detection efficiency over that of the single-crystal detector. The visible light is channelled down the individual crystal elements and distributed to the PMTs in different combinations by slotting the block at increasing depths with increasing distance from the centre of the block. The crystal in which the interaction occured is identified by comparing the sums of the outputs of adjacent PMTs. The output of all four PMTs is also summed and sent to a pulse processing unit in order to determine the energy absorbed in the detector (from the pulse height) and the

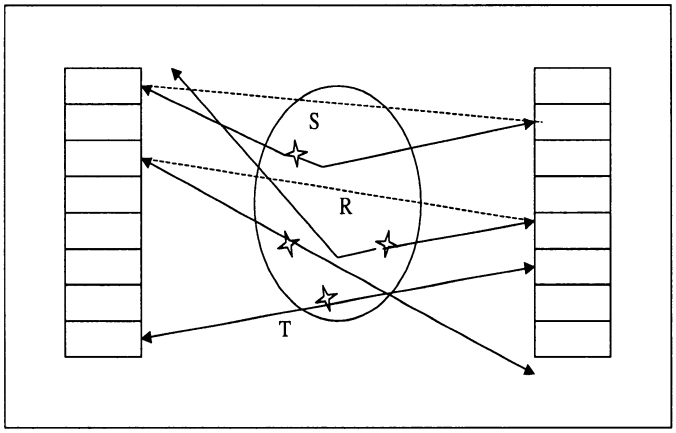

Figure 2.1: *Types of coincidence events (depicted in axial view): Scatter (S), random (R) and true (T) coincidences.*

time of arrival of the incident photon (from the pulse leading edge). This design, intially created for BGO, is also applied to LSO, although alternative designs that make better use of LSO properties are being developed (Nutt, 2002).

Coincidence counting

Following positron emission, two annihilation photons are emitted simultaneously in a direction opposite to each other. Coincidence events are detected by comparing the output of two detectors to a coincidence unit. Whenever two pulses are received within a given time interval, called *coincidence time window*, a binary pulse is generated by the coincidence unit. The width of the coincidence time window is selected to include the time resolution of the detectors, time variations between branches due to additional electronic components in the detector circuits, and the maximum time that a photon can take to cross the entire field of view (FOV).

As illustrated in **Figure 2.1**, three types of coincidence events are detected by the tomograph: True, scatter and random. If two photons created from the same annihilation event reach their respective detectors without being scattered, then a *true coincidence* is recorded. True coincidences are the events of interest since their count rate is proportional to the regional radioactivity concentration. If either or both photons are scattered while crossing the FOV, then a *scatter coincidence* can be detected. Scatter coincidences carry incorrect positioning information since the photon paths are no longer collinear. Due to the

limited energy resolution of scintillators, many scattered photons successfully pass through the pulse processing unit. Even though the scattered photons travel an extra distance, they are not sufficiently delayed to fall outside the coincidence time window. A *random coincidence* occurs when two photons that originated from two different annihilation events are detected within the coincidence time window. The count rate of the random coincidences is proportional to the product of the count rate in the two individual detectors (called *singles*), with the constant of proportionality given by the coincidence time window. Therefore, the random count rate increases faster than the true count rate with increasing radioactivity in the FOV, but can be reduced by shortening the coincidence time window. More than two photons can strike the detectors within the coincidence time window. Even though these *multiple coincidence* events are not recorded, they can prevent the detection of true coincidences while being processed (see **Corrections for High Count Rates** below).

Detection Geometry

The most common design for PET cameras makes use of the cylindrical geometry by stacking together individual rings of detectors. In the two-dimensional (2D) acquisition mode, annular septa are inserted between rings to shield most coincidence events that occur between non-adjacent rings. Coincidence events detected within the same rings form *direct planes*, whereas those detected between adjacent rings define *cross planes*. This configuration minimizes the detection of out-of-plane random and scatter coincidences. Removing inter-ring septa eliminates physical collimation in the axial direction, thus allowing for more oblique coincidence events to be detected as illustrated in **Figure 2.2**. The expansion to the three-dimensional (3D) acquisition mode increases the tomograph overall sensitivity to true coincidences, but also to random and scatter coincidences from both inside and outside the FOV (Bendriem and Townsend, 1998).

Data Sampling

The line joining two detectors is called a *line of response* (LOR). An LOR represents the line integral through the radioactivity distribution connecting a given pair of detectors. All parallel LORs correspond to a *projection* of the radioactivity distribution. Multiple projections are obtained by rotating the set of parallel LORs. In 2D mode, an LOR can thus be described by a radial distance x_r from the center of the transaxial FOV and a projection angle θ. The number of events in each LOR is stored in a bin or element

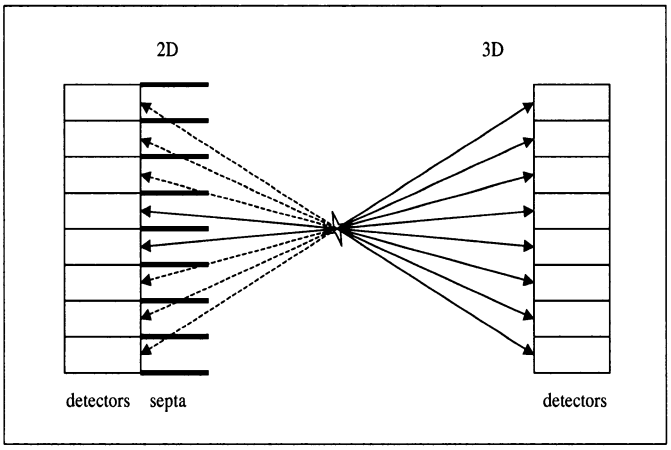

Figure 2.2: *2D vs. 3D detection geometry: The removal of the inter-plane septa increases the axial acceptance angle and thus the tomograph overall sensitivity.*

(x_r, θ) of a matrix called *sinogram.* The term sinogram is derived from the observation that a point source located off-center in the FOV traces a sine wave in the matrix of LOR values. In 2D mode, a sinogram is generated for each (direct and cross) plane. In 3D mode, a sinogram is generated for each ring pair. When the sinograms are sparse matrices as is often the case in 3D mode, it becomes advantageous to store the data on an event-by-event basis called *list mode.* Information on the pair of detectors corresponding to the coincidence event together with the time of the event are recorded as the events are detected, and sorted into sinograms later once the data acquisition is completed.

2.1.1.3 Corrections

Not all annihilation events are detected as coincidence events. And not all coincidence events carry accurate positioning information. Corrections thus need to be applied to the total coincidence events in order to restore the linear relationship with the radioactivity concentration before recovering the radioactivity distribution.

High Count Rates

It takes a minimum time for a detection system, comprising the detector itself and the associated electronics, to generate and process an electronic pulse. If more than one event is detected within that time, called *deadtime*, pulses are lost or distorted. The

probability of losing an event is always present in PET because of the random nature of radioactive decay, but becomes significant at very high count rates. The large number of detectors and the complexity of the pulse processing and recording electronics render the modelling of the deadtime behavior difficult (Moisan *et al*, 1997). Instead, a more *ad hoc* method is used to correct for deadtime losses. The count rate response of the tomograph is characterised by counting a high activity source of known strength over several half lifes. When a source of unknown activity is subsequently measured, the true source activity is obtained by interpolating the count rate response curve.

At count rates just below saturation of the detectors, the count rate is dominated by random coincidences. As the count rate decreases, a greater proportion of the count rate is attributed to true coincidences. Two methods are commonly used to estimate random events. If the coincidence time window is known accurately, the random coincidence rate can be calculated from the singles count rates at a pair of detectors. Alternatively, the random coincidence rate can be measured by introducing a variable delay in one branch of the coincidence unit. The method is based on the observation that the arrival times of the photons associated to random events are uniformly distributed in time, whereas those associated to true (and scatter) events fall within the coincidence window. The delay is first adjusted such that the centre of the coincidence time window is aligned with the true (and scatter) coincidence peak, and all three types of coincidences are measured. The delay is then changed such that the coincidence time window is moved away from the peak and only random coincidences are measured. Whether the random coincidences are calculated or measured, they are subtracted from the total coincidences. The singles method is more precise because the singles rates are much higher than the coincidence rates. Unlike the singles, the delayed coincidences are measured under the same conditions of deadtime as the true coincidences, making the delayed window method more accurate (Casey and Hoffman, 1986).

If not corrected for, the effect of deadtime is an underestimation of the radioactivity concentration in the reconstructed PET images whereas that of random coincidences is an overestimation (Hoffman *et al*, 1981). In dynamic PET studies, where the source activity in the FOV varies with time due to changes in the biodistribution of the radiotracer and radioactive decay, the recovery of the count rate linearity between true coincidences and source activity is crucial.

Photon Attenuation and Scatter

Most annihilation photons emitted inside the body are scattered or absorbed on their way out. The probability P_i that a photon does not interact as it propagates through tissues is given by

$$P_i = exp\left(\int_l -\mu(\mathbf{x})d\mathbf{x}\right), \tag{2.2}$$

where $\mu(\mathbf{x})$ is the linear attenuation coefficient. The integral is evaluated along a path l defined by the pair of detectors i (located at a given distance x_r from the center of the projection at a given angle θ). Since a pair of annihilation photons undergoes the same attenuation regardless of the origin of the annihilation event along the path, PET data can be corrected for attenuation before reconstruction, i.e. without knowledge of the radioactivity distribution.

A map of the survival probabilities can be obtained from two separate scans using an external radioactive source which is rotated about the center of the FOV. Prior to injection of the radiotracer, a *transmission scan* is performed while the subject is lying inside the tomograph. These data provide an estimate of the attenuated flux of photons (T_i) along each path. Under the same conditions as the transmission scan, a *blank scan* is acquired without anything in the tomograph. These data give an estimate of the incident flux of photons (B_i) along the same paths. The survival probabilities are approximated by the ratio of the two maps:

$$\hat{P}_i \sim \frac{T_i}{B_i}. \tag{2.3}$$

When obtained using a positron emitting source (^{68}Ge/^{68}Ga), these estimates are noisy because the source strength must be kept low in order not to saturate the detector close to the source. This problem can be overcome by using a source emitting γ-rays of energy close to 511 keV (662 keV for ^{137}Cs) and sequentially switching off the detector close to the source. Corrections must be made for the diameter difference between the detector ring and the source orbit (deKemp and Nahmias, 1994), and for the energy difference of the linear attenuation coefficients (Yu and Nahmias, 1995). For comparable statistics, the singles method is ten times faster than the coincidence method (Karp *et al*, 1995). The noise propagation from the measured attenuation map to the emission data can be eliminated by segmenting the attenuation map and assigning theoretical values of linear attenuation coefficients to the corresponding anatomical regions (Xu *et al*, 1994).

The fraction of scatter coincidences is approximately 10-15% of total coincidences in 2D mode, but rises to 30-50% in 3D mode. The scatter fraction can be estimated using an analytical model of the radiation transport through an object from emission to detection (Watson *et al*, 1996; Ollinger, 1996). Given the attenuation map, a physical description of the tomograph and an initial estimate of the radioactivity distribution, the algorithm simulates the number of single scatters. The multiple scatter contribution can be modelled empirically from the single scatter distribution (Ollinger, 1996). Because of the presence of scatter in the preliminary emission image, the algorithm is run iteratively, correcting each time the estimate of the radioactivity distribution using the improved scatter estimate. This method fails to account for radioactivity outside the FOV since information is only available from inside the FOV. For brain PET studies, the scatter fraction can also be inferred from measurements of coincidence events made in a second lower energy window in addition to the photopeak window (Grootoonk *et al*, 1996). A scaled subtraction of the two energy windows yields the number of scatter events in the upper energy window. This method offers the advantage of correcting for scatter events originating from radioactivity outside the FOV.

Mismatches between the true and assumed attenuation correction factors, e.g. due to subject movement, lead to image artefacts, particularly at the boundary between tissues of different densities, and to inaccurate estimates of the radioactivity concentration across the PET images (Huang *et al*, 1979). Residual scatter coincidences degrade the spatial resolution in the PET image by transfering radioactivity from high to low radioactivity regions (Watson , 1996). Whereas scatter correction can be omitted in 2D mode or compensated for by adjusting the linear attenuation coefficients, it is essential in 3D mode in order to obtain quantitative PET images.

Non-Uniform Detector Response

The detection efficiency of annihilation photons varies not only from block detector to block detector, but also across the elements of a block detector, depending on the location of the energy deposition in the crystal and the incidence angle of the photon. The detection efficiency of crystal elements located in the center of the block detector is higher than those located on the edges. Because Compton scattered photons have lower energies and more oblique incidence angles than unscattered photons, the detection efficiency is also different between the two types of coincidences (Ollinger, 1995). These differences are exacerbated

in 3D mode with the larger scatter fraction and the wider range of acceptance angles than in 2D mode.

Normalization can be approached from two directions. In the direct method, a uniform low activity source illuminates sequentially all LORs. The measured data are inverted to provide an efficiency value for each LOR. Given the very large number of LORs in 3D mode, the acquisition time required to obtain good counting statistics for each LOR is prohibitively long. Component-based models of increasing complexity (Hoffman *et al*, 1989; Bailey *et al*, 1996; Badawi and Marsden, 1999) have been proposed along with measurement protocols in order to determine separately the main factors contributing to the efficiency. This indirect method allows for the effects of the individual factors to be investigated. Failure to correct for the differential detector response and geometric effects creates artefacts in PET images of a uniform cylindrical phantom — ranging from the addition of high frequency noise to low frequency characteristic (transaxial and axial) patterns — that can lead to severe quantification errors in the radioactivity distribution (Badawi and Marsden, 1999).

The number of annihilation events N_i originating from photons emitted at a given angle can be expressed as a function of the number of total coincidences Y_i recorded in a pair of detectors i by combining the above described corrections in the appropriate sequence as summarized in the following equation (Ollinger and Fessler, 1997):

$$N_i = \frac{1}{d_i \eta_i^t \hat{P}_i} \left[Y_i - d_i \eta_i^r \hat{R}_i - d_i \eta_i^s \hat{S}_i \right], \tag{2.4}$$

where d_i is the probability of an event being lost due to deadtime, $\hat{P}_i$ is the measured survival probability as previous defined (see equations (2.2) and (2.3)), η_i are the detection probabilities of a true (superscript t), random (superscript r) or scatter (superscript s) events, and $\hat{R}_i$ and $\hat{S}_i$ are the estimated number of random and scatter coincidences. Note that the corrections for deadtime, detector efficiency and photon attenuation are multiplicative while those for random and scatter coincidences are subtractive.

2.1.1.4 Signal Localization: Image Reconstruction

A pair of annihilation photons striking two opposite detectors connected in coincidence carries the information that an annihilation event occured somewhere along the LOR. The point of origin of the annihilation event is inferred back by combining multiple

LORs.

2D Filtered Backprojection (FBP) Algorithm

In 2D mode, a projection $p(x_r, \theta)$ corresponds to a line integral at an angle θ and at a distance x_r from the center of the FOV through the unknown radioactivity distribution $\lambda(x, y)$,

$$p(x_r, \theta) = \int_{\ell} \lambda(x, y) dy_r, \tag{2.5}$$

where (x_r, y_r) is the coordinate system (x, y) rotated by an azimuthal angle θ. Equation (2.5) describes the forward projection operation of the PET data acquisition process. The backprojection operation, given by equation (2.6), is the adjoint to the forward projection operation.

$$b(x, y) = \int_0^{\pi} p(x_r, \theta) d\theta, \tag{2.6}$$

where $b(x, y)$ is the backprojected radioactivity distribution. Backprojecting basically consists of assigning the value of the line integral to all the points that fall on the path of the line integral, and repeating this operation for all line integrals. Using the *central-section theorem* which states that the 1D Fourier transform ($F_1\{\}$) of a projection at an angle θ is equivalent to a line through the origin of the 2D Fourier transform ($F_2\{\}$) of the original radioactivity distribution, the filtered backprojected radioactivity distribution can be calculated as

$$\lambda(x, y) = \int_0^{\pi} \Big[p(x_r, \theta) \otimes h_1(x_r) \Big] d\theta \tag{2.7a}$$

$$= \int_0^{\pi} \Big[F_1^{-1} \Big\{ |\nu_{xr}| \, F_1 \Big\{ p(x_r, \theta) \Big\} \Big\} \Big] d\theta \tag{2.7b}$$

where $h_1(x_r) = F_1^{-1}\{|\nu_{xr}|\}$ is the 1D filter kernel, and $|\nu_{xr}|$ is the ramp filter arising from the change of variables from rectangular to polar coordinates (the Jacobian of the transformation). In practice, the projections are sampled at discrete intervals Δx_r, setting the maximum recoverable frequency to Nyquist frequency $\nu_{max} = (2\Delta x_r)^{-1}$. Furthermore, the projections are contaminated by high frequency noise which can be attenuated by multiplying the ramp filter with an apodizing window that rolls off the higher frequencies. A 3D volume image can then be formed by separately acquiring and reconstructing a set of 2D cross-sectional images, and stacking them together.

3D Reprojection (RP) Algorithm

Since the set of projections acquired in 2D mode is sufficient to reconstruct a 3D image, the additional projections collected in 3D mode provide redundant data that can be used to improve image variance. However, the finite axial extent of the PET scanner hinders the measurement of the complete set of projections in 3D. Kinahan and Rogers (1989) proposed to reconstruct the 3D volume image in two steps. First, reconstruct with the 2D FBP algorithm a first-pass image $\lambda_{2D}(x, y, z)$ from the subset of direct projections corresponding to the complete set of projection acquired in 2D, and use this image to forward project in 3D the missing projections. Then, reconstruct with the 3D FBP algorithm a second-pass image $\lambda(x, y, z)$ from the merged set of measured and estimated projections in 3D. The 3D FBP algorithm is simply the extension of the 2D FBP algorithm to one more dimension with the ramp filter being replaced by the Colsher filter (Colsher, 1980). This procedure is equivalent to extending the axial FOV of the PET scanner by adding virtual rings of detectors (Defrise *et al*, 1990). Image variance increases from the center to the periphery of the axial FOV, reflecting the axial variations in the tomograph sensitivity (Kinahan and Rogers, 1989). To restrict noise amplification, the Colsher filter can be multiplied by a 2D apodizing window.

Rebinning Algorithms

The time it takes to reconstruct a 3D volume image using the 3D reprojection algorithm is more than an order of magnitude longer than that to reconstruct the subset of direct projections using the 2D FBP algorithm (Defrise *et al*, 1994). If the 3D PET dataset could be sorted or rebinned into a 2D dataset prior to reconstruction, the high sensitivity of the 3D acquisition mode could be combined with the fast computational speed of the 2D reconstruction algorithm to yield low variance images in short times. A number of rebinning algorithms have been developed for 3D PET data, e.g. the single-slice rebinning (SSRB) algorithm (Daube-Witherspoon and Muehllehner 1987; Erlandsson *et al*, 1994), the multi-slice rebinning (MSRB) algorithm (Lewitt *et al*, 1994), and the approximate and exact Fourier rebinning (FORE and FOREX) algorithms (Defrise, 1995; Defrise *et al*, 1997; Liu *et al*, 1999), with varying degree of accuracy and computational speed.

Iterative Reconstruction

The FPB methods ignore the discrete nature of the data and the measurement

noise, and further amplify (via the ramp and Colsher filters) the noise in the reconstructed PET images. In contrast, iterative reconstruction algorithms are based on models of the PET data acquisition process, incorporating the tomograph physical characteristics as well as the Poisson distributed measurement noise. The radioactivity distribution $\lambda(\mathbf{x})$ can be discretised into a finite set of basis functions $b_j(\mathbf{x})$, usually voxels:

$$\lambda(\mathbf{x}) = \sum_{j=1}^{p} \theta_j b_j(\mathbf{x}). \tag{2.8}$$

In the reconstruction, $\Theta = \{\theta_j\}$ are the unknown coefficients that must be computed from the comparison between the measured projection data Y_i and the model predictions $Y_i(\Theta)$:

$$Y_i(\Theta) = \sum_{j=1}^{p} a_{ij}\theta_j + s_i + r_i + e_i, \tag{2.9}$$

where

$$a_{ij} = T\left(d_i \int p_i(\mathbf{x}) b_j(\mathbf{x}) d\mathbf{x}\right). \tag{2.10}$$

Equations (2.9) and (2.10) are simply equation (2.4) rewritten in terms of counts over the scan time T (rather than count rates) and to which a term for measurement errors e_i was added. The point response of the detector pair $p_i(\mathbf{x})$ now combines the measured linear attenuation coefficients and detector (intrinsic and geometric) efficiency estimates, and represents the probability of a photon emitted at location $\mathbf{x}$ to be counted in detector pair i. Although a non-trivial problem, the *system matrix* $A = \{a_{ij}\}$ offers the possibility of accounting for the detector dimensions and the positron range in the reconstruction process. The random r_i and scatter s_i counts are estimated independently and incorporated into equation (2.9). Given the linear form of the model and measurement errors distributed as independent Poisson noise, the unknown coefficients can be estimated by maximizing the log-likelihood $L(\Theta)$ defined as:

$$L(\Theta) = \sum_{i=1}^{n} \big(Y_i \ln Y_i(\Theta) - Y_i(\Theta) - \ln(Y_i!)\big). \tag{2.11}$$

Finding the maximum of equation (2.11) is a non-linear problem which is solved iteratively. The computation time for each iteration is comparable to that of the 3D RP method, and the number of iterations depends on noise in the projection data. Several algorithms have been developed in order to limit the number of iterations required to reach convergence.

The problems of slow convergence and image noise can be overcome by adding priors and replacing the log-likelihood criterion by a penalized-likelihood objective function where a measure of the image roughness (the penalty function) can be adjusted (with Bayes weights). Regularisation can also be accomplished by filtering at different stages on the reconstruction. However, these modifications can introduce non-uniformities in the spatial resolution and the noise variance in the reconstructed PET image (Ollinger and Fessler, 1997).

2.1.2 Image Characteristics

PET images are noisy and offer poor tissue delineation compared to detailed anatomical images. For a given signal, improvement in the image variance is usually achieved with a concomitant degradation of the spatial resolution (see **NEMA/SNM Performance Tests** below).

2.1.2.1 Signal-to-Noise Ratio

The noise in the projections is independent and Poisson distributed since it originates from counting radioactive sources. After reconstruction, the noise in the PET images is correlated via the point spread function. The *noise equivalent count rate* (NEC) attempts to relate the image signal-to-noise ratio (SNR) to the scatter S, random R and true T coincidence rates (Strother *et al*, 1990) via

$$NEC = \frac{T}{(1 + SF^2)(1 + \frac{S}{T} + 2\frac{R}{T})}, \tag{2.12}$$

where SF is the scatter fraction $SF = S/(S + T)$, ignoring the deadtime and attenuation corrections. Setting $S = R = 0$ in equation (2.12) shows that the NEC can be interpreted as the reduced true coincidence rate which, without random and scatter coincidence events, would produce the same SNR as the true coincidence rate obtained after subtracting random and scatter coincidence rates from the total coincidence rate (Strother *et al*, 1990).

The spatial noise distribution in the PET images is also influenced by the attenuation and emission distributions and by the reconstruction method. When the PET images are reconstructed with 3D reprojection algorithm, the noise distribution is uniform for a homogeneous or heterogeneous radioactivity distribution and homogeneously attenuating media like in the brain. The image variance can then considered to be similar throughout the image, and mostly dependent on the count rate. This approximation no longer

holds in the presence of heterogeneously attenuating media like in the chest, where the noise distribution becomes non-uniform (Pajevic *et al*, 1998). By definition, the image variance is strongly dependent on the radioactivity distribution when the PET images are reconstructed using an iterative reconstruction algorithm.

2.1.2.2 NEMA/SNM Performance Tests

In an effort to standardise performance measurements of PET cameras, the National Electrical Manufacturers Association (NEMA) and the Society of Nuclear Medicine (SNM) developed a series of standardized tests (Karp *et al*, 1991) from which the abilities and limitations of PET cameras for *in vivo* studies could be evaluated. Most tests use either a cylindrical phantom having a diameter of 20.0 cm and a length of 18.5 cm (or longer if the axial field of view extends over that length) and/or line and point sources. The sources are filled with a fluorine-18 solution and the images are acquired and reconstructed using the operating parameters of typical PET studies. The NEMA/SNM standards have recently been revised (Daube-Witherspoon *et al*, 2002) to accomodate, amongst other things, the 3D acquisition mode and whole-body imaging, but since the performance of two PET cameras used in this thesis were assessed prior to the revision, reference will be made to the old standards.

The following four tests aim at characterizing the intrinsic response of the tomograph, the results of which can serve to compare different PET cameras. Measurements of the intrinsic *spatial resolution* aim to characterize the shape of the point spread function (PSF) with the full-width at half maximum (FWHM) in all three orthogonal directions. The PSF, the spatial extent of a point source, depends intrinsically on the dimensions of the detectors. Tomographs with a narrow PSF are better able to image sharp edges or to separate two objects that are closely spaced than those having a wide PSF. The *scatter fraction* is an indicator of the tomograph sensitivity to scattered photons and depends on the geometry and shielding design of the tomograph as well as the energy window selected for the detectors. The scatter fraction decreases radially from the center to the edges of the object. The average scatter fraction over the whole cross-sectional area of the phantom is calculated by taking the ratio of the sum of the number of scattered events weighted by the area of the annulus over the weighted sum of the total number of events. A small scatter fraction is desirable because scatter coincidences are subtracted from total coincidences and

hence introduce noise and, if incorrectly measured or modelled, inaccuracies in proportion to the number of scatter coincidences. The *sensitivity* is given by the ratio of the measured radioactivity over the known radioactivity in the phantom. For a tomograph operated in 3D mode, the axial sensitivity is lowest at the extremities and is highest for a number of planes at the center of the axial FOV depending on the acceptance angle. The tomograph overall sensitivity depends on the axial FOV and acceptance angle, as well as the detector efficiencies, energy and time resolutions. A tomograph offering a high sensitivity is prefered over a less sensitive tomograph because the former provides a higher signal-to-noise ratio than the latter for a given radioactive source strength. The *count rate behavior* of a tomograph can be quoted using different radioactivity levels, most often the point at which the NEC reaches a maximum. The count rate behavior depends on the tomograph design and shielding, as well as the coincidence time window. A high sensitivity tomograph will likely saturate at a lower radioactivity level than a low sensitivity one. However, the true count rate of the high sensitivity tomograph at that level should be higher than that of the low sensitivity one, enabling smaller radioactive doses to be administered for an equivalent signal-to-noise ratio.

Four additional tests are recommended for the evaluation of the quantitative accuracy of the corrections applied to the PET data. The accuracy of the *normalization* is quantified using the plus and minus nonuniformity indices (NU_+ and NU_-) derived according to equations (2.13a) and (2.13b) after having drawn a matrix of contiguous 1×1 cm^2 square regions of interest (ROI) centered into each cross-sectional image of the uniform phantom:

$$NU_+ = +\frac{C_{max}-C_{avg}}{C_{avg}} \tag{2.13a}$$

$$NU_- = -\frac{C_{avg}-C_{min}}{C_{avg}}, \tag{2.13b}$$

where C_{max}, C_{min} and C_{avg} are the maximum, minimum and average number of counts over all ROIs in each plane, respectively. The closer to zero are the indices NU_+ and NU_-, the more uniform is the response of the system. The accuracy of the *scatter correction* method is assessed with the phantom in which is inserted a smaller cylinder containing water. The accuracy of the transmission method for *attenuation correction* is assessed with the phantom in which are inserted three smaller cylinders, each made of a material having a linear attenuation coefficient which mimics different tissues: air (lungs), water (soft tissue) and teflon (bone). The accuracy of the *corrections for deadtime losses and*

random coincidences is verified by analysing the reconstructed images of the data acquired when studying the count rate behavior of the tomograph. The expected count rate is determined from the last three scans performed when the radioactivity level was low, under the assumption that at that level the count rate varies linearly with radioactivity.

The performance of any tomograph depends strongly on the radioactivity distribution in the FOV. The cylindrical phantom used for the NEMA/SNM tests is only a crude approximation of the radioactivity distribution in a human subject. Even though its size was chosen to be half way between the size of a head and that of a trunk, its simplistic shape, composition and radioactivity distribution make the phantom an unrealistic representation of the variety of cases encountered clinically. Furthermore, a phantom is an inanimate object and, as such, its radioactivity distribution does not change with time, nor does the phantom itself move during the scanning period. These two effects, not considered in any of the NEMA/SNM tests, complicate the radioactivity quantification in the PET images. In contrast to human subjects, however, an independent measurement of the radioactivity concentration in the phantom can be performed and used for the determination of the accuracy of the PET measurement on the phantom. Corrections can then be applied until the required accuracy is reached. Therefore, the NEMA/SNM tests do not provide a precise estimate of the accuracy of any PET image, but instead give an indication of the level of accuracy achievable in the measurement of the radioactivity concentration in the PET images acquired with a particular tomograph.

The data presented in this thesis were acquired on two different tomographs: The high-sensitivity high-resolution ECAT/EXACT3D tomograph (CTI/Siemens, Knoxville, TN, USA) at the Hammersmith Hospital (London, UK) and the partial-ring rotating ECAT/ART tomograph (CTI/Siemens, Knoxville, TN, USA) at the McMaster University Medical Centre (Hamilton, Canada). The physical characteristics of each tomograph are presented in **Appendix A** and their performance compared using the NEMA/SNM tests.

2.2 Compartmental Modelling

The time course of radioactivity concentration in tissue contains physiological information which can be extracted using the mathematical modelling techniques presented in this section. But before this overview, some pharmacokinetic concepts to which reference will be made throughout the thesis are introduced.

2.2.1 Concepts of Pharmacokinetics

2.2.1.1 Definitions

When a radiotracer is injected into the blood, the PET images reflect the uptake of the radiotracer from blood to tissue. Depending on the radiotracer, the uptake signal contains information on transport and trapping or binding mechanisms. The following concepts are commonly used to describe quantitatively the exchange of a radiotracer between blood and tissue (Leendeers *et al*, 1997).

Perfusion is the flow per unit volume and is expressed in ml of fluid per min per ml of tissue. This concept is more appropriate than flow to describe the delivery of a radiotracer to tissue since substance requirements of a tissue depend on its volume.

Extraction fraction is the fraction of the radiotracer leaving the plasma into the tissue during one capillary passage. It is calculated by dividing the difference between the vein and artery concentrations by the artery concentration. Perfusion is measured with radiotracers having a high extraction fraction whereas low extraction radiotracers are used to determine the fractional volume of tissue occupied by blood, the *blood volume.*

Equilibrium is reached when the rate of change of the concentration in a compartment is zero. This is translated mathematically by setting to zero the differential equations describing the compartmental system. In practice, however, this theoretical equilibrium is not encountered since the system is not closed. Pseudoequilibrium is reached when the exchange between the plasma and the tissue compartments is small while the loss from the plasma compartment may be not negligible. *Steady-state* is reached when the net flux of radiotracer between the two compartments is zero.

The *volume of distribution* to which the PET literature refers is defined as the ratio of the volume occupied by the radiotracer at equilibrium over the total tissue volume. A volume of distribution smaller than one corresponds to a radiotracer concentration in tissue

smaller than that in plasma. Inversely, the concentration in tissue is greater than that in plasma when the volume of distribution is larger than one. The volume of distribution is unitless and equivalent to the pharmacological concept of *partition coefficient* which is defined as the ratio of concentrations of two compartments at equilibrium. Volumes of distribution can be derived from the parameters of compartmental models (see **Appendix B**).

2.2.1.2 Enzyme Kinetics

The two radiotracers used in this thesis probe the activity of an enzyme (see sections 2.3.2 and 2.3.3). Here a derivation is presented that allows the concentration of an enzyme to be inferred from the kinetics of a radiotracer.

Enzymes are proteins that catalyze biochemical reactions. They are specific to both the binding substrates and the catalyzing reactions. In general, enzymes take the name of their substrate, followed by a word ending in -ase that specifies the type of reaction. The catalytic activities of many enzymes are regulated in two ways: The enzyme availability is determined by both its rate of synthesis and its rate of degradation, and the enzyme activity is controlled by alteration in the binding-substrate affinity. The binding affinities of substrates and inhibitors to an enzyme, the maximum catalytic reaction rate of an enzyme, and ultimately the amount of enzyme present can be inferred from the study of enzyme kinetics (Voet and Voet, 1995).

Consider the following reaction in which the enzyme **E** binds with the substrate **S** to form an enzyme-substrate complex **ES** with a rate constant k_1. The complex can either dissociate back to its components with a rate constant k_{-1} or proceed to form the products **P** with a rate constant k_2. The products are assumed not to revert back to the initial substrate.

$$E + S \underset{k_{-1}}{\overset{k_1}{\rightleftharpoons}} ES \xrightarrow{k_2} P + E \tag{2.14}$$

The rate of production of a compound is equal to the difference between reaction rates leading to its appearance and the reaction rates resulting in its disappearance, where the reaction rate is proportional to the product of the concentrations ([ ]) of the reactants and

the coefficient of proportionality corresponds to the rate constant:

$$\frac{d[P]}{dt} = k_2[ES] \tag{2.15}$$

$$\frac{d[ES]}{dt} = k_1[E][S] - k_{-1}[ES] - k_2[ES]. \tag{2.16}$$

Under the assumption of steady state, [ES] remains approximatively constant until the substrate, originally present in much higher concentration than the enzyme, is almost depleted.

$$\frac{d[ES]}{dt} = 0 \;\Rightarrow\; k_1[E][S] = (k_{-1} + k_2)[ES] \tag{2.17}$$

The previous equation can be rewritten in terms of the total enzyme concentration, $[E]_T = [E] + [ES]$, the quantity which is experimently measurable:

$$[ES] = \frac{[E]_T[S]}{K_M + [S]}, \tag{2.18}$$

where $K_M = \frac{k_{-1}+k_2}{k_1}$ is the *Michaelis constant.* Inserting equation (2.18) into the reaction velocity equation (2.15), one gets

$$v = k_2 \frac{[E]_T[S]}{K_M + [S]}. \tag{2.19}$$

The *maximal reaction velocity* V_{max} is reached when the enzyme is completely saturated.

$$[ES] = [E]_T \;\Rightarrow\; V_{max} = k_2[E]_T \tag{2.20}$$

After substituting the expression for V_{max} into equation (2.19), one obtains

$$v = \frac{V_{max}[S]}{K_M + [S]}, \tag{2.21}$$

the *Michaelis-Menten equation*, the basic equation to describe enzyme kinetics (Voet and Voet, 1995).

At low substrate concentrations, the reaction velocity varies linearly with the substrate concentration with a slope equal to V_{max}/K_M. At high substrate concentrations, the reaction velocity saturates asymptotically towards V_{max}. When $[S] = K_M$, the reaction velocity is half its maximum value. If $k_{-1} \gg k_2$, $K_M \sim k_{-1}/k_1$ and K_M becomes the dissociation constant, a measure of the binding affinity of the enzyme for its substrate. An enzyme has the highest affinity for the substrate having the lowest K_M value.

The parameters K_M and V_{max} can be estimated by measuring the reaction velocity at varying substrate concentrations. A plot of the reciprocal of the reaction velocity vs. the

reciprocal of the substrate concentration, called a *Lineweaver-Burk plot*, will yield a straight line with a slope of K_M/V_{max}, a y-intercept of $1/V_{max}$ and a x-intercept of $-1/K_M$.

Now consider the situation encountered in PET where the labelled substrate **S'** is competing with the endogenous substrate **S** to bind to the same enzyme **E**.

$$E + S \underset{k_{-1}}{\overset{k_1}{\rightleftharpoons}} ES \overset{k_2}{\rightarrow} P + E \tag{2.22a}$$

$$E + S' \underset{k'_{-1}}{\overset{k'_1}{\rightleftharpoons}} ES' \overset{k'_2}{\rightarrow} P' + E \tag{2.22b}$$

The rates of production of the labelled and unlabelled enzyme-substrate complexes are given by

$$\frac{d[ES]}{dt} = k_1[E][S] - k_{-1}[ES] - k_2[ES] \tag{2.23a}$$

$$\frac{d[ES']}{dt} = k'_1[E][S'] - k'_{-1}[ES'] - k'_2[ES']. \tag{2.23b}$$

Assuming that steady state prevails for both the labelled and unlabelled enzyme-substate complexes, equations (2.23a) and (2.23b) can be rearranged so that the concentration of the labelled enzyme-substrate complex is expressed in terms of the total enzyme concentration $[E]_T = [E] + [ES] + [ES']$:

$$[ES'] = \frac{[E]_T[S']}{K'_M\left(1 + \frac{[S]}{K_M} + \frac{[S']}{K'_M}\right)}. \tag{2.24}$$

The reaction velocity for the labelled substrate $v' = k'_2[ES']$ is then derived using equation (2.24) and the expression for the corresponding maximal reaction velocity $V'_{max} = k'_2[E]_T$:

$$v' = \frac{V'_{max}[S']}{K'_M\left(1 + \frac{[S]}{K_M} + \frac{[S']}{K'_M}\right)}. \tag{2.25}$$

If the kinetics parameters of the labelled substrate are similar to those of the unlabelled substrate, i.e. $K'_M \sim K_M$ and $V'_{max} \sim V_{max}$, and taking advantage of the fact that the labelled substate is present in trace quantities, i.e. $[S'] \ll [S]$, equation (2.25) can be simplified to (Barrio *et al*, 1997, Kuwabara *et al*, 1993)

$$v' \sim \frac{V_{max}[S']}{K_M + [S]} = k'[S']. \tag{2.26}$$

Under the conditions that the unlabelled substrate concentration [S] and the enzyme-substrate binding affinity K_M do not vary, the apparent rate constant k' becomes proportional to the maximal reaction velocity, which in turn is proportional to the total concentration of enzyme present, as indicated by equation (2.20).

2.2.2 Theory of Linear Compartmental Systems with Constant Transfer Coefficients

A typical PET data set contains the time course of radioactivity concentration, or time-activity curve (TAC), in plasma and in various tissues, measured after the injection of a radiotracer. The tissue TACs constitute the measured output of a system probed by an exogenous input, the plasma TAC. The purpose of making these measurements is to quantify the characteristic response of the physiological system given these input and output data.

A compartmental system is one that is composed of a series of interconnected compartments. A *compartment* is defined as an amount of material that is well mixed and kinetically distinct (*homogeneity* assumption) (DiStefano and Landaw, 1984). Material in a given form and/or in a given location qualify as compartments. Material is exchanged between compartments and with the external environment. Exchange can occur when the material crosses a physical barrier (e.g. membrane transport) or when it is transformed physically or chemically (e.g. metabolism). In the standard representation of compartmental systems, a box is used to represent a compartment and an arrow for the transfer of material into or out of that compartment. Mathematically, the exchange of material between compartments is expressed as a system of mass-balance equations in which the rate of change in the amount of material in each compartment is equal to the difference between the amount of material entering and exiting that compartment (Jacquez, 1988):

$$\frac{dq_i}{dt} = -k_{0i}q_i(t) - \sum_{j\neq i} k_{ji}q_i(t) + \sum_{j\neq i} k_{ij}q_j(t) + u_i(t), \tag{2.27}$$

where $q_j(t)$ and $q_i(t)$ are the *amount* of material in compartments j and i, respectively, and k_{ji} is the *rate constant* for the transfer of material from compartment i to compartment j. $u_i(t)$ is the rate at which material enters compartment i from the outside whereas $-k_{0i}q_i(t)$ is the rate at which material leaves compartment i to the outside. If the rate constants k's are independent of both the time interval (*stationarity* assumption) and the conjugate q's (*linearity* assumption), equation (2.27) becomes a first-order linear differential equation with constant coefficients. In matrix form, equation (2.27) can then be rewritten as

$$\dot{\mathbf{q}} = K\mathbf{q}(t) + \mathbf{u}(t), \tag{2.28}$$

where $k_{ii} = -k_{0i} - \sum_{j\neq i} k_{ji}$. If $\mathbf{u}(t) = 0$, the solution to the system of n homogeneous

differential equations is the sum of the n linearly independent exponential functions $\mathbf{q}(t) = \mathbf{v}\exp(\lambda t)$, of equation (2.28):

$$\mathbf{q}(t) = \sum_{i=1}^{n} c_i \mathbf{v}_i \exp(\lambda_i t), \tag{2.29}$$

where n is the number of compartments. The λ's are the system eigenvalues which are the non-trivial solutions to the characteristic polynomial $(K - \lambda I)\mathbf{v} = \mathbf{0}$, where I is the identity matrix. The $\mathbf{v}$'s are the corresponding system eigenvectors and each is found by solving the equation $K\mathbf{v}_i = \lambda_i \mathbf{v}_i$. The constants c_i's are determined by the initial conditions. When the initial conditions are set to $q_i(0) = 1$ and $q_{j\neq i} = 0$ for $j = 1, 2, ...n$, equation (2.29) represents the characteristic *impulse response* of the system.

Most often in PET, the compartments are not measured individually, but instead only the sum of the compartments of the system is available:

$$\begin{aligned} q_t(t) &= \sum_{j=1}^{n} q_j(t) \\ &= c_1\left(\sum_{i=1}^{n} v_{i1}\right)\exp(\lambda_1 t) + c_2\left(\sum_{i=1}^{n} v_{i2}\right)\exp(\lambda_2 t) + ...c_n\left(\sum_{i=1}^{n} v_{in}\right)\exp(\lambda_n t) \\ &= \sum_{i=1}^{n} A_i \exp(\lambda_i t), \end{aligned} \tag{2.30}$$

where the *macroparameters* A_i and λ_i are a combination of the *microparameters* k_{ji}. The number of microparameters must be less than or equal to the number of macroparameters ($2n = nA$'s+$n\lambda$'s) in order to uniquely identify the microparameters (Cobelli and DiStefano, 1980). Otherwise, either certain k's must be set to zero or some estimation strategy (like including *a priori* information or performing additional independent measurements) must be adopted in order to reduce the number of microparameters to be determined (Cobelli and DiStefano, 1980; Zierler, 1981; Landaw and DiStefano, 1984). Identifiability of all microparameters does not however guarantee a unique solution (Cobelli and DiStefano, 1980).

It is common practice in PET studies to inject the radiotracer into the blood stream such that the time course of radioactivity concentration in arterial plasma represents a time varying input function, $u_i(t)$, to the system. The response of the system, because it is linear and time invariant, can be calculated by convolving the impulse response of the system with

the input function:

$$y(t) = \int_0^t u_i(t) q_t(t-\tau) d\tau = u_i(t) \otimes \sum_{i=1}^{n} A_i \exp(\lambda_i t). \tag{2.31}$$

When the *concentrations* $C_i(t)$ are measured instead of the amounts of material $q_i(t)$, the above equations can easily be adapted by using the relation $q_i(t) = V_i \times C_i(t)$, where V_i is the space occupied by the material in compartment i (Zierler, 1981). **Appendix B** catalogs the solutions for the compartmental models that will be referred to in later parts of this thesis.

2.2.3 Parameters Estimation

The application of compartmental modelling can be divided into three separate steps (Jacquez, 1988). First, the development of plausible models should be based on background knowledge of the system under study and the chosen structures should lead to a physiological interpretation of the model parameters. Given a compartmental model, the second step is concerned with formulating and solving the equations that predict the behavior of the system. These first two steps constitute the forward problem and are treated in section 2.2.2 and **Appendix B**. The third step is the inverse problem of finding the parameter estimates and the plausible model that best describe the collected data. This difficult problem is addressed in the next two sections.

2.2.3.1 Non-Linear Least-Squares Analysis

Let us assume that the only source of deviation between the measurements $\mathbf{z}(t)$ and the model predictions $\mathbf{y}(t, \mathbf{p})$ is random measurement errors $\mathbf{e}(t)$:

$$\mathbf{z}(t) = \mathbf{y}(t, \mathbf{p}) + \mathbf{e}(t). \tag{2.32}$$

Let us further assume that $e_i(t)$ are independent and Gaussian distributed with zero mean and variances σ_i^2. The least-squares method then tries to find an estimate of $\mathbf{p}$ ($\hat{\mathbf{p}}$) that minimizes the weighted residual sum of squares (WRSS) between the N measurements $\mathbf{z}(t)$ and model predictions $\mathbf{y}(t)$:

$$WRSS(\hat{\mathbf{p}}) = \sum_{i=1}^{N} w_i [z(t_i) - y(t_i, \hat{\mathbf{p}})]^2, \tag{2.33}$$

where the weights are set to $w_i = 1/\sigma_i^2$. Data points having the smallest associated errors are given the greatest relative importance in the least-squares estimation procedure. Equation (2.33) has a unique minimum when the model $y(t_i, \mathbf{p})$ is linear in all its parameters $\mathbf{p}$. However, equation (2.30) is linear in the parameters A_i but non-linear in the parameters λ_i. Multiple minima can thus exist, and an iterative search of the parameter space does not guarantee finding the absolute minimum. Furthermore, starting values for $\mathbf{p}$ are required which influence both the number of iterations and the minimum (local or absolute) found. It is recommended to guide the search procedure by imposing boundary conditions on the values of $\mathbf{p}$, in particular that the values of k_{ji} must be non-negative or those of λ_i non-positive (Landaw and DiStefano, 1984).

Precision on the Parameter Estimates

The standard error (SE) on the estimate $\hat{p_i}$ can be calculated by taking the square root of the i^{th} diagonal element of the covariance matrix COV (Landaw and DiStefano, 1984) which is defined as

$$COV(t, \hat{\mathbf{p}}) = (J^T W^{-1} J)^{-1} \hat{\sigma^2}, \tag{2.34}$$

where J is the jacobian matrix with elements $j_{ij} = \frac{\partial y_i}{\partial p_j}$ for $i = 1, 2, ...N$ data points and $j = 1, 2, ...P$ parameters, and W is the diagonal matrix with elements w_i. When σ^2 is unknown, the unbiased estimate $\hat{\sigma^2} = WRSS(\hat{\mathbf{p}})/(N - P)$ can be used. The i, j^{th} element of the covariance matrix corresponds to the covariance between the two parameters $\hat{p_i}$ and $\hat{p_j}$. The correlation coefficient, which takes values between -1 and 1, can also be derived from the covariance matrix by dividing the i, j^{th} element by the product $SE(\hat{p_i})SE(\hat{p_j})$.

Strong correlations between parameters and poor precision on parameter estimates are signs that the covariance matrix is ill-conditioned (Landaw and DiStefano, 1984). This problem can result from a poor experimental design. The data sampling must be long and frequent enough to capture the full dynamic range of the model. Otherwise, two exponential terms that are close but distinct will not be distinguished. Ill-conditioning of the covariance matrix can also be caused by overparametrization, i.e. fitting the measurements to a model of order $n + 1$ when the system should really be modelled with n compartments. The least-squares method then attempts to separate two exponential terms that have indistinguishable λ's and for which only the sum of the corresponding A's can be estimated precisely. Confirmation of this diagnosis can be obtained with statistical tests.

Discrimination Amongst Compartmental Models

Models of increasing order can sequentially be compared by performing an F-test under the null hypothesis that the model of order $n+1$ does not give a better fit to the measurements than the model of order n (Landaw and DiStefano, 1984):

$$F = \frac{(WRSS_n - WRSS_{n+1})/(P_{n+1} - P_n)}{WRSS_{n+1}/(N - P_{n+1})}. \tag{2.35}$$

The F distribution has $(P_{n+1} - P_n, N - P_{n+1})$ degrees of freedom where again P_i is the number of parameters in model i and N is the number of data points. When the probability of obtaining a larger F-value is no longer significant, the lower-order model is accepted as the best model in a statistical sense. It is then usually symptomatic to find, in the higher-order model, one value of A_i that cannot be distinguished from zero within its SE.

2.2.3.2 Multiple-Time Graphical Analyses

Compartmental analysis yields parameter estimates that are highly dependent upon the particular model chosen. The complexity of the physiological system under study often precludes the derivation of a model that faithfully describes all underlying processes. Rather than solving the system of differential equations for the individual rate constants, graphical analyses integrate, linearise and solve the equations for lumped rate constants that can be interpreted independently of the details of the compartmental model. Typically, the measured variables are transformed into variables that, when plotted against each other, reveal the asymptotic behavior of the system. Linear regression is then used instead of non-linear least squares to estimate the system parameters. This approach requires that the system reaches steady state within the duration of the study after which time the uptake rate constant or the volume of distribution are determined for irreversible and reversible systems, respectively.

Irreversible Compartmental Models

The graphical approach developed by Patlak *et al*(1983, 1985) is applicable to all compartmental models that have the following structure:

1. The radiotracer enters the system only from the plasma.

2. The radiotracer rapidly exchanges between the plasma and a first tissue region, made up of any number of compartments. The radiotracer can flow directly or indirectly into any of these compartments, transfer freely from one compartment to another, and flow back into the plasma. This first region is reversible.

3. The radiotracer can enter a second tissue region either from the plasma or from the reversible tissue region but cannot leave from it. This irreversible tissue region consists of one or more compartments lumped together into a single compartment.

4. The radiotracer can only be metabolised in the irreversible region, and the metabolites must also be trapped in that region.

5. The radiotracer is not initially present in either the reversible or the irreversible compartments.

6. The compartmental model must also obey the conditions of linearity and stationarity.

Let us study such an irreversible compartmental system for an infinite time. Let us assume that after the time t, the radiotracer concentration in plasma $C_p(t)$ tends to zero. The radiotracer concentration in tissue at infinite time $C_t(\infty)$ is equal to the radiotracer concentration in tissue at time t $C_t(t)$ diminished by the amount of the radiotracer in the reversible compartment that leaves the system thereafter:

$$C_t(\infty) = C_t(t) - (f(t)C_e(t) + V_pC_p(t)) \tag{2.36}$$

$$\Rightarrow C_t(t) = C_t(\infty) + f(t)C_e(t) + V_pC_p(t), \tag{2.37}$$

where V_p is the fractional volume of tissue occupied by plasma, and $f(t)$ is the fraction of the radiotracer concentration in the reversible compartment $C_e(t)$ that does not enter the irreversible compartment. If after a certain time t^*, the radiotracer concentration in plasma changes slowly enough for the radiotracer concentration in the reversible compartment to reach effective steady state with the radiotracer concentration in plasma, then the fraction $f(t)$ becomes constant and

$$VD_e = \frac{C_e(t)}{C_p(t)} \quad \Rightarrow \quad C_e(t) = VD_eC_p(t), \tag{2.38}$$

where VD_e is the volume of distribution of the radiotracer in the reversible compartment. Replacing in equation (2.37) yields

$$C_t(t) = C_t(\infty) + (fVD_e + V_p)C_p(t). \tag{2.39}$$

Defining the *uptake rate constant* K_i (Patlak *et al*, 1981) as the fraction of the integrated radiotracer concentration in the plasma that has accumulated in tissue at infinite time:

$$K_i = \frac{C_t(\infty)}{\int_0^\infty C_p(T)dT} \sim \frac{C_t(\infty)}{\int_0^t C_p(T)dT}, \tag{2.40}$$

since $C_p(T > t) = 0$. Inserting the above expression for K_i in equation (2.39) gives

$$C_t(t) = K_i \int_0^t C_p(T)dT + (fVD_e + V_p)C_p(t). \tag{2.41}$$

Dividing each term by $C_p(t)$ yields

$$\frac{C_t(t)}{C_p(t)} = K_i \frac{\int_0^t C_p(T)dT}{C_p(t)} + (fVD_e + V_p). \tag{2.42}$$

A plot of the instantaneous tissue concentration vs. the integrated plasma concentration both normalized to the instantaneous plasma concentration produces a curve that becomes a straight line after a time t^*, which depends on the individual rate constants of the comparmental model. The linear portion of the *Patlak plot* has a positive slope corresponding to the uptake rate constant K_i and a positive intercept. The uptake rate constant can be related to the individual rate constants as demonstrated in **Appendix B**. For an example of a Patlak plot, see **Figure 6.3a)**.

Reversible Compartmental Models

A reversible system is one which lacks an irreversible compartment. A Patlak plot will confirm that a compartmental system is reversible when the slope of the linear portion is zero. It however will not provide a useful parameter to characterize such systems. Another transformation is thus called for.

In a reversible compartmental system, the radiotracer concentration in tissue at infinite time $C_t'(\infty)$ is zero because the radiotracer is not trapped in tissue. Since there is no irreversible compartment, the fraction of the radiotracer that leaves the system $f'(t)$ is

equal to one at all times. Equation (2.37) then becomes

$$C'_t(t) = C'_e(t) + V'_p C_p(t) \tag{2.43}$$

$$\Rightarrow C'_e(t) = C'_t(t) - V'_p C_p(t), \tag{2.44}$$

where $C'_e(t)$ is the concentration in the reversible compartment, and V'_p is the fractional volume of plasma in tissue, respectively. A general structure for the reversible compartmental system can be defined using equation (2.28) and expressing $\mathbf{u}(t)$ as $\mathbf{Q}'C_p(t)$:

$$\dot{\mathbf{C}}' = K'\mathbf{C}'(t) + \mathbf{Q}'C_p(t), \tag{2.45}$$

where $\mathbf{Q}'$ is the column vector that contains the rate constants from the plasma to each of the exchangeable compartments. Integrating equation (2.45) and setting $\mathbf{C}'(0) = \mathbf{0}$ gives

$$\mathbf{C}'(t) = K' \int_0^t \mathbf{C}'(T)dT + \mathbf{Q}' \int_0^t C_p(T)dT. \tag{2.46}$$

The steady-state volume of distribution in the individual compartments can be derived from (Patlak *et al*, 1983) to be

$$\mathbf{VD}' = \frac{\mathbf{C}'(t)}{C_p(t)} = -(K')^{-1}\mathbf{Q}'. \tag{2.47}$$

Using the unity column vector $\mathbf{U}$, the total activity concentration in the exchangeable compartments and the associated total volume of distribution can be expressed as

$$C'_e(t) = \mathbf{U}^T\mathbf{C}'(t) \tag{2.48}$$

$$VD'_e = \mathbf{U}^T\mathbf{VD}' = -\mathbf{U}^T(K')^{-1}\mathbf{Q}'. \tag{2.49}$$

Multiplying both sides of equation (2.46) with $\mathbf{U}^T(K')^{-1}$ and using the identities given by equations (2.48) and (2.49) yields

$$\mathbf{U}^T(K')^{-1}\mathbf{C}'(t) = \int_0^t C'_e(T)dT - VD'_e \int_0^t C_p(T)dT. \tag{2.50}$$

Replacing $C_e(t)$ with equation (2.44) and rearranging gives

$$\mathbf{U}^T(K')^{-1}\mathbf{C}'(t) = \int_0^t C'_t(T)dT - (VD'_e + V'_p) \int_0^t C_p(T)dT. \tag{2.51}$$

Once steady state is reached, equations (2.43) and (2.45) become

$$C'_t(t) = (VD'_e + V'_p)C_p(t) \tag{2.52}$$

$$\begin{aligned} 0 &= (K')\mathbf{C}'(t) + \mathbf{Q}'C_p(t) \\ \Rightarrow \mathbf{C}'(t) &= -(K')^{-1}\mathbf{Q}'\frac{C'_t(t)}{VD'_e + V'_p}. \end{aligned} \tag{2.53}$$

Replacing $\mathbf{C}'(t)$ in equation (2.51) with its expression given by equation (2.53) and rearranging yields

$$\int_0^t C'_t(T)dT = (VD'_e + V'_p)\int_0^t C_p(T)dT - \mathbf{U}^T(K')^{-2}\mathbf{Q}'\frac{C'_t(t)}{VD'_e + V'_p}. \tag{2.54}$$

As noticed by Logan *et al*(1990), dividing both sides with $C'_t(t)$ gives

$$\frac{\int_0^t C'_t(T)dT}{C'_t(t)} = (VD'_e + V'_p)\frac{\int_0^t C_p(T)dT}{C'_t(t)} - \frac{\mathbf{U}^T(K')^{-2}\mathbf{Q}'}{VD'_e + V'_p}. \tag{2.55}$$

A *Logan plot* can be constructed by plotting the integrated tissue concentration against the integrated plasma concentration both normalized to the instantaneous tissue concentration. After a time t^*, which again depends on the individual rate constants of the compartmental model, the curve approaches a straight line with a positive slope corresponding to the total volume of distribution of the radiotracer and a negative intercept. The volume of distribution can also be infered from the individual rate constants as shown in **Appendix B**. An example of a Logan plot can be found in **Figure 6.3b)**. Note that a Logan plot will fail to characterize an irreversible compartmental system because the slope of the linear portion will take very large (or infinite) values regardless of the tissue uptake.

2.2.4 Input Functions

The tissue TAC is extracted from the PET dynamic images either from a single voxel or from several voxels grouped into a region of interest. The input function in PET corresponds to time course of radioactivity concentration in plasma attributable to the injected radiotracer. The input function is typically measured by sampling blood from the radial artery, fairly rapidly initially and at longer time intervals as the PET study continues. The blood data acquired in this way are inevitably distorted by delay and dispersion between the points of radiotracer assay and delivery to tissue (Meyer, 1989). For radiotracers with kinetics slower than blood flow, these effects can be accounted for by the inclusion of a

delay (Δt) and a blood volume (V_b) term in the equation of the compartmental model (Cunningham and Lammertsma, 1994):

$$y(t) = u_i(t + \Delta t) \otimes q_t(t) + V_b \times u_i(t + \Delta t). \tag{2.56}$$

When the blood and tissue data are acquired with different devices, these must be cross-calibrated such that the units of the input function and the tissue TAC are the same. This can be achieved by preparing a phantom and an aliquot from the same solution and measuring their respective radioactivity concentration in the PET camera and in the radiation detector used to measure the blood concentration. Alternatively, each device can be calibrated against a third device that has previously been calibrated with a standard radioactive source.

Additional measurements are required when the radiotracer is compartmentalized in the erythrocytes and/or metabolised in peripheral tissue. The effect of the former is to reduce the availability of the radiotracer to cross the blood-brain barrier. The effect of the latter is to transfer the radiolabel to molecules other than the injected radiotracer. The partition of radioactivity between plasma and erythrocytes can be corrected for by measuring the radioactivity concentration in both plasma and whole blood. The contribution of the metabolites to the total plasma radioactivity can be separated from that of the unmetabolised parent using analytical chemistry procedures, most commonly high pressure liquid chromatography (HPLC) analysis. Unlike whole blood which can be sampled continuously and counted on-line, the measurements for the determination of blood partition and peripheral metabolism can only be performed at a few discrete times. Interpolation and extrapolation of these corrections over the duration of the PET study is therefore necessary.

The complications associated with blood sampling and analyses have led to the development of reference tissue approaches which use a reference tissue as an indirect input function to the target tissue.

2.2.4.1 Reference Tissue Compartmental Models

The reference tissue models were originally developed for radioligands that bind reversibly to receptors (Cunningham *et al*, 1991; Hume *et al*, 1992; Lammertsma and Hume, 1996) and have been applied to radioligands for which a tissue with negligible concentration of specific binding sites exists (Lammertsma *et al*, 1996; Gunn *et al*, 1997; Gunn *et al*,

1998). The models can however be extended to radiotracers that are trapped irreversibly, provided that a tissue with negligible trapping can be found (Gunn *et al*, 2001). The reference tissue models further assume that the volume of distribution of the radiotracer in the reference tissue approximates the volume of distribution of the radiotracer in the state of not specifically bound or not trapped in the target tissue. In its general form, equation (2.31) becomes

$$y(t) = R_1 C_r(t) + R_1 C_r(t) \otimes \left[\sum_{i=1}^{n} A_i \left(\frac{k_2'}{R_1} + \lambda_i\right) \exp\left(\lambda_i t\right)\right], \tag{2.57}$$

where the radioactive concentration in the reference tissue $C_r(t)$ was assumed to be described by a one-compartment two-parameter (K_1' and k_2') model (see **Appendix B.1**). Without the availability of blood data, the reference tissue models cannot allow the estimation of the individual clearance for the target (K_1) and reference (K_1') tissue. Instead, differences in the radiotracer delivery to these tissue are accounted for by the ratio $R_1 = K_1/K_1'$. The contribution of the blood volume to the radioactivity concentration in either tissue cannot be estimated and thus is assumed to be negligible. The specific equations for the full, irreversible and simplified reference tissue models are derived in **Appendix C**.

2.2.4.2 Reference Tissue Graphical Analyses

Patlak and Blasberg (1985) extended their approach to the situation where the radiotracer concentration could be measured in a target tissue which irreversibly traps the radiotracer as well as a reference tissue devoid of trapping.

Expressing $C_p(t)$ and $\int_0^t C_p(T)dT$ in terms of $C_t'(t)$ and $\int_0^t C_t'(T)dT$ using equations (2.52) and (2.54), respectively, one gets

$$C_p(t) = \frac{C_t'(t)}{VD_e' + V_p'} \tag{2.58}$$

$$\int_0^t C_p(T)dT = \frac{1}{VD_e' + V_p'} \int_0^t C_t'(T)dT + \frac{\mathbf{U}^T(K')^{-2}\mathbf{Q}'}{(VD_e' + V_p')^2} C_t'(t). \tag{2.59}$$

Inserting into equation (2.42) and rearranging yields

$$\frac{C_t(t)}{C_t'(t)} = \frac{K_i}{VD_e' + V_p'} \frac{\int_0^t C_t'(T)dT}{C_t'(t)} + \left[K_i \frac{\mathbf{U}^T(K')^{-2}\mathbf{Q}'}{(VD_e' + V_p')^2} - \frac{fVD_e + V_p}{VD_e' + V_p'}\right]. \tag{2.60}$$

Plotting the instantaneous target tissue concentration vs. the integrated reference tissue concentration both normalized to the instantaneous reference tissue concentration

gives after a certain time t^* a straight line with a slope equal to $\frac{K_i}{VD'_e+V'_p}$ and a positive y-intercept. The slope of this graph is thus equal to the slope of the graph obtained with a plasma input function normalized by the volume of distribution of the reference tissue. It is important to note that the time to reach steady state with the reference tissue input function may differ from that of the plasma input function. Refer to **Figure 6.3c)** for an example of a reference tissue Patlak plot.

Logan *et al*(1996) also extended their approach to accomodate a reference tissue input. Assuming, similarly to the reference tissue model, that the radioactive concentration in the reference tissue $C_r(t)$ is described by a one-compartment two-parameter (K'_1 and k'_2) model (again see **Appendix B.1**), one gets

$$\frac{\int_0^t C_r(T)dT}{C_r(t)} = (VD_r + V_p)\frac{\int_0^t C_p(T)dT}{C_r(t)} - \frac{1}{k'_2}. \tag{2.61}$$

Isolating $\int_0^t C_p(T)dT$ in equation (2.61) and inserting it into equation (2.55) gives

$$\frac{\int_0^t C'_t(T)dT}{C'_t(t)} = \frac{VD'_e + V'_p}{VD_r + V_p}\frac{\int_0^t C_r(T)dT + \frac{1}{k'_2}C_r(t)}{C'_t(t)} - \frac{\mathbf{U}^T(K')^{-2}\mathbf{Q}'}{VD'_e + V'_p}. \tag{2.62}$$

Plotting the integrated target tissue concentration normalized to the instantaneous target tissue concentration against the sum of the integrated reference tissue concentration and the instantaneous reference tissue concentration over k'_2 also normalized to the instantaneous target tissue concentration gives after a certain time t^* a straight line with a slope equal to the ratio of the volumes of distribution in the target and reference tissue and a negative y-intercept. The implementation of this approach is limited by the value of k'_2 which is unknown. For k'_2 values sufficiently large, the term $C_r(t)/k'_2$ can be neglected, or otherwise approximated by a population value. However, as the value for k'_2 becomes smaller, small deviations from its estimate introduce large variations in the estimates of the abscissa and consequently in the calculation of the slope. The derivations of the slope of the reference tissue Patlak and Logan plots in terms of the individual rate constants for the commonly used compartmental models are given in **Appendix C**.

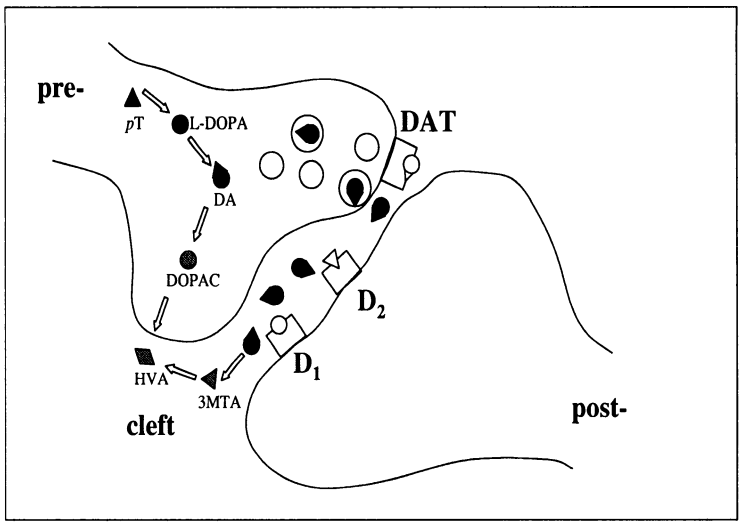

Figure 2.3: *Synaptic transmission from a dopaminergic neuron: Dopamine (DA) is synthesized in the pre-synaptic neuron, released into the synapse from where it binds to specific receptors at the surface of the post-synaptic neuron. Dopamine can also be broken down into several metabolites or taken up and stored into vesicles. (See text for details and abreviations)*

2.3 The Brain Dopaminergic System

2.3.1 Dopamine Metabolism and Pathways

This section serves as a short introduction to biological concepts referred to in the following two sections.

Two types of cells are found in brain tissues (McGeer *et al*, 1987): Nerve cells (or *neurons*), which carry the electrical nerve impulse, are interleaved with supporting *glial cells*, broadly divided into oligodendroglia, astroglia and microglia. Neurons are composed of a cell body (or *soma*) from which extend a single long stem (or *axon*) and multiple branches (or *dendrites*). The electrical nerve impulse is propagated between neurons via the transmission of specific chemical messengers (called *neurotransmitters*) across the small cleft separating two nerve terminals, together forming a junction (called *synapse*). In the brain, the transport of substances from capillary blood to tissue is tighly regulated. Unlike elsewhere in the body, the capillary endothelial cells overlap and are enclosed by sealed astroglial cells, together creating a diffusion barrier, the *blood-brain barrier* (BBB). Furthermore, specific active transport systems allow penetration of critical substances, amongst others glucose and essential amino acids, against concentration gradients.

Dopamine (DA) is a catecholamine neurotransmitter present in the brain in concentrations of nmol/g of tissue (McGeer *et al*, 1987). As depicted in **Figure 2.3**, it is synthesized *in situ* from the successive action of tyrosine hydroxylase (TH) on the endogenous amino acid L-*p*-tyrosine (*p*T) followed by aromatic L-amino acid decarboxylase (AADC) on L-3,4-dihydroxyphenylalanine (L-DOPA). DA is packaged into pre-synaptic vesicles by the vesicular monoamine transporter (VMAT) where it is protected from further metabolism by monoamine oxidase (MAO). Upon stimulation, DA is released into the synaptic cleft. From there DA can either bind to post-synaptic dopamine receptors (eliciting an excitatory or inhibitory metabotropic action on the D_1-like or D_2-like receptors, respectively), be transformed by the combined actions of catechol-*O*-methyl transferase (COMT) and MAO into several metabolites (3-methoxy-tyramine (3MTA), 3,4-dihydroxy-phenylacetic acid (DOPAC) and homovanillic acid (HVA)) which diffuse away from the synapse, or be recaptured at the pre-synaptic reuptake site, the dopamine transporter (DAT). The synthesis of dopamine is regulated at the tyrosine hydroxylation step. Newly synthesized dopamine is preferentially released and metabolised over stored dopamine. The turnover time of dopamine in the striatum has been estimated to be of the order of 1.5 to 4 hours (McGeer *et al*, 1987).

There are three major dopaminergic pathways in the brain (Volkow *et al*, 1996; McGeer *et al*, 1987): The *nigrostriatal pathway* originates from cell bodies located in the substantia nigra (in the brainstem) which project predominantly to the striatum (in the basal ganglia); cells bodies in the ventral tegmental area (in the brainstem) projecting to regions in the limbic system (hippocampus, amygdala, nucleus accumbens, cingulate gyrus and frontal cortex) form the *mesolimbic-mesocortical pathway*; the *tuberoinfundibular pathway* plays a role in coupling the hypothalamus (in the diencephalon) to the pituitary gland (outside the BBB), thereby contributing to the stimulation and inhibition of various hormones. Disruption of dopamine function in the nigrostriatal pathway, which is involved in the initiation and execution of movements, leads to neurological disorders such as Parkinson's disease (PD). The mesolimbic-mesocortical pathway is associated with mood, reinforcement and thought organisation, and is implicated in psychiatric illnesses such as schizophrenia and substance abuse. The number of dopamine neurons declines with age (McGeer *et al*, 1977).

Dopamine function can be selectively altered, whether reversibly or irreversibly, at different levels using various pharmacological agents. Animal models have been developed

to investigate mechanisms and explore possible therapies for the disturbed dopaminergic system. Of particular interest for this thesis, the repeated administration of the neurotoxin 1-methyl-4-phenyl-1,2,3,6-tetrahydropyridine (MPTP) leads to the development of persistent symptoms of Parkinsonism in human subjects and non-human primates (Burns *et al*, 1983). The MPTP-induced dopaminergic lesions in human subjects progress with time at a similar rate as PD (Vingerhoets *et al*, 1994b), but create a striatal pattern of dopamine loss which is different from that observed in PD (Snow *et al*, 2000). An alternative lesion, applied to rats which are resistant to MPTP, uses the neurotoxin 6-hydroxydopamine (6-OHDA) to unilaterally and selectively destroy the nigrostriatal pathway and create a hemiparkinsonian rat model (Perese *et al*, 1989). Dopamine function can also be probed with PET in combination with a variety of radiotracers labelling dopamine precursors, degrading enzymes, transporters or receptors, and pharmacological or behavioral challenges (Volkow *et al*, 1996).

2.3.2 Studying Dopamine Synthesis using 6F-DOPA

Dopamine does not cross the BBB and thus must be synthesized *in situ* from its precursors, L-*p*-tyrosine and L-DOPA, which can cross the BBB. 6-[^{18}F]fluoro-L-DOPA, L-DOPA labelled with fluorine-18 in position 6 on the benzene ring, was developed as an analogue of L-DOPA in order to visualize dopamine producing neurons *in vivo* (Garnett *et al*, 1983). The detection of 6F-DOPA metabolites — 6-[^{18}F]fluoro-3-*O*-methyl-DOPA (6F-3OMD), 6-[^{18}F]fluoro-dopamine (6F-DA), 3-methoxy-6-[^{18}F]fluoro-tyramine (6F-3MTA), 3,4-dihydroxy-6-[^{18}F]fluoro-phenylacetic acid (6F-DOPAC), 6-[^{18}F]fluoro-homovanillic acid (6F-HVA) and 6F-DA sulfated conjugates — in blood analysis and bioassays of brain homogenates has demonstrated that 6F-DOPA follows the same metabolic pathways as L-DOPA (Firnau *et al*, 1988; McLellan *et al*, 1991; Melega *et al*, 1991). Using various quantitative methods, fluorine-18 accumulation after the injection of 6F-DOPA has been shown to be reduced in the striatum of non-human primates lesioned with MPTP injections (Pate *et al*, 1993), and in the striatum of subjects suffering from Parkinson's disease and other movement disorders (Snow *et al*, 1993a). Although these studies have confirmed that 6F-DOPA distribution and kinetics reflect the functional integrity of presynaptic dopaminergic neurons, no concensus has been reached on what is the most appropriate method of quantifying PET/6F-DOPA data.

The PET/6F-DOPA images contain information about at least two distinct processes in the brain dopaminergic system: The transport of 6F-DOPA across the BBB (Leenders *et al*, 1986) and the central decarboxylation of 6F-DOPA by the enzyme AADC. Disagreement among research groups remains on whether information on the vesicular storage of 6F-DA, the clearance of 6F-DA metabolites and the central *O*-methylation of 6F-DOPA can be inferred from the PET/6F-DOPA images. Another unresolved issue concerns how to model properly 6F-3OMD, the major 6F-DOPA metabolite which is produced in peripheral organs (liver, kidney) and erythrocytes and which can cross the BBB, therefore contributing to the fluorine-18 uptake signal in brain tissue.

2.3.2.1 Biochemical Data

The configuration of the different models for 6F-DOPA and 6F-3OMD as well as their underlying assumptions are based on the following biochemical evidence gathered from rodent and non-human primate studies:

1. The peripheral metabolism of 6F-DOPA can be restricted to the formation of 6F-3OMD with a peripheral AADC inhibitor like carbidopa (L-α-hydrazino-α-methyl-β-(3,4-dihydroxyphenyl)propionic acid) (Melega *et al*, 1990);

2. Significant amounts of 6F-3OMD cross the BBB, and thus the time course of the methylated metabolite in the brain must be accounted for (Doudet *et al*, 1991; Wahl *et al*, 1994);

3. The volume of distribution of 6F-3OMD is close to one in all brain tissue (Wahl *et al*, 1994);

4. The kinetics of 6F-3OMD varies in different brain tissue and is adequately modelled by a single reversible compartment (Doudet *et al*, 1991; Wahl *et al*, 1994);

5. In the striatum, 6F-DA is synthesized in significant amounts, and further metabolised to 6F-DOPAC and 6F-HVA (Melega *et al*, 1991);

6. In the cortex, only the metabolites of 6F-DA were detected, suggestive of an increased turnover rate of 6F-DA relative to that in the striatum (Melega *et al*, 1991);

7. Neither 6F-DA nor its metabolites were detected in the cerebellum (Melega *et al*, 1991).

2.3.2.2 Compartmental Analysis

A number of compartmental models for 6F-DOPA metabolism have been proposed (Gjedde *et al*, 1991; Kuwabara *et al*, 1993; Huang *et al*, 1991a; Shoghi-Jadid *et al*, 2000; Wahl and Nahmias, 1996a,b; Dhawan *et al*, 1996). As summarized in **Figure 2.4**, they differ in the number of compartments and rate constants as well as in the biological constraints that are invoked in order to estimate the parameters of interest. The solutions to the unconstrained compartmental systems are given in **Appendix B**.

Starting with the most elaborate compartmental model (**Figure 2.4a)**), the Gjedde *et al* model (1991; Kuwabara *et al*, 1993) accounts for the transport of 6F-DOPA from plasma to brain tissue (K_1^D for the target tissue, and $K_1^{D\prime}$ for the reference tissue) and back to plasma (k_2^D and $k_2^{D\prime}$ for the target and reference tissue, respectively). In brain tissue, 6F-DOPA is decarboxylated to 6F-DA by the enzyme AADC (k_3 and k_3' for the target and reference tissue, respectively). 6F-DA is then either stored in neuronal vesicles or further metabolised (k_4). The non-diffusable metabolite 6F-3MT resides in the brain with the stored 6F-DA while the diffusible metabolites 6F-DOPAC and 6F-HVA leave the brain (k_5). In the brain, the *O*-methylation of 6F-DOPA into 6F-3OMD (k_6 and k_6' for the target and reference tissue, respectively) is assumed to be negligible. In the periphery, 6F-DOPA is metabolised to 6F-3OMD. Plasma born 6F-3OMD crosses the BBB bidirectionally (K_1^M and k_2^M for the target tissue, and K'^M_1 and k'^M_2 for the reference tissue) but does not undergo any further metabolism in brain tissue. The time course of 6F-DOPA and 6F-3OMD concentrations in plasma are used as separate input functions to the 6F-DOPA and 6F-3OMD compartmental models, respectively, which are summed together to give the total radioactivity concentration in tissue. The number of parameters is reduced from seven to five by assuming that the relative transport of 6F-DOPA and 6F-3OMD across the BBB (q value) is uniform in all brain tissue and set to be equal to that determined in rats (Reith *et al*, 1990). The number of parameters is further reduced from five to three by assigning to the rate constants k_4 and k_5 in the target tissue the values of 0.02 and 0.005 min^{-1}, respectively, determined in six human subjects (Kuwabara *et al*, 1993), and by setting them to zero in the reference tissue. The constrained model for the reference tissue (taken to be the frontal cortex) is first solved for the parameters K'^D_1, k'^D_2 and k_3'. Then, under the assumption that the distribution of 6F-DOPA is uniform in all brain tissue, the parameters K_1^D and k_3 are estimated using the volume of distribution of 6F-DOPA determined in the

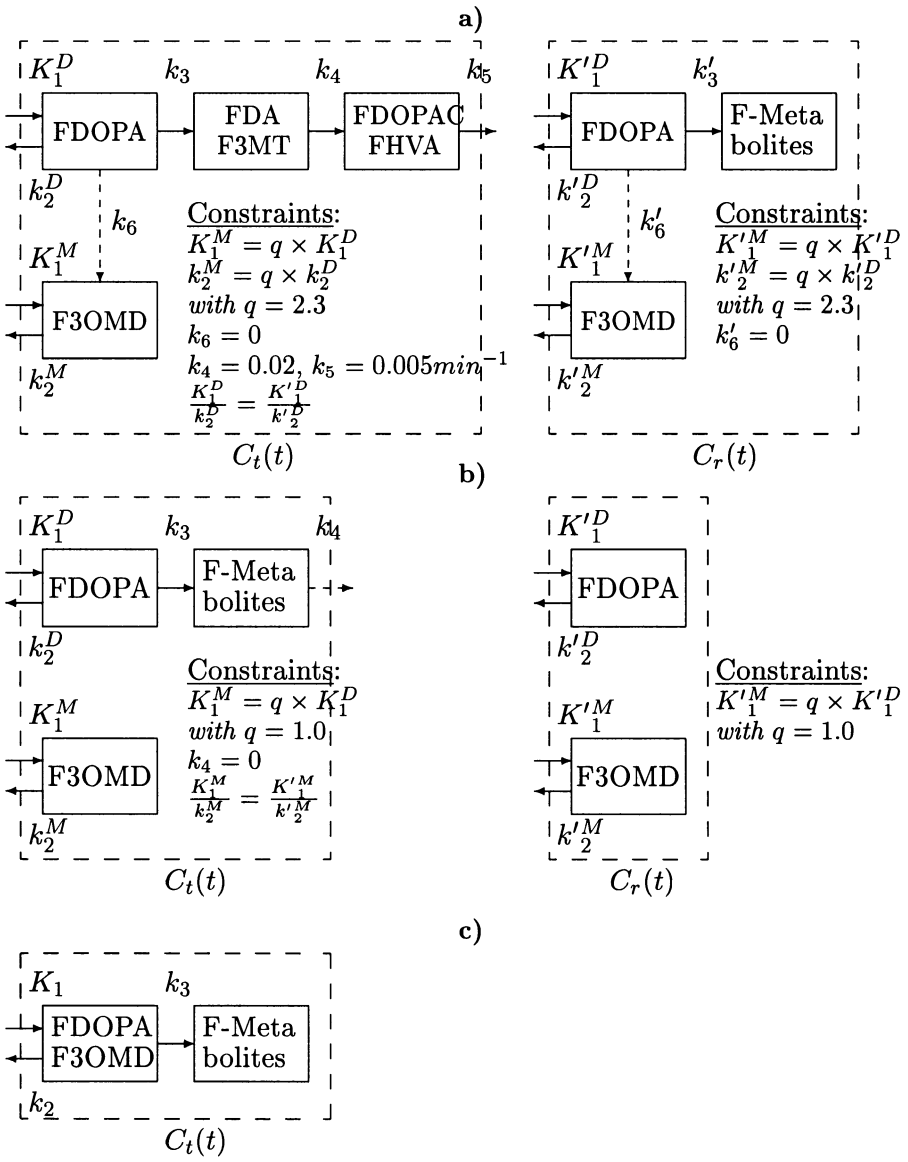

Figure 2.4: *Comparison of the different compartmental models proposed for the metabolism of 6F-DOPA:* **a**) *The Gjedde et al model (1991) as revised by Kuwabara et al(1993),* **b**) *the Huang et al model (1991a) as revised by Shoghi-Jadid et al(2000), and* **c**) *the Wahl and Nahmias model (1996b).* $C_t(t)$ *and* $C_r(t)$ *refer to the total radioactivity concentration in the target (left) and reference tissue (right), respectively. (See text for details and abreviations)*

reference region.

Huang *et al*(1991a) proposed a simpler compartmental model (**Figure 2.4b)**) which was later modified by Shoghi-Jadid *et al*(2000). The frontal cortex was replaced by the cerebellum, thereby eliminating the metabolism and trapping processes from the reference tissue. The distinction between diffusible and non-diffusible metabolites was removed, and with it the need for the rate constant k_5. The rate constant k_4 now represents the metabolism of 6F-DA and the clearance of its metabolites from the target tissue. In the original version of the model, the average value of k_4 was found to be an order of magnitude smaller than the average value of k_3. Including it in the model yielded significantly better fits to the data and increased the estmate of k_3 by 50%. In the revised version, k_4 was set to zero. Since both 6F-DOPA and 6F-3OMD are transported across the BBB via the same large neutral amino acid (LNAA) carrier system, the q value was set to unity in both the target and reference tissues. Instead of 6F-DOPA, 6F-3OMD is assumed to be distributed uniformly in all brain tissue (Wahl *et al*, 1994) and the volume of distribution of 6F-3OMD in the target tissue is accordingly set to that found in the reference region (Stout *et al*, 1998). These constraints reduced the number of parameters to estimate for the target tissue from six to three: K_1^D, k_2^D and k_3.

A way to circumvent making assumptions about the kinetics of 6F-3OMD in brain tissue is to determine the kinetics of 6F-OMD independently from that of 6F-DOPA by separate injections of each labelled compound in the same individual (Wahl and Nahmias, 1996a; Dhawan *et al*, 1996). Both studies found that the ratio of the forward rates of transport of 6F-3OMD and 6F-DOPA (q value) is on average close to unity, in support of the Huang *et al* model over the Gjedde *et al* model. The inclusion of the rate constants k_4 and k_5 did not improve the fits to the data from either studies. Dhawan *et al*(1996) estimated the volume of distribution of 6F-DOPA in the frontal cortex (K'^D_1/k'^D_2) to be 20-30% lower than in the striatum (K_1^D/k_2^D), further invalidating the constraint in the Gjedde *et al*model. Dhawan *et al*(1996) proposed another model for 6F-DOPA kinetics similar to the Huang *et al*model, but used population values for K_1^M(=0.040 min^{-1}) and k_2^M(=0.042 min^{-1}) instead of applying constraints based on parameters estimated from reference tissue. Combined 6F-DOPA and 6F-3OMD studies in an individual are not clinically practical since the dual injections double the radiation dose to the subject and the time necessary to complete the studies (Wahl and Nahmias, 1996a). Population values can be used only when the 6F-DOPA study is performed under the same conditions as those of the 6F-3OMD

study and if the parameters of interest are proven to be relatively insensitive to intersubjects variations in the rate constants for 6F-3OMD (Dhawan *et al*, 1996; Stout *et al*, 1998; Huang *et al*, 1998).

Wahl and Nahmias (1996b) also approached the problem from another angle. They compared a series of increasingly complex compartmental models for 6F-DOPA metabolism and proposed the simplest model that adequately fitted, in a statistical sense, the PET/6F-DOPA data: a two-compartment three-parameter model (**Figure 2.4c)**). Models that include additional compartments and/or rate constants, like the Gjedde *et al*and the Huang *et al*models, or models that use population values for the rate constants of 6F-3OMD, like the Dhawan *et al*model, failed to improve the fit to the data as indicated by an F-test. From a purely mathematical point of view, they concluded that it was unjustifiable to separate the kinetics of 6F-3OMD from that of 6F-DOPA in plasma and brain tissue, unless independent measures can be obtained in the subjects being studied, or to take into account the metabolism of 6F-DA and the clearance of its metabolites. The simplicity of the model, however, is counterbalanced by a more complicated physiological interpretation of the rate constants, in particular k_3.

The compartmental models presented above were validated on different datasets, some acquired on humans (Huang *et al*, 1991a; Kuwabara *et al*, 1993; Wahl and Nahmias, 1996a,b; Dhawan *et al*, 1996), others on non-human primates (Shoghi-Jadid *et al*, 2000), rendering a comparison between the parameter estimates difficult. On the same two groups of human subjects, one comprising normal controls, the other Parkinson's disease subjects at different stages of the disease, Ishikawa *et al*(1996) compared the ability of the parameter estimates given by three different compartmental models (Kuwabara *et al*, 1993; Wahl and Nahmias, 1996b; Dhawan *et al*, 1996) to discriminate between these two groups and to correlate the parameter estimates with independent indices of disease severity. The Gjedde *et al*model estimated the decarboxylation rate constant (k_3) in the normal group to be 0.082 $\pm$0.051 min^{-1}, which is four times larger than that estimated using the Dhawan *et al*model (0.021 $\pm$0.010 min^{-1}) and an order of magnitude larger than the Wahl and Nahmias model estimate (0.0065 $\pm$0.0031 min^{-1}). Only the first two models yielded k_3 estimates that distinguished between normal controls and PD subjects. However, the uptake rate constant (K_i) and the simple striatal-to-occipital ratio (SOR) were found to be better discriminants than k_3. Furthermore, the same two model estimates of k_3 and K_i correlated significantly with scores of disease severity. The inferior sensitivity of k_3 over K_i

to discriminate PD subjects from normal controls is probably due to the larger intersubject variations in the k_3 estimates among the normal group (COV~50%) compared to that in K_i (COV~20%) and SOR (COV~10%). Hoshi *et al*(1993) reported the opposite finding that the k_3 estimates derived from either the Gjedde *et al*model or the original Huang *et al*model discriminated between bilaterally affected PD subjects and normal controls better than did the K_i estimates. These conflicting conclusions demonstrate that the sensitivity of the different analysis methods to extraneous factors and model assumptions are not well understood nor controlled.

2.3.2.3 Graphical Analysis

Graphical analyses, as derived by Patlak *et al*(1983, 1985), require modification in order the take into account the contribution of 6F-3OMD radioactivity to the PET images. The most common approach is to calculate the *specific* striatal radioactivity concentration by subtracting the radioactivity concentration in a reference tissue (cortical or cerebellar) from that in the striatum (Martin *et al*, 1989). Using a plasma input function, the time to reach steady state is typically taken to be 30 min, although shorter and longer times are also used. The slope of the linear portion of the Patlak plot, the uptake rate constant K_i, is considered to reflect the rate of decarboxylation of 6F-DOPA and vesicular storage of 6F-DA. Since the time course of 6F-DOPA and 6F-3OMD are different from each other and in different brain tissue (Melega *et al*, 1991; Wahl *et al*, 1994), the specific striatal TAC is a biased approximation of the TAC of F-DOPA and its metabolites other than 6F-3OMD in the striatum. Yu *et al*(1995) demonstrated with simulation studies that this bias is propagated in the estimation of the uptake rate constant and that the magnitude of the bias depends on difference between the rate constants of the compartmental systems describing the striatum and the reference tissue. Since there exists brain tissues that lack (cerebellum) or contain relatively few (occipital cortex) dopaminergic cells, the reference tissue graphical analysis (Patlak and Blasberg, 1985) has been used intensively with 6F-DOPA. Using a reference tissue input function, this simple and non-invasive variant of the Patlak plot has been shown to reach steady state 30 min post-injection (Brooks *et al*, 1990a), like the one using a plasma input function, but tends to deviate from strict linearity at later times more than does the one using a plasma input function (Hoshi *et al*, 1993).

If significant over the duration of the PET study, the clearance of metabolites of

6F-DA from the striatum would affect the linear portion of the Patlak plot by decreasing the slope at later times, hence lowering the K_i value. Holden *et al*(1997) described a method, based on another extension of the graphical analysis (Patlak and Blasberg, 1985), to quantify the loss of radioactivity from the irreversible compartment. Using a plasma input function, the negative curvature is interpreted as the abscissa increasing too rapidly and the integral time is redefined as

$$\theta(t) = \frac{\int_0^t C_p(t')\,dt'}{C_p(t)} \Rightarrow \theta'(t) = \frac{\int_0^t C_p(t')\exp\left(-k_{loss}(t-t')\right)dt'}{C_p(t)} \tag{2.63}$$

where k_{loss} is a first-order rate constant describing the loss of trapped radioactivity. At the true value of k_{loss}, the straight-line behavior is restored; lower or higher values of k_{loss} would accentuate the negative curvature or change it to positive, respectively. The introduction of the exponential term in the equation prohibits the use of standard linear least squares to calculate the uptake rate constant. Instead, a basis function approach is adopted where k_{loss} is assigned values ranging from 0 to 0.008 min^{-1} and a series of quadratic fits to the extended Patlak plot is generated. The true value of k_{loss} is found when the coefficient of the quadratic term is zero, i.e. a straight line is obtained. The coefficient of the linear term then corresponds to uptake rate constant K_i. The extended graphical analysis was validated on monkeys that were studied over four hours after the injection of 6F-DOPA in order to accentuate the loss of trapped radioactivity. The K_i values obtained from the conventional graphical analysis on two hours of data were lower than those estimated using the extended graphical analysis on four hours of data, implying that the effects of k_{loss}, although not visible graphically, are present in the data as early as two hours post-injection. Since the formation of 6F-3OMD was only partially blocked in these monkeys pretreated with peripheral AADC (carbidopa) and COMT (nitecapone) inhibitors prior to the injection of 6F-DOPA, the possibility remains that the k_{loss} values simply reflect the biases introduced by subtracting the occipital TAC from the striatal TAC.

The slopes of the Patlak plots using either a plasma or a reference tissue input function have been compared in a few studies which have reached conflicting conclusions. Hoshi *et al*(1993) found that occipital K_i (K_{io}), but not plasma K_i (K_{ip}), discriminated between Parkinson's disease subjects and normal controls. Takikawa *et al*(1994) refuted the previous study by showing that K_{ip} was a superior marker to K_{io} since K_{ip} discriminated between subjects with Parkinson's disease better than did K_{io}, and only K_{ip} correlated with scores of disease severity. Vingerhoets *et al*(1996) determined that K_{io} was a more

reproducible index than K_{ip}, thus providing the best discrimination between PD subjects and normal controls, in support to the first study. The disagreement most likely arises from the relative quality of the plasma and cortical radioactivity concentration measurements, thus underlining the importance of the measurement of the input function (Vingerhoets *et al*, 1994a).

2.3.3 An Alternative to 6F-DOPA: F*m*T

The cerebral metabolism of 6F-DOPA parallels that of endogenous L-DOPA: 6F-DOPA is transported into the brain via the LNAA carrier system (Leenders *et al*, 1986), is decarboxylated by AADC, its metabolite 6F-DA is stored in neuronal vesicles and further metabolised by MAO and COMT (Melega *et al*, 1991; Endres *et al*, 1997). 6F-DOPA preferentially accumulates in dopaminergic brain tissue as visualized on PET images (Garnett *et al*, 1983) and the uptake rate constant correlates with dopaminergic cell densities in the substantia nigra and with dopamine levels in the striatum (Snow *et al*, 1993a; Pate *et al*, 1993). However, the use of 6F-DOPA to evaluate dopaminergic function is complicated by the formation in the periphery of the methylated metabolite 6F-3OMD which also crosses the BBB and contaminates the PET images with non-specific radioactivity (Wahl *et al*, 1994).

Several models of 6F-DOPA metabolism (Kuwabara *et al*, 1993; Wahl and Nahmias, 1996a; Dhawan *et al*, 1996; Shoghi-Jadid *et al*, 2000) have accounted for the contribution of 6F-3OMD. However, different approaches to the characterisation of the two input functions (plasma concentrations of 6F-DOPA and 6F-3OMD), the determination of the relative transport of 6F-DOPA and 6F-3OMD across the BBB (q value), and the determination of the volume of distribution of 6F-3OMD have yielded parameter estimates of varying precision and accuracy (see section 2.3.2.2). Blocking the formation of 6F-3OMD by pretreatment with COMT inhibitors (Ishikawa *et al*, 1996) or preferentially blocking the entrance of 6F-3OMD into the brain by delayed infusion of L-phenylalanine (Doudet *et al*, 1992) have been proposed as pharmacological solutions to the 6F-3OMD problem. The complexity and variability that the administration of these pharmaceuticals introduces to the PET/6F-DOPA study protocols has led to the search for another more practical solution.

Radiofluorinated *m*-tyrosines were originally proposed by DeJesus *et al*(1988) as

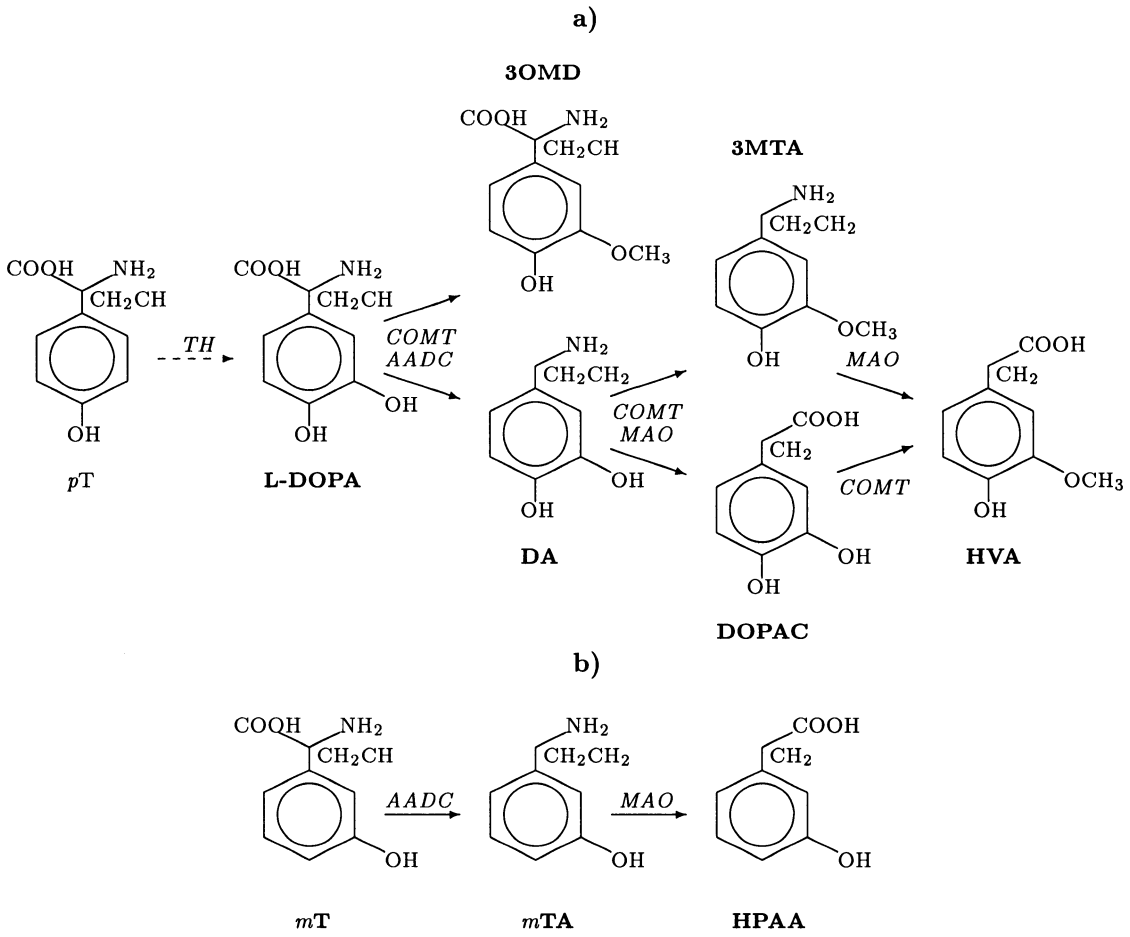

Transport Synthesis StorageMetabolism

Figure 2.5: *Comparaison of the biochemistry of* **a)** L-*DOPA and* **b)** L-*meta-tyrosine (mT): mT is not a substrate to the enzyme catechol-O-methyltransferase (COMT) due to the absence of a hydroxyl group on the benzene ring in the para position, thereby reducing the number of metabolic pathways.* L-*para-tyrosine (pT); 3-O-methyl-DOPA (3OMD); dopamine (DA); 3-methoxy-tyramine (3MTA); 3,4-dihydroxyphenylacetic acid (DOPAC); homovanillic acid (HVA); meta-tyramine (mTA); 3-hydroxyphenylacetic acid (HPAA); tyrosine hydroxylase (TH); aromatic* L-*amino acid decarboxylase (AADC); monoamine oxydase (MAO).*

alternative radiotracers to 6F-DOPA. The chemical structure of L-*m*-tyrosine is identical to that of L-DOPA except that it is missing a hydroxyl group in position 4 on the benzene ring. Since it lacks the catechol structure (two adjacent hydroxyl groups on the benzene ring), L-*m*-tyrosine is *not* methylated by COMT, but still undergoes decarboxylation by AADC. **Figure 2.5** depicts the simplified metabolic pathway of L-*m*-tyrosine compared to that of L-DOPA. Four radiofluorinated *m*-tyrosine analogs have been synthesized and have had their *in vivo* distribution and kinetics imaged by PET (Melega *et al*, 1989; Barrio *et al*, 1996; DeJesus *et al*, 1997): 2-, 4- and 6-[^{18}F]fluoro-L-*m*-tyrosine (2F*m*T , 4F*m*T and 6F*m*T) and 6-[^{18}F]fluoro-β-fluoromethylene-DL-*m*-tyrosine (6F-FM*m*T). In monkeys, the striatal-to-occipital ratio of 6F*m*T was two to three times that of 2F*m*T , 6F-FM*m*T and 6F-DOPA (DeJesus *et al*, 1997) and comparable to that of 4F*m*T 90 min postinjection (Barrio *et al*, 1996). The half life of 6F*m*T in plasma was twice as long of that of 4F*m*T (Barrio *et al*, 1996). Of these four *m*-tyrosine analogs, 6F*m*T (referred to as F*m*T thereafter) has the most favorable kinetics in brain tissue and plasma for a PET radiotracer. The superior quality of the PET/F*m*T images over the PET/6F-DOPA images makes F*m*T a potentially better probe than 6F-DOPA to study the presynaptic dopaminergic system.

2.3.3.1 Biochemical Data

The improvement in the striatal-to-occipital ratio of the PET/F*m*T images compared to that of the PET/6F-DOPA images can be explained with the following biochemical evidence gathered from rodent and non-human primate studies:

1. In striatal homogenates, F*m*T metabolites, 6-[^{18}F]fluoro-*m*-tyramine (6F-TA), its sulfated amine conjugates, and 6-[^{18}F]fluoro3-hydroxyphenylacetic acid (6F-HPAA), were detected in large amounts, thereby confirming that F*m*T is a substrate for AADC and that 6F-TA is also a substrate for MAO in dopaminergic brain tissue (Firnau *et al*, 1995; Jordan *et al*, 1997);

2. The vast majority of the striatal radioactivity was attributable to 6F-HPAA, indicating that 6F-TA is preferentially metabolised by MAO over being stored into neuronal vesicles (Jordan *et al*, 1997);

3. In cerebellar homogenates, all three fluorinated compounds were present in similar amounts (Jordan *et al*, 1997);

4. Pretreatment with a peripheral AADC inhibitor results in larger amounts of unmetabolised F*m*T in plasma, bringing further evidence that F*m*T is a substrate for AADC (Jordan *et al*, 1997);

5. No methylated metabolites of F*m*T were detected in either brain tissue or plasma (Firnau *et al*, 1995; Barrio *et al*, 1996; Jordan *et al*, 1997).

On one hand, the absence of COMT products of F*m*T results in an important decrease of the non-specific radioactivity. On the other hand, the specific accumulation of AADC products of F*m*T appears to be increased (see section 2.3.3.4).

Before attempting to model the PET/F*m*T images, two important questions remain unanswered: Do the metabolites of F*m*T cross the BBB and contribute to the radioactivity measured in the non-dopaminergic tissue? And what is the mechanism responsible for the trapping of the F*m*T metabolites in dopaminergic brain tissue?

The answer to the first question was given by Firnau *et al*(1995) who studied with PET the same normal subject four times, following separate injections of 6F-DOPA and F*m*T , and their main peripheral metabolites, 6F-3OMD and 6F-HPAA, respectively. Sixty minutes postinjection, the striatal radioactivity concentration of 6F-3OMD was found to be about half of that of 6F-DOPA whereas 6F-HPAA represented only about one twentieth of the radioactivity concentration of F*m*T . This simple *in vivo* experiment provided convincing evidence that the acid metabolite of F*m*T does not cross the BBB in significant amounts. Although it has not yet been verified if the amine metabolite of F*m*T crosses the BBB, it is likely that the amounts of 6F-HPAA and 6F-TA detected in cerebellar homogenates of rodents and non-human primates originate from the vasculature.

The second question was answered by Endres *et al*(1997) who measured *in vitro* the affinities of the two fluorinated amines, 6F-DA and 6F-TA, for the synaptic vesicular amine transporter (SVAT) and the presynaptic dopamine transporter (DAT). The affinity of 6F-TA for the SVAT system was determined to be about fifteen times less than that of 6F-DA or dopamine. Similarly, the affinity of 6F-TA for the DAT system was also lower than that of dopamine by a factor of about seven compared to a factor of two for 6F-DA. It is likely that unprotected 6F-TA, which is not stored in significant amounts in the neuronal vesicles, is rapidly metabolised by MAO into 6F-HPAA, which is turn is trapped or cleared very slowly from dopaminergic neurons. This hypothesis can explain the repeated observation that most of the radioactivity in the striatum following the injection of F*m*T is in the form

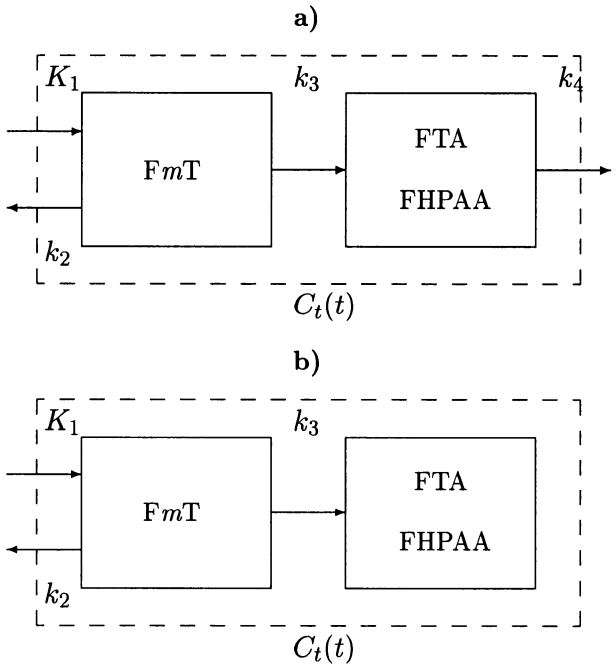

Figure 2.6: *Comparison of the different compartmental models proposed for the metabolism of FmT :* **a)** *The Barrio et almodel (1996) and* **b)** *the Nahmias et almodel (1995). (See text for details and abreviations)*

of 6F-HPAA (Firnau *et al*, 1995; Jordan *et al*, 1997). 6F-DA thus follows more closely the entire metabolic pathway of endogenous dopamine than does 6F-TA. Nevertheless, FmT does trace the decarboxylase step and its simpler peripheral metabolism provides higher quality PET images which can be more easily quantified.

2.3.3.2 Compartmental Analysis

The compartmental models for FmT , illustrated in **Figure 2.6**, are inspired by those of 6F-DOPA. The major difference is that the contribution from peripherally produced metabolites of FmT is neglected, and consequently, only a single input function (the plasma concentration of FmT) is required. The only remaining issue is whether or not the clearance of the acid metabolite 6F-HPAA is significant over the duration of the PET study. Barrio *et al*(1996) found that striatal data from PET/FmT studies in monkeys lasting 120 min are better fitted with a two-compartment four-rate constant model, even though the k_4 estimates were small. Two other studies of the same duration, one in monkeys (Jordan *et al*, 1997) and the other one in humans (Nahmias *et al*, 1995), arrived at the different

conclusion that the striatal data could only support a two-compartment three-rate constant model. All three studies (Nahmias *et al*, 1995; Barrio *et al*, 1996; Jordan *et al*, 1997) agreed that the cerebellum and the occipital cortex were best fitted with a two-compartment three-rate constant model. The k_3 values in these brain tissues were estimated to be five to ten times smaller than the k_3 values in the striatum. No interpretation was advanced for the non-zero estimates of k_3 in non-dopaminergic brain tissue. The unavailability of a reference region devoid of irreversible trapping questions the validity of applying the graphical analysis approach with a reference tissue input function to F*m*T data. It also complicates the application of a reference tissue model to F*m*T data.

The effects of pretreating with a peripheral AADC inhibitor were investigated in human subjects by Nahmias *et al*(1995). Carbidopa pretreatment increased the availability of F*m*T in plasma, which resulted in increased radioactivity concentration in all brain tissues examined. Compartmental modelling yielded similar values for the rate constants, even though the shape of the plasma and tissue TACs were very different with or without carbidopa pretreatment.

2.3.3.3 Graphical Analysis

The absence of peripherally produced metabolites of F*m*T that cross the BBB allows for the graphical analysis approach to be implemented without the need to apply corrections as with 6F-DOPA. The uptake rate constant has been calculated with either a plasma or an occipital input function and used to compare F*m*T and 6F-DOPA (Barrio *et al*, 1996; DeJesus *et al*, 1997; Doudet *et al*, 1999), and to detect differences between naive and MPTP-lesioned monkeys (Jordan *et al*, 1997; Doudet *et al*, 1999). Doudet *et al*(1999) have also tried to estimate the rate of loss of trapped metabolites of F*m*T (k_{loss}) using the extended graphical analysis approach of Holden *et al*(1997) and compared the k_{loss} estimates of F*m*T with those of 6F-DOPA.

2.3.3.4 Comparison with 6F-DOPA

The motivation behind the development of F*m*T was that it is not a substrate for COMT, hence eliminating the formation of 6F-3OMD, the confounding methylated metabolite of 6F-DOPA. The resulting improvement in the specific-to-nonspecific radioactivity ratio not only enhances the delineation of the striatum, but also reveals brain tissue with lower

uptake of F*m*T , in particular the brainstem, the thalamus, the hypothalamus, the nucleus accumbens, the amygdala and the hippocampus (Brown *et al*, 1999). Some of these brain tissues do not have dopaminergic innervation, but instead contain noradrenaline and serotonin, two neurotransmitters that, like dopamine, are synthesized *in situ* under the action of the enzyme AADC on their precursors. The uptake rate constant K_{io}, calculated for all tissue with visible uptake of F*m*T , was found to correlate better with the sum of the concentrations of these monoamine neurotransmitters than with the dopamine concentration alone, and even better with regional AADC activity (Brown *et al*, 1999). F*m*T thus appears to localise in monoaminergic brain tissue that contain AADC. In tissue where dopamine is the dominant monoamine, like in the striatum, F*m*T specifically targets the dopaminergic system. Since 6F-DOPA is also a probe for AADC activity, the radiotracer is most probably taken up by the same monoaminergic brain tissue as F*m*T . The extra-striatal tissue cannot be clearly visualised on the PET/6F-DOPA images because the specific signal is buried under the non-specific signal from 6F-3OMD.

The fact that F*m*T is not a substrate for COMT brings about other important advantages. In plasma, fewer labelled metabolites need to be identified: 6F-TA and 6F-HPAA for F*m*T (Firnau *et al*, 1995) *versus* 6F-DA, 6F-DOPAC, 6F-HVA and 6F-3OMD for 6F-DOPA (Firnau *et al*, 1988), thus simplifying the procedures for plasma metabolite analyses. In monkeys pretreated with carbidopa, the half life of F*m*T in plasma was determined to be about twice as long as that of 6F-DOPA (Barrio *et al*, 1996). This increase in the plasma availability of F*m*T results in an increase of radioactivity entering the brain and a concomitant improvement in image statistics.

The preferential accumulation of AADC products in AADC-containing brain tissue confirms that F*m*T is a good substrate for AADC. A number of PET studies in monkeys have been conducted in order to systematically compare the uptake of F*m*T with that of 6F-DOPA (Barrio *et al*, 1996; DeJesus *et al*, 1997; Doudet *et al*, 1999). Graphical analysis, using either a plasma (Barrio *et al*, 1996; Doudet *et al*, 1999) or an occipital input function (DeJesus *et al*, 1997; Doudet *et al*, 1999), have yielded striatal uptake rate constants for F*m*T that are consistently about twice as large as those for 6F-DOPA. Using compartmental modelling, Barrio *et al*(1996) separated the contribution of the uptake rate constant that was arising from an increased delivery of radiotracer to brain tissue *versus* an increased decarboxylation rate. The volumes of distribution of F*m*T and 6F-DOPA were found to be comparable in the striatum and the cerebellum whereas the decarboxylation rate constant

k_3 in the striatum was about twice as large as that of 6F-DOPA, implying that F*m*T is a better substrate for AADC than 6F-DOPA. The increase in k_3, however, could partially be an artefact of having included a fourth rate constant in the compartmental model of F*m*T and not in that of 6F-DOPA. Nevertheless, these comparative studies have shown that the improvement in the striatal-to-occipital ratio is not only attributable to a reduction of the non-specific radioactivity, but also to an increase in the specific uptake of F*m*T over that of 6F-DOPA.

Biochemical studies (Jordan *et al*, 1998; Endres *et al*, 1997) have raised doubts on the ability of F*m*T to probe dopamine turnover. In response to degeneration of the substantia nigra, the nigrostriatal dopaminergic system can increase dopamine turnover as a compensatory mechanism (Barrio *et al*, 1990). Using the extended graphical analysis approach of Holden *et al*(1997) on 6F-DOPA data, Doudet *et al*(1999) were able to detect a significant increase in dopamine turnover as indicated by an elevated value of k_{loss} in the striatum of MPTP-lesioned monkeys compared with normal monkeys. This finding was not replicated with F*m*T data, limiting the use of F*m*T to probe the decarboxylation step in the dopamine metabolic pathway.

To be useful, F*m*T must be sensitive to alterations in the dopamine metabolic pathway. The uptake rate constant K_{ip} of F*m*T was significantly correlated with dopamine levels in striatal homogenates of a group of normal and MPTP-lesioned monkeys sacrificed following their PET scan (Eberling *et al*, 2000). In another group of normal and MPTP-lesioned monkeys that were scanned twice, once with 6F-DOPA, the other time with F*m*T , the uptake rate constants (K_{ip} and K_{io}) of both radiotracers were significantly decreased in the MPTP-lesioned monkeys compared to the normal monkeys (Doudet *et al*, 1999). Furthermore, the uptake rate constants of F*m*T were correlated with those of 6F-DOPA (Doudet *et al*, 1999). In a subject suffering from Parkinson's disease, the accumulation of radioactivity was reduced in the putamen contralateral to the clinical symptoms, on both the 6F-DOPA and F*m*T PET images (Nahmias *et al*, 1995). In the same group of young (3-11 years) and aged (25-37 years) rhesus monkeys, the 6F-DOPA uptake declined with age while the F*m*T uptake increased slightly with age (DeJesus *et al*, 2001). These conflicting results were interpreted as the two radiotracers probing different ageing related mechanisms, 6F-DOPA reflecting mainly the increased striatal dopamine turnover whereas F*m*T suggesting the maintenance or upregulation of AADC activity. These preliminary studies indicate that F*m*T can detect changes in AADC activity more specifically than

6F-DOPA. Further studies are required to determine if the improved delineation of brain tissue combined with the simplified modelling of PET/F*m*T images translate into a better power of discrimination between normal and disease states in the presynaptic dopaminergic system.

2.3.4 Discussion

6F-DOPA has been used widely to assess the functional integrity of presynaptic dopaminergic neurons in human diseases and animal models (Cumming and Gjedde, 1998). Because the behavior of this radiotracer parallels so well that of the endogenous substance L-DOPA, its kinetics do not only reflect its transformation into dopamine, but also the saturable transport of the precursor into the brain and its alternative metabolic pathways as well as the storage and turnover of the neurotransmitter. However, it has proven difficult, even with complex compartmental models, to separately identify these steps using PET data. The practical approach has been to derive a global parameter, most often the uptake rate constant, which was found to be proportional to nigral cell counts and correlated with striatal dopamine levels in *post-mortem* brains (Snow *et al*, 1993a; Pate *et al*, 1993). The non-zero intercept of the latter plot indicates that the 6F-DOPA uptake rate constant overestimates the dopamine concentration in the surviving terminals. Nevertheless, this macroparameter has been shown to be sensitive to several disruptions in the nigrostriatal pathway, whether degeneration of dopaminergic neurons or compensatory regulation of dopaminergic enzymes (Lee *et al*, 2000). These effects cannot be untangled without additional information, and confounds the *interpretation* of detectable changes.

F*m*T was designed to undergo fewer metabolic pathways, thereby selectively probing the AADC step in the synthesis of dopamine (DeJesus, 2003). However, the retention of radioactivity in monoaminergic neurons relies not on the storage of the radiolabelled amine analogue, like with 6F-DOPA, but on the rapid formation of the radiolabelled acid metabolite which diffuses slowly from the terminal. From the measurement of the tissue radioactivity, only the first metabolic step can theoretically be inferred (see **Appendix B.5**). The insensitivity of the measurement to varying MAO activities awaits experimental confirmation. The improved selectivity of F*m*T over 6F-DOPA results in an increased sensitivity: Not only has the uptake rate constant doubled in high terminal density regions (Barrio *et al*, 1996), but also the uptake rate constant has become quantifiable in lower terminal

density regions (Brown *et al*, 1999). On the other hand, F*m*T is more sensitive to plasma concentrations of large neutral amino acids than 6F-DOPA (Stout *et al*, 2001), making it even more important to separate changes in transport from changes in metabolism. This can more easily be accomplished with the substantially simplied compartmental model of F*m*T compared to that of 6F-DOPA (see **Figures 2.4** and **2.6**).

The rate-limiting step in the synthesis of dopamine is the transformation of L-*p*-tyrosine into L-DOPA by tyrosine hydroxylase. Both 6F-DOPA and F*m*T bypass this step. L-*p*-tyrosine is ineffective in assessing dopamine synthesis because it is predominantly used in protein synthesis, making the radiolabelled analogues probes for cell proliferation (Laverman *et al*, 2002). Nevertheless, AADC is a regulated enzyme: The transformation of L-phenylalanine by AADC the rate-limiting step in the synthesis of 2-phenylethylamine (PE), a neuromodulator of dopamine transmission, and striatal AADC activity is enhanced and reduced by D_1 and D_2 receptor antagonists and agonists, respectively (Zhu *et al*, 1992; Hadjiconstantinou *et al*, 1993). This gives the impetus for measuring AADC activity *in vivo*. Using compartmental modelling of PET data with a radiolabelled substrate for AADC, the rate constant k_3 will reflect the activity of the enzyme (see equation (2.26)). AADC is not exclusively localised in dopaminergic neurons, but also in other catecholaminergic and serotoninergic neurons as well as in endothelial and glial cells. Therefore, F*m*T , like 6F-DOPA, is not selectively probing dopaminergic neurons. Whereas measurements in the intact striatum are predominantly influenced by the dopaminergic neurons, this approximation becomes less valid when the contribution of the nigral cells to the striatal projections is diminished in the lesioned or diseased striatum. The uncertainties related to the function and localisation of AADC complicate the *quantification* of changes specific to the presynaptic dopaminergic neurons as measured with radiolabelled analogues of dopamine precursors (Opacka-Juffry and Brooks, 1995).

The physiological quantification of F*m*T data is feasible and essential in order to improve the *detectability* of changes in dopamine metabolism between normal and disease states. The objective should not be to quantify the changes *per se* nor to attribute the changes to a specific physiological process, as the limited selectivity of F*m*T , although superior to that of 6F-DOPA, does not allow such conclusions, at least based solely on F*m*T data. Kinetic analyses of dynamic PET data requires the availability of an input function. Large cerebral blood vessels are visible in PET images acquired with current PET cameras. Working with a spatial resolution of about 5 mm, a sensitivity of more than 1% and a

uniformity around 10% (see **Appendix A**), it is worthwhile attempting to extract from the PET images an accurate and precise measurement of the time course of the radioactivity concentration in the blood. This would obviate the need for taking blood samples, thereby simplifying the experimental procedure for quantitative PET studies. With the growing number of clinical PET centres, this would in turn make accessible quantitative PET studies to a wider population. The methodology presented in this thesis, although developed for FmT , is generalisable to other radiotracers, provided that the underlying assumptions are satisfied, or can be adapted otherwise.

Chapter 3

Derivation of a Blood Time-Activity Curve From PET Brain Images

3.1 Overview

[1] The purpose of the work presented in this chapter was to study the feasibility of a non-invasive method for obtaining a blood input function from dynamic brain PET studies without arterial cannulation. The method is based on regions of interest (ROI) drawn on the superior sagittal sinus visible in the PET images. The ROI-based method used for partial volume and spillover correction was verified to be accurate when applied to glass tubes filled with a radioactive solution. Two subjects, one normal and one early Parkinsonian (PD), were studied in the high resolution high sensitivity ECAT/EXACT3D tomograph after the intravenous injection of FmT . The time course of radioactivity in the cerebral blood, corrected for partial volume and spillover, was compared to that in the arterial blood sampled on-line. The results of compartmental and graphical analyses of FmT using the directly sampled and the image-derived plasma input functions were also compared. Shape differences were observed in the time to peak, peak height and the area under the two blood curves. The use of the image-derived plasma input function enabled the discrimination of normal and PD subjects and the identification of the affected and unaffected sides of the PD subject, as indicated by the model parameter reflecting presynaptic dopaminergic

[1] *This work was presented in part at the BrainPET'99 International Conference, Copenhagen (Denmark), June 1999 and published in part in the journal J. Nucl. Med. (1999)* **40***: 1666-75.*

metabolism (k_3) and the graphically determined influx constant (K_i). This method of non-invasively obtaining a blood input function for quantitative analysis of PET brain data provides a compromise between simplicity and accuracy adequate for use with the clinical population.

3.2 Introduction

The estimation of physiological parameters from dynamic PET images requires an input function in order to separate the contribution of the radiotracer delivery from its uptake in tissue. Arterial blood sampling is currently considered to be the most accurate method to obtain the time course of radioactivity concentration in the blood. It consists of performing a cannulation of the radial artery and drawing serial blood samples, either manually or automatically with a peristaltic pump. A measured volume of each radioactive blood sample is counted in a radiation detector. The method exposes the subject to the low but real risks of hand ischemia associated with an arterial cannulation (Slogoff *et al*, 1983). When the blood is sampled manually, the method exposes the staff to additional radiation as well as to the risks associated with the handling of blood samples. The use of an automated blood sampling system reduces the burden on the staff but requires that complex corrections for delay and dispersion be applied to the measured blood radioactivity (Eriksson and Kanno, 1991). Whether blood sampling is done manually or automatically, the radiation detector used to count blood radioactivity must be carefully cross-calibrated against the PET camera in order to ensure compatibility between the blood and tissue data. These practical difficulties have limited the use of arterial blood sampling in clinical populations, thereby impeding the full realization of quantitative PET (Correia, 1992).

A number of alternatives to arterial blood sampling have been investigated, such as arterialized venous blood sampling (Phelps *et al*, 1979), continuous sampling of expired air (Koeppe *et al*, 1985; Gunn *et al*, 2000), use of an external lung monitor (Nelson *et al*, 1993), continuous infusion of the radiotracer (Carson *et al*, 1993), population-based input functions (Takikawa *et al*, 1993), and reference tissue input models (Lammertsma *et al*, 1996; Di Bella *et al*, 1999). A promising method that circumvents many of the problems related to arterial blood sampling consists of drawing regions of interest (ROI) in the blood pools visible on the PET images. Methods to extract the blood time-activity curve (TAC) from the aorta (Germano *et al*, 1992; Watabe *et al*, 2001) and the left ventricle of the heart

(Iida *et al*, 1992; Wu *et al*, 1996) have been developed when imaging the thorax. For brain studies, however, these blood pools are not located within the field of view of the tomograph, unless the thorax and the brain can be imaged either sequentially (Dhawan *et al*, 1994) or simultaneously (Iida *et al*, 1998). Litton (1997) and Chen *et al*(1998) explored the use of the largest cerebral arteries, the internal carotid arteries (ICA), with [^{11}C]flumazenil and 2-[^{18}F]fluoro-2-deoxy-D-glucose (FDG), respectively.

This chapter investigates the feasibility of obtaining the radioactivity concentration in the cerebral blood from ROIs drawn on the larger superior sagittal sinus. Since the extraction fraction of F*m*T is small, the venous sinuses are visible in the brain PET images and the radioactivity concentration in venous blood can be used to approximate that in arterial blood. The radioactivity concentration was first corrected at each time point for partial volume and spillover using the method of Kessler *et al*(1984) with analytically derived values for the recovery coefficient (RC). The accuracy of these RC estimates was assessed by imaging glass tubes of different diameters filled with a solution of known radioactivity concentration. The noise in the ROI-based blood curves was reduced by fitting the radioactivity concentration averaged over several planes with a mathematical function. The method was tested on two subjects, one normal and one early Parkinsonian (PD), who were injected with F*m*T and from whom arterial blood samples were collected during the PET study. The tissue curves were first fitted with compartmental models of increasing complexity and the directly sampled blood data in order to determine the model that best fitted, in a statistical sense, the PET/F*m*T data. The tissue data were also analysed using the graphical approach of Patlak *et al*(1983, 1985) with blood data. The results of the compartmental and graphical analyses on PET/F*m*T data using the image-derived plasma input function were compared with those obtained using the directly sampled plasma input function in order to evaluate the accuracy of the newly proposed method.

3.3 Materials and Methods

3.3.1 Correction for Partial Volume and Spillover on ROIs

The location of a radioactive point source in the field of view (FOV) can only be determined with an uncertainty quantified by the full width at half maximum (FWHM) of the point spread function (PSF) of the tomograph. Under the assumption that the

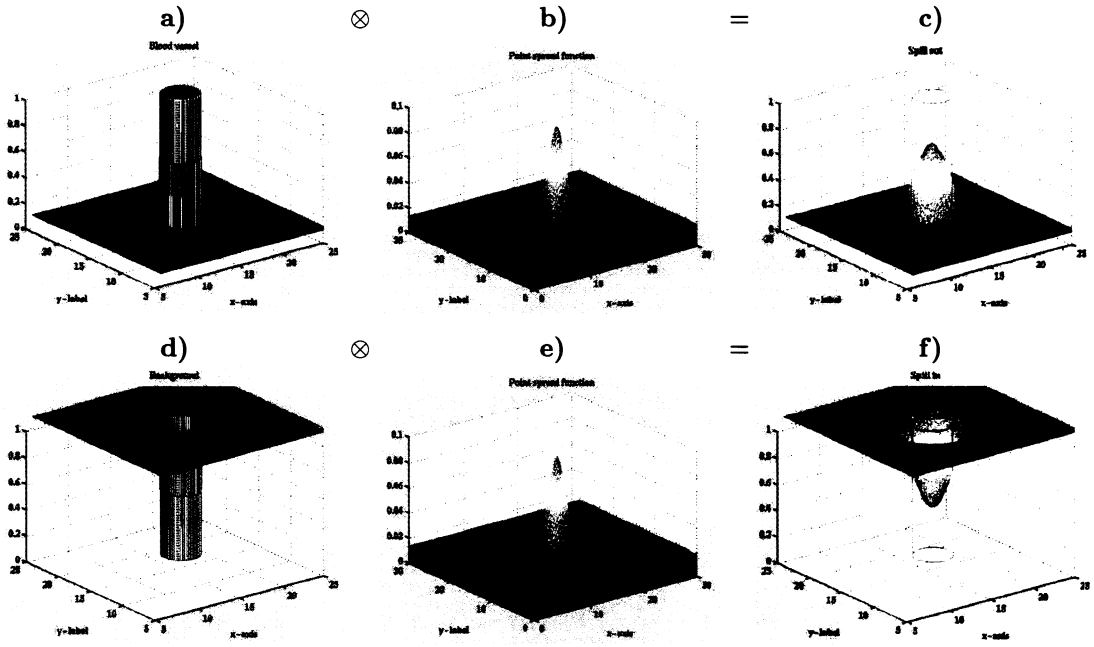

Figure 3.1: **Spill over: a)-c)** *Counts that spill out of the blood vessel into the surrounding tissue need to be recovered;* **d)-f)** *counts that spill into the blood vessel from the surrounding tissue need to be removed.*

tomograph is a linear system, the PET image of an extended radioactive source can simply be obtained by convolving the true radioactivity distribution with the PSF. The correction for finite detector dimension thus consists in deconvolving the PET image with the PSF, operation which is commonly referred to as *partial volume correction.*

When the size of an object is more than twice the FWHM of the PSF, the uncalibrated PET image contains voxel values which are linearly related to the radioactivity concentration in the object. This relation no longer holds for smaller objects. Accurate inference of the true object size and radioactivity concentration from the PET image then requires knowledge of the response of the tomograph as a function of object size and shape (Hoffman *et al*, 1979). The *recovery coefficient* (RC) is defined as the ratio of the apparent radioactivity concentration in the image (C_{image}) to the true radioactivity concentration in the object (C_{object}), and as such is determined specifically for the tomograph and reconstruction parameters used (Hoffman *et al*, 1979). When the object size and shape as well as the tomograph PSF are known, pre-determined RC values can be used to correct the radioactivity concentration measured in the image. The use of the recovery coefficient is correct only in the case for which it was derived, i.e. a hot spot in a cold background.

Kessler *et al*(1984) pointed out that in the more common case of a hot spot in a warm background, not only a fraction of the object radioactivity spills out to the background, but also the object is contaminated by radioactivity that spills in from the background:

$$C_{image} = RC \times C_{object} + (1 - RC) \times C_{bkg}, \tag{3.1}$$

where C_{bkg} is the true radioactivity concentration in the background.

The simple geometry of the superior sagittal sinus allows the approach of Kessler *et al*(1984) to be used for the correction of the non-negligible effects of partial volume and spillover. The correction must be applied at each time frame individually since the contrast between the blood vessel and its sourrounding tissue varies as the study progresses. Counts that spilled out of the blood vessel into surrounding tissue need to be recovered, especially soon after the bolus injection (**Figures 3.1a)-c)**). After the radiotracer has perfused brain tissue, counts that spilled into the blood vessel from surrounding tissue need to be subtracted (**Figures 3.1d)-f)**). Scaling the entire time-activity curve is therefore incorrect as it would distort the shape of the blood curve. Rewriting equation (3.1), the true radioactivity concentration in the blood vessel (C_{vsl}) at each mid-frame time t is obtained after correcting both the radioactivity concentration measured in the ROI on the superior sagittal sinus (C_{ROI}), and the true radioactivity concentration in surrounding tissue (C_{tis}):

$$C_{vsl}(t) = \frac{1}{RC}(C_{ROI}(t) - C_{tis}(t)) + C_{tis}(t). \tag{3.2}$$

Again, the radioactivity concentration in surrounding tissue is assumed not to be contaminated by counts from the blood vessel. Equation (3.2) highlights that the correction for spillover is applied to the *difference* between the radioactivity concentration measured in the blood vessel and surrounding tissue (Wahl *et al*, 1999b).

The RC values can be derived analytically from a simple simulation (Wahl *et al*, 1999b). The blood vessel is modelled as a cylinder with a circular cross-section and the surrounding tissues are assumed to have a uniform radiotracer uptake. A 60 mm×60 mm grid of 0.1 mm×0.1 mm pixels is first created. Pixels located within a given radius from the center of the grid are assigned a value of unity whereas those outside this area are set to zero. This binarized disk is then convolved with a two-dimensional Gaussian operator having the measured transaxial FWHM of the tomograph and an area normalized to unity. Circular ROIs of increasing diameter are centered on the grid and the average pixel value within each ROI is computed on both the binarized and blurred disks. The

recovery coefficients are finally calculated for a set of ROIs and a blood vessel of a given calibre as RC=ROI(blurred disk)/ROI(binarized disk).

3.3.2 Data Acquisition

3.3.2.1 Phantom data

The accuracy of the RC estimates was assessed by imaging six glass tubes of inner diameters 3.20, 3.95, 5.90, 7.70, 12.5 and 17.2 mm in the ECAT/ART PET camera (CTI/Siemens, Knoxville, TN, USA). The tubes were filled with an F-18 solution of 67 MBq/ml at the start of the first scan. Each tube, starting with the smallest one, was scanned for 5 min and the images were reconstructed using the 3D reprojection algorithm (Kinahan and Rogers, 1989) with Colsher and ramp filters set at Nyquist cut-off frequency. The images were corrected for attenuation using ROIs sized to the measured outer diameter of the glass tube and the linear attenuation coefficient of water, as well as for scatter using the model-based method of Watson *et al*(1996). Referring to the original definition of Hoffmann *et al*(1979), the RC values were calculated for each tube as the ratio of the radioactivity concentration measured in ROIs of diameter ranging from 2 to 50mm over the decayed radioactivity concentration of the F-18 solution. The measured RC values were compared with those predicted by the simulation described above which was performed for each tube and each ROI with FWHM=6.4mm, corresponding to the spatial resolution of the ECAT/ART tomograph 1cm away from the center of the FOV (see **Figure 4.3a)**).

3.3.2.2 Human data

Two subjects, one normal (47 year-old man) and one early Parkinsonian (60 year-old woman) affected on the right side (Hoehn and Yahr stage 1 — see **Table 6.1**), underwent a two-hour PET study (ECAT/EXACT3D, CTI/Siemens, Knoxville, TN, USA) after the intravenous injection of 110 MBq of FmT (Asselin *et al*, 2001). The normal subject was given 150 mg of carbidopa one hour prior to the start of the PET study, and the Parkinsonian subject was withdrawn from medication four hours before the PET study started. Arterial blood was counted continuously on-line (Ranicar *et al*, 1991) for the duration of the study. In addition, eight blood samples were taken in order to measure the partition of radioactivity between plasma and erythrocytes, and to determine the contribution of FmT to the total plasma radioactivity using solid phase extraction and HPLC (Luthra *et al*, 1993). The scan

data were acquired in list mode so that the frame duration of the reconstructed data could be defined post acquisition using the whole head time-activity curve – typically 1 frame at 50s per frame, 8 frames at 5s per frame, 3 frames at 10s per frame, 2 frames at 30s per frame, 4 frames at 60s per frame, 4 frames at 120s per frame, 5 frames at 300s per frame and 8 frames at 600s per frame. This enabled the accurate definition of the early time course in the cerebral blood vessel. The PET images were reconstructed using the 3D reprojection algorithm (Kinahan and Rogers, 1989) with the Colsher and ramp filters set at Nyquist cut-off frequency. Correction for attenuation was performed using the reconstructed single-photon transmission images segmented with the local threshold technique (Xu *et al*, 1994). The attenuation map was also used by the model-based scatter correction developed by Watson *et al*(1996).

3.3.3 Data Analysis

3.3.3.1 Definition of the regions of interest

Cluster analysis (Ashburner *et al*, 1996) was carried out on the dynamic PET images to segment the cerebral blood vessels based on the characteristic shape of the time-activity curve. The PET image of the first three minutes summed (referred to as *blood volume image*) is compared with the blood cluster image in **Figure 3.2**. The blood cluster image confirmed that the small intense areas seen at the back of the head in the blood volume image corresponded to the superior sagittal sinus.

On the blood volume image, circular ROIs (diameter=0.5 cm) were drawn manually around the voxels having the highest radioactivity concentration at the expected location for the superior sagittal sinus (see **Figures 4.6** and **4.7**). Additional ROIs were drawn manually on the summed PET images from the second hour of the study (referred to as *equilibrium image*). In order to correct for the partial volume and spillover effects relating to the blood vessel, a background ROI was delimited as an annulus (outer ellipse area=13.2 cm^2, inner circle diameter=1.5 cm) outside the superior sagittal sinus in the occipital lobe. The diameter of the inner circle of the annulus defining the background region was set to the sum of the blood vessel calibre (assumed to be 0.5 cm) and twice the FWHM of the tomograph (5.0 mm at 5 cm from the center of the field of view as measured by Spinks *et al*(2000)) in order to avoid spillover from the blood vessel into the background region. Elliptical ROIs were also drawn around the cerebellum (area=12.7 cm^2, one on each side

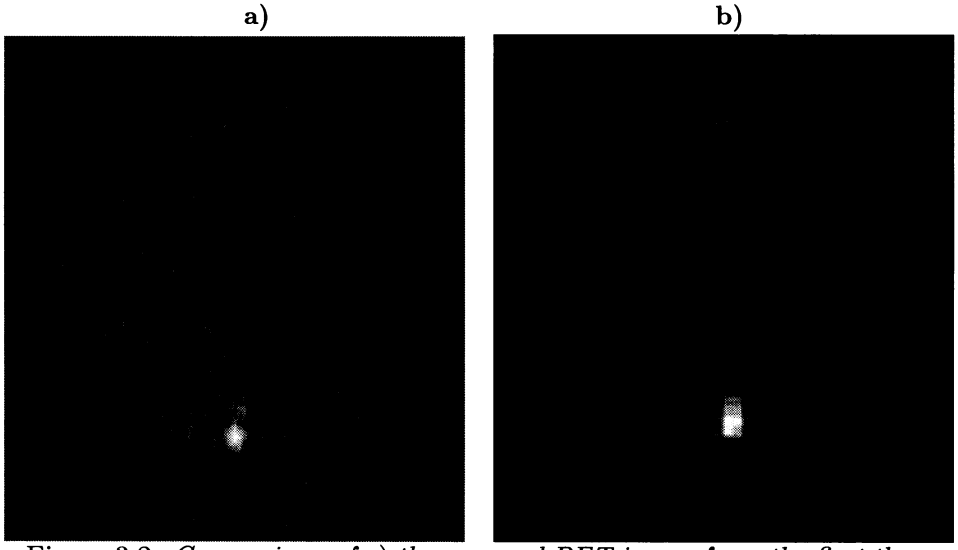

Figure 3.2: *Comparison of* **a**) *the summed PET image from the first three minutes with* **b**) *the blood cluster image for the normal subject. In these images, the back of the head is located at the bottom of the image, and the left side of the subject on the right of the image. High voxel values are displayed in white, and low voxel values in black. The voxel values in the PET image express the integrated radioactivity concentration (in kBq/ml over 3 min) whereas those in the cluster image contain the probability (from 0 to 1) of belonging to the blood cluster.*

per plane) and the left and right putamina (area=1.2 cm^2, two on each side per plane) on four to six consecutive planes. These ROIs served as target regions for the compartmental and graphical analyses. All ROIs were overlayed on the dynamic PET images to generate the time course of the radioactivity concentration in blood and tissue.

The time course of radioactivity concentration measured from the blood vessel was corrected for partial volume and spillover using equation (3.2) with the time course of radioactivity concentration in the background taken from that measured in the occipital lobe. For a blood vessel calibre, FWHM and ROI diameter all equal to 5.0mm, the simulation described above gave an RC value of 0.39.

3.3.3.2 Noise reduction

Noise in the plasma input function propagates to the fitted tissue TACs through the convolution operation, therefore increasing the uncertainty on the parameter estimates. Two methods of reducing the noise level in the ROI-based blood TAC were investigated:

1. *Average ROIs over several planes* – The calibre of the superior sagittal sinus was measured to be relatively constant over 5-6cm (see **Figure 4.8**), thereby allowing ROIs drawn on several consecutive planes (up to 15 on the ECAT/ART and 20 on the ECAT/EXACT3D) to be averaged.

2. *Fit the blood TAC with a mathematical function* – Two mathematical functions were investigated:

   (a) Sum of exponentials:

$$\begin{aligned} y(t) &= (A_1(t-\tau) - A_2 - A_3)\exp(-\lambda_1(t-\tau)) \\ &+ A_2\exp(-\lambda_2(t-\tau)) + A_3\exp(-\lambda_3(t-\tau)) \end{aligned} \tag{3.3}$$

   The blood TAC was manually shifted to the origin such that the delay parameter τ can be set to zero. This function with six parameters (three A's and three λ's) mathematically describes a four-compartment model having a pair of repeated eigenvalues. This model approximates the behavior of a radiotracer in the blood circulation, having been injected in a venous space and being sampled in an arterial space after having transited through tissue vascular and interstitial spaces (Feng *et al*, 1993). The initial values 10, 8, 5 kBq/ml and 3, 0.2 and 0.01 s^{-1}

for A_1, A_2, A_3, and λ_1, λ_2, λ_3, respectively, were found to produce reasonable fits to the data.

(b) Power function convolved with a square wave:

$$y(t) = At^{-a} \otimes f(t) \tag{3.4}$$

where

$$f(t) = \begin{cases} 1 & \text{if } \tau < t < \tau + W \\ 0 & \text{otherwise} \end{cases} \tag{3.5}$$

This function has four parameters: Two are used for the description of the injection as a square wave (delay τ and duration W); the other two arise from approximating the processes involved in the blood circulation and the peripheral metabolism of the radiotracer with an infinite number of compartments, the limit of which is a power function (Norwich, 1997). When τ was set initially to the rising time of the blood peak, W to the FWHM of the peak, A to the maximum of the peak over W, and $a = 0.7$, reasonable fits to the data were obtained.

Using either mathematical function, each data point was assigned equal weight in the minimization procedure.

3.3.3.3 Comparisons of input functions

The peak height, time to peak and the total integral of the four ROI-based blood TACs were compared with those of the directly sampled blood TAC. The directly sampled and the ROI-based blood TACs were then corrected for blood partition and radiolabelled metabolites using *ad hoc* mathematical functions (see section 5.4.2.3) in order to be used as plasma input functions to the cerebellum and left and right putamina.

The effects of using plasma input functions derived from either arterial blood sampling or the PET images on the results of both compartmental and graphical analyses were also evaluated. Using first the directly sampled plasma input function, the tissue TACs were fitted to the sequence of compartmental models illustrated in **Figure 3.3** (see **Appendix B** for the unconstrained solution of each model). The cerebral blood volume was included as an additional parameter and the delay between the blood and tissue TACs was fixed to the values presented in **Table 3.1**. The tissue data were weighted by the frame

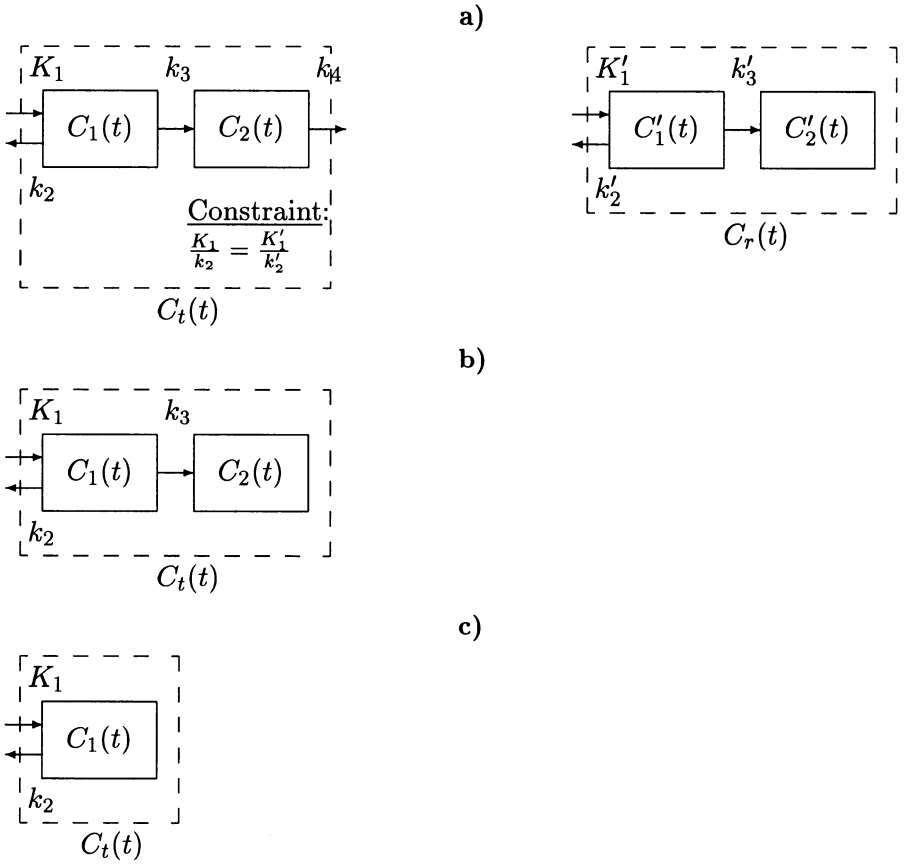

Figure 3.3: *Compartmental models for the uptake of FmT in cerebral tissue:* **a)** *K_1 and k_2 represent the forward and reverse transport rate constants of FmT between plasma and tissue, k_3 is the rate constant of decarboxylation of FmT in tissue by the enzyme aromatic amino-acid decarboxylase (AADC), and k_4 is the rate constant of clearance of radiolabelled metabolites from tissue. $C_1(t)$ thus represents the tissue concentration of unmetabolised FmT , and $C_2(t)$, the tissue concentration of radiolabelled metabolites. Because the solution to this two-compartment four-parameter model is not unique (see* **Appendix B.3***), the volume of distribution of unmetabolised FmT was constrained to that found in a reference region (cerebellum). $C_t(t)$ and $C_r(t)$ refer to the total radioactivity concentration in the target and reference tissue, respectively. The two-compartment four-parameter model can be simplified to* **b)** *a two-compartment three-parameter configuration by assuming negligible loss of radiolabelled metabolites from tissue ($k_4 = 0$). In tissue where decarboxylation of FmT is negligible ($k_3 = 0$), the model can further be simplified to* **c)** *the one-compartment two-parameter configuration.*

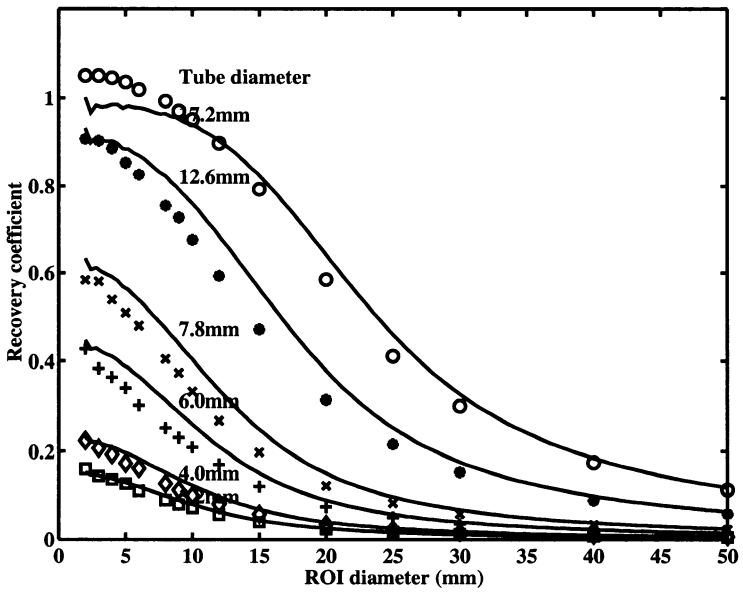

Figure 3.4: *Comparison between experimentally measured (symbols) and analytically derived (lines) recovery coefficients for tubes of varying diameters.*

length (L_i) squared over the number of true counts (C_i) in that frame ($w_i = 1/\sigma_i^2 = L_i^2/C_i$), assuming uniform Poisson noise across each PET brain image (Pajevic *et al*, 1998). The compartmental models of increasing complexity were compared using an F-test (DiStefano and Landaw, 1984), and the one beyond which no significant improvement was found was chosen to be the best model. This model was then used with the image-derived plasma input function to fit the tissue TACs. For graphical analysis, Patlak plots were generated using each plasma input function (Patlak *et al*, 1983, 1985) and fitted by the method proposed by Wong *et al*(1986). By fitting the entire plot with an exponential approach to a straight line, this method avoids the determination of an equilibrium time.

3.4 Results

3.4.1 Correction for Partial Volume and Spillover

The recovery coefficients measured experimentally are compared in **Figure 3.4** with those derived analytically for a set of six glass tubes of varying diameters. Only for

the largest tube could the radioactivity concentration be fully recovered in ROIs smaller than the tube itself. This is in agreement with the findings of Hoffman *et al*(1979) since the diameter of this tube was larger that twice the FWHM of the ECAT/ART PET camera. The experimental *RC* values greater than unity probably reflect an inaccurate measurement of the radioactivity concentration in the tube at the start of the scan. Shape differences between the experimental points and the analytical curves may result from the approximation of the tomograph PSF by a Gaussian function in the simulation. For the other tubes, the *RC* values were below unity regardless of the size of the ROI, with the highest *RC* values obtained for the smallest ROIs. Furthermore, the underestimation of the true radioactivity concentration worsened severely with decreasing tube size. For ROIs of diameter equal to that of the tube, the analytical *RC* values were estimated to be 0.75, 0.67, 0.49, 0.37, 0.21 and 0.14 for the 17.2, 12.6, 7.8, 6.0, 4.0, and 3.2 mm tubes, respectively.

Whilst the ROI diameter is a user-defined variable, the blood vessel calibre and the spatial resolution of the tomograph are fixed. In the human studies, the value for the former was extrapolated from literature values for the calibre of the confluence of the sinuses (Wahl *et al*, 1999b). Since the spatial resolution of the tomograph is spatially variant, the value for the latter was estimated at the position of the blood vessel from the measurements of a line source in air (Spinks *et al*, 2000). As shown on **Figure 3.5a)**, smaller ROIs produce larger *RC* values, but at the expense of a greater sensitivity to small variations in the tube diameter. Setting the ROIs diameter equal to that of the tubes was found to ease visualisation while drawing the ROIs. **Figure 3.5b)** further illustrates that the choice of the ROI diameter becomes more critical with PET cameras offering a better spatial resolution, at least for tubes smaller than twice the FWHM of the tomograph. It remains that, for a given ROI diameter and blood vessel calibre, the magnitude of the partial volume correction is reduced as the spatial resolution of the tomograph improves.

The effects of partial volume and spillover correction on the time course of radioactivity concentration in the blood as measured from the PET images are shown in **Figure 3.6**. The early peak height was enlarged by the positive difference between the blood and occipital radioactivity concentrations; the negative difference between these values at later times lowered the tail level. The process of dividing these differences by the recovery coefficient amplified the noise in the corrected blood curve.

a)

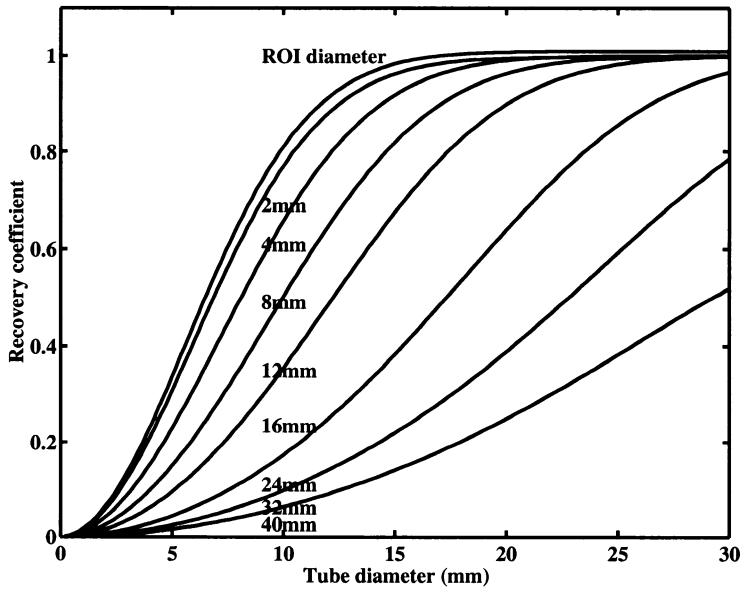

b)

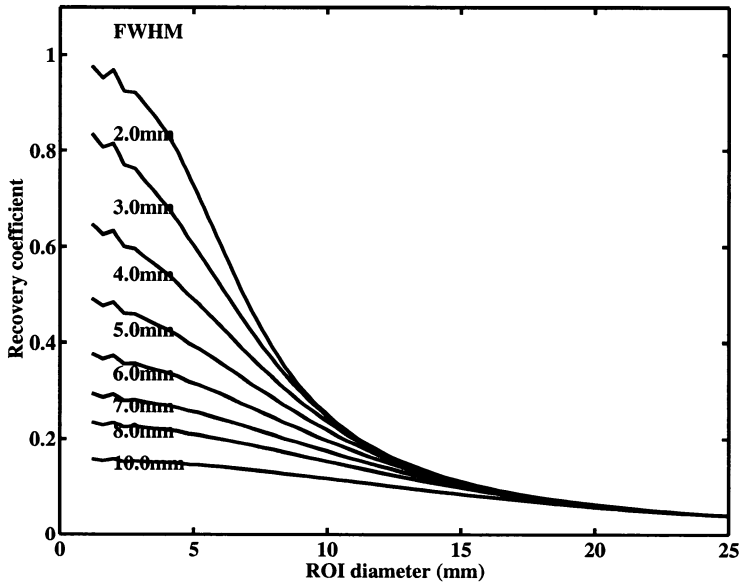

Figure 3.5: *Variation in the recovery coefficient with* **a)** *the uncertainty in the tube diameter for the ECAT/ART (FWHM=6.4 mm), and* **b)** *the choice of ROI diameter a for a tube of 5 mm in diameter.*

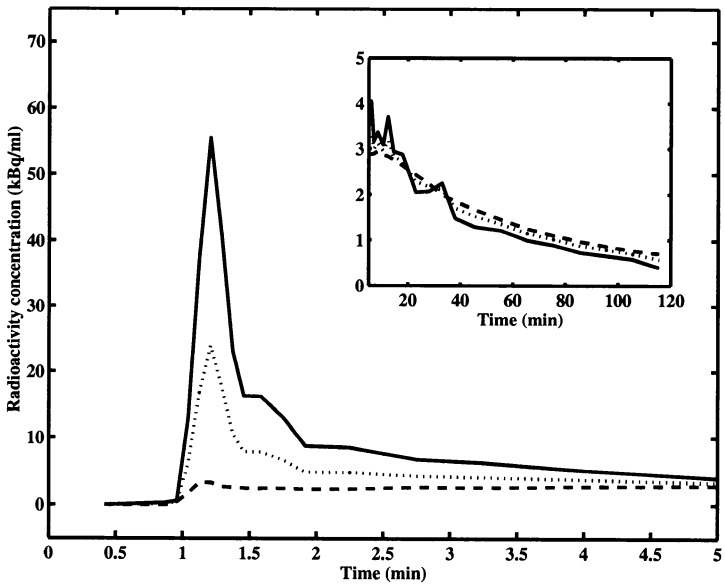

Figure 3.6: *Time course of radioactivity concentration in the blood vessel before (·····) and after (——) partial volume and spillover correction. The occipital time course (- - - -) was used as the background region. Note the underestimation of the peak height and the overestimation of the tail level (insert) resulting from spill out and in, respectively.*

3.4.2 Direct Comparison of Input Functions

The corrected ROI-based blood TACs are compared with the directly sampled blood TAC in **Figure 3.7** and to the fitted curves in **Figure 3.8**. As shown in **Table 3.1**, all ROI-based blood curves peaked earlier than the directly sampled curve for both the normal and PD subjects. Note that the delay values for the directly sampled blood TACs are consistent with the values typically used in compartmental analysis. The peak height of the ROI-based blood curves were more or less comparable in the normal subject but systematically smaller in the PD subject than that of the directly sampled one. The area under all ROI-based blood curves was smaller than under the directly sampled blood curve for both the normal and PD subjects. Looking back at **Figure 3.7**, averaging over planes significantly reduced the noise in the blood TAC. In particular, the blood radioactivity concentration no longer goes below zero at the early frames. As illustrated in **Figure 3.8**, the power function approximated the initial peak more closely than the sum of exponentials, but failed to follow the shoulder and the tail of the blood curve. Using either function, the fitted curves were dependent on the initial values.

3.4.3 Compartmental Models for FmT in Tissue

Results from compartmental modelling of the tissue curves are collated in **Tables 3.2a)** and **b)**. The fitted curves to the three models are illustrated in **Figures 3.9a)** and **b)**. The two-compartment three-parameter model provided a significantly better fit to the cerebellar data than the simpler one-compartment two-parameter model (p[F=70,1,32]<0.001 for the normal and p[F=88,1,33]<0.001 for the PD subjects). The two-compartment four-parameter model did not significantly improve the fit to the same data (p[F=1.5,1,31]>0.10 for the normal and p[F=,1,32]> for the PD subjects). In contrast, the F-test on the two-compartment four-parameter model indicated that a non-zero k_4 is required to fit the striatal data (p[F=7.8,1,32]<0.01 for the normal and p[F=4.2,1,33]<0.05 for the PD subjects). Because the solution of the two-compartment four-parameter model is not unique (see **Appendix B.3**), the K_1/k_2 ratio was constrained to the value found for the cerebellum. The resulting normalized χ^2 value was higher than that of the unconstrained fit but remained lower than that of the simpler models. The small bias introduced by the application of this constraint is compensated by a substantial decrease in variance on the estimates of the parameter of interest, k_3. Even though the simplest one-compartment two-parameter model

a)

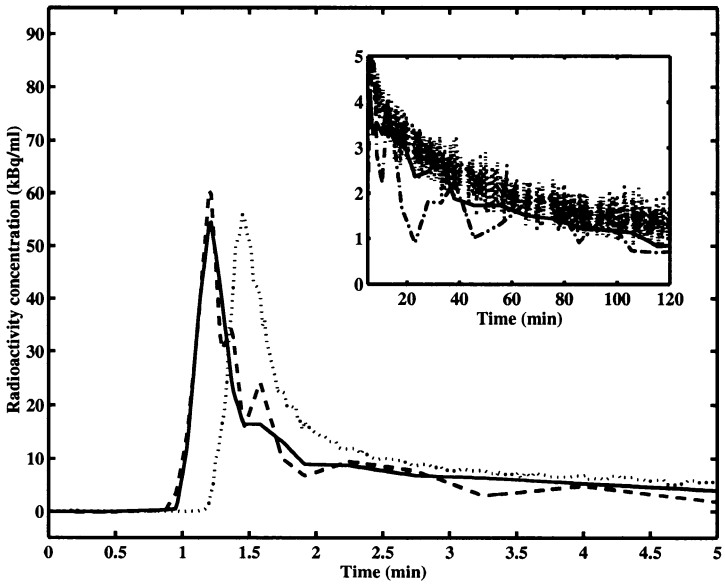

b)

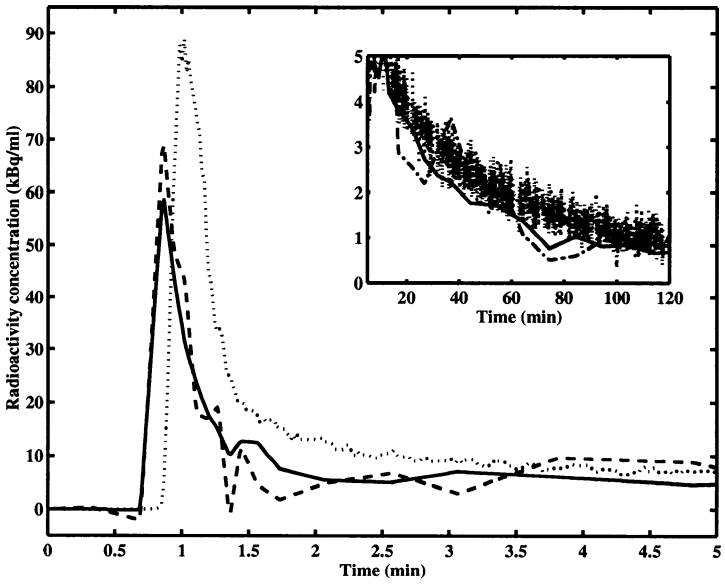

Figure 3.7: *Comparison between the ROI-based blood curve after correction for partial volume and spillover (- - - -, single plane; ——, average of several planes) and the directly sampled blood curve (· · · · · ·) plotted without correction for delay and dispersion for* **a**) *the normal and* **b**) *the Parkinsonian subjects. The insert enlarges the shoulder and the tail of the time-activity curves.*

a)

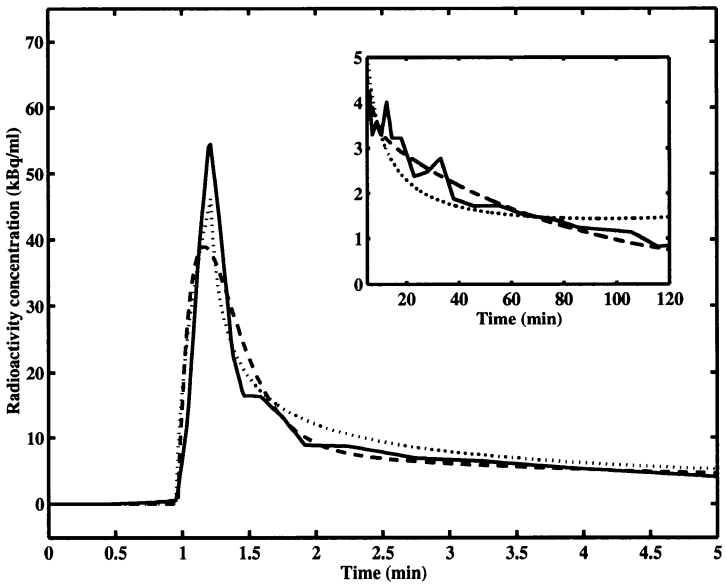

b)

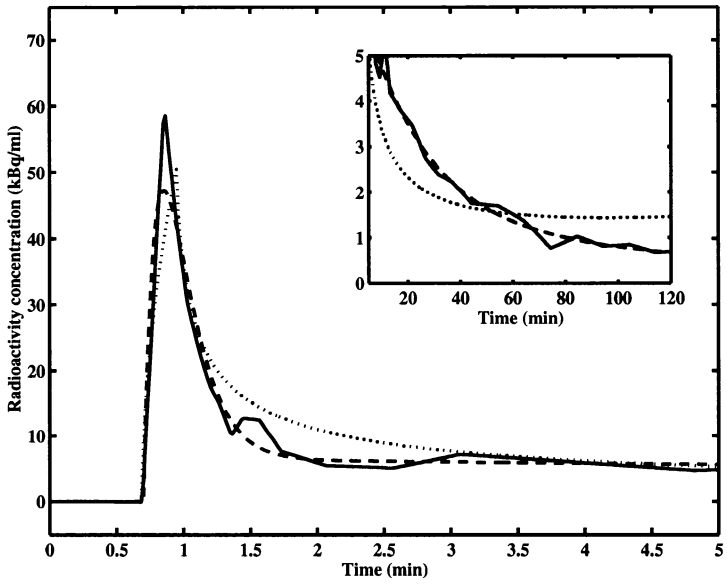

Figure 3.8: *Comparison between the fitted curves to the corrected ROI-based blood time-activity curve (——) for* **a**) *the normal and* **b**) *the Parkinsonian subjects. The power function (· · · · · ·) approximates the initial peak more closely than the sum of exponentials (- - - -), but fails to follows the shoulder and the tail of the curve (insert).*

Table 3.1: *Comparison between the shape of the directly sampled and the corrected ROI-based blood time-activity curves for* **a)** *the normal and* **b)** *the Parkinsonian subjects.*

Peak position [a] (s)	Peak height [b] (kBq/ml)	Total area [b] (MBq.s/ml)	χ^2/ν [c]
	a)		
Directly sampled blood TAC			
87	55.4	13.9	n/a
ROI-based blood TAC: Single plane			
73 (-14)	62.6 (+13)	10.1 (-27)	n/a
ROI-based blood TAC: Average over several planes			
73 (-14)	55.5 (+0.2)	11.7 (-16)	n/a
ROI-based blood TAC: Fitted to sum of exponentials			
70 (-17)	38.7 (-30)	11.8 (-15)	93.5
ROI-based blood TAC: Fitted to power function			
73 (-14)	45.9 (-17)	11.7 (-16)	92.7
	b)		
Directly sampled blood TAC			
61	88.2	16.1	n/a
ROI-based blood TAC: Single plane			
51 (-10)	70.7 (-20)	13.6 (-16)	n/a
ROI-based blood TAC: Average over several planes			
51 (-10)	59.9 (-32)	12.2 (-24)	n/a
ROI-based blood TAC: Fitted to sum of exponentials			
51 (-10)	47.1 (-47)	12.3 (-24)	36.6
ROI-based blood TAC: Fitted to power function			
57 (-4)	50.2 (-43)	12.0 (-25)	165

[a] Delay (in s) = ROI-based - Directly sampled

[b] Difference (in %) $= \frac{\text{ROI-based}-\text{Directly sampled}}{\text{Directly sampled}} \times 100$

[c] Residual sum of squares normalized to the number of degrees of freedom.

Table 3.2: *Comparison between parameters*[a] *estimated using the two-, three- and four-parameter models with the directly sampled plasma input function for* **a)** *the normal and* **b)** *the Parkinsonian subjects.*

a)

Tissue	K_1 (ml/min·ml)	k_2 (1/min)	k_3 (1/min)	k_4 (1/min)	V_b	χ^2/ν [b]
One-compartment two-parameter model						
Cerebellum	0.0458	0.0497	n/a	n/a	0.094	2.39E-5
	±0.0013	±0.0018			±0.011	
Left	0.03704	0.00485	n/a	n/a	0.096	6.17E-5
putamen	±0.00084	±0.00040			±0.015	
Right	0.03672	0.00505	n/a	n/a	0.107	5.11E-5
putamen	±0.00077	±0.00037			±0.014	
Two-compartment three-parameter model						
Cerebellum	0.0512	0.0613	0.00197	n/a	0.0829	7.73E-6
	±0.0013	±0.0020	±0.00023		±0.0062	
Left	0.0463	0.0195	0.0215	n/a	0.065	2.55E-5
putamen	±0.0017	±0.0030	±0.0026		±0.011	
Right	0.0450	0.0180	0.0194	n/a	0.0788	1.89E-5
putamen	±0.0014	±0.0024	±0.0022		±0.0094	
Two-compartment four-parameter model						
Cerebellum	0.0523	0.0647	0.0044	0.0098	0.0814	7.61E-6
	±0.0016	±0.0039	±0.0027	±0.0077	±0.0063	
Left	0.0509	0.036	0.053	0.00259	0.058	2.11E-5
putamen	±0.0031	±0.011	±0.015	±0.00060	±0.011	
Right	0.0496	0.0345	0.053	0.00284	0.0715	1.49E-5
putamen	±0.0025	±0.0090	±0.014	±0.00053	±0.0089	
Two-compartment three-parameter model with K_1/k_2 fixed						
Left	0.0571	n/a	0.0911	0.00335	0.053	2.37E-5
putamen	±0.0024		±0.0083	±0.00034	±0.011	
Right	0.0557	n/a	0.0928	0.00360	0.0667	1.74E-5
putamen	±0.0020		±0.0076	±0.00030	±0.0095	

Table 3.2: *Continued...*

b)

Tissue	K_1 (ml/min·ml)	k_2 (1/min)	k_3 (1/min)	k_4 (1/min)	V_b	χ^2/ν^b
One-compartment two-parameter model						
Cerebellum	0.0476	0.0572	n/a	n/a	0.0593	3.48E-5
	±0.0018	±0.0021			±0.0096	
Left	0.0284	0.0112	n/a	n/a	0.0111	3.28E-4
putamen	±0.0020	±0.0013			±0.028	
Right	0.0304	0.00754	n/a	n/a	0.107	2.55E-4
putamen	±0.0015	±0.00085			±0.024	
Two-compartment three-parameter model						
Cerebellum	0.0530	0.0688	0.00166	n/a	0.0492	9.81E-6
	±0.0012	±0.0019	±0.00018		±0.0052	
Left	0.0561	0.0598	0.01648	n/a	0.0498	2.28E-5
putamen	±0.0020	±0.0036	±0.00067		±0.0080	
Right	0.0531	0.0467	0.0216	n/a	0.052	3.97E-5
putamen	±0.0024	±0.0044	±0.0013		±0.011	
Two-compartment four-parameter model						
Cerebellum	0.0558	0.0776	0.0076	0.0188	0.0463	7.98E-6
	±0.0016	±0.0041	±0.0031	±0.0053	±0.0048	
Left	0.0585	0.0676	0.0212	0.00189	0.0471	2.08E-5
putamen	±0.0024	±0.0058	±0.0025	±0.00083	±0.0078	
Right	0.0603	0.0709	0.0377	0.00285	0.0450	3.06E-5
putamen	±0.0034	±0.0097	±0.0050	±0.00061	±0.0095	
Two-compartment three-parameter model with K_1/k_2 fixed						
Left	0.0609	n/a	0.0271	0.00322	0.0494	2.35E-5
putamen	±0.0022		±0.0013	±0.00054	±0.0083	
Right	0.0637	n/a	0.0429	0.00330	0.0425	3.06E-5
putamen	±0.0025		±0.0021	±0.00042	±0.0095	

[a] The model parameters are expressed as least-square estimates ±standard error.

[b] Residual sum of squares normalized to the number of degrees of freedom.

a)

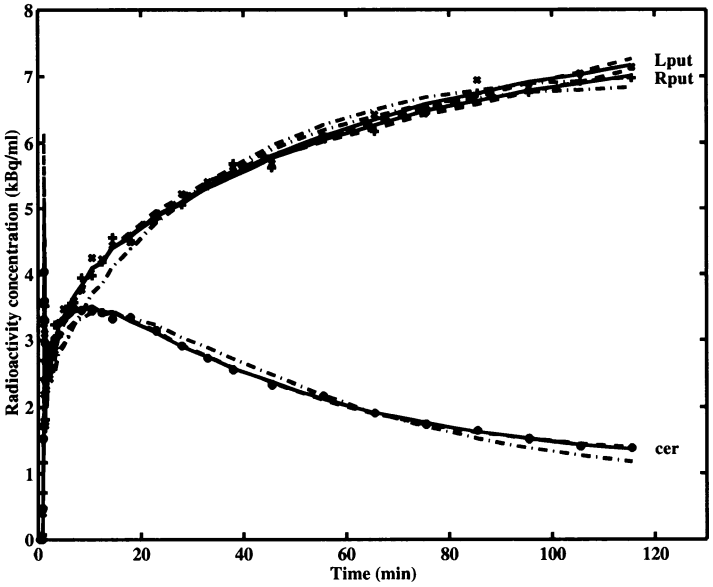

b)

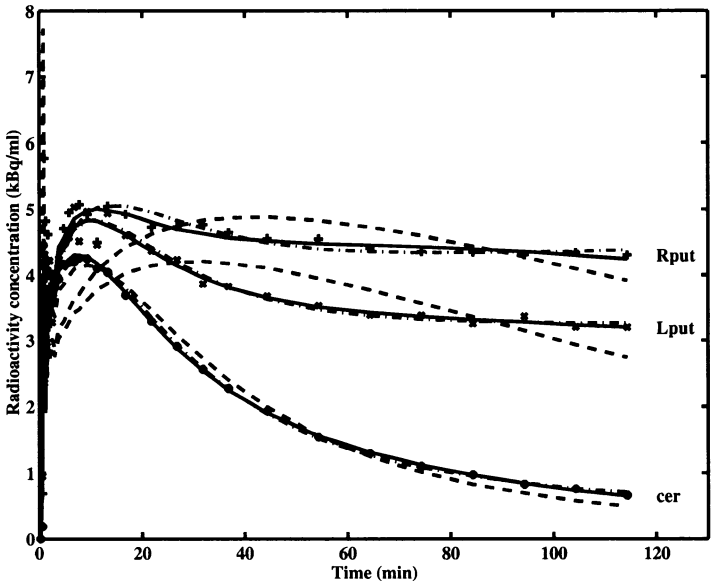

Figure 3.9: *Comparison between the fits to the PET data by the two- (- - - -), three- (— · —) and four-parameter (——) models with the directly sampled plasma input function for* **a**) *the normal (with carbidopa) and* **b**) *the Parkinsonian (without carbidopa) subjects. The cerebellum (∗) was best fitted by a two-compartment three-parameter model whereas the left (×) and right (+) putamina were best fitted to a four-parameter model.*

gave reasonable, albeit not the best fits, to the data from the normal volunteer (**Figure 3.9a)**), it totally failed to fit those of the PD subject (**Figure 3.9b)**).

3.4.4 Comparison of Parameter Estimates from Compartmental Analysis

The results of the compartmental modelling are presented in **Table 3.3** for both subjects and illustrated in **Figure 3.10** for the PD subject only. Comparing **Table 3.3** and **Table 3.2**, the estimates of the forward transport rate constant K_1 were larger when derived using the average image-derived input function than with the directly sampled input function. The metabolic rate constant k_3, on the other hand, was estimated to be smaller using the average image-derived input function compared to the directly sampled input function. As expected from the shape differences observed in the previous section, the parameter estimates obtained using the exponentially fitted blood curve were very close to those from the average blood curve. In contrast, the K_1 estimates derived from the blood curve fitted to power function were much smaller and the k_3 estimates were much higher — more so for the normal subject — than those from the average blood curve. The bias introduced by the improper fit of the power function can also be noticed in the larger errors on the parameter estimates. The performance of the input function derived from a single plane is also poor as indicated by the large bias and variance on the parameter estimates. Notice also in **Figure 3.10a)** the noise propagation to the fitted tissue curves, which is particularly severe when the input function is derived from a single plane. Using any input function, the metabolic rate constant k_3 is lower for the affected side of the PD subject than for the unaffected side, and the k_3 for both sides of the PD subject are lower than that of the normal subject.

3.4.5 Comparison of Parameter Estimates from Graphical Analysis

The Patlak plots of the cerebellum and the left and right putamina are displayed in **Figure 3.11** for the PD subject only. Note that these results are in agreement with the results of the compartmental analysis. The apparent accumulation in the left and right putamina is consistent with the small value of k_4 (see **Table 3.3**). The near zero slope of the cerebellum curve is likewise consistent with the small value of k_3 (again see **Table 3.3**). In **Table 3.4**, the influx constant K_i of either putamina is lower for the PD subject than the normal volunteer. The affected side of the PD subject has a lower influx constant than

Table 3.3: *Results of compartmental analysis*[a] *using the image-derived plasma input functions for* **a)** *the normal and* **b)** *the Parkinsonian subjects.*

a)

Tissue	K_1 (ml/min·ml)	k_2 (1/min)	k_3 (1/min)	k_4 (1/min)	V_b
Image-derived plasma input function: Single plane					
Cerebellum	0.0580	0.0469	0.00079	n/a	0.075
	±0.0022	±0.0027	±0.00046		±0.012
Left	0.0617	n/a	0.147	0.00421	0.049
putamen	±0.0030		±0.032	±0.00037	±0.013
Right	0.0607	n/a	0.152	0.00448	0.063
putamen	±0.0026		±0.031	±0.00033	±0.011
Image-derived plasma input function: Average over several planes					
Cerebellum	0.0602	0.0674	0.00341	n/a	0.0887
	±0.0017	±0.0026	±0.00028		±0.0079
Left	0.0673	n/a	0.0815	0.00213	0.056
putamen	±0.0026		±0.0057	±0.00031	±0.012
Right	0.0663	n/a	0.0817	0.00236	0.067
putamen	±0.0022		±0.0049	±0.00026	±0.010
Image-derived plasma input function: Fitted to sum of exponentials					
Cerebellum	0.0616	0.0704	0.00383	n/a	0.0835
	±0.0016	±0.0025	±0.00025		±0.0070
Left	0.0681	n/a	0.0772	0.00170	0.056
putamen	±0.0029		±0.0055	±0.00034	±0.013
Right	0.0677	n/a	0.0766	0.00194	0.063
putamen	±0.0026		±0.0051	±0.00032	±0.012
Image-derived plasma input function: Fitted to power function					
Cerebellum	0.0492	0.0456	0.00080	n/a	0.0933
	±0.0013	±0.0018	±0.00031		±0.0080
Left	0.0524	n/a	0.164	0.00383	0.066
putamen	±0.0021		±0.032	±0.00026	±0.010
Right	0.0515	n/a	0.172	0.00412	0.077
putamen	±0.0019		±0.033	±0.00024	±0.010

Table 3.3: *Continued...*

b)

Tissue	K_1 (ml/min·ml)	k_2 (1/min)	k_3 (1/min)	k_4 (1/min)	V_b
Image-derived plasma input function: Single plane					
Cerebellum	0.0720	0.0917	0.00336	n/a	0.082
	±0.0056	±0.0077	±0.00049		±0.020
Left	0.0959	n/a	0.0274	0.00196	0.056
putamen	±0.0083		±0.0017	±0.00079	±0.021
Right	0.1037	n/a	0.0394	0.00183	0.043
putamen	±0.0091		±0.0021	±0.00058	±0.023
Image-derived plasma input function: Average over several planes					
Cerebellum	0.0770	0.0842	0.00259	n/a	0.100
	±0.0030	±0.0035	±0.00025		±0.012
Left	0.0963	n/a	0.0273	0.00244	0.079
putamen	±0.0046		±0.0011	±0.00049	±0.014
Right	0.0999	n/a	0.0412	0.00245	0.072
putamen	±0.0052		±0.0016	±0.00039	±0.017
Image-derived plasma input function: Fitted to sum of exponentials					
Cerebellum	0.0768	0.0840	0.00259	n/a	0.099
	±0.0029	±0.0035	±0.00024		±0.012
Left	0.0949	n/a	0.0273	0.00244	0.083
putamen	±0.0042		±0.0010	±0.00046	±0.014
Right	0.0987	n/a	0.0412	0.00245	0.074
putamen	±0.0048		±0.0015	±0.00037	±0.016
Image-derived plasma input function: Fitted to power function					
Cerebellum	0.0617	0.0512	-0.00100	n/a	0.1055
	±0.0013	±0.0013	±0.00017		±0.0077
Left	0.0724	n/a	0.0333	0.00733	0.099
putamen	±0.0024		±0.0023	±0.00065	±0.013
Right	0.0728	n/a	0.0584	0.00664	0.103
putamen	±0.0026		±0.0043	±0.00044	±0.014

[a] The model parameters are expressed as least-square estimates ±standard error.

a)

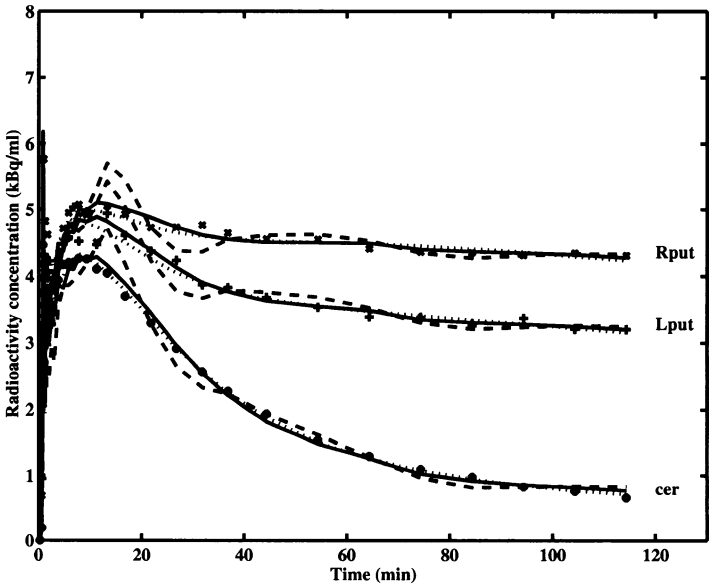

b)

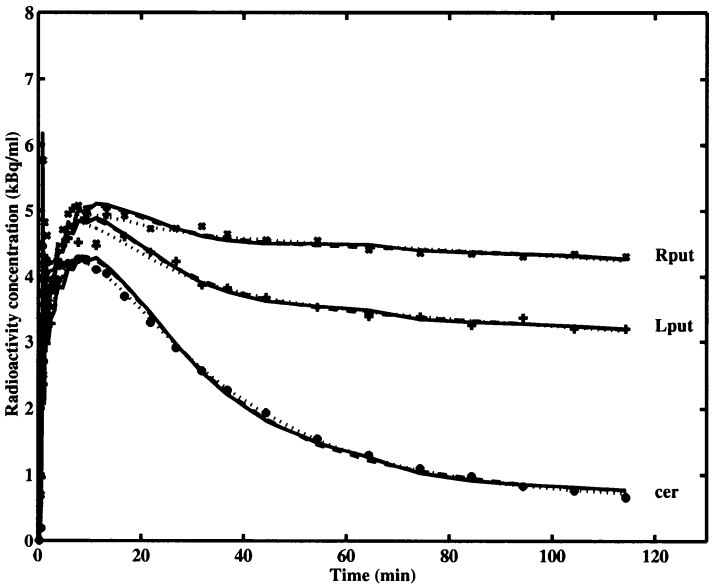

Figure 3.10: *Fitted curves to the PET data for the cerebellum (∗), and the left (+) and right (×) putamina of the PD subject using* **a**) *the directly sampled (· · · · · ·) and the image-derived (- - - -, single plane; ——, average of several planes) plasma input functions, and* **b**) *the fitted (- - - -, sum of exponentials; · · · · · ·, power function) plasma input functions.*

Table 3.4: *Results of graphical analysis*[a] *using the directly sampled and the image-derived plasma input functions for* **a**) *the normal and* **b**) *the Parkinsonian subjects.*

a)

Tissue	K_i (ml/min·ml)	Intercept (ml/ml)
Directly sampled plasma input function		
Cerebellum	0.00051 ±0.00042	1.238 ±0.073
Left putamen	0.02337 ±0.00059	0.82 ±0.11
Right putamen	0.02283 ±0.00081	0.83 ±0.15
Image-derived plasma input function: Single plane		
Cerebellum	0.0026 ±0.0012	1.76 ±0.29
Left putamen	0.03256 ±0.00084	1.10 ±0.24
Right putamen	0.03155 ±0.00090	1.20 ±0.27
Image-derived plasma input function: Average over several planes		
Cerebellum	0.00254 ±0.00028	1.227 ±0.059
Left putamen	0.02893 ±0.00026	0.627 ±0.056
Right putamen	0.02812 ±0.00031	0.688 ±0.068
Image-derived plasma input function: Fitted to sum of exponentials		
Cerebellum	0.003159 ±0.000069	1.125 ±0.015
Left putamen	0.02937 ±0.00015	0.539 ±0.033
Right putamen	0.02867 ±0.00013	0.574 ±0.028
Image-derived plasma input function: Fitted to power function		
Cerebellum	-0.00439 ±0.00044	2.436 ±0.089
Left putamen	0.003 ±0.021	11 ±13
Right putamen	0.002 ±0.020	11 ±12

Table 3.4: *...Continued*

b)

Tissue	K_i (ml/min·ml)	Intercept (ml/ml)
Directly sampled plasma input function		
Cerebellum	0.00072 ±0.00014	1.481 ±0.056
Left putamen	0.01194 ±0.00015	1.122 ±0.058
Right putamen	0.01659 ±0.00012	1.091 ±0.046
Image-derived plasma input function: Single plane		
Cerebellum	0.00286 ±0.00042	1.31 ±0.18
Left putamen	0.01557 ±0.00035	0.99 ±0.15
Right putamen	0.02114 ±0.00032	0.89 ±0.14
Image-derived plasma input function: Average over several planes		
Cerebellum	0.00147 ±0.00026	1.74 ±0.10
Left putamen	0.01610 ±0.00027	1.26 ±0.10
Right putamen	0.02214 ±0.00023	1.224 ±0.089
Image-derived plasma input function: Fitted to sum of exponentials		
Cerebellum	0.00115 ±0.00013	1.801 ±0.051
Left putamen	0.01572 ±0.00015	1.323 ±0.056
Right putamen	0.02183 ±0.00017	1.269 ±0.063
Image-derived plasma input function: Fitted to power function		
Cerebellum	-0.00818 ±0.00029	3.783 ±0.078
Left putamen	0.00760 ±0.00063	3.30 ±0.17
Right putamen	0.0105 ±0.0013	4.38 ±0.45

[a] The model parameters are expressed as least-square estimates ±standard error.

a)

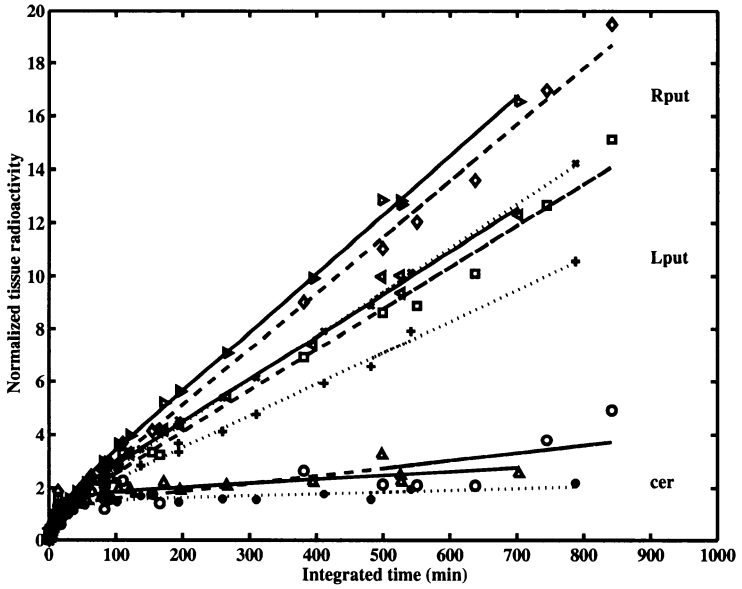

b)

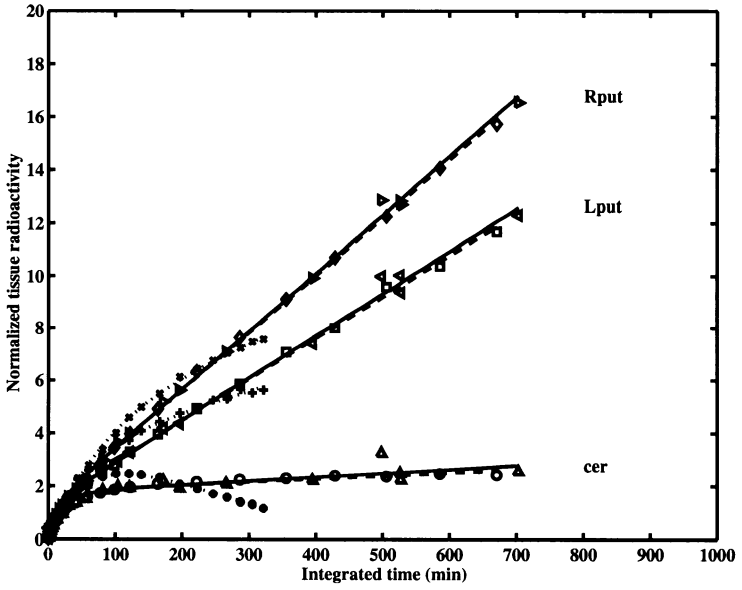

Figure 3.11: *Patlak plots for the cerebellum (∗,○,△), and the left (+,□,◁) and right (×,◇,▷) putamina of the PD subject using* **a**) *the directly sampled (· · · · · ·) and the image-derived (- - - -, single plane; ——, average of several planes) plasma input functions, and* **b**) *the fitted (- - - -, sum of exponentials; · · · · · ·, power function) plasma input functions.*

the unaffected side. These differences between the two subjects and between the affected and unaffected sides of the PD subject are observed using all plasma input functions except the one derived from the fit to power function. The improper fit distorted the overall shape of the Patlak plot from which invalid values of K_i were derived.

3.5 Discussion

The results of the compartmental and graphical analyses of FmT using the image-derived plasma input function were similar to those obtained using the directly sampled plasma input function, despite the shape differences of the two input functions. The use of the image-derived plasma input function enabled the discrimination of the normal and early PD subjects and the identification of the affected and unaffected sides of the PD subject, as indicated by the parameters k_3 and K_i. However, the precision on these parameters was slightly poorer when using the image-derived plasma input function compared to the directly sampled plasma input function.

Partial volume correction reduces bias in the blood TAC extracted from the PET images at the expense of introducing variance. Averaging over several planes was shown to be sufficient for data from the high sensitivity high resolution tomograph ECAT/EXACT3D. For the ECAT/ART tomograph, curve fitting is likely to be necessary. On one side, noise in the blood and tissue TACs will be increased because of the lower sensitivity of the tomograph. On the other side, noise amplification by the partial volume correction will be increased by the poorer spatial resolution of the tomograph (lower RC values). The proposed method requires that ROIs of a given diameter be drawn manually on the blood volume image. Small ROIs correspond to high RC values, thereby limiting the magnitude of the partial volume correction; large ROIs are more robust to statistical noise and variations in the blood vessel calibre. The choice of the ROI diameter is thus a compromise between these factors.

The difference in the shape of the ROI-based blood TAC compared to the directly sampled blood TAC probably reflects in large part errors in the correction for partial volume and spillover. To be more accurate, the correction should account for the heterogeneity of FmT uptake in the tissue surrounding the superior sagittal sinus (mostly the skull, the cerebrospinal fluid and the occipital cortex) and use the actual size of the blood vessel for each individual (Strul and Bendriem, 1999). On the other hand, the directly sampled blood TAC

is confounded by the delay and dispersion occuring at the peripheral blood sampling site. The accuracy of the directly sampled blood TAC is also dependent upon cross-calibration between the PET camera and the radiation detector used to count the radioactive blood. These problems are circumvented by extracting the time course of radioactivity in the blood from the PET images, hence insuring compatibility between the blood and tissue data.

A two-compartment four-parameter model was found to be the best model to describe the uptake of F*m*T in the normal and diseased putamina. It was assumed that k_4 represented loss of radiolabelled metabolites from tissue, but this being an apparent effect of tissue heterogeneity cannot be excluded (Schmidt *et al*, 1991 and 1992). The resulting curvature in the Patlak plot was not apparent nor could k_{loss} (Holden *et al*, 1997) be estimated due to the slower clearance of F*m*T in humans compared to monkeys (Doudet *et al*, 1999) and the relatively short study duration. In contrast, the cerebellum was best described by a two-compartment three-parameter model. Nahmias *et al*(1995), Barrio *et al*(1996) and Jordan *et al*(1997) also detected an irreversible compartment in the cerebellum. This compartment may reflect the trapping of labelled metabolites produced in monoaminergic cells other than dopaminergic cells. The non-zero value of k_3 of the cerebellum may compromise its use as a reference tissue input function. When incorrectly modeled as a one-compartment two-parameter model, the biased volume of distribution of the cerebellum (VD_r) would bias the uptake constants derived from either a reference tissue Patlak plot (Patlak and Blasberg, 1985) or from a reversible reference tissue model (Gunn *et al*, 2001). When correctly modeled as a two-compartment three-parameter model, the small uptake constant of the cerebellum (K_{ir}) would limit the robustness of uptake constants given by the irreversible reference tissue model (Gunn *et al*, 2001).

The blood TACs were extracted from the superior sagittal sinus because it is a large and long isolated blood vessel. By comparison, the internal carotid arteries are small tortuous paired blood vessels. Taking the 3.2 mm and 5.9 mm tubes as models for the ICA and the SSS respectively, the data presented in section 3.4.1 then predict the recovery coefficient of the ICA to be approximately half that of the SSS. These values highlight the greater magnitude of the partial volume and spillover correction for the smaller blood vessels, and consequently the greater accuracy with which their calibre must be determined. The SSS spans over 15 planes in the PET images whereas the ICA can only be viewed on about five planes. This limits the precision with which the radioactivity concentration of the ICA can be estimated from PET images. The close proximity of the two adjacent ICA

in certain subjects imposes an additional correction to account for the spill of radioactivity between the two blood vessels. Even though the superior sagittal sinus is a vein and the internal carotids are arteries, the latter are surrounded by the cavernous sinuses (Curé *et al*, 1994), thereby making it difficult to extract a pure arterial blood signal from outlined ROIs (Litton, 1997; Chen *et al*, 1998).

For radiotracers which, like F*m*T , have a low extraction fraction, the time course of radioactivity concentration in the superior sagittal sinus can be used as a good approximation of the arterial blood input to the brain. Furthermore, the superior sagittal sinus can be delineated on the PET images of the first few minutes following radiotracer administration. The proposed method can still be used with radiotracers having a higher extraction fraction provided that an accurate correction be made to relate the venous to the arterial signal (Knudsen *et al*, 1994; Wahl *et al*, 1999b). The blood vessel can then be outlined from a [^{15}O]CO study done prior to the main study, as has been proposed for blood flow radiotracers (Iida *et al*, 1992; Watabe *et al*, 2001). Extraction of the time course of blood radioactivity concentration from the PET images does not provide a plasma input function for radiotracers which, like F*m*T , are metabolized in peripheral organs and/or distribute unevenly between blood components. A few additional blood samples must still be taken during the PET study in order to transform the blood radioactivity concentration into the plasma concentration of unmetabolised radiotracer. Alternatively, if intersubject variations in peripheral metabolism and blood partition of the radiotracer have been demonstrated to be small (Wahl *et al*, 1999a; Lammertsma *et al*, 1996), population values can be used, thereby making the characterization of a plasma input function entirely noninvasive.

3.6 Conclusion

The method presented in this chapter provides a non-invasive blood input function for PET brain studies. Like the directly sampled plasma input function, the image-derived plasma input function enabled the discrimination of normal and PD subjects and the identification of the affected and unaffected sides of the PD subject. Since the blood input function is extracted from the PET images, this method removes the need for the correction for delay and dispersion associated with blood sampling at a peripheral site as well as for the cross-calibration procedure between multiple radiation detection systems. The method however depends on user input to delineate the superior sagittal sinus. Drawing

ROIs manually on PET images is subjective and time consuming. Furthermore, the method requires prior knowledge of the blood vessel calibre and assumes that the radiotracer uptake is uniform in tissue surrounding the blood vessel. Modifications that address the limitations of this preliminary method may improve further the promising results obtained in this chapter. In the next chapter, the individual calibre of the blood vessel and the heterogeneity of the surrounding tissue will be taken into account by applying the partial volume and spillover correction at the voxel level rather than at the ROI level. A model for the supplementary blood data which are required to transform the blood TAC into a plasma input function will be developed in the chapter after next.

Chapter 4

Parametrically Defined ROIs to Recover the Calibre and Radioactivity Concentration in Cerebral Blood Vessels

4.1 Overview

[1] A new method of obtaining a blood input function for PET brain studies is developed in an attempt to overcome the limitations of the method presented in the previous chapter. The refined method aims to extract the calibre of the blood vessel directly from PET images and to simultaneously correct the radioactivity concentration for partial volume and spillover. This involves simulation of the tomographic imaging process to generate images of different blood vessel and background geometries and selecting the one that best fits, in a least-squares sense, the acquired PET image. A phantom experiment was conducted to validate the method which was then applied to PET images from eight subjects injected with 6-[^{18}F]fluoro-L-DOPA and one subject injected with [^{11}C]CO-labelled red blood cells. In the phantom study, the diameters of syringes filled with an ^{11}C solution and inserted into a water-filled cylinder were estimated with an accuracy of half a pixel (1mm).

[1] *This work was presented in part at the World Congress on Medical Physics and Biomedical Engineering, Chicago (USA), July 2000, and at the BrainPET'01 International Conference, Taipei (Taiwan), June 2001, and published in part in the journal Phys. Med. Biol. (2004)* **49***: 1033-54.*

The radioactivity concentration was recovered to 100 ±4% in the 8.7mm diameter syringe, the one that most closely approximated the superior sagittal sinus (SSS). In the human studies, the method systematically overestimated the SSS calibre by 2-3mm compared with measurements made in magnetic resonance venograms (MRV) on the same subjects. This measure on MRV, whose reliability has not been formally established, was the best one available. Sources of discrepancies related to the anatomy of the blood vessel were found not to be fundamental limitations to the applicability of the method to human subjects. This method has the potential to provide an accurate measurement of the blood radioactivity concentration from PET brain images without the need for blood samples, corrections for delay and dispersion, co-registered anatomical images, or manually defined regions of interest.

4.2 Introduction

Because the cerebral blood vessels are smaller than twice the spatial resolution of most tomographs, the radioactivity concentration extracted from PET images must be corrected for partial volume and spillover (Hoffman *et al*, 1979, Kessler *et al*, 1984) in order to recover the true radioactivity concentration in the blood flowing through these vessels. This correction requires knowledge of the blood vessel calibre as well as the relative positions of different tissues surrounding the blood vessel. This information can be obtained from magnetic resonance (MR) images segmented and co-registered with the PET images. The precision and accuracy of the segmentation and co-registration procedures (Kiebel *et al*, 1997) limit the applicability of the anatomically guided partial volume correction methods (Labbé *et al*, 1996; Rousset *et al*, 1998) to relatively large structures. As correction artefacts tend to be located on the boundary of objects (Strul and Bendriem, 1999), suppressing edge voxels can improve the robustness of partial volume and spillover correction. However, this option is not feasible with small objects since partial volume correction errors propagate to all voxels.

In this chapter, a method which aims to extract the calibre of the superior sagittal sinus (SSS) directly from PET images and, at the same time, to correct the radioactivity concentration inside and outside the blood vessel for partial volume and spillover is presented. The method involves simulation of the tomographic imaging process to generate images of different blood vessel and background geometries and selecting the one that best

fits, in a least-squares sense, the acquired PET image. This method is an adaptation of the model-based optimization method developed by Chen *et al*(1999) for small spheroids surrounded by a uniform background to the cylindrical geometry of blood vessels surrounded by a non-uniform background. A basis function approach (Koeppe *et al*, 1985; Gunn *et al*, 1997) to search through parameter space was implemented to replace the principal axis method used by Chen *et al*(1999).

The method was validated with syringes having diameters ranging from 5 to 15mm inserted into a 20-cm diameter 30-cm long cylindrical phantom filled with water. The diameters of the different syringes were chosen to span the range of calibres of the SSS in humans. The cylindrical phantom simulated the attenuation and scatter conditions typically encountered when imaging the brain. The method was then applied to PET images from eight subjects injected with 6-[^{18}F]fluoro-L-DOPA and one subject injected with [^{11}C]CO-labelled red blood cells. These nine subjects also underwent an MR venogram on which the blood vessel calibre was measured for comparison. Assumptions such as approximating the cross-section of the SSS with a circular disk, modelling the background region as homogeneous and neglecting the curvature of the SSS were investigated in these subjects. Finally, the feasibility of using a population value instead of subject-specific values for the SSS calibre was investigated.

4.3 Materials and Methods

4.3.1 Correction for Partial Volume and Spillover on Voxels

In a PET image, the radioactivity distribution in an object is distorted by the response of the tomograph to a point source of radioactivity, the point spread function (PSF). If the PSF has been characterised accurately, commonly as a Gaussian function specified by a full width at half maximum (FWHM), it is possible to take it into account in order to recover both the dimensions of the object and its true radioactivity concentration.

The dual ROI approach of Kessler *et al*(1984) can be extented to cases where the partial volume and spillover correction is applied to n adjacent objects in a PET image

(Rousset *et al*, 1998):

$$\begin{pmatrix} C_{i1} \\ C_{i2} \\ \vdots \\ C_{in} \end{pmatrix} = \begin{pmatrix} \omega_{11} & \omega_{12} & \cdots & \omega_{1n} \\ \omega_{21} & \omega_{22} & \cdots & \omega_{2n} \\ \vdots & \vdots & \ddots & \vdots \\ \omega_{n1} & \omega_{n2} & \cdots & \omega_{nn} \end{pmatrix} \begin{pmatrix} C_{o1} \\ C_{o2} \\ \vdots \\ C_{on} \end{pmatrix}.$$

The diagonal elements ω_{ii} of the *geometric transfer matrix* (GTM) are the recovery coefficients (Hoffman *et al*, 1979) while the off-diagonal elements ω_{ij} $(i \neq j)$ represent the fraction of true radioactivity concentration in object j which spilled over to the region represented by object i in the PET image. In the Rousset formulation, the true radioactivity concentration values (C_o's) are recovered after applying the inverse of the GTM to the radioactivity concentration values (C_i's) measured in the PET image. Each measured value is obtained by averaging all the voxels contained in the region represented by the object in the PET image. Note that the true radioactivity concentration is assumed to be uniform within each object. The determination of the number of objects should thus be based on fulfulling this stringent assumption.

This problem can be reformulated at the voxel level in a least-squares framework (Labbé *et al*, 1996). Let the $(n \times 1)$ vector x contain the unknown true radioactivity concentration of n adjacent objects in the PET image. Let the $(m \times 1)$ vector b contain the radioactivity concentration measured in each of the m voxels of the PET image. Assuming that each voxel within an object represents an independent measurement of the radioactivity concentration in the object, an $(m \times n)$ matrix $A = PO$ can be set up to represent the linear operation of combining n adjacent objects spatially defined in the $(m \times n)$ matrix O and separately blurred by the PSF defined by the $(m \times m)$ matrix P. The radioactivity concentration of each voxel in the PET image is then given by the equation $b = Ax$. In the Labbé formulation, the true radioactivity concentration values are given by the least-square solution

$$x = [A^T A]^{-1} A^T b \tag{4.1}$$

where A^T is the transpose of matrix A and A^{-1} its inverse. Like in the Rousset formulation, the objects delineated in the Labbé formulation are assumed to have a uniform radioactivity concentration.

As pointed out by Aston *et al*(2002), both the Rousset and Labbé formulations give unbiased estimates of the corrected radioactivity concentration. These two methods,

however, yield different and erroneous estimates of the variance on these estimates because of the improper weighting implicit in their formulation. In the more general weighted least-square framework, the solution to the partial volume problem is

$$x = [O^T W O]^{-1} O^T W P^{-1} b \tag{4.2}$$

where W is the inverse of the covariance matrix. By assuming that the voxels are uncorrelated, the Labbé formulation yields

$$x = [(PO)^T (PO)]^{-1} (PO)^T b \tag{4.3}$$

which corresponds to setting the weighting matrix to $W = P^T P$. The Rousset formulation is equivalent to the solution

$$x = [O^T P O]^{-1} O^T b \tag{4.4}$$

in which the weighting matrix is set to $W = P$. A more realistic description of the noise in the PET image should include both an uncorrelated component (due to Poisson statistics) and a correlated component (due to the reprojection and correction steps in the reconstruction) in the weighting matrix. However, the multiple processes involved in the acquisition, reconstruction and corrections of a PET image make the quantification of the resulting noise properties extremely difficult (Aston *et al*, 2002).

4.3.2 Description of the Algorithm

The approach adopted here models an object and its background with simple geometric shapes that can be defined by a small set of parameters. The tomographic imaging process is then simulated by convolving the parametrised objects with the PSF of the tomograph. This process is repeated with different sets of parameters that cover all the anatomically possible sizes and positions of the objects. For each set of parameters, the true radioactivity concentrations of the objects are estimated using the unweighted linear least-square formulation of Labbé *et al*(1996). The set of parameters that produces the simulated PET image associated with the smallest residual sum of squares when compared with the acquired PET image determines the dimensions and the corrected radioactivity concentrations of the objects.

The particular case of interest here is that of a blood vessel containing a high radioactivity concentration imbedded in tissue of low radioactivity concentrations. The small

spatial extent of the blood vessel (diameter~8 mm) and that of the PSF (FWHM~7 mm) allows for only a small region or *subimage* (~40×40 mm^2) of the whole image (~270×270 mm^2) centered on the blood vessel to be considered. The cylindrical symmetry of the blood vessel can be taken advantage of by decomposing the blood vessel into a stack of aligned thin circular disks, each of the same diameter and having the thickness of the PET planes (3.4 mm). The problem of partial volume and spillover correction is thereby greatly simplified since the two-dimensional (2D) PSF can be considered to be spatially invariant over the region. In addition, the blood vessel and the surrounding tissue can be modelled with simple geometric shapes, thereby obviating the need for segmentation and co-registration of anatomical images.

The model assumes that the blood vessel is a circular cylinder perpendicular to the transaxial planes of the tomograph. The simplest model further assumes that all the tissues surrounding the blood vessel are homogeneous with regards to radiotracer uptake, and thus form a uniform background region. In matrix representation, all the pixels in the subimage located within a circle of radius r centred on the pixel located at coordinates (x_c,y_c) define the blood vessel region of interest (ROI), R_{vsl}, and all pixels located outside that circle define the background ROI, R_{bkg}. These regions are individually convolved with the PSF matrix P and then multiplied by the radioactivity concentrations, c_{blood} and c_{bkg}, respectively. For the *uniform background model*, the simulated image I_{sim1} is finally obtained by summing the two blurred regions as expressed by equation (4.5), under the assumption that the tomographic imaging process is a linear operation.

$$I_{sim1} = c_{blood} P \otimes R_{vsl}(r, x_c, y_c) + c_{bkg} P \otimes R_{bkg}(r, x_c, y_c) \tag{4.5}$$

However, the blood vessel of interest, the superior sagittal sinus, is surrounded mostly by the occipital lobe and the cerebrospinal fluid anteriorly, and by the skull and the scalp posteriorly. The model can be refined by dividing the background region into two regions, each satisfying the homogeneity assumption. On the subimage, the boundary between these regions can be approximated by a circular arc of radius r_0 and centred at pixel coordinates (x_0,y_0). Given the coordinates of two points on the circular arc, one, (x_1,y_1), aligned horizontally with the center of the circle, the other one, (x_2,y_2), located at the right edge of the subimage, the parameters of the circle generating the arc can be calculated using simple geometry (see **Figure 4.1**).

In the subimage, all pixels located within the circle of radius r_0 define the first

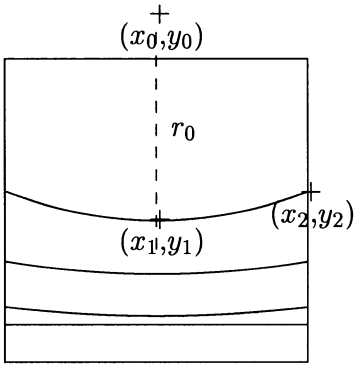

Figure 4.1: *Explanatory diagram of the circular arcs defining the background region in the subimage. Point* (x_0,y_0) *corresponds to the center of the circle subtending the arc. Coordinates* (x_1,y_1) *translate the circular arc horizontally and vertically, respectively. Coordinate* x_2 *is always set at the right edge of the subimage. The curvature of the circular arc is adjusted by the coordinates difference* y_2-y_1. *By defining the background region with pixel coordinates, the number the anatomically possible head sizes and positions (i.e. basis functions) to be calculated is greatly reduced.*

background ROI, R_{bkg1}, and all pixels located outside that circle define the second background ROI, R_{bkg2}. These regions are individually convolved with the PSF matrix P and then multiplied by the radioactivity concentrations, c_{bkg1} and c_{bkg2}, respectively. The simulated background image I_{bkg2} is similarly obtained by summing the two blurred background ROIs as given by equation (4.6).

$$I_{bkg2} = c_{bkg1} P \otimes R_{bkg1}(r_0, x_0, y_0) + c_{bkg2} P \otimes R_{bkg2}(r_0, x_0, y_0) \tag{4.6}$$

For the *non-uniform background model*, the simulated image is generated by summing the blood vessel ROI blurred by the PSF and multiplied by the radioactivity concentration, c_{blood}, with the non-uniform background image, as expressed by equation (4.7). Note that all pixels located within the circle defining the blood vessel are set to zero in the background ROIs R_{bkg1} and R_{bkg2} so that each pixel in the subimage belongs to only one of the three ROIs.

$$\begin{aligned} I_{sim2} &= c_{blood} P \otimes R_{vsl}(r, x_c, y_c) \\ &+ c_{bkg1} P \otimes R_{bkg1}(r, x_c, y_c, r_0, x_0, y_0) \\ &+ c_{bkg2} P \otimes R_{bkg2}(r, x_c, y_c, r_0, x_0, y_0) \end{aligned} \tag{4.7}$$

The residual sum of squares between the simulated image and the acquired image I_{acq} is minimised via unweighted linear least squares in order to estimate the true radioactivity concentrations. A set of simulated images is generated by varying the blood vessel parameters r, x_c and y_c. The blood vessel calibre, centroid coordinates and corrected radioactivity concentration are determined by the simulated image that yields the smallest χ^2 value.

$$\chi^2(c_{blood}, c_{bkg}, r, x_c, y_c) = \Sigma_{x,y}(I_{sim1}(x,y) - I_{acq}(x,y))^2 \quad (4.8a)$$

$$\text{or} \quad \chi^2(c_{blood}, c_{bkg1}, c_{bkg1}, r, x_c, y_c) = \Sigma_{x,y}(I_{sim2}(x,y,r_0,x_0,y_0) - I_{acq}(x,y))^2 \quad (4.8b)$$

4.3.3 Implementation of the Algorithm

The best contrast between the blood vessel and the surrounding tissue is obtained on images of the first few minutes following radiotracer administration, before the radiotracer perfuses the surrounding tissue (referred to as *blood volume image*). On the other hand, the background regions are clearly delineated on PET images obtained after most of the radiotracer has been taken up by the tissues (referred to as *equilibrium image*).

The algorithm first finds on the blood volume image the pixel having the maximum radioactivity concentration. Centered on that pixel, a subimage (20×20 pixels) is extracted from the entire blood volume image (128×128 pixels). Taking advantage of the fact that equations (4.5) and (4.7) are non-linear in the radius and centroid coordinates parameters but linear in the radioactivity concentration parameters, a *basis function approach* is then followed to search through the parameter space $\chi^2(c_{blood}, c_{bkg}, r, x_c, y_c)$. In other words, a semi-exhaustive grid search is used to determine the size and position of the blood vessel, while linear least squares is used to find the radioactivity concentrations. The parameters r, x_c and y_c are varied ($0.5 < r < 4$ pixels and $8 < (x_c, y_c) < 13$ pixels in sampling intervals of 0.1 and 0.5 pixel, respectively) to generate several sets of basis functions, $P \otimes R_{vsl}$ and $P \otimes R_{bkg}$. The diameter of the blood vessel was hence allowed to vary from one pixel (~2 mm) to twice the expected calibre (~16 mm), and the centroid could be located anywhere within an area of ~16 mm in diameter centered on the pixel with the maximum value. Note that the regions R_{vsl} and R_{bkg} are defined at the subpixel level in order to better meet the homogeneity assumption, i.e. that each pixel contains only tissue specific to each region. The smooth circular shape of these regions could thus be preserved, even for the smallest radius values. The basis functions $P \otimes R_{vsl}$ and $P \otimes R_{bkg}$ are evaluated prior to the pixel-to-

pixel comparison with the PET subimage. For each set of basis functions, the radioactivity concentrations, c_{blood} and c_{bkg}, that yield the minimum of equation (4.8a) or (4.8b) are found by using unweighted linear least squares solved by single value decomposition. The uncertainties on all of the fitted parameters are derived from the diagonal elements of the covariance matrix (Landaw and DiStefano, 1984).

The large number of parameters to be estimated (five or six) in the presence of high statistical noise calls for a robust search strategy. The advantages of the basis function approach over other non-linear least squares are twofold. First, the possibility of stopping the search at a local minimum rather than at a global minimum is eliminated by performing a direct search through a parameter space bound by anatomically defined constraints. Second, a careful estimation of the initial values (Chen *et al*, 1999) on which the best fit parameters could be dependent is avoided by finding a linear least-squares solution for each set of basis functions. The basis function approach provides a third practical advantage. For a given PSF, set of parameters r, x_c and y_c and sampling intervals, the matrix containing the basis functions does not need to be re-calculated for every PET image. Instead, it is generated once and stored for subsequent retrieval. The computation times are hence significantly reduced, especially when the search is repeated over several planes. This last advantage is not valid for the non-uniform background model since the non-uniform background region needs to be redefined on each plane.

When using the non-uniform background model, the fitting procedure is applied in two steps. First, the parameters r_0, x_0 and y_0 that best define the background regions are determined on a subimage extracted from the equilibrium image and centered on the pixel having the maximum radioactivity concentration on the blood volume image. The parameters x_1, y_1 and y_2 are varied from 8 to 13, 8 to 20 and 8 to 20 pixels, respectively, at a sampling interval of 1 pixel and with the constraint $y_1 < y_2$. Recall that x_2 is set to 20, at the right edge of the subimage (see **Figure 4.1**). Second, given the best fit parameters for the background regions, the parameters r, x_c and y_c that best define the blood vessel as well as the radioactivity concentrations c_{blood}, c_{bkg1} and c_{bkg2} are found on the subimage extracted from the blood volume image and centered on the same pixel as the equilibrium image. This two-step procedure offers the advantage of reducing the number of fitting parameters for each step compared to a single step procedure, and hence reducing the uncertainties on the fitted parameters.

The calibre of the blood vessel is finally obtained by averaging the estimates over

all the planes that do not satisfy the following *rejection rules.* These rules aim at discarding those planes for which a true minimum was not found in parameter space.

1. *Eliminate the plane if the maximum is not found on the blood vessel.* This is achieved by calculating for each plane the distance between the pixel having the maximum value in the whole image and the pixel located at the centre of the whole image. In order *not* to be eliminated, the distance must be within ten pixels of the median distance calculated over all the planes.

2. *Eliminate the plane if a minimum is found on the boundaries of the parameter space.* In order *not* to be eliminated, the parameters r, x_c and y_c must not take the values delimiting the corresponding parameter space.

3. *Eliminate the plane if no minimum exists in the parameter space.* In order *not* to be eliminated, the standard errors on the parameters r, x_c and y_c must be smaller than half the dimensions of the corresponding parameter space.

For each plane that was not rejected, the radioactivity concentration is calculated by finding the least-squares solution to equation (4.8a) or (4.8b) with the average radius value and the individual values of the centroid coordinates. Ultimately, the radioactivity concentration in the blood vessel is estimated as the average of the radioactivity concentration over all the remaining planes.

4.3.4 Validation with Phantom Data

The *intrinsic* spatial resolution of the tomograph was measured at different locations within the transaxial FOV with and without post-reconstruction smoothing of the PET images. Two phantom experiments were devised to study the accuracy and precision of the algorithm with cylinders of known dimensions and filled with known radioactivity concentrations.

4.3.4.1 Determination of the point spread function

The response of the ECAT/ART tomograph (CTI/Siemens, Knoxville, TN, USA) to a line source of radioactivity, defined as the line spread function but referred to here as point spread function, was measured in air using a 1mm-diameter stainless steel needle

filled with an ^{18}F solution (30 kBq/ml at the start of the first acquisition). The needle was first positioned 10 mm from the centre of the transaxial FOV of the tomograph and then moved in 30-mm steps radially to cover a total distance of 150 mm from the centre of the FOV. Images of 5 to 10 min duration were acquired in three-dimensional (3D) mode at each position in order to map the spatial dependence of the PSF. The images were reconstructed using the 3D reprojection algorithm (Kinahan and Rogers, 1989) with the ramp and Colsher filters cut-off at the Nyquist frequency and with a zoom of 4 (pixel size= 1.3×1.3 mm^2). Neither attenuation nor scatter corrections were applied during the reconstruction. The FWHM of the PSF was estimated by using a modified version of the algorithm described in the previous section: the radius of the circle was set to 0.5 mm and the fitting parameter r was replaced by the width ($fwhm$) of the PSF.

$$I'_{sim1} = c_{blood}P(fhwm) \otimes R_{vsl}(r = 0.5mm, x_c, y_c) + c_{bkg}P(fhwm) \otimes R_{bkg}(r = 0.5mm, x_c, y_c) \tag{4.9}$$

For each needle position, the algorithm was run on seven (planes 16, 18, 21, 27, 30, 32, 36, each 3.4 mm thick) of the total 47 planes, covering an axial FOV of about 70 mm. The reconstructed images were also smoothed with a 2D Gaussian filter having a FWHM of 3.9 mm (3 pixels) or 6.4 mm (5 pixels). The resulting degradation in the intrinsic spatial resolution was determined using the procedure described above.

4.3.4.2 Determination of the diameter and radioactivity concentration of four syringes

Four syringes of inner diameter 14.8±0.1, 11.9±0.1, 8.7±0.1 and 4.7±0.1 mm were filled with an ^{11}C solution (76 kBq/ml at the start of the first acquisition) and inserted into a cylinder, 20 cm in diameter and 30 cm in length, filled with water. The phantom was scanned in the tomograph for 10 sec, four times, one half life apart each time, in order to assess the performance of the algorithm under different noise levels. The images were reconstructed using the 3D reprojection algorithm with the ramp and Colsher filters cut-off at the Nyquist frequency and with a zoom of 2.5 (pixel size= 2.1×2.1 mm^2). Correction for attenuation was performed by manually drawing circles around each cross-sectional image of the cylindrical phantom and using a linear attenuation coefficient of 0.095 cm^{-1} for water at 511 keV. The model-based scatter correction developed by Watson *et al*(1996) was also applied during reconstruction. The reconstructed images were smoothed with a 2D Gaussian

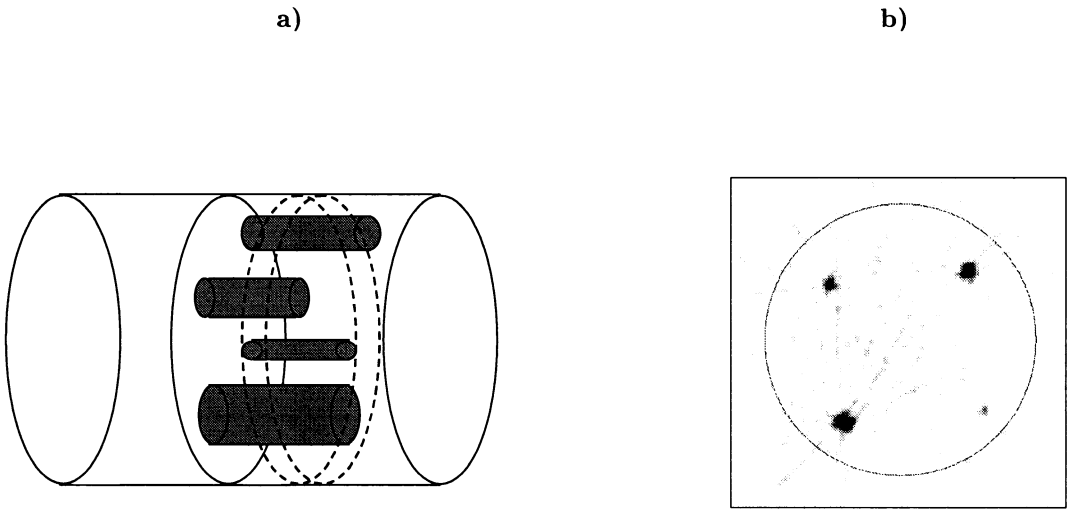

Figure 4.2: *a) Schematic diagram of the phantom: Four syringes (inner diameter 14.8 mm, 11.9 mm, 8.7 mm and 4.7 mm) filled with an ^{11}C solution (76 kBq/ml at the start of the first acquisition) were inserted into a cylinder, 20 cm in diameter and 30 cm in length, filled with water. b) Corresponding PET image for frame 1 without smoothing: 14.8 mm (bottom left), 11.9 mm (top right), 8.7 mm (top left), and 4.7 mm (bottom right). The circle delimits the edge of the cylinder.*

filter having a FWHM of 3.9 mm or 6.4 mm in order to improve the performance of the algorithm on noisy images. The images were divided into four quadrants (64×64 pixels) so that each syringe could be analysed individually. The uniform bakground algorithm (equation (4.5)) was run with the appropriate PSF on the seven planes (planes 21 to 27) in which all four syringes could be seen. The diameter of each syringe was estimated for each frame and smoothing level.

The recovery coefficient (RC) was calculated to assess the accuracy with which the radioactivity concentration was estimated: the closer the RC is to unity, the more accurate is the estimate. Two methods of deriving the true radioactivity concentration in the syringes, C_{syr}, were compared: the estimate obtained from the algorithm, c_{blood} (equation (4.10a)) and that found by taking the mean pixel value in an ROI, C_{roi}, of radius and centroid coordinates given by the algorithm (equation (4.10b)).

$$RC_{sim} = \frac{c_{blood}}{C_{syr}} \tag{4.10a}$$

$$RC_{roi} = \frac{C_{roi}}{C_{syr}} \tag{4.10b}$$

4.3.4.3 Determination of the diameter and radioactivity concentration of the cylindrical phantom

The cylindrical phantom was filled with an ^{11}C solution (4.9 kBq/ml at the start of the acquisition) and scanned in the tomograph for 300 sec. These are typical values of the radioactivity concentration in brain tissue as measured in PET images an hour following the injection of 185 MBq of FDOPA. The images were reconstructed with the same parameters as those used for the four syringes and smoothed post-reconstruction with a 2D Gaussian filter having a FWHM of 3.9 mm. The background algorithm (equation (4.6)) was then run with the appropriate PSF on seven planes (planes 24 to 30) and the cylindrical phantom was estimated to have a diameter of 200 ±80 mm and a radioactivity concentration of 6.0 ±0.3 kBq/ml.

4.3.5 Application to Human Data

4.3.5.1 FDOPA/PET images

Eight early Parkinsonian subjects (six men and two women, age range 37 to 77 years) underwent a two and a half-hour dynamic PET study following the intravenous

injection of 185 MBq of 6-[^{18}F]fluoro-L-DOPA (FDOPA). The head was immobilised in a head holder and positioned so that the orbitomeatal line was perpendicular to the gantry. The room lights and the ambient noise were kept to a minimum during the study. The dynamic PET data were acquired as a sequence of 59 frames (2×10s, 20×5s, 6×10s, 4×180s and 27×300s) so that the very short frames at the beginning of the scan enabled the precise definition of the early time course of the radiotracer in the cerebral blood vessels. The images were reconstructed using the 3D reprojection algorithm with the ramp and Colsher filters cut-off at the Nyquist frequency and with a zoom of 2.5. Correction for attenuation was performed using the reconstructed single-photon transmission images (Yu and Nahmias, 1995) that were acquired immediately prior to the injection of the radiotracer. The model-based scatter correction developed by Watson *et al*(1996) was also applied during reconstruction. The reconstructed images were smoothed with a 2D Gaussian filter having a FWHM of 3.9 mm. A blood volume image was obtained by summing the first two minutes of each study. An equilibrium image was also generated by summing the second hour of each study. The background algorithm (equation (4.6)) was first run on the equilibrium image in order to find the parameters defining the background region. The uniform and non-uniform background algorithms (equations (4.5) and (4.7)) were then run on the blood volume image in order to determine the SSS calibre. The procedure was applied to the planes located above the inferior part of the thalamus (see section 4.4.3.1).

4.3.5.2 CO-RBC/PET images

One normal subject (a 53 year-old man) was injected with 370 MBq of [^{11}C]CO-labelled red blood cells (CO-RBC) and studied for twenty minutes in the tomograph. The dynamic PET data were acquired according to the following frame definition: 24 frames at 5s per frame, 18 frames at 10s per frame, and 3 frames at 300s per frame. The images were reconstructed and smoothed post-reconstruction using the same parameters as those used for the FDOPA/PET studies. A blood volume image was obtained by summing the frames of the first two minutes of the study. The uniform background algorithm was run, with and without axial blurring (see section 4.4.3.3), on the blood volume image in order to determine the SSS calibre.

4.3.5.3 Comparison with MR venograms

Magnetic resonance venograms (MRV) were acquired on the same nine subjects using a head coil inside a 1.5 T Signa Horizon MR imaging unit (GE, Milwaukee, WI, USA). A two-dimensional spoiled gradient recalled vascular time-of-flight (TOF) sequence was chosen with a 46 ms repetition time, a 4.8 ms echo time, a 60° flip angle and a 10.4 kHz bandwidth. An inferior saturation pulse was used to eliminate the arterial flow signal. The transaxial slices were displayed as a 256×128 matrix with a 0.78×1.56 mm^2 pixel size and a 2-mm thickness (without gap). An experienced radiologist measured the SSS calibre as the mean of the long and short axes of the blood vessel. This procedure was repeated on a separate group of 17 normal subjects (nine males and eight females, age range 2-84 years) for the determination of a population value for the calibre of the SSS.

4.4 Results

4.4.1 Phantom Studies

The spatial dependence of the PSF is shown in **Figure 4.3a)** for different smoothing levels of the PET images. These measurements are in good agreement with those published by Bailey *et al*(1997) for the same type of tomograph. At 50 mm from the center of the transaxial FOV, the FWHM is 6.7 mm for unsmoothed images. When images are smoothed post-reconstruction with a 2D Gaussian filter having a FWHM of 3.9 mm or 6.4 mm, the *intrinsic* spatial resolution is further degraded to 7.8 mm or 9.4 mm, respectively. Up to a radial distance of about 80 mm from the centre of the FOV, the PSF varies slowly with distance (approximately 0.1 mm per 10 mm), and even more slowly when the reconstructed images are smoothed. The syringes in the phantom study and the superior sagittal sinus in the human studies were all located within that distance. **Figure 4.3b)** demonstrates that accurate estimates of the syringe diameters can be obtained only if the PSF has been accurately determined at the location of the syringe. An underestimation of the PSF would result in an overestimation of the syringe diameter (and an underestimation of the radioactivity concentration) whereas the syringe diameter would be underestimated (and the radioactivity concentration overestimated) if the PSF was overestimated.

Figure 4.4 displays, as one-dimensional (1D) profiles, examples of best fits to the subimages of the syringes. Approximating the PSF with a 2D Gaussian function appears

a)

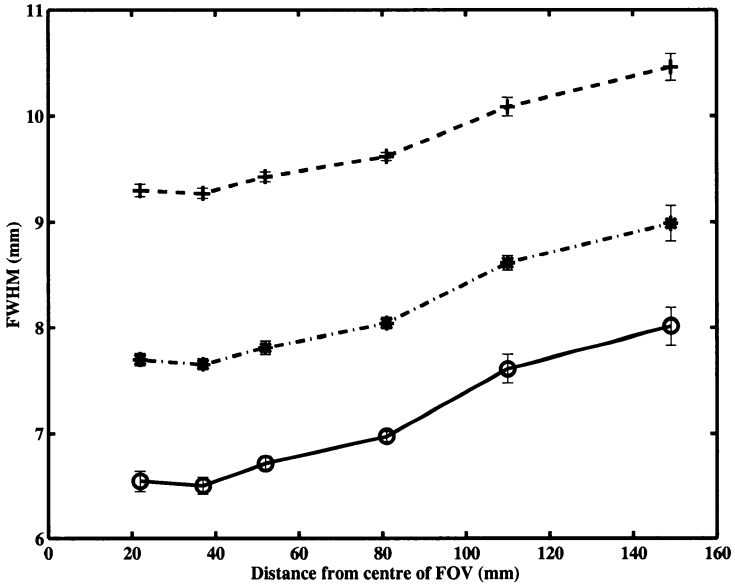

b)

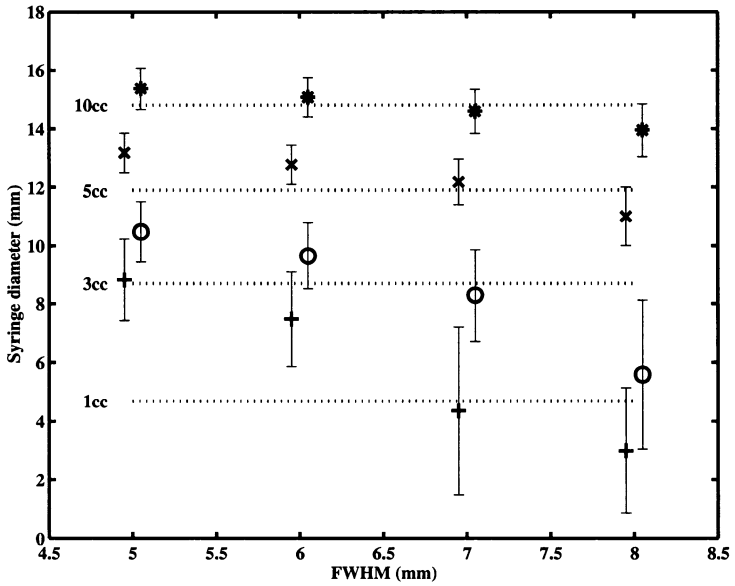

Figure 4.3: **a**) *Variation of the width of the point spread function (PSF) with distance from the centre of the field of view for different smoothing levels: no smoothing ——o, 2D Gaussian filter with FWHM=3.9mm — · —* and with FWHM=6.4mm - - - -+.* **b**) *Variations of the estimated syringe diameters with the width of the PSF: 10ml *, 5ml x, 3ml o and 1ml syringes +. ····· indicates the true value of the syringe diameters. The data points have been offset by 0.05 mm to ease the readability of the plot.*

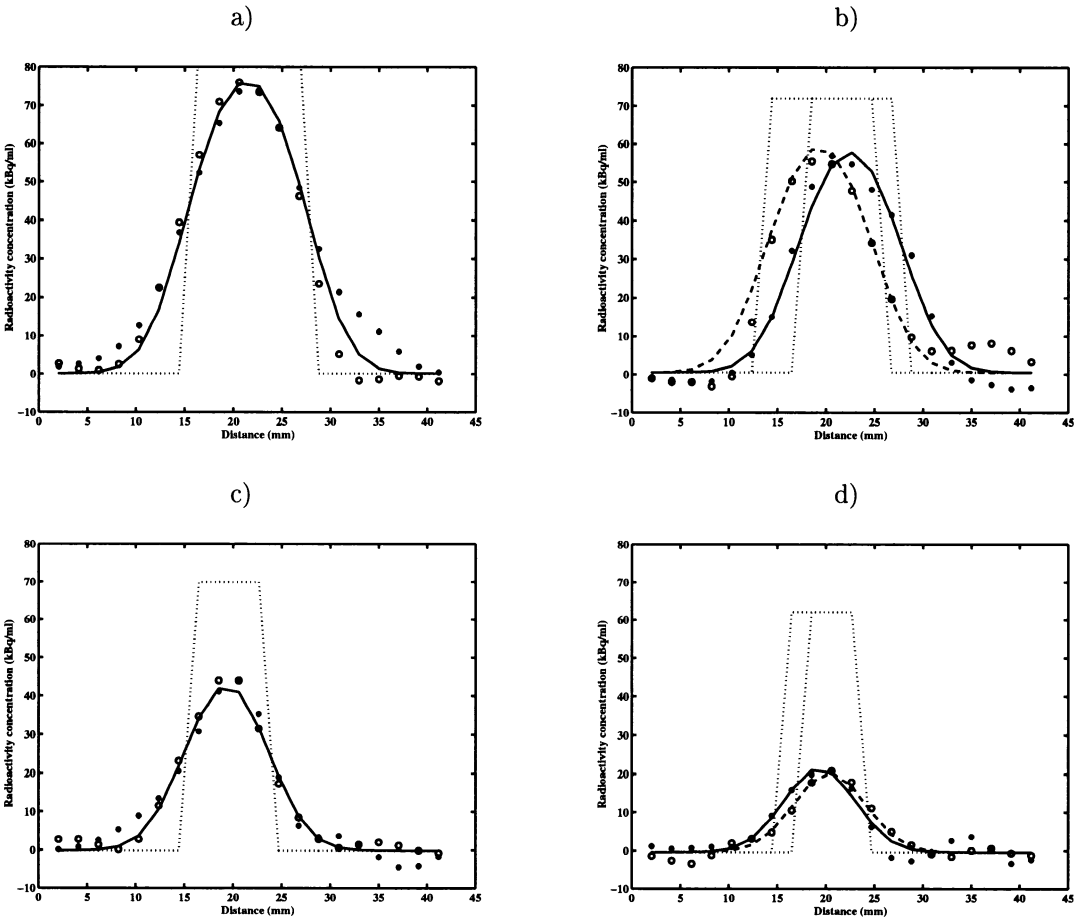

Figure 4.4: *Comparison between the measured one-dimensional profiles (* horizontal; ∘ vertical) through the two-dimensional subimages (I_{acq} in equation (4.8a)) of the syringes crossing at the location of the maximum pixel value in each subimage, the best fit (I_{sim1} in equations (4.5) and (4.8a)) to these profiles (—— horizontal; - - - - vertical, if maximum not centered on subimage) and the estimated profiles (· · · · · ·) after correction for partial volume and spillover ($c_{blood}R_{vsl}(r, x_c, y_c)$ in equation (4.5)), for* **(a)** *10ml syringe,* **(b)** *5ml syringe,* **(c)** *3ml syringe and* **(d)** *1ml syringe. The data were extracted from plane 22 at frame 1 and smoothed post-reconstruction with a 2D Gaussian filter with a FWHM of 3.9mm.*

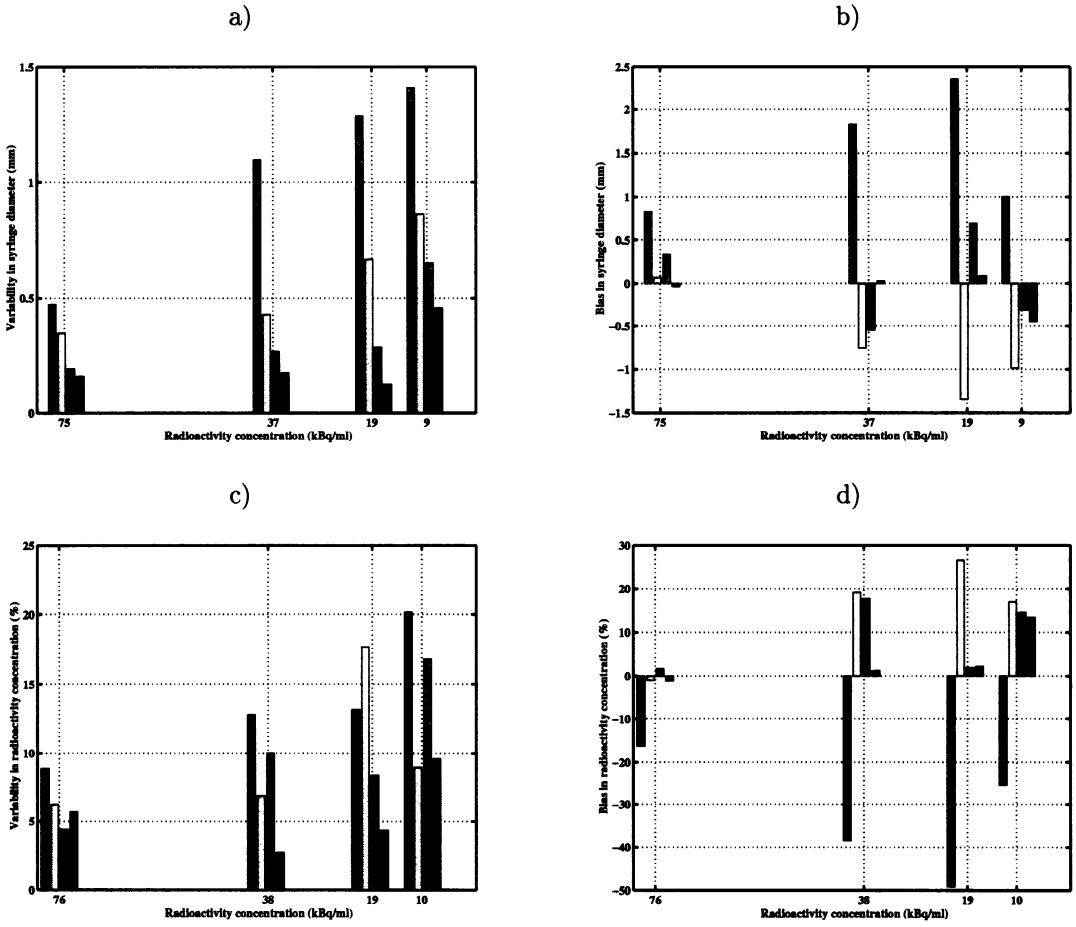

Figure 4.5: *Effects of statistical noise in the PET image on* **a**) *the precision and* **b**) *the accuracy of the estimates of the syringes diameters (in mm), and on* **c**) *the precision and* **d**) *the accuracy of the estimates of the radioactivity concentration in the syringes (in %). Bias is calculated as the difference between the true and estimated values; variability is given by the standard deviations of the mean estimates (over planes 21 to 27). The images were acquired for the same duration one half life apart. For each frame, the results are plotted in increasing order of syringe diameter (the left most bar corresponds to the 1ml syringe and the right most bar to the 10ml syringe).*

Table 4.1: *Comparison of the measured (with a micrometer) and estimated (from the PET images) syringe diameters at different smoothing levels (for frame 1).*

Syringe volume	Micrometer (mm)[a]	PET image (mm)[b]		
		FWHM=6.7mm	FWHM=7.8mm	FWHM=9.4mm
10ml	14.8 ±0.1	14.9 ±0.8	14.8 ±0.6	14.9 ±0.6
5ml	11.9 ±0.1	12.4 ±0.8	12.2 ±0.8	12.2 ±0.7
3ml	8.7 ±0.1	8.9 ±1.4	8.8 ±1.4	8.5 ±1.5
1ml	4.7 ±0.1	5.9 ±2.0	5.5 ±1.9	5.4 ±2.1

[a] Reading ±precision of micrometer.

[b] Mean ±standard deviation (over planes 21 to 27).

to adequately fit the PET data. For frame 1, the mean estimates of the syringe diameters, gathered in **Table 4.1**, lie at most 1 mm away from the true values. Smoothing the PET images reduces the uncertainties on the individual estimates, but not the spread of the estimates from plane to plane, as expressed by the standard deviation on the mean estimates over planes. When the statistical noise in the PET image increases with the decaying radioactivity concentration in the syringes, the syringe diameters are estimated with less precision, as shown in **Figure 4.5a)**. **Figure 4.5b)** illustrates that the syringe diameters are also estimated less accurately from noisier PET images. However, the 1 to 2 mm biases are both positive and negative.

Tables 4.2a) and **b)** contain the recovery coefficients of the four syringes with and without partial volume and spillover correction for different smoothing levels. For frame 1, the radioactivity concentration *before* correction decreases with decreasing syringe diameter and increasing smoothing level to as low as 15% of its true value. *After* correction, the radioactivity concentration is recovered on average to 100 ±4% of its true value, independent of the smoothing level or the syringe diameter, except for the smallest syringe. For subsequent noisier frames, the precision on the estimates of the radioactivity concentration decreases in all four syringes, as plotted in **Figure 4.5c)**. **Figure 4.5d)** shows that the increase in statistical noise does not worsen the accuracy with which the radioactivity concentration is estimated. However, comparison of **Figures 4.5b)** and **d)** reveals that biases in the estimates of the radioactivity concentration influence the biases in the estimates of

Table 4.2: *Recovery coefficients at different smoothing levels* **a**) *before* (RC_{roi}) *and* **b**) *after* (RC_{sim}) *partial volume correction (for frame 1).*

Syringe volume	PET image[a]		
	FWHM=6.7mm	FWHM=7.8mm	FWHM=9.4mm
		a)	
10ml	0.67 ±0.04	0.63 ±0.04	0.57 ±0.03
5ml	0.65 ±0.03	0.60 ±0.03	0.53 ±0.03
3ml	0.49 ±0.04	0.43 ±0.03	0.37 ±0.03
1ml	0.26 ±0.04	0.21 ±0.02	0.16 ±0.02
		b)	
10ml	0.97 ±0.06	0.99 ±0.06	0.98 ±0.06
5ml	1.00 ±0.04	1.02 ±0.04	1.03 ±0.04
3ml	0.96 ±0.07	0.99 ±0.06	1.04 ±0.06
1ml	0.74 ±0.08	0.84 ±0.09	0.88 ±0.09

[a] Mean ±standard deviation (over planes 21 to 27).

the syringe diameters, the extent of which is greater for the smallest syringe than for the larger ones.

The magnitude of the partial volume and spillover correction increases with the width of the PSF relative to the syringe diameter (see **Table 4.2a)**). When the PET images are smoothed with a 2D Gaussian filter having a FWHM of 3.9 mm, the resulting PSF has a width of 7.8 mm, which is comparable to the SSS calibre (see **Table 4.3**). This level of smoothing was thus considered to give the best compromise between edge preservation and noise reduction. Smoothing the PET images post-reconstruction offers the additional advantage of increasing the likehood that the algorithm finds the pixel having the maximum radioactivity concentration within the syringes, rather than in the noisy background.

4.4.2 Human Studies

Figure 4.6 displays the venous sinuses as viewed on a volumetric MRV. The superior sagittal sinus was selected among the venous sinuses for a number of reasons:

1. The superior sagittal sinus has a relatively large calibre, thereby limiting the magni-

Figure 4.6: *Volumetric MR venogram displaying the major venous sinuses:* $\Rightarrow$ *superior sagittal sinus;* $\Downarrow$ *straight sinus;* $\Uparrow$ *transverse sinuses; and* $\Leftarrow$ *confluence of the sinuses (for subject FDOPA-8). The nose points to the left and the back of the head is located on the right.*

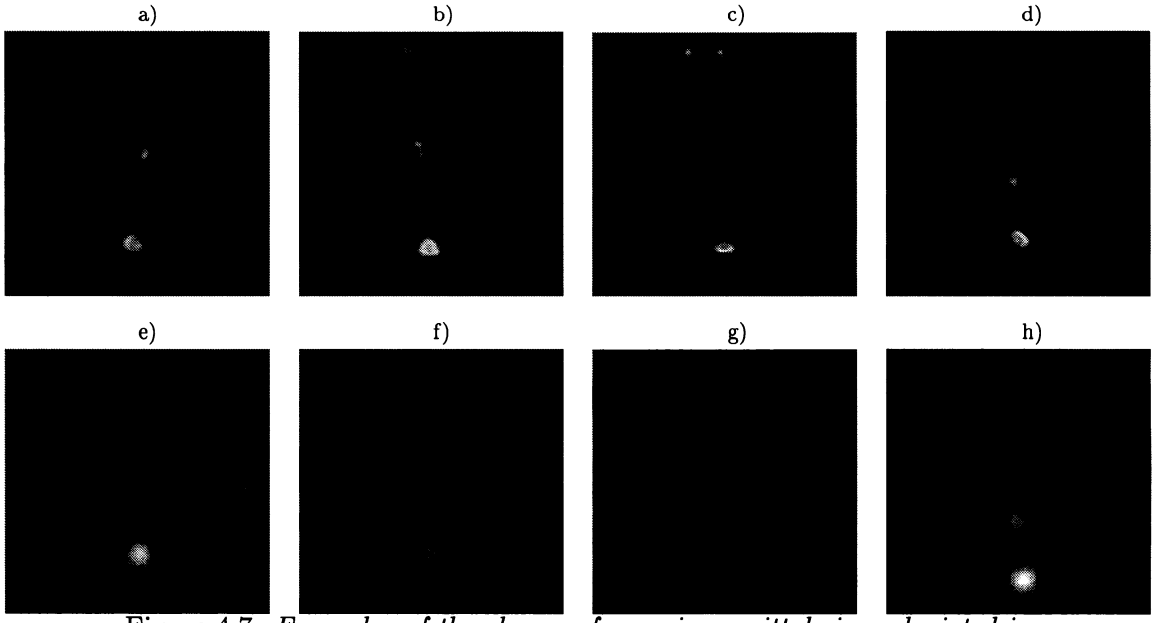

Figure 4.7: *Examples of the shapes of superior sagittal sinus depicted in transaxial slices of MR venograms (top) and PET blood volume images (bottom):* **a**) and **e**) *circular (subject FDOPA-8);* **b**) and **f**) *triangular (subject FDOPA-7);* **c**) and **g**) *elliptical (subject FDOPA-1);* **d**) and **h**) *elliptical (subject CO-RBC). All eight images cover a transaxial field of view of* $84 \times 84 mm^2$.

tude of the partial volume and spillover correction;

2. Its calibre varies slowly over tens of millimeters axially. This allows for calibre estimates made on several consecutive planes to be averaged, hence improving the precision of the estimates;

3. The background region around the blood vessel can be modelled (see section 4.3.2) for radiotracers that are taken up differentially in the tissue surrounding the superior sagittal sinus, as seen on transaxial slices through volumetric MRVs (**Figures 4.7a)**, **b)**, **c)** and **d)**).

Figures 4.7a), **b)**, **c)** and **d)** further illustrate that the shape of the superior sagittal sinus is preserved in the transaxial slice of the high spatial resolution MRVs. In the corresponding plane of the noisy low spatial resolution PET image of **Figures 4.7e)**, **f)**, **g)** and **h)**, the same blood vessel is blurred to the point where it appears to have a circular shape, regardless of its true shape.

The algorithm did not perform as well on the human data as on the phantom data. The SSS calibre obtained from the PET images is systematically overestimated on average by 2 to 3 mm compared with the measurements made on the MR venograms. This conclusion holds true for both the FDOPA and CO-RBC PET studies, as indicated in **Table 4.3**.

4.4.3 Investigation of Model Assumptions

The algorithm is based on a simplified anatomical description of the superior sagittal sinus. The superior sagittal sinus is not a straight cylindrical blood vessel with a circular cross-section nor is it surrounded by uniform brain tissue. The effects that violating these assumptions may have on the calibre estimates were further investigated in search of an explanation for the discrepancies observed between the phantom and human studies.

4.4.3.1 Non-circular shape of the blood vessel region

The superior sagittal sinus is a low pressure vein located between the meninges at the junction of the two cerebral hemispheres (see **Figure 4.7**). The triangular or elliptical shape, rather than circular shape, of the superior sagittal sinus may bias the algorithm to systematically fit the outer points on the blood vessel boundary. The MRVs were binarized

Table 4.3: *Comparison of the measured (on the MR venograms) and estimated (from the PET images) calibres of the superior sagittal sinus in the human subjects.*

Subject	MRV calibre (mm)[a]	PET calibre (mm)[b]
FDOPA-1	7.3 ±0.4 (15)	11.5 ±3.5 (6)
FDOPA-2	7.6 ±0.8 (15)	9.5 ±4.7 (2)
FDOPA-3	8.4 ±0.3 (18)	8.8 ±3.3 (7)
FDOPA-4	7.6 ±0.5 (17)	9.2 ±2.2 (13)
FDOPA-5	7.9 ±0.9 (14)	9.8 ±2.9 (15)
FDOPA-6	7.3 ±0.3 (14)	10.9 ±3.0 (10)
FDOPA-7	8.1 ±0.3 (17)	10.3 ±2.2 (14)
FDOPA-8	8.8 ±0.4 (14)	11.7 ±2.3 (14)
CO-RBC	7.3 ±0.4 (12)	9.4 ±1.8 (16)

[a] Mean ±standard deviation over MRV slices (number of slices).

[b] Mean ±standard deviation over PET planes (number of planes).

Table 4.4: *Best fit diameter and recovery of radioactivity concentration in the superior sagittal sinus from the binarized MR venograms.*

Subject	Direct length measurements[a]	Algorithm estimates[a]	
	Average of axes (mm)	Best fit diameter (mm)	Recovery coefficient
FDOPA-1	7.2 ±0.4 (16)	6.6 ±0.3 (16)	0.97 ±0.14
FDOPA-2	7.7 ±1.1 (10)	7.5 ±1.2 (10)	0.87 ±0.21
FDOPA-3	8.1 ±0.4 (8)	7.9 ±0.4 (8)	1.04 ±0.12
FDOPA-4	7.7 ±0.4 (11)	8.0 ±0.6 (11)	1.03 ±0.11
FDOPA-5	7.6 ±1.0 (16)	7.8 ±0.8 (16)	1.05 ±0.23
FDOPA-6	7.3 ±0.3 (11)	7.9 ±0.4 (11)	1.02 ±0.12
FDOPA-7	7.9 ±0.4 (15)	8.3 ±0.3 (15)	0.93 ±0.11
FDOPA-8	8.8 ±0.5 (14)	8.6 ±0.5 (14)	0.99 ±0.10
CO-RBC	7.1 ±0.5 (12)	7.5 ±0.3 (12)	1.02 ±0.13

[a] Mean ±standard deviation over slices (number of slices).

[b] The best fit diameters from the binarized MRVs were not significantly higher (Student's paired t-test, p(t=0.5937,df=8)>0.25) from the axes length measurements made on the original MRVs.

by assigning a value of 1 to all the pixels whose value was above half the maximum pixel value and a value of 0 to the other pixels. The uniform background algorithm was then run on the binarized MRVs. The calibre estimates from the algorithm were compared to the axes length measurements made on the original MRVs.

The variations in calibre and shape of the superior sagittal sinus with distance from the confluence are illustrated in **Figure 4.8**. For eight of the nine subjects studied, the SSS calibre is relatively constant over the planes encompassing the basal ganglia. The RC values presented in **Table 4.4** indicate that the radioactivity concentration is determined to within 5% of the true value, except for the subject whose SSS calibre is not constant across slices (FDOPA-2). **Figure 4.8** and **Table 4.4** further show that the diameter estimates obtained by running the algorithm on the binarized MRVs are not systematically higher than the average of the long and short axes of the superior sagittal sinus measured on the original MRVs. Approximating the non-circular shape of the superior sagittal sinus with a circle thus does not impede the accurate determination of the radioactivity concentration

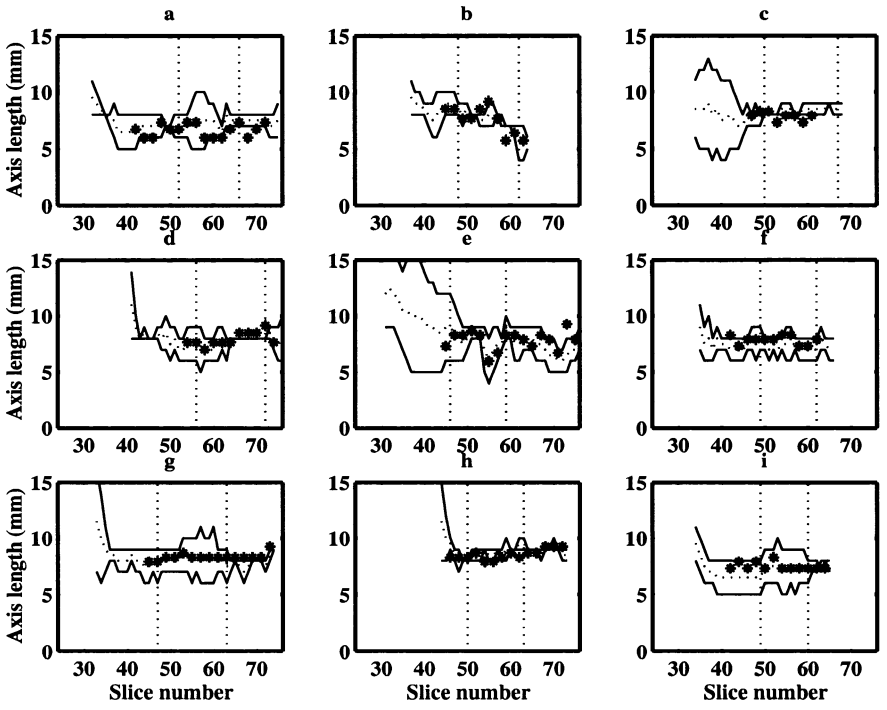

Figure 4.8: *Variations of the superior sagittal sinus calibre with distance from the confluence of the sinuses: —— long (top) and short (bottom) axes length measured on the original MRV, ····· average of the long and short axes length, and * diameter that best fits the binarized MRV. Panels* **a)** *through* **h)**: *subjects FDOPA-1 through FDOPA-8; panel* **i)**: *subject CO-RBC. The MRV slices are 2mm thick (without gap). The two vertical dotted lines delimit the basal ganglia: the left line indicates the inferior part of the thalamus while the right line indicates the superior part of the head of the caudate.*

Table 4.5: *Improvements in the estimates of the calibre of the superior sagittal sinus by accounting for heterogeneity of the surrounding tissue.*

Subject	MRV calibre (mm)	PET calibre (mm)[a]	
		Uniform bkg	Non-uniform bkg
FDOPA-1	7.3 ±0.4	13.6 ±1.0	13.2 ±2.0
FDOPA-2	7.6 ±0.8	12.8 ±0.8	n/a[b]
FDOPA-3	8.4 ±0.3	10.7 ±0.6	10.7 ±1.2
FDOPA-4	7.6 ±0.5	9.1 ±1.3	7.8 ±1.6
FDOPA-5	7.9 ±0.9	9.9 ±0.5	9.5 ±1.5
FDOPA-6	7.3 ±0.3	11.5 ±1.2	10.7 ±2.0
		11.4 ±2.7 (9)[c]	10.7 ±2.3 (9)[c]
FDOPA-7	8.1 ±0.3	9.5 ±0.9	7.4 ±2.3
FDOPA-8	8.8 ±0.4	11.1 ±1.0	10.7 ±1.6
CO-RBC	7.3 ±0.4	9.9 ±0.5	n/a

[a] Best fit estimate ±standard error on the estimate for the plane whose calibre estimate is close to the average calibre estimate over all planes (see **Table 4.3**).

[b] None of the planes considered for subject FDOPA-2 yielded a calibre estimate close to the average calibre over all planes.

[c] Mean ±standard deviation over planes (number of planes).

in the blood vessel.

4.4.3.2 Heterogeneity of the background region

The uniform background may overestimate the SSS calibre as an attempt to compensate for the non-uniform background region. The calibre estimates obtained by running the non-uniform background algorithm (equation (4.7)) on the FDOPA/PET images are compared in **Table 4.5** to those given by the uniform background algorithm (equation (4.5)). All but one of the SSS calibre estimates obtained from the FDOPA/PET images are brought closer to the values measured on the MRV by accounting for the heterogeneous uptake of the radiotracer in the tissue surrounding the superior sagittal sinus. The addition of one more parameter to the model enlarges the standard errors on the calibre estimates, but

not the standard deviation over all planes (see subject FDOPA-6). Nevertheless, the calibre estimates from the PET images remain on average 2mm higher than the corresponding measurements made on the MRVs.

4.4.3.3 Curvature of the superior sagittal sinus

Modelling the CO-RBC/PET subimages with a non-uniform background is not applicable because the radiotracer remains confined to the vasculature, thereby distributing uniformly in low concentrations in all tissue surrounding the superior sagittal sinus. Other factors should thus be responsible for the overestimation of the SSS calibre. Straight cylindrical objects, such as the syringes, can be aligned with the axis of the tomograph, and therefore are not affected by partial volume and spillover in the axial direction. However, the superior sagittal sinus follows the curvature of the head (see **Figure 4.6**), and is therefore prone to blurring in the axial direction. Neglecting axial blurring will lead to an overestimation of the SSS calibre from having underestimated the width of the PSF. Accounting for axial blurring complicates the fitting procedure considerably because the parameters defining the blood vessel on one plane depend on the best fit parameters of adjacent planes. The problem can be simplified by running the uniform background algorithm twice on the CO-RBC/PET subimage. The first run was performed with a 2D PSF in order to extract the centroid coordinates of the blood vessel on each plane. These were fixed in the second run which was performed with a 3D PSF (with an axial FWHM of 6.8 mm (Bailey *et al*, 1997)) from which the remaining parameters, the radius and the radioactivity concentrations, were determined.

The extent of axial blurring in the CO-RBC/PET image, like in the FDOPA/PET images, depends on the SSS curvature and the plane thickness of the PET image. The SSS curvature was calculated from the blood vessel centroid coordinates as the angle between the planes that were the furthest and the closest to the centre of the FOV and the axis of the tomograph. If the superior sagittal sinus were straight, this angle would be zero since the centroid coordinates on all planes would be equidistant to the centre of the FOV. The average SSS curvature was estimated to be relatively small (18±2°) and consistent between subjects (range from 15° to 22°). Correcting for partial volume and spillover in the axial direction brings the estimate of the SSS calibre for subject CO-RBC (SSS curvature of 16°) to 8.9 ±3.0 mm, which is 1mm closer to the measurement made on the MRV (see

Table 4.6: *Apparent width of the point spread function in the human subjects*[a].

Subject	MRV calibre (mm)	PET calibre (mm)	FWHM (mm)[b]
FDOPA-1	7.3 ±0.4	13.6 ±1.0	9.6 ±0.8
FDOPA-2	7.6 ±0.8	12.8 ±0.8	n/a[c]
FDOPA-3	8.4 ±0.3	8.6 ±1.0	9.3 ±0.8
FDOPA-4	7.6 ±0.5	9.1 ±1.3	8.4 ±1.0
FDOPA-5	7.9 ±0.9	9.9 ±0.5	8.7 ±0.5
FDOPA-6	7.3 ±0.3	11.5 ±1.2	11.9 ±1.0
FDOPA-7	8.1 ±0.3	9.5 ±0.9	8.5 ±0.6
FDOPA-8	8.8 ±0.4	11.1 ±1.0	9.5 ±0.7
CO-RBC	7.3 ±0.4	9.9 ±0.5	9.4 ±0.3

[a] The reconstructed PET images were smoothed with a 2D Gaussian filter (FWHM=3.9mm), resulting in an intrinsic spatial resolution of 7.8mm.

[b] Best fit estimate ±standard error on the estimate for the plane whose calibre estimate is the closest to the average calibre estimate over all planes (see **Table 4.3**).

[c] None of the planes considered for subject FDOPA-2 yielded a calibre estimate close to the average calibre over all planes.

Table 4.3). This is in agreement with the 1mm increase in the calibre estimate predicted from running the uniform background algorithm with a 2D PSF on a simulated PET image obtained by convolving with a 3D PSF a stack of circular disks given the SSS calibre and centroid coordinates of subject CO-RBC. However, the improvement achieved by accounting for axial blurring is counteracted by a concomitant increase in the uncertainty on the calibre estimate.

As pointed out earlier, an overestimation of the SSS calibre can be viewed as resulting from an underestimation of the FWHM of the PSF. The broadening of the PSF was estimated for each subject by running the uniform background algorithm modified to search for FWHM of the PSF given a diameter fixed to the SSS calibre measured on the MRV (equation (4.9)). The results presented in **Table 4.6** indicate that the PSF would need to be widened by 0.5 to 4mm in order to match the calibre estimates from the PET

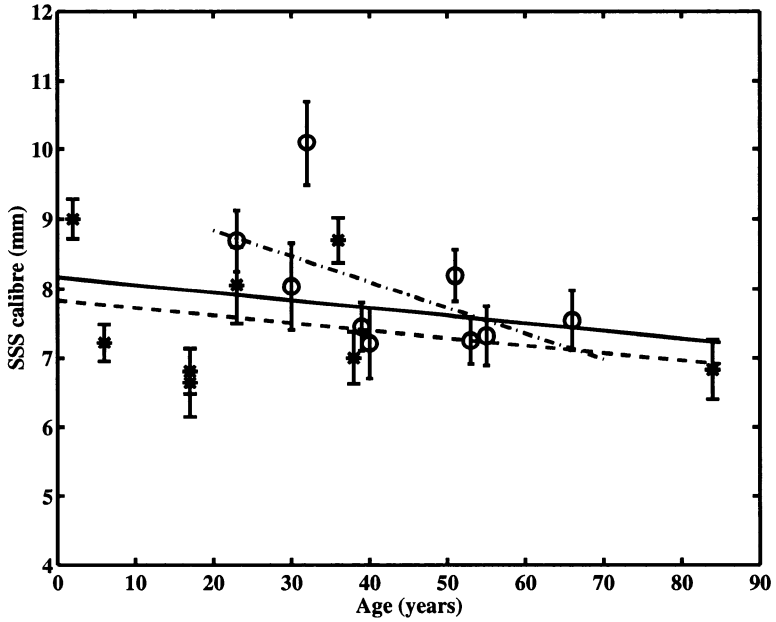

Figure 4.9: *Variations in the calibre of the superior sagittal sinus with age and gender (o,— · —: males; *,- - - -: females, ——: all).*

images with those from the MR venograms.

4.4.4 Determination of a Population Value for the Calibre of the Superior Sagittal Sinus

The measurements from the separate group of 17 subjects are depicted in **Figure 4.9**. The average SSS calibre was measured to be 7.8±0.9mm (range of 6.6 to 10.1 mm), and the average value for the subgroup of females (7.5±0.9mm) was not statistically different from that in the subgroup of males (8.0±0.9mm), as indicated by a two-tailed two-mean *t*-test ($p>0.30$). No significant correlation with age was detected in either the total group or the male and female subgroups ($p>0.10$). The methodology developed in section 3.3.3.1 was used to create blood TACs using both the population and the subject-specific values for the calibre of the superior sagittal sinus. Examination of **Table 4.7** reveals that for subjects whose SSS calibre was increasingly larger than the population value, the area under the blood TAC generated with the population value was overestimated by less than 10% compared to that obtained using the subject-specific value.

Table 4.7: *Shape differences in the blood time-activity curve arising from using* **a)** *a population value instead of* **b)** *a subject-specific value for the calibre of the superior sagittal sinus (SSS) for subjects whose SSS calibre is increasingly larger than the population value.*

Subject	Calibre (mm)	Total area (MBq.s/ml)	Peak height (kBq/ml)
		a)	
FDOPA-7	7.5[a] [+7.4][b]	30.1 [+2.8][b]	41.4 [+12][b]
FDOPA-3	7.5 [+11]	18.2 [+9.2]	28.5 [+36]
FDOPA-8	7.5 [+15]	42.3 [+6.0]	34.5 [+37]
		b)	
FDOPA-7	8.1 ±0.3[c]	29.3	36.9
FDOPA-3	8.4 ±0.3	16.7	21.0
FDOPA-8	8.8 ±0.4	39.9	25.1

[a] Average value determined from an independent group of 17 subjects.

[b] Relative difference between population and subject-specific values (in %).

[c] Mean ±standard deviation over MRV slices for each individual subject.

4.5 Discussion

The diameter of small cylindrical objects inbedded into an attenuating and scattering medium is infered from PET images with an accuracy of half a pixel (1mm). After correction for partial volume and spillover, the true radioactivity concentration in the 8.7mm syringe is recovered to 100 ±4%, regardless of the degree of post-reconstruction smoothing. Before correction for partial volume and spillover, only 40 to 50% of the radioactivity concentration is measured in this syringe which is the closest approximation to the superior sagittal sinus. The validated method is not able to determine as accurately the SSS calibre in human subjects when compared to the MRV measurements. The systematic 2 to 3mm overestimation of the cerebral blood vessel calibre impedes the accurate estimation of the radioactivity concentration in the blood.

Geometrical differences between the superior sagittal sinus and the syringes were investigated as potential fundamental limitations to the applicability of the method to human subjects. The approximation of the cross-section of the superior sagittal sinus with a circular disk does not lead to a systematic overestimation of the calibre, nor does it introduce a bias in the estimated radioactivity concentration. On the other hand, the blood vessel calibre is overestimated by about 1mm when the radiotracer was assumed to be distributed uniformly in tissue having a heterogeneous uptake. Furthermore, applying axial blurring to the curved superior sagittal sinus results in an apparent increase in the blood vessel calibre of about 1mm in the PET planes.

The proposed method can be modified to take into account the heterogeneous uptake of the radiotracer in the tissue surrounding the superior sagittal sinus. With a radiotracer like FDOPA that has a relatively low uptake in the occipital lobe, a partial volume and spillover correction that uses a non-uniform background region yields more accurate SSS calibre estimates than a uniform background region. This correction will become even more important for radiotracers that have a high uptake in the cerebral cortices. Moreover, the radioactivity concentration in the blood at later times cannot be recovered without an accurate correction for spillover (Iida *et al*, 1992; Watabe *et al*, 2001). This requirement applies to all radiotracers that perfuse the tissue surrounding the blood vessel.

In order to correctly account for axial blurring, the SSS centroid coordinates should not be fixed to those found using a 2D PSF, but rather be left as free parameters when the algorithm is run with a 3D PSF. Depending on the curvature of the blood vessel, axial

blurring not only increases the apparent calibre in the PET planes, but also shifts the centroid coordinates to other pixels. The increase in the uncertainty of the calibre estimate observed after accounting for axial blurring is probably due to this mispositioning. However, the correct approach would increase the number of basis functions that need to be generated to the point where a search strategy other than a basis function approach should be used (Chen *et al*, 1999).

The lack of an agreed method to quantify statistical noise in PET images makes a direct comparison between the phantom and the human studies difficult. Nevertheless, the presence of radioactivity in the tissue surrounding the superior sagittal sinus obscures the signal from the blood in statistical noise, unlike the syringes which were inserted into a non-radioactive background. The plane-to-plane variations in both the syringe diameter and the radioactivity concentration increase with an increase in statistical noise, but no systematic bias is introduced. Complementary phantom experiments could be devised in order to study the accuracy and precision of the correction for the spill of radioactivity from a hot background into cold syringes. These more complicated studies remain an approximation of the conditions encountered with human subjects. It remains that the background radioactivity concentration in the human CO-RBC study was very low and uniform, and despite that, the overestimation of the SSS calibre was similar to that obtained in the F-DOPA studies for which the background was higher and non-uniform.

The unweighted least square estimation procedure for estimating the blood vessel parameters assumes that the noise in the PET images is white, when in fact it is both coloured and non-stationary. The least-square formulation of the partial volume correction adopted here is that of Labbé *et al*(1996). As derived by Aston *et al*(2002), this formulation gives unbiased estimates of the corrected radioactivity concentration, but incorrectly estimates the variance on these estimates because of the improper weighting implicit in the formulation. However, accurate quantification of the noise correlation in the PET images is very difficult bacause of the multiple processes involved in the acquisition, reconstruction and corrections of PET images. When the PET images are reconstructed analytically using the 3D reprojection algorithm, Pajevic *et al*(1998) have demonstrated that in a homogeneously attenuating medium, the noise distribution is uniform whether the radioactivity concentration is homogeneous or heterogeneous. Because the linear attenuation coefficient does not vary much across brain tissues (except for the surrounding skull), the image variance was considered to be similar throughout the brain.

The sources of discrepancies that are related to the anatomy of the superior sagittal sinus, when corrected for, can only overcome part of the systematic overestimation of the calibre of the blood vessel. The source of the overestimation appears to be subject specific. Factors that could lead to an apparent widening of the PSF include positron range, inaccuracies in attenuation and scatter corrections and head motion. The accuracy of the results obtained in the phantom experiments precludes the neglected positron range as a possible factor. Furthermore, the phantom studies used an ^{11}C (mean positron range in water of 1.2 mm) solution whereas most human studies were performed with a tracer radiolabelled with ^{18}F (mean positron range in water of 0.6 mm). Inaccuracies in attenuation maps propagate into errors in the estimates of scatter by model-based correction methods (Watson *et al*, 1997). When the PET data are not corrected for scatter, the PSF is broadened in an object-dependent manner (Chen *et al*, 1999). Green *et al*(1994) estimated that head movements of 5 mm can widen the apparent FWHM by as much as 2 mm for a tomograph offering an intrinsic FWHM of 8 mm. The movement artefacts were shown to vary in space and time and to be reduced by head restraint. The head holder used in the human studies and the short duration of the blood volume images should have limited movements of large amplitude and drifts over time, but would not have prevented small oscillatory movements.

Large inaccuracies in the determination of the SSS calibre result in large errors in the estimates of the radioactivity concentration in the blood vessel. It is believed that once a subject-specific FWHM can be independently measured (e.g. by monitoring the subject for head movement), it will become possible to determine the blood vessel parameters accurately using the proposed method. These can then be used to derive a blood TAC by sequentially applying equation (4.1) to all frames in the dynamic PET images.

Unlike other methods that have been developed (Iida *et al*, 1992; Wu *et al*, 1996; Chen *et al*, 1998; Watabe *et al*, 2001), the method presented in this chapter does not require additional venous blood samples for the partial volume and spillover correction. It is also more objective than methods that rely on an observer to interpret the PET images in order to manually draw ROIs over the blood pools (Iida *et al*, 1992; Chen *et al*, 1998; Wahl, *et al*, 1999b; Asselin *et al*, 2001) or to identify the pixel having the maximum radioactivity concentration (Germano *et al*, 1992; Watabe *et al*, 2001). Furthermore, it does not necessitate the availability of an MR image (Litton, 1997) to define the blood vessel ROI. It should be pointed out that most of these methods also suffer from inaccuracies in the determination of the apparent PSF in human subjects.

The differences between the PET and MR estimates could be attributed in part to an underestimation of the SSS calibre as measured on the MR venograms. The MR venograms were acquired using a flow sensitive (TOF) sequence and signal losses due to either slow or disturbed blood flow have been shown to produce image distorsions (Tsuruda *et al*, 1992), which effects may be a reduction in the apparent calibre of the blood vessel. Andrews *et al*(1989) measured in ten human brains at autopsy the SSS calibre in the occipital region to be 10mm on average. These measurements, however, probably overestimated the *in vivo* SSS calibre due to the net displacement of fluids that occurs *post mortem* towards the vasculature. No other study, to my knowledge, has attempted to measure the calibre of the venous sinuses.

The SSS calibre was measured to vary between 6 and 10 mm with a mean of 8mm and a standard deviation of 1mm on the MR venograms of 17 human subjects of ages 2 to 83 years (Asselin *et al*, 2002b). Furthermore, the blood vessel calibre was found to be independent of gender and age. This between-subject variations in the SSS calibre are smaller than the errors of the present method and comparable to the errors of MRI/PET co-registration algorithms (Kiebel *et al*, 1997). Errors in the vessel calibre mainly affect the peak height of the blood TAC, and to a lesser extent the area under the curve. Discrepancies between input functions comparable to those reported in **Table 4.7** were shown in Chapter 3 not to limit the ability of rate constants to discriminate between normal and Parkinsonian subjects as well as to identify the affected and unaffected sides of the Parkinsonian subject. Until methods to obtain subject-specific values of the SSS calibre are improved, a population value for the SSS calibre can alternatively be used to obtain blood input functions noninvasively from brain PET images.

4.6 Conclusion

The method as refined in this chapter estimates the diameter of cylinders with an accuracy of half a pixel (1 mm) and fully recovers the radioactivity concentration in phantom studies. The method does not depend on the input from a subjective observer other than for the selection of the planes on which to carry out the analysis, and can therefore be implemented as an automatic procedure. It also offers the flexibility to model with simple geometric shapes a non-uniform background region for more accurate partial volume and spillover correction. The method does not require co-registered anatomical

images, which are not always available in clinical settings. Technical advances towards tomographs offering higher sensitivity and finer spatial resolution (Wienhard *et al*, 2002) coupled with improvements in scatter correction methods (Watson *et al*, 2000), and the introduction of head motion correction systems (Bloomfield *et al*, 2003) may render this method applicable to human studies with an accuracy approaching that achieved in phantom studies. The between-subject variations in the SSS calibre are small enough to warrant the use of a population value, thereby eliminating the requirement for subject-specific values to obtain blood input functions non-invasively from brain PET images. Ultimately, this method will simplify the procedures involved in performing a PET study without sacrificing the capability of PET to provide quantitative measures of physiological processes.

Chapter 5

Development of a Unified Compartmental Model for the Correction of the *In Vivo* Metabolism and Partitioning of Radiotracers in Whole Blood

5.1 Overview

[1] A compartmental model relating the radiotracer FmT , its main radiolabelled metabolite and their exchange between plasma and erythrocytes is presented in this chapter. This model allows for the time course of total radioactivity measured in whole blood to be transformed into the time course of the unmetabolised radiotracer in plasma. A three-compartment four-parameter model is shown to yield significantly better fits to the blood data than related lower and higher order models. This model is found to be robust to measurement noise, and yet sensitive to the metabolic changes induced by pretreatment with carbidopa. The between-subject variations are shown to be small enough to warrant the use of a population-based correction; tissue time-activity curves were simulated to verify that this correction does not significantly affect the precision and accuracy on the derived

[1] *This work has been published in part in the journal* Phys.Med.Biol. (2002) **47**: 1961-77.

rate constants. When time-activity curves are extracted from blood pools visible in the PET images, the unified compartmental model with a population-based correction allows the plasma input function to be determined non-invasively, thereby eliminating the need to draw and process blood. The unified blood model can be adapted for radiotracers other than F*m*T as long as the blood partition ratio of the parent radiotracer differs from that of its metabolites and/or the rate at which they equilibrate between plasma and erythrocytes is different.

5.2 Introduction

The radioactivity concentration extracted from blood pools in dynamic PET images corresponds to the time course of total radioactivity in whole blood. This time-activity curve can be used as an input function for kinetic analyses only for radiotracers that are exchanged rapidly and distributed equally in plasma and erythrocytes, as is approximately the case for 2-[^{18}F]fluoro-2-deoxy-D-glucose (FDG) (Chen *et al*, 1998). However, radiotracers that either equilibrate slowly between blood components and/or are actively concentrated by or excluded from erythrocytes require that the radioactivity concentration measured in whole blood be transformed into the radioactivity concentration in plasma. The PET study must then be supplemented by blood samples that are drawn at discrete times and centrifuged in order to measure the radioactivity in plasma. If, in addition, the radiotracer is metabolised in peripheral tissue, blood sampling cannot be avoided regardless of the kinetics of equilibration of the radiotracer in whole blood. More blood samples are drawn and assayed biochemically in order to determine the contribution of the various radiolabelled compounds to the measured radioactivity in plasma. The processing of these blood samples typically involves multiple steps, thereby making the procedure time consuming and the measurements prone to noise. Only a few blood samples can thus be analysed for each PET study and one typically has recourse to exponential and/or polynomial functions in order to interpolate between and extrapolate from these data points.

The total radioactivity concentration in whole blood is usually corrected in two independent steps, first to yield the total radioactivity concentration in plasma, and second to obtain the parent radiotracer concentration in plasma. For both corrections, separate compartmental models have been proposed as alternatives to arbitrary mathematical functions for the extrapolation of the incomplete blood data over the duration of the PET study.

In contrast with arbitrary mathematical functions, compartmental models can incorporate *a priori* knowledge of the dominant processes of the system being measured. Huang *et al*(1991b) introduced a general compartmental model that relates the time course of a radiotracer in plasma to that of its metabolites, and illustrated the utility of their model with 6-[^{18}F]fluoro-L-DOPA (FDOPA) and [^{15}O]oxygen. Their model was later modified and applied to [^{11}C]L-deprenyl (Lammertsma *et al*, 1993) and [^{11}C]raclopride (Carson *et al*, 1997). Nahmias *et al*(2000) described the *in vitro* exchange of a radiotracer between plasma and erythrocytes with simple closed compartmental models. Blood samples collected following the injection of a radiotracer in human subjects contain radioactivity arising from both the unmetabolised radiotracer and its radioactive metabolites, all of which can be exchanged between plasma and erythrocytes. The partitioning of radioactivity between plasma and eythrocytes is therefore linked to the metabolism of the radiotracer. Gunn *et al*(2001) recently suggested that these two processes could be addressed in a unified compartmental model. Such a blood model could be used to extract the contribution of the parent radiotracer in plasma from the total radioactivity measured in whole blood.

Previous studies have demonstrated that F*m*T equilibrates slowly between plasma and erythrocytes (Nahmias *et al*, 2000). Furthermore, radiolabelled metabolites of F*m*T have been identified in plasma (Barrio *et al*, 1996; DeJesus *et al*, 1997; Wahl *et al*1999a). In this chapter, prior knowledge of the behaviour of F*m*T is incorporated into the design of a compartmental model that describes the partitioning of F*m*T and its main metabolite in whole blood. The model is applied to blood data collected from human subjects who were injected with F*m*T . The possibility of reducing the number of blood samples is tested with the unified blood model, and its robustness to noise is compared to that of the separate *ad hoc* functional forms previously used. The need to draw and process discrete blood samples can be eliminated if between-subject variations in the blood data are sufficiently small (Iida *et al*, 1993; Wahl *et al*, 1999a). With this in mind, a population-based correction is derived from the values provided by the unified blood model. The applicability of this correction is tested on a separate group of human subjects. The effects of replacing individual values with population-based values for correcting the blood data on the estimation of tissue kinetic parameters is evaluated with a simulation study.

5.3 Theory

Consider a simple system: a parent radiotracer and one predominant radiolabelled metabolite coexist in 1 ml of blood at a given time. Ignoring for the moment any tissue effects, the goal is to determine the radioactivity attributable to the parent radiotracer in plasma at that time. The total radioactivity will be distributed between four distinct compartments: the parent radiotracer in plasma or in erythrocytes, and the main metabolite in the same two physical compartments. Throughout the chapter, the subscripts 1 and 2 are used to denote the parent and the metabolite, respectively, which are followed by either the subscripts p or e to denote in plasma or erythrocytes, respectively. Thus M_{2p} refers to the quantity of the plasma metabolite in 1 ml of blood at a specific time (expressed in kBq per ml of blood).

Suppose that the total radioactivity in whole blood can be easily determined, providing a measure of $M_{1p}+M_{2p}+M_{1e}+M_{2e}$. The ratio of the radioactivity in erythrocytes to that in plasma can be derived from the results of the blood analyses. We can solve for $M_{1p} + M_{2p}$ and $M_{1e} + M_{2e}$ from the sum of the two quantities and their ratio. The blood analyses also yield the ratio of the metabolite to the parent in plasma, allowing the solution of M_{1p} and M_{2p}. The measurement of the haematocrit will then give the concentration of the parent radiotracer in plasma, C_{1p} (expressed in kBq per ml of plasma).

In principle, the concentration of the parent radiotracer in plasma can be obtained at any given time from knowledge of the total radioactivity concentration in whole blood and the two ratios described above. Note that the concentration of the main metabolite in plasma can also be inferred from these data, but additional measurements would be required in order to separate the parent radiotracer concentration from the main metabolite concentration in erythrocytes. This analysis can be repeated at all times, thereby providing a unified functional form that can be used for the extrapolation and interpolation of the limited blood data.

5.3.1 General Model

A compartmental model which describes the *in vitro* equilibration of a radiotracer between plasma and erythrocytes has recently been proposed (Nahmias *et al*, 2000). The following sections extend this model to include the peripheral metabolism of the radiotracer that occurs *in vivo*. The extended model is illustrated in **Figure 5.1a**. A suite of related

models based on the general model will be statistically tested later in order to select the model which is most appropriate for the *in vivo* data.

Unlike L-DOPA and the fluorinated analog FDOPA, F*m*T is not a substrate for the enzyme cathechol-*O*-methyl transferase (COMT), thereby limiting the metabolic pathways of F*m*T to that engaged by the enzyme aromatic L-amino acid decarboxylase (AADC). F*m*T is believed to be decarboxylated to 6-[^{18}F]fluoro-*m*-tyramine (F*m*TA), which in turn is oxydated to 6-[^{18}F]fluoro-3-hydroxyphenylacetic acid (FHPAA) (Barrio *et al*, 1996; DeJesus *et al*, 1997). Together, F*m*T and FHPAA account for more than 95% of the radiolabelled species in plasma for up to two hours post-injection (Wahl *et al*, 1999a). F*m*T was found to be equally distributed in the water fraction of both plasma and erythrocytes and to have reached equilibrium after about an hour of incubation (Nahmias *et al*, 2000). FHPAA equilibrates much faster than F*m*T (within 5 min of incubation) and is slightly less concentrated in erythrocytes than in plasma (Nahmias *et al*, 2000). The differences in kinetics observed for these two compounds can be attributed in large part to the different transport systems that carry them from plasma to erythrocytes. F*m*T is likely to enter the erythrocytes by facilitated diffusion via the L and T transport systems for amino acids (Tunnicliff, 1994; Widmer *et al*, 1986). FHPAA is thought to cross the erythrocyte membrane via the specific H^+/HCO_3^- co-transporter, which is the dominant transport system for monocarboxylates (Poole and Halestrap, 1993).

Based on this information, the exchange of the parent radiotracer between plasma and erythrocytes is modelled by two rate constants, k_1 and k_2, and that of the main metabolite is described by two distinct rate constants, k_1' and k_2'. The parent radiotracer is transformed irreversibly to its main metabolite with the rate constant k_3. The parent and the metabolite leave the blood to the tissues with the rate constants k_5 and k_6, respectively. The volume V_e of the erythrocytes compartments $C_{1e}(t)$ and $C_{2e}(t)$ is set to the haematocrit H, and the volume V_p of the plasma compartments $C_{1p}(t)$ and $C_{2p}(t)$ to $(1-H)$, such that the volume of whole blood is equal to unity. Under the assumptions of linearity and

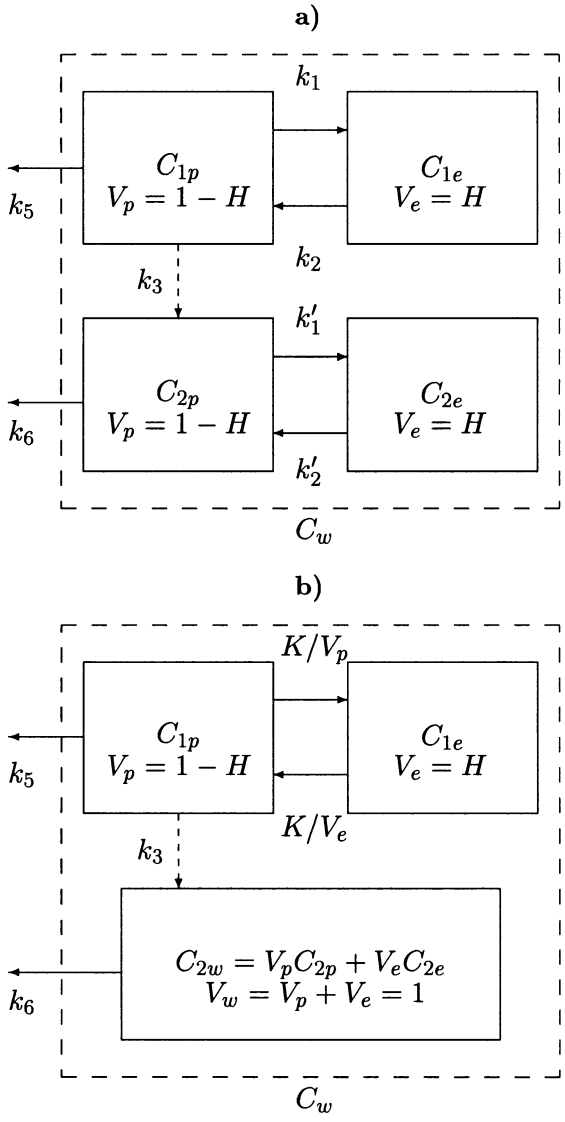

Figure 5.1: *Compartmental models describing the distribution of radioactivity in whole blood. The parent radiotracer is exchanged between the plasma and erythrocytes compartments ($C_{1p}(t)$ and $C_{1e}(t)$):* **a) The general case**: *k_1 and k_2 represent the rate constants of influx and backflux to and from the erythrocytes;* **b) The simplified case**: *when at equilibrium, the parent concentration in plasma is the same as in erythrocytes ($V_p k_1 = V_e k_2 = K$, where V_p and V_e are the volumes of plasma and erythrocytes in 1 ml of blood, respectively, and H is the haematocrit). The parent (FmT) is transformed into its main metabolite (FHPAA) with the rate constant k_3. The parent and its metabolite leave the whole blood compartment ($C_w(t)$) with the rate constants k_5 and k_6, respectively. The models also include the exchange of the metabolite between the plasma and erythrocyte compartments ($C_{2p}(t)$ and $C_{2e}(t)$):* **a)** *when the rate constants of influx k_1' and backflux k_2' to and from the erythrocytes are small, and* **b)** *when they are much larger than those of the parent ($V_p k_1', V_e k_2' \gg K$).*

stationarity, the rates of change of the concentration in each compartment are given by

$$V_p\frac{dC_{1p}}{dt} = -(k_1+k_3+k_5)V_pC_{1p}(t)+k_2V_eC_{1e}(t) \quad (5.1a)$$

$$V_e\frac{dC_{1e}}{dt} = k_1V_pC_{1p}(t)-k_2V_eC_{1e}(t) \quad (5.1b)$$

$$V_p\frac{dC_{2p}}{dt} = k_3V_pC_{1p}(t)-(k_1'+k_6)V_pC_{2p}(t)+k_2'V_eC_{2e}(t) \quad (5.1c)$$

$$V_e\frac{dC_{2e}}{dt} = k_1'V_pC_{1p}(t)-k_2'V_eC_{2e}(t). \quad (5.1d)$$

Rewriting equations (5.1a), (5.1b), (5.1c) and (5.1d) in matrix form,

$$\begin{pmatrix} \dot{C}_{1p} \\ \dot{C}_{1e} \\ \dot{C}_{2p} \\ \dot{C}_{2e} \end{pmatrix} = \begin{pmatrix} -k_1-k_3-k_5 & k_2\left(\frac{V_e}{V_p}\right) & 0 & 0 \\ k_1\left(\frac{V_p}{V_e}\right) & -k_2 & 0 & 0 \\ k_3 & 0 & -k_1'-k_6 & k_2'\left(\frac{V_e}{V_p}\right) \\ 0 & 0 & k_1'\left(\frac{V_p}{V_e}\right) & -k_2' \end{pmatrix} \begin{pmatrix} C_{1p} \\ C_{1e} \\ C_{2p} \\ C_{2e} \end{pmatrix}.$$

Equations (5.1a) and (5.1b) are coupled to equations (5.1c) and (5.1d) via only the rate constant k_3. Compartments $C_{1p}(t)$ and $C_{1e}(t)$ can thus be solved as a two compartment four-rate constant reversible system with the initial conditions $C_{1p}(0) \neq 0$ and $C_{1e}(0) = 0$. This formulation assumes that the radioactivity is injected as a true bolus and mixed instantaneously in the compartment $C_{1p}(t)$:

$$C_{1p}(t) = \left(\frac{1}{\lambda_1-\lambda_2}\right)\Big[(\lambda_1+k_2)\exp(\lambda_1 t)-(\lambda_2+k_2)\exp(\lambda_2 t)\Big]C_{1p}(0) \quad (5.2a)$$

$$C_{1e}(t) = \left(\frac{V_p}{V_e}\right)\left(\frac{k_1}{\lambda_1-\lambda_2}\right)\Big[\exp(\lambda_1 t)-\exp(\lambda_2 t)\Big]C_{1p}(0) \quad (5.2b)$$

where

$$\lambda_{1,2} = -\frac{1}{2}(k_1+k_2+k_3+k_5) \pm \frac{1}{2}\sqrt{(k_1+k_2+k_3+k_5)^2-4k_2(k_3+k_5)}. \quad (5.3)$$

Compartments $C_{2p}(t)$ and $C_{2e}(t)$ can similarly be solved as a two compartment four-rate constant reversible system, but with $k_3C_{1p}(t)$ as the input to compartment $C_{2p}(t)$, and the initial conditions $C_{2p}(0) = C_{2e}(0) = 0$:

$$C_{2p}(t) = \left(\frac{1}{\lambda_3-\lambda_4}\right)\Big[(\lambda_3+k_2')\exp(\lambda_3 t)-(\lambda_4+k_2')\exp(\lambda_4 t)\Big] \otimes k_3C_{1p}(t) \quad (5.4a)$$

$$C_{2e}(t) = \left(\frac{V_p}{V_e}\right)\left(\frac{k_1'}{\lambda_3-\lambda_4}\right)\Big[\exp(\lambda_3 t)-\exp(\lambda_4 t)\Big] \otimes k_3C_{1p}(t) \quad (5.4b)$$

where

$$\lambda_{3,4} = -\frac{1}{2}\left(k_6 + k_1' + k_2'\right) \pm \frac{1}{2}\sqrt{\left(k_6 + k_1' + k_2'\right)^2 - 4k_6k_2'}. \tag{5.5}$$

The full model will be referred to as the *four-compartment seven-parameter* (k_1, k_2, k_3, k_5, k_6, k_1' and k_2') *blood model.*

5.3.2 Simplified Models

The goodness-of-fit of the full blood model will be compared statistically to that of simpler models which are derived under the following assumptions:

1. (a) In the case when at equilibrium, the concentration of the parent radiotracer in plasma is the same as in erythrocytes, i.e. $\frac{C_{1e}}{C_{1p}} = \frac{V_p}{V_e}\frac{k_1}{k_2} = 1$, the influx and efflux rate constants can be expressed as $k_1 = K/V_p$ and $k_2 = K/V_e$, where the *clearance* K is the volume exchanged per unit time between the two compartments.

   (b) If the parent radiotracer occupies the water fraction of the plasma and erythrocyte spaces, the equilibrium condition becomes $\frac{C_{1e}}{C_{1p}} = \frac{V_p}{V_e}\frac{k_1}{k_2} = 0.73/0.94 = 0.777$, assuming that 1 ml of plasma and 1 ml of erythrocytes contain 0.94 g and 0.73 g of water, respectively (Hagenfeldt and Arvidsson, 1980). The influx and efflux rate constants can then be expressed as $k_1 = K/(0.94 \times V_p)$ and $k_2 = K/(0.73 \times V_e)$.

   This model will be referred to as the *four-compartment six-parameter* (K, k_3, k_5, k_6, k_1' and k_2') *blood model.*

2. When, in addition, the exchange between plasma and erythrocytes is much faster for the metabolite than for the parent, the compartments $C_{2p}(t)$ and $C_{2e}(t)$ cannot be kinetically distinguished. Equations (5.2a) and (5.2b) remain unchanged, while equations (5.4a) and (5.4b) are replaced by

$$\begin{aligned} C_{2w}(t) &= V_pC_{2p}(t) + V_eC_{2e}(t) && \text{(5.6a)} \\ &= V_p \exp(-k_6t) \otimes k_3C_{1p}(t). && \text{(5.6b)} \end{aligned}$$

   This solution corresponds to the solution of a one-compartment two-rate constant model with the input $k_3C_{1p}(t)$. The partition of the main metabolite between plasma

and erythrocytes is inferred from equation (5.6a) and the equilibrium condition $\frac{C_{2e}}{C_{2p}} = \frac{k_1'}{k_2'}\frac{V_p}{V_e}$ to be

$$C_{2p}(t) = \frac{C_{2w}(t)}{V_p\left(1+\frac{k_1'}{k_2'}\right)} \tag{5.7a}$$

$$C_{2e}(t) = \frac{\frac{k_1'}{k_2'}C_{2w}(t)}{V_e\left(1+\frac{k_1'}{k_2'}\right)}. \tag{5.7b}$$

This model, which is illustrated in **Figure 5.1b**, will be referred to as the *three-compartment five-parameter* (K, k_3, k_5, k_6 and k_1'/k_2') *blood model.*

3. If the main metabolite is excluded from the erythrocytes, i.e. $k_1'/k_2' = 0$, the system reduces to the *three-compartment four-parameter* (K, k_3, k_5 and k_6) *blood model.*

4. If the radiolabelled compounds are extracted from the whole blood at the same rate, i.e. $k_6 = k_5$, the system further simplifies to the *three-compartment three-parameter* (K, k_3 and k_5) *blood model.*

Note that the *in vivo* blood models reduce to the *in vitro* blood models (see **Appendix D**) when $k_3 = k_5 = 0$. These models will be referred to as the *two-compartment one-* (K) and *two-parameter* (k_1 and k_2) *blood models.*

5.4 Materials and Methods

5.4.1 Data Collection

The blood data were collected on thirty human subjects who underwent a two-hour PET study following an intravenous bolus injection of 185 MBq of F*m*T . F*m*T was prepared according to the protocol used routinely at our institution (Chirakal *et al*, 1991). Two groups of subjects were studied: the *prediction group* comprised ten subjects (nine males and one female, mean age 43 ±12 years) in whom more than ten venous blood samples were taken at increasing intervals throughout the PET study (typically at 0, 2, 3, 4, 5, 10, 15, 20, 30, 40, 50, 60, 75, 90, 105 and 120 min relative to the time of injection). Note

that the blood samples taken in the first two minutes post-injection were rejected because the radiotracer had not yet reached uniform mixing. In the remaining twenty subjects who formed the *validation group* (ten males and ten females, mean age 49 ± 15 years), only three blood samples were taken (at 5, 30 and 90 min post-injection).

At each time point, 5 ml volume of blood was manually drawn over 10 s from a 20-gauge intravenous catheter inserted into the antecubital vein. This sample was divided into 2 ml and 3 ml aliquots in heparinized glass tubes that were stored immediately in an ice bath. Haematocrit was measured using a micro-haematocrit technique with a Readacrit centrifuge (Clay Adams, Parsippany, NJ, USA) operated for 5 min and a micro-capillary reader (International Equipment Company, Needham Heights, MA, USA). The haematocrit values were not corrected for plasma trapped in packed erythrocytes. The erythrocytes in the 2 ml aliquot were lysed by the addition of 20 mg of Saponin (Sigma Chemicals, St-Louis, MO, USA). A 1 ml volume of haemolysed blood was extracted for the measurement of the radioactivity concentration using a NaI(Tl) gamma counter (Cobra II, Packard Bioscience, Meriden, CT, USA). The 3 ml aliquot was spun at 3000 rpm for 10 min using a Centra-7R centrifuge (International Equipment Company, Needham Heights, MA, USA) cooled down to 4°C. A 1 ml volume of plasma was pipetted and transferred to a plastic tube that was later counted with the same radiation detector. The radioactivity concentration was corrected for background, dead time, detection efficiency and physical decay to the time of injection. The radioactivity in the erythrocytes was calculated from the haematocrit H, the radioactivity concentration in plasma $C_p(t)$ and that in whole blood $C_w(t)$ using

$$C_w(t) = HC_e(t) + (1-H)C_p(t) \tag{5.8a}$$

$$\Rightarrow C_e(t) = \frac{1}{H}C_w(t) - \frac{1-H}{H}C_p(t). \tag{5.8b}$$

The partition of radioactivity between plasma and erythrocytes was calculated at each sampling time as the ratio $C_e(t)/C_p(t)$.

Three to six additional blood samples were drawn (at 5, 10, 20, 30, 60 and 90 min post-injection), centrifuged as previously described, and the plasma was assayed for F*m*T and its metabolites using the cation/anion exchange columns method (Nahmias *et al*, 1995). The fraction of F*m*T in plasma was calculated at each sampling time as the ratio of the radioactivity concentration in the supernatant over the sum of the radioactivity concentration in the supernatant with that in the three columns.

5.4.2 Data Analyses

5.4.2.1 Selection of the best model

For each subject in the prediction group, the measured partition of radioactivity between plasma and erythrocytes and contribution of FmT to the total radioactivity in plasma were fitted simultaneously to equations (5.9) and (5.10), respectively, using non-linear least squares.

$$R_{eop}(t) = \frac{C_{1e}(t) + C_{2e}(t)}{C_{1p}(t) + C_{2p}(t)} \tag{5.9}$$

$$R_{fmt}(t) = \frac{C_{1p}(t)}{C_{1p}(t) + C_{2p}(t)}. \tag{5.10}$$

Models of increasing complexity were successively compared using an F-test in order to select the one that best describes, in a statistical sense, the blood data. The erythrocytes to plasma ratio ($R_{eop}(t)$) and the FmT fraction in plasma ($R_{fmt}(t)$) were calculated at each sampling time using $C_{1p}(t)$, $C_{1e}(t)$, $C_{2p}(t)$ and $C_{2e}(t)$ as predicted by the three- to seven-parameter models. The cost function was defined as the sum of the reduced χ^2 calculated separately for the $R_{eop}(t)$ and $R_{fmt}(t)$ curves. This assumed equal variance on the different time points, and ensured that each dataset bore equal weight in the minimization procedure despite their differing size. Note that the values of the two ratios were in the same range [0-1].

5.4.2.2 Response of the best model to a pharmacological challenge

The sensitivity of the best model to pharmacologically induced changes in the peripheral metabolism of FmT was assessed by analysing blood data previously collected from a 47 year-old male pretreated with 150 mg of carbidopa, an inhibitor of the enzyme AADC, 60 min prior to the injection 110 MBq of FmT (the normal subject in **Chapter 3**). In order to ensure that the differences were not attributable to the different method used for the metabolites analysis, the results were compared with those of a 60 year-old female who had been studied using the same protocol, but who had not received carbidopa (the Parkinsonian subject in **Chapter 3**). The parameters obtained for these two subjects were compared to the mean estimate of the parameters for the prediction group using a z-score.

5.4.2.3 Comparison with *ad hoc* functional forms

The *ad hoc* functions that were used in chapter 3 to interpolate between and extrapolate from the blood data were compared to the best blood model. In particular, the robustness to noise of both approaches with a reduced number of data points was tested by fitting a subset of three blood samples and comparing the fitted curves to those obtained by fitting the whole dataset (n=15).

The correction for the partitioning of radioactivity between plasma and erythrocytes (Asselin *et al*, 2001) was previously obtained by fitting the plasma to whole blood ratio to an exponential decrease followed by a linear increase,

$$R_{pow}(t) = \left(\frac{1}{1-H} - p_1\right)\exp\left(-p_2 t\right) + p_3 t + p_1 \tag{5.11}$$

where H is again the measured haematocrit. The time constant which describes the influx of radioactivity from plasma to erythrocytes is defined by the parameter p_2. The slope of the straight line is given by parameter p_3 which, if positive, allows for the efflux of radioactivity from erythrocytes back to plasma. This three-parameter function can fit at minimum three data points.

The correction for the peripheral metabolism of FmT (Wahl *et al*, 1999a) was derived by fitting the parent fraction in plasma to the sum of two exponentials normalized to unity at the time of injection (t=0).

$$R_{fmt}(t) = (1-p_1')\exp\left(-p_2' t\right) + p_1'\exp\left(-p_3' t\right) \tag{5.12}$$

Likewise, a minimum of three data points is required to fit by this three-parameter (p_1', p_2' and p_3') function.

The subset contained only the measurements made at 5, 30 and 90 min which follow the main changes in the blood kinetics of FmT . Subject 8 for whom the 90 min sample appears to be an outlier was selected in order to challenge the robustness of the two approaches.

5.4.2.4 Derivation of population-based curves

The quantity of interest for kinetic modelling of the PET tissue response is the concentration of unmetabolised FmT in plasma whereas the quantity that is typically measured is the total radioactivity concentration in whole blood. However, the concentration of

FmT in plasma can be obtained by sequentially multiplying the radioactivity concentration in whole blood with the plasma to whole blood ratio and the FmT fraction in plasma as given by equation (5.13),

$$C_{1p}(t) = C_w(t) \times R_{pow}(t) \times R_{fmt}(t) \tag{5.13}$$

where the plasma to whole blood ratio $R_{pow}(t)$ can be inferred from the erythrocytes to plasma ratio $R_{eop}(t)$ using

$$\begin{aligned} R_{pow}(t) &= \left[(1-H) + HR_{eop}(t)\right]^{-1} && \text{(5.14a)} \\ &= \frac{C_{1p}(t) + C_{2p}(t)}{V_e\left[C_{1e}(t) + C_{2e}(t)\right] + V_p\left[C_{1p}(t) + C_{2p}(t)\right]}. && \text{(5.14b)} \end{aligned}$$

The product of $R_{pow}(t)$ and $R_{fmt}(t)$ will be referred to as the *blood correction factor* (BCF).

The small variability in the time course of the plasma to whole blood ratio as well as in the FmT fraction in plasma suggests that population-based curves could approximate individual values, thereby eliminating the need for collecting and processing discrete blood samples. Population-based curves were thus derived by averaging the fitted values for the ratios $R_{eop}(t)$ and $R_{fmt}(t)$ evaluated at the sampling times (fifteen for R_{eop} and six for R_{fmt}) over the ten subjects in the prediction group. These two datasets were then fitted as previously described (see section 5.4.2.1) to the best model but this time each squared difference was weighted by the inverse of the variance on the mean value. Note that the data points were obtained using the individual haematocrit values whereas the fitted curves were derived using the mean haematocrit value for the prediction group ($H = 0.42 \pm 0.04$). The population-based curve for the time course of the BCF was finally generated by multipling point by point the curves fitted to the ratios $R_{pow}(t)$ and $R_{fmt}(t)$. In order to assess the generality of the population-based BCF curve, the mean BCF estimates (from the fitted curves) of the prediction group were compared to the mean BCF estimates (from measurements) of the validation group using a two-tailed two-mean t-test.

5.4.2.5 Gender differences in blood kinetics

Given that, in general, the haematocrit is lower for females than for males, the data from the prediction and validation groups were pooled together in order to investigate gender differences in the blood kinetics of FmT . The blood correction factors at 0, 5, 30 and

90 min were averaged amongst males and females and the genders were compared to each other using a one-tailed two-mean t-test under the assumption that the lower proportion of erythrocytes in females than in males results in a lower concentration of FmT in whole blood. Whether this difference is simply the consequence of a larger plasma volume or is exacerbated by an increase in peripheral metabolism due to increased availability of FmT was further tested by comparing the average of the parameters given by the best blood model for males and females using a two-tailed two-mean t-test.

5.4.2.6 Error sensitivity analysis

A simulation was performed in order to investigate the propagation of errors to the parameters of clinical interest that occurs when individual BCF values are replaced with the population-based BCF curve. One hundred input functions were generated by multiplying a typical curve for the time course of total radioactivity in whole blood (blood curve) after the injection of FmT (the normal subject in **Chapter 3**) with one hundred different BCF curves. The individual BCF curves were obtained by

1. adding to the mean values of the population ratios $R_{eop}(t)$ and $R_{fmt}(t)$ their respective standard deviation weighted by a number randomly selected from the Normal distribution $\mathrm{N}(\mu = 0, \sigma = 1)$;

2. repeating this operation for each sampling time (again fifteen for R_{eop} and six for R_{fmt});

3. fitting the resulting curves to equations (5.9) and (5.10) as described in section 5.4.2.1;

4. and multiplying point by point the two fitted curves.

Tissue curves were then generated using these input functions and typical values of the rate constants (see **Tables 3.2a)** and **b)**) for the cerebellum, left and right putamina of a normal individual (*subject 1*) and a subject suffering from Parkinson's disease (*subject 2*). Each tissue curve was fitted to the appropriate compartmental model using the input function derived from the same blood curve corrected with the population-based BCF curve. The mean and standard deviation of the one hundred evaluations of the rate constants were computed and compared with the values used to generate the tissue curves in order to estimate the bias and variability introduced by the population-based BCF curve.

Table 5.1: *Statistical determination of the best compartmental model.*

Model 1	Model 2	F($P_2 - P_1$,$N - P_2$)[a]	p-value
K fixed[b]	K variable	F(10,159)=40.6533	<0.001[c]
K variable	k_1, k_2	F(10,149)=9.7998	<0.001[c]
k_1, k_2	K, k_3, k_5	F(10,139)=2.5685	<0.01[c]
k_1, k_2	K, k_3, k_5, k_6	F(20,129)=1.6620	<0.05[d]
K, k_3, k_5	K, k_3, k_5, k_6^e	F(10,186)=2.9338	<0.01[d]
K, k_3, k_5, k_6^e	$K, k_3, k_5, k_6, k_1'/k_2'$	F(10,176)= 2.3652	<0.01[c]
$K, k_3, k_5, k_6, k_1'/k_2'$	$K, k_3, k_5, k_6, k_1', k_2'$	F(10,166)=-1.3957[d]	
$K, k_3, k_5, k_6, k_1', k_2'$	$k_1, k_2, k_3, k_5, k_6, k_1', k_2'$	F(10,156)=-0.0001[d]	

[a] P_1: number of parameters in the simpler model; P_2: number of parameters in the more complex model; and N: total number of points.

[b] $K = 0.017$ min^{-1} as determined *in vitro* (Nahmias *et al*, 2000).

[c] Comparison made on the R_{eop} ratio only.

[d] Comparison made on both R_{eop} and R_{fmt} ratios.

[e] The parent radiotracer is set to occupy the water fraction of the plasma and erythrocyte spaces.

5.5 Results

5.5.1 Unified Blood Model for FmT

The results of the statistical comparison between the different models (see **Figure 5.1** and section 5.3.2) are presented in **Table 5.1**. Note that the fits were performed on the data for each subject individually, but that the F-statistic was computed for the fit of the model to the dataset as a whole. As indicated by the F-tests, the three-compartment four-parameter model provides a significantly better fit ($p<0.05$) to the dataset for the partition of radioactivity between plasma and erythrocytes than the *in vitro* models of **Appendix D**. When the dataset for the FmT fraction in plasma is also considered, significantly better fits ($p<0.01$) were obtained using the three-compartment four-parameter model compared to the three-compartment three-parameter model. Negative rate constants were no longer obtained with the three-compartment four-parameter model when setting the parent radio-

tracer to occupy the water fraction of the plasma and eythrocyte spaces rather than the whole physical space. This finding is in agreement with the *in vitro* experiments (Nahmias *et al*, 2000). Even though fitting for the partition coefficient of the main metabolite (k_1'/k_2') using the three-compartment five-parameter model resulted in a significantly better fit to the dataset ($p<0.01$) than fixing it to zero using the three-compartment four-parameter model, the best fit values of the ratio were negative, and hence were rejected. Furthermore, when adding more parameters, i.e. solving for individual values of the parameters k_1', k_2' and/or k_1, k_2, the fitted curves started to follow the noise in the blood data, indicating that the four-compartment models were overparameterized.

The best fit parameters to the three-compartment four parameter model for each of the ten subjects in the prediction group are gathered in **Table 5.2**. None of the parameters are equal to zero within the standard error on the estimates, indicating that the three-compartment four-parameter model is not overdetermined. Using a two-tailed two-parameter *t*-test, the rate constant k_6 was found to be significantly different ($p<0.05$) from the rate constant k_5 in four out of ten subjects, invalidating in these cases the assumption made by the simpler three-compartment three-parameter model.

Typical examples of the fitted curves are displayed in **Figures 5.2a**, **b**, and **c**. A first measurement of the erythrocytes to plasma ratio close to zero indicates that the parent compound stays in the plasma where it was initially injected. A rise in this ratio reveals that it is eventually taken up by the erythrocytes. At an equilibration ratio of one, the parent compound would be equally distributed between erythrocytes and plasma. As metabolites appear in the blood, this ratio should remain close to one if the metabolites also enter the erythrocytes, or decrease if they are excluded from them. The exchange of radiolabelled compounds between plasma and erythrocytes that occurs *in vivo* appears to be faster than that of F*m*T as measured *in vitro* (Nahmias *et al*, 2000). In contrast with the *in vitro* experiments, this exchange does not reach equilibrium within a two-hour study (**Figure 5.2a**). Instead, the erythrocytes to plasma ratio is observed to decrease which can be explained by accounting for the metabolism of F*m*T as well as for the clearance of F*m*T and its metabolites from plasma (**Figure 5.2b**).

Comparing **Table 5.3** and **Table 5.2**, all four parameters for the subject without carbidopa fell within one standard deviation of the mean estimates of the prediction group. This confirms the applicability of the blood model to data generated using different experimental methods at a different laboratory. In contrast, pre-treatment with the

Table 5.2: *Best fit parameters*[a] *to the three-compartment four-parameter blood model.*

Subject	K (ml/min)	k_3 (1/min)	k_5 (1/min)	k_6 (1/min)
1	0.059 ±0.012	0.030 ±0.013	0.109 ±0.029	0.107 ±0.033
2	0.0614 ±0.0051	0.0301 ±0.0052	0.151 ±0.014	0.110 ±0.012[d]
3	0.085 ±0.017	0.031 ±0.015	0.304 ±0.060	0.152 ±0.038[d]
4	0.0420 ±0.0083	0.0346 ±0.0086	0.043 ±0.016	0.071 ±0.015
5	0.0337 ±0.0032	0.0367 ±0.0067	0.0491 ±0.0089	0.084 ±0.012
6	0.0229 ±0.0038	0.0232 ±0.0052	0.031 ±0.010	0.0440 ±0.0094
7	0.0746 ±0.0067	0.0337 ±0.0051	0.131 ±0.015	0.107 ±0.012
8	0.0484 ±0.0036	0.0403 ±0.0051	0.0453 ±0.0083	0.0905 ±0.0092[d]
9	0.0653 ±0.0056	0.0366 ±0.0051	0.178 ±0.016	0.125 ±0.012[d]
10	0.0558 ±0.0070	0.0255 ±0.0068	0.065 ±0.013	0.086 ±0.018
Mean ± SD[b]	0.055 ±0.019	0.0322 ±0.0053	0.111 ±0.085	0.098 ±0.030
Best ± SE[c]	0.0553 ±0.0005	0.0323 ±0.0003	0.1022 ±0.0013	0.0988 ±0.0008

[a] Best estimate ± standard error (SE).

[b] Mean value ± standard deviation (SD).

[c] Fitting results to the average over the ten subjects of the fitted values for the ratios R_{eop} and R_{fmt} evaluated at the sampling times.

[d] The estimate of k_6 is significantly different ($p<0.05$) from that of k_5 using a two-tailed two-parameter t-test.

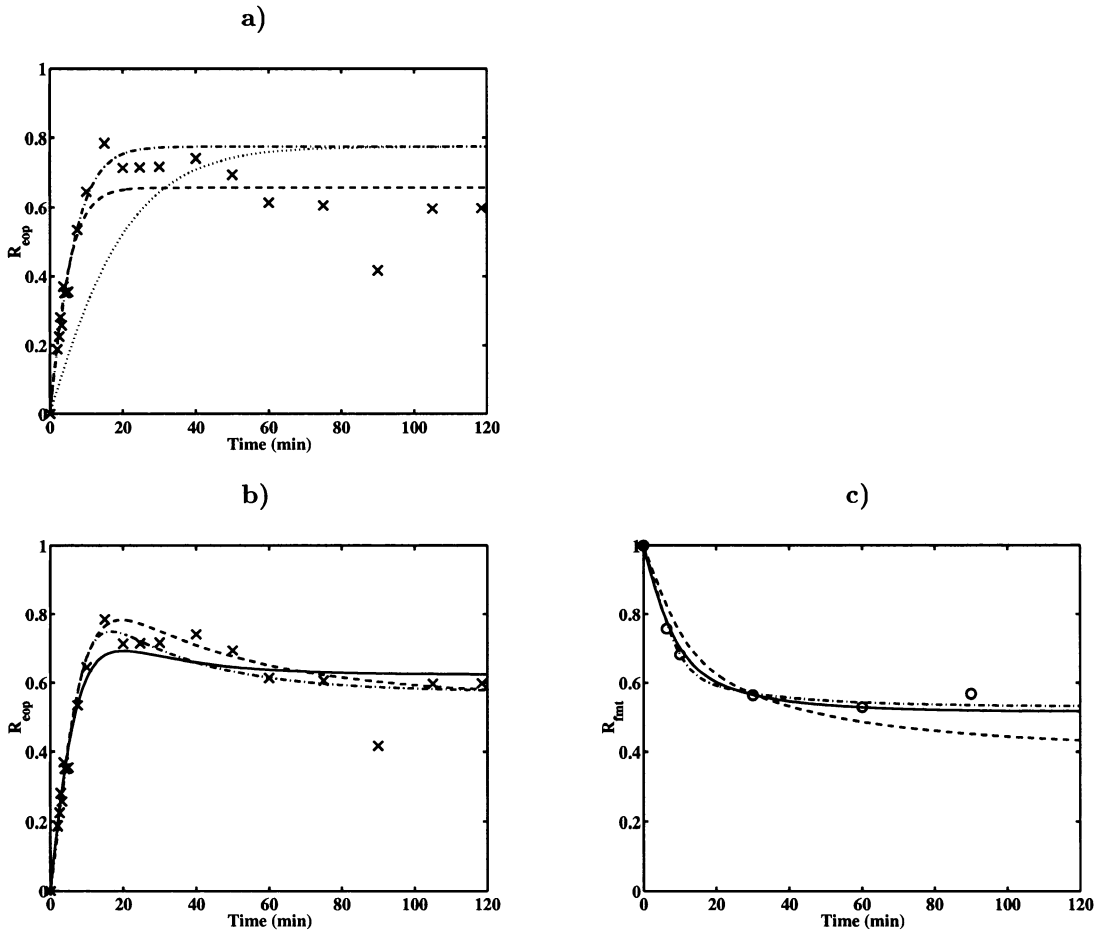

Figure 5.2: **a**) *Inability of the in vitro models to fit the erythrocytes to plasma ratio (R_{eop}) illustrated with data from subject 8: Two-compartment one-parameter model (· · · · · ·) with the clearance fixed to the value determined in vitro (K = 0.017 ml/min (Nahmias et al, 2000)); two-compartment one-(— · —) and two-(- - - -) parameter models with the rate constants inferred from the in vivo data. Recall that the two-compartment one-parameter model forces the R_{eop} ratio to reach the value 0.777 at equilibrium. Comparison between the fitted curves for* **b**) *R_{eop} and* **c**) *the FmT fraction in plasma (R_{fmt}) given by the three-compartment three- (- - - -), four- (——) and five- (— · —) parameter models computed from the same data.*

Table 5.3: *Effect of pretreatment with carbidopa (a peripheral AADC inhibitor) on the parameters[a] of the three-compartment four-parameter blood model.*

Treatment	K (ml/min)	k_3 (1/min)	k_5 (1/min)	k_6 (1/min)
None (n=1)	0.0375 ±0.0055	0.0360 ±0.0082	0.081 ±0.015	0.088 ±0.016
Carbi[b](n=1)	0.0552 ±0.0053	0.0136 ±0.0045	0.0764 ±0.0077	0.088 ±0.021

[a] Best estimate ± standard error.

[b] 150 mg of carbidopa administered orally 60 min prior to the injection of FmT .

Table 5.4: *Comparison of the bias[a] introduced in the blood correction factor (BCF) by applying the ad hoc functions or the blood model to measurements from only three blood samples (subject 8).*

Fit	t = 5 min	t = 30 min	t = 90 min	t = 120 min
Blood model[b]	+0.37%	-1.0%	+3.7%	+4.0%
Ad hoc functions[c]	+2.5%	+2.5%	+11%	+16%

[a] bias = $\frac{\text{subset}-\text{all}}{\text{all}} \times 100$, for each fitting approach.

[b] Subset made of R_{eop} at 5 and 30min, and R_{fmt} at 5, 30 and 90min.

[c] Subset made of R_{pow} and R_{fmt}, each at 5, 30 and 90min.

AADC inhibitor substantially decreased the rate constant k_3 (which is more than three standard deviations below the mean estimate of the prediction group) without affecting the other three parameters (which are less than one standard deviation away from the mean estimates of the prediction group).

The use of the *ad hoc* functions for FmT requires at least three blood samples from which three measurements of the plasma to whole blood ratio and three more of the parent fraction in plasma must be made. **Figure 5.3** and **Table 5.4** demonstrate that when one of these six measurements (in this example the 90 min R_{pow}, and to a lesser extent the 90 min R_{fmt}) is inaccurate, the extrapolated values for the BCF given by the *ad hoc* functions can be seriously biased (up to 16% at the end of the study in this case).

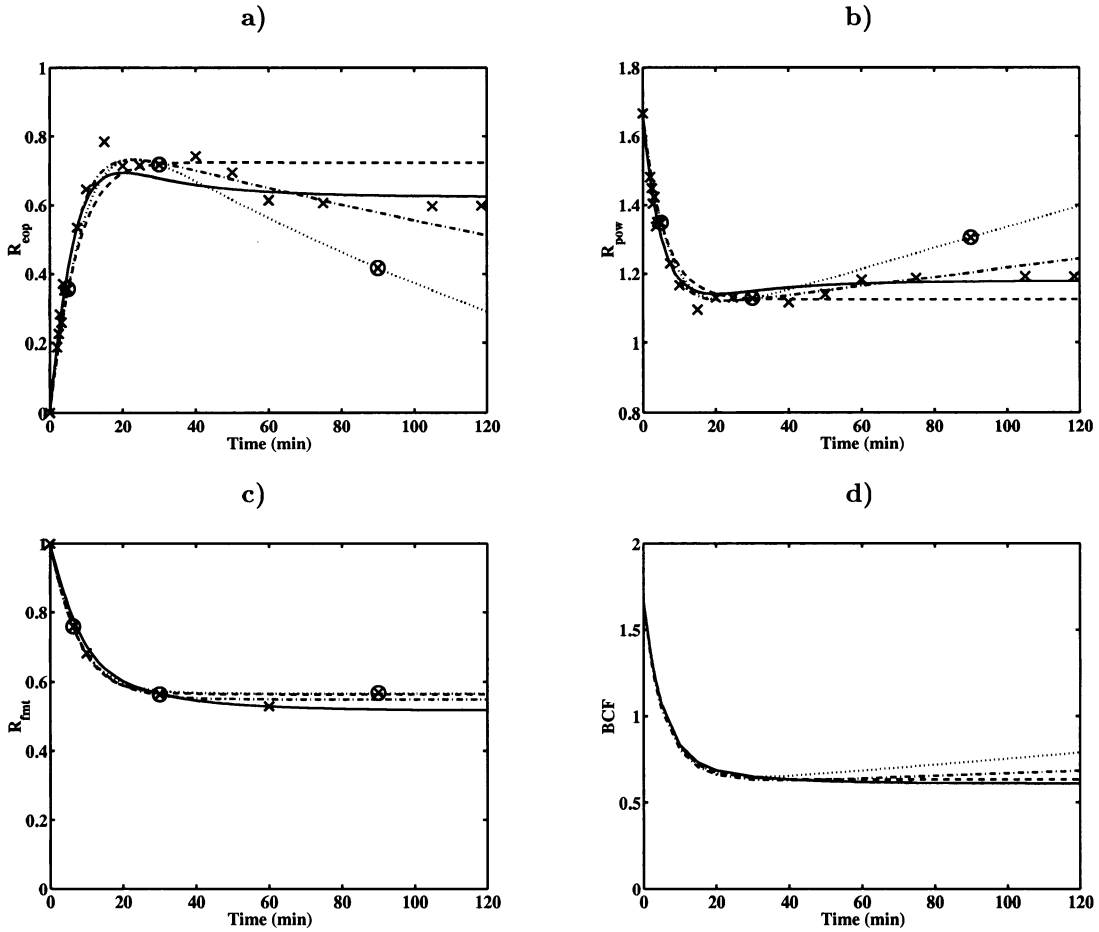

Figure 5.3: *Robustness of the blood model to outliers illustrated with data from subject 8 (for whom the 90 min measurements appear to be outliers): All (×) or a small subset (○) of data were fitted to the three-compartment four-parameter blood model (——: all, - - - -: subset) and to ad hoc functions (— · —: all, ·····: subset). The time course of* **c**) *FmT fraction in plasma (R_{fmt}) is used by the blood model to infer the behavior of the* **a**) *erythrocytes to plasma ratio (R_{eop}). The error in the measurement of the time course of* **b**) *plasma to whole blood ratio (R_{pow}) propagates to the* **d**) *blood correction factor (BCF).*

Table 5.5: *Comparison[a] between the blood correction factors[b] (BCF) of the validation group (measured values) and those of the prediction group (fitted values) at four sampling times.*

Group	t = 0 min	t = 5 min	t = 30 min	t = 90 min
Prediction (n=10)	1.72	1.05	0.622	0.567
	±0.11 (6.6)	±0.11 (11)	±0.053 (8.5)	±0.058 (10)
Validation (n=20)	1.703	1.10	0.623[c]	0.602[c]
	±0.088 (5.2)	±0.14 (12)	±0.084 (14)	±0.069 (11)

[a] No significant difference (p>0.20) was found between the two groups at any of the sampling times.

[b] Mean ±standard deviation (coefficient of variation in %).

[c] n=19

In contrast, the applicability of the three-compartment four-parameter blood model is not compromised by rejecting the faulty measurement and the bias introduced by fitting the reduced subset of data is much smaller (less than 5%). This property of the blood model should not be misused to reduce the number of blood samples or to lower the quality of the measurements in situations where sufficient and proper blood data can be acquired.

5.5.2 Population-Based Curves for FmT

Figure 5.4 visually compares the $R_{pow}(t)$ and $R_{fmt}(t)$ ratios as well as the BCFs derived from the validation group to those of the prediction group. The BCFs of two groups were not significantly different (p>0.20) at any of the four sampling times given in **Table 5.5**.

The data in **Table 5.6** and **Figure 5.5** reveal that the significantly lower BCF values (p<0.05) of females compared to males observed at various times throughout the study (**Table 5.6a**) are in large part attributable to their significantly lower haematocrit value (p<0.01). The between-subject variations in the parameters of the blood model were found to be larger than the gender differences (**Table 5.6b**). Furthermore, recomputing the population-based curves (see **Table 5.2**) with the different haematocrit values for males and females presented in **Table 5.6b** gave lower BCF values for females than for males

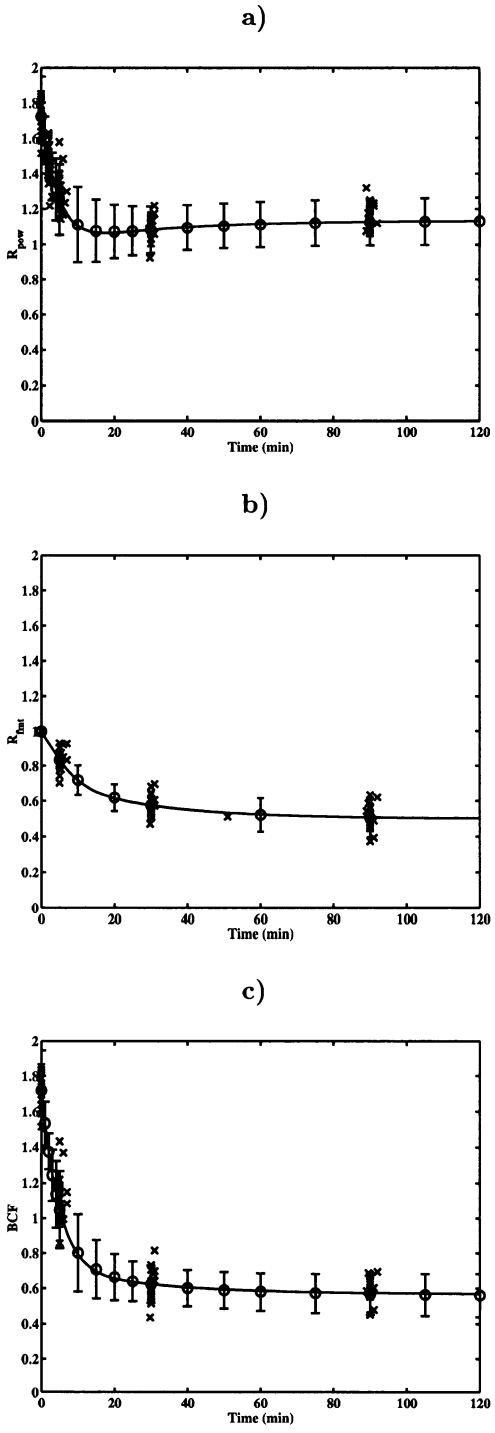

Figure 5.4: *Comparison between the population-based curves for* **a**) *plasma to whole blood ratio (R_{pow}),* **b**) *FmT fraction in plasma (R_{fmt}) and* **c**) *the resulting blood correction factor (BCF) derived from the prediction group (n=10) and the measured values for individual subjects (×) from the validation group (n=20). The solid lines correspond to the fit of the three-compartment four-parameter blood model computed on the mean values (∘) of the prediction group, and the errorbars indicate the ±95% confidence intervals on these values.*

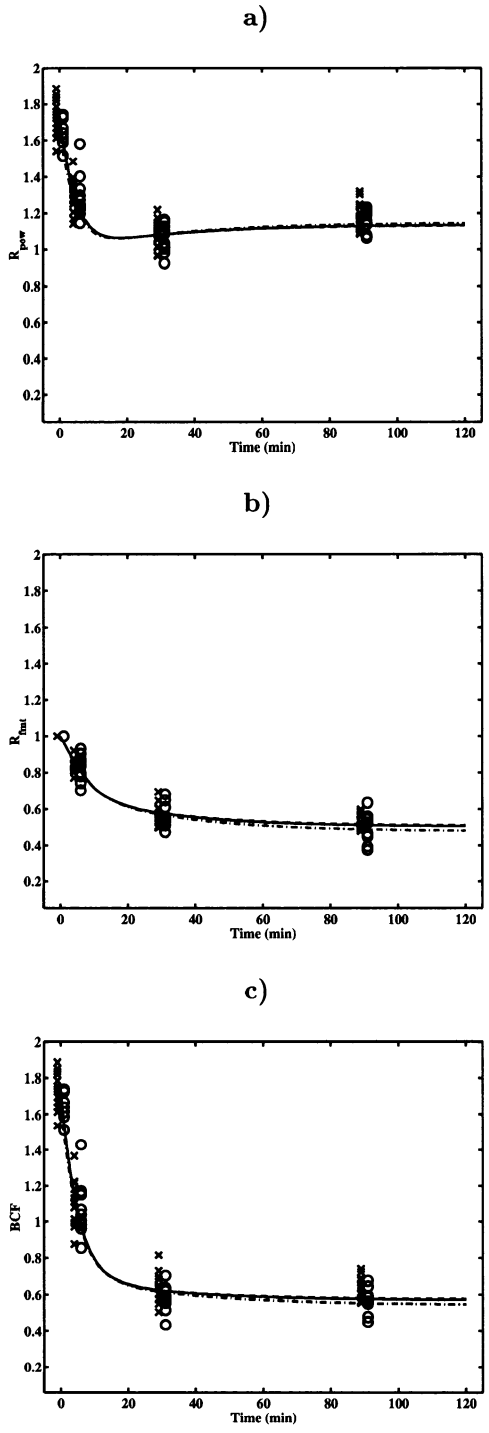

Figure 5.5: *Comparison between the population-based curves for* **a**) *plasma to whole blood ratio (R_{pow}),* **b**) *FmT fraction in plasma (R_{fmt}) and* **c**) *the resulting blood correction factor (BCF) for males (n=19, ×) and females (n=11, ○) pooled together from the validation and prediction groups. The curves derived from the prediction group (H=0.42±0.04, ——) are recomputed using the haematocrit of the group of males (H=0.43±0.03, - - - -) and that of the group of females (H=0.40±0.03, — · —).*

Table 5.6: *Gender differences between* **a)** *the blood correction factors (BCF) and* **b)** *the parameters of the three-compartment four-parameter blood model*[a].

a)

Group[b]	t = 0 min	t = 5 min	t = 30 min	t = 90 min
All	1.709	1.09	0.618	0.608
	±0.096 (30)	±0.13 (25)	±0.078 (25)	±0.068 (26)
Males	1.742	1.11	0.641	0.632
	±0.095 (19)	±0.12 (14)	±0.077 (14)	±0.058 (16)
Females	1.653	1.08	0.588	0.569
	±0.071 (11)	±0.15 (11)	±0.071 (11)	±0.068 (10)
t-test[c]	2.9133 (25)	0.5411 (18)	1.7848 (22)	2.4291 (16)
p-value	<0.005	>0.25	<0.05	<0.02

b)

Group[d]	K (ml/min)	k_3 (1/min)	k_5 (1/min)	k_6 (1/min)	Haematocrit
All	0.052	0.0323	0.093	0.093	0.414
(n=30)	±0.016 (31)	±0.0088 (27)	±0.062 (67)	±0.027 (29)	±0.034 (8.2)
Males	0.052	0.0308	0.089	0.089	0.425
(n=19)	±0.017 (33)	±0.0069 (22)	±0.071 (80)	±0.030 (34)	±0.032 (7.5)
Females	0.052	0.035	0.100	0.101	0.395
(n=11)	±0.015 (29)	±0.011 (31)	±0.045 (45)	±0.021 (21)	±0.027 (6.8)
t-test	0.000 (23)[e]	1.1429 (14)[e]	0.5189 (27)[e]	1.2832 (26)[e]	2.7367 (24)[c]
p-value	>0.50	>0.25	>0.50	>0.20	<0.01

[a] Prediction and validation groups merged together (n=30).

[b] Mean ± standard deviation (number of subjects).

[c] One-tailed two-mean *t*-test (degrees of freedom).

[d] Mean ± standard deviation (coefficient of variation in %).

[e] Two-tailed two-mean *t*-test (degrees of freedom).

(**Figure 5.5**). Separating males and females into different groups does not systematically increase the between-subject variations in the BCF values within each group compared to the total group, suggesting that it might be advantageous to derive population-based curves independently for males and females.

The results of the simulation study are summarized in **Table 5.7**. The 5-15% between-subject variability in the BCFs observed throughout the two-hour sampling period following injection of F*m*T (see **Table 5.5**) translated into a 0-5% variability in the transport parameters K_1 and k_2, and a 0-10% variability in k_3, the rate constant reflecting the enzymatic activity of AADC. However, the variability in k_3 was found to increase with decreasing values of the rate constant. The bias on all parameters tended to be negative and smaller than the corresponding variability. The macroparameter K_i was less affected by replacing the individual values by the population-based BCF curve than the individual microparameters (bias and variability ~1-2%).

5.6 Discussion

A compartmental model that allows data for the plasma parent fraction to be combined with data for the partitioning of total radioactivity between plasma and erythrocytes was presented. This model was used to relate the plasma input function to the time course of radioactivity concentration in whole blood. The blood correction factors (BCF) describing this relation did not vary substantially from subject to subject, thereby allowing the derivation of a population-based BCF curve. The bias and the variability introduced by using this curve instead of the individual values for the BCFs did not impede the accurate and precise estimation of the rate constants describing simulated tissue time-activity curves.

Separate *ad hoc* functional forms have previously been used to interpolate between and extrapolate from the few available measurements of the partition of radioactivity between plasma and erythrocytes and of the contribution of F*m*T to the total radioactivity in plasma (Wahl *et al*, 1999b; Asselin *et al*, 2001). The primary purpose for developing the proposed blood model was to provide reasonable fits to these data. To that end, the *in vivo* models significantly improved these fits over those provided by the *in vitro* models. The blood model has also proven to be more robust than separate *ad hoc* functions in the situation where only very limited data, some even noisy, are available. The blood model however performs best with complete, high quality blood data which should be acquired

Table 5.7: *Bias and variability introduced by using a population-based curve for the blood correction factor (BCF) instead of the curve that generated the simulated tissue curves:* **a**) *subject 1 (normal individual) and* **b**) *subject 2 (Parkinsonian affected on the right side).*

Tissue	K_1[a] (ml/min/ml)	k_2[a] (1/min)	k_3[a] (1/min)	k_4[a] (1/min)	K_i[b] (ml/min/ml)
			a)		
Cerebellum	**0.0526**[c]	**0.0638**	**0.0023**		**0.0015**
	0.0510[-3.1][d]	0.0629[-1.4]	0.0024[+3.1]	n/a	0.0016[+1.8]
	±0.0015(2.9)	±0.0008(1.2)	±0.0002(6.6)		±0.0001(3.8)
Left	**0.0556**[c]	**0.0674**	**0.0890**	**0.0045**	**0.0226**
putamen	0.0536[-3.7][d]	0.0661[-2.0]	0.0886[-0.43]	0.0044[-2.6]	0.0224[-1.0]
	±0.0020(3.7)	±0.0029(4.4)	±0.0038(4.3)	±0.0002(4.6)	±0.0003(1.2)
Right	**0.0563**[c]	**0.0683**	**0.0888**	**0.0043**	**0.0232**
putamen	0.0542[-3.7][d]	0.0669[-2.0]	0.0884[-0.45]	0.0042[-2.6]	0.0230[-1.0]
	±0.0020(3.7)	±0.0030(4.4)	±0.0037(4.2)	±0.0002(4.7)	±0.0003(1.2)
			b)		
Cerebellum	**0.0542**[c]	**0.0681**	**0.0014**		**0.0008**
	0.0525[-3.2][d]	0.0671[-1.4]	0.0015[+4.9]	n/a	0.0008[+4.5]
	±0.0015(2.9)	±0.0008(1.2)	±0.0001(9.9)		±0.0001(7.7)
Left	**0.0612**[c]	**0.0769**	**0.0224**	**0.0034**	**0.0137**
putamen	0.0586[-4.2][d]	0.0749[-2.6]	0.0210[-6.3]	0.0029[-14]	0.0135[-0.90]
	±0.0027(4.7)	±0.0039(5.3)	±0.0021(9.9)	±0.0007(23)	±0.0001(1.1)
Right	**0.0578**[c]	**0.0726**	**0.0337**	**0.0026**	**0.0185**
putamen	0.0555[-4.0][d]	0.0709[-2.4]	0.0325[-3.7]	0.0024[-8.5]	0.0183[-1.1]
	±0.0024(4.4)	±0.0035(5.0)	±0.0020(6.2)	±0.0003(15)	±0.0002(1.2)

[a] K_1 and k_2 represent the forward and reverse transport rate constants of FmT from plasma to tissue, k_3 is the rate constant for the metabolism of FmT in tissue, and k_4 is the rate constant for the clearance of FmT metabolites out of tissue. The cerebral blood volume was included as an additional parameter. The K_1/k_2 ratio of the putamina was fixed to that of the cerebellum.

[b] Influx constant inferred from the slope of the Patlak plot using a plasma input function.

[c] Values used to generate the simulated tissue curves.

[d] Mean [difference between estimated and true values in %]

±standard deviation (coefficient of variation in %) over one hundred simulated tissue curves.

whenever possible. Even under the best conditions, the parameters which define the fitted curves must be interpreted with caution, because the blood model is only a simplified description of the system under study. In this regard, a few issues deserve to be clarified.

Firstly, F*m*T (and its main metabolite) are not metabolised in whole blood *per se* (Nahmias *et al*, 2000). The rate constant k_3 therefore aggregates a series of steps that, when combined together, result in the transformation of F*m*T into its main metabolite (F*m*T to F*m*TA and to FHPAA). The substantial decrease in the estimate of k_3 following the administration of the AADC inhibitor carbidopa supports this interpretation. A more complex model that would separate the processes involved in the transformation of F*m*T (transport to tissue, metabolism in tissue and transport back to plasma) is unlikely to be supported by the data as measured in the present study. Complicating the blood model with the addition of a compartment representing the concentration of F*m*T in tissue is difficult to justify given the lack of data on the time course of F*m*T in peripheral tissue and the failure of the four-compartment models to improve the fits given by the three-compartment model.

Secondly, the blood data could not be adequately fitted when the partition ratio for the main metabolite was set to the value measured *in vitro* ($k_1'/k_2' = 0.449$ (Nahmias *et al*, 2000)). The results suggest instead that the main metabolite is excluded from the erythrocytes ($k_1'/k_2' = 0$). This finding can be explained if FHPAA is in a conjugated form *in vivo*, unlike that measured *in vitro*. Furthermore, the *in vivo* value for the parameter K was found to be three times greater than the *in vitro* estimate. These discrepancies highlight inconsistencies that can be introduced if assumptions based on findings from *in vitro* experiments are applied to *in vivo* data without verification.

Thirdly, the between-subject variability in the parameter k_5 (COV$\sim$76%) is twice as large as that of the parameters K and k_6 (COV$\sim$25-35%), and five times larger than the parameter k_3 (COV$\sim$16%). Whether this reflects considerable variability among different subjects in the rate of transport of F*m*T from plasma to tissue or whether it is due to the interdependence of the parameters k_3 and k_5 in the model cannot be resolved with the current data. Reformulating the model to include the time course of radioactivity measured in whole blood, as can be done with the state space approach of Gunn *et al*(2001), could potentially resolve the issue. This more general approach could also accommodate injections that are not given as a sharp bolus.

A standard concern in compartmental modelling is structural identifiability —

whether the individual parameters could be uniquely determined given perfect data. Because of the separability of the parent and metabolite subsystems as described above, it is clear that all parameters could be uniquely determined if each compartment could be observed separately (Godfrey, 1983). Unfortunately, the measured data are the sum of the radioactivity in all compartments, the ratio of the total radioactivity in plasma to that in whole blood, and the ratio of the parent to metabolite in plasma. These ratios are non-linear combinations of the total radioactivity in each compartment and the resulting identifiability analysis is non-trivial (results not shown). The overall goal, however, is to determine the concentration of the parent radiotracer in plasma. It is immediately clear from the arguments presented in the introduction of section 5.3 that this concentration is uniquely identifiable from the measured ratios.

The approach of a unified compartmental model for blood data offers several advantages. Fitting the plasma to erythrocytes ratio simultaneously with the FmT fraction in plasma reduced the influence of outliers on the best model fitted curves. The robustness of the blood model with regard to noise results on the one hand from imposing consistency between the two datasets, and on the other hand from increasing the number of data points as well as decreasing the number of parameters needed to describe the whole dataset. The three-compartment four-parameter model correctly discarded the sudden decrease in the erythrocytes to plasma ratio as well as the apparent increase in the FmT fraction in plasma observed at later times. When one of the two measurements from the same blood sample was found to be inaccurate and rejected, the blood model could rely on the remaining measurement to infer the relevant information at that time point. Nevertheless, the fitted curves remained sensitive to changes in the peripheral metabolism of FmT induced by the administration of carbidopa. Indeed, the model correctly predicted both the parameter affected by the change and the direction of the change. Using the blood model, the effects of the haematocrit on the gender differences observed in the blood partition and the peripheral metabolism of FmT could be separated from those of the rate constants describing these processes. The model can also be used to derive population-based curves, thereby allowing one to bypass invasive blood sampling and elaborate blood analyses in future studies, and yet to have a plasma input function with which to perform kinetic analyses of PET data.

The population-based curves were shown to be representative not only of the group of ten subjects from which they were derived, but also of a second independent group of twenty subjects that were studied using the same protocol. As indicated by the

fitting results for the subject pretreated with carbidopa, the population-based curves are *not* applicable to subjects studied with a different protocol or to subjects whose peripheral metabolism is altered. The variability that is introduced by using a population-based instead of the individual curve for the BCFs is comparable to the standard error on the parameters estimated using real PET data (see **Table 3.2**). The small biases observed in k_3 and K_i, the rate constants reflecting the enzymatic activity of AADC, enlarged the difference between the Parkinsonian subject and the normal individual as well as that between the affected and unaffected sides of the Parkinsonian subject. These biases could potentially be reduced by the use of separate population-based curves for males and females derived from the same blood model parameters but with gender-specific haematocrit values.

Finally, the general applicability of the unified blood model relies on two principles:

1. There is a difference in the blood partition ratio of the parent radiotracer and its metabolites;

2. there is a difference in the rate at which they equilibrate between plasma and erythrocytes.

Only if either or both of these conditions are met, the partition of radioactivity between plasma and erythrocytes can be used to supplement the assay of the parent fraction in plasma. The simplifications applied to the full blood model are based on these principles, and their implementation is specific to each radiotracer. *In vitro* experiments conducted to study separately the equilibration of the radiotracer and its metabolites between plasma and eythrocytes can be valuable in deciding the way to carry out these simplifications. As always, care must be exercised to ensure that the selected model can be supported by the available blood data.

5.7 Conclusion

This chapter illustrates how data for the partition of total radioactivity between plasma and erythrocytes can be used to complement direct assays of the parent radiotracer in plasma. A three-compartment four-parameter model successfully fitted blood data from the pre-synaptic dopaminergic radiotracer FmT . This model enables a more robust extrapolation and interpolation of blood data which is particularly important when only a few

blood samples can be taken. The blood model also allowed the derivation of population-based curves which can be used to obtain estimates of the plasma input function simply from measurement of the total radioactivity in blood. The general blood model can be adapted for other radiotracers as long as the blood partition ratio of the parent radiotracer differs from that of its metabolites and/or the rate at which they equilibrate between plasma and erythrocytes is different.

Chapter 6

Patterns of Distribution of FmT in PET Images of Patients with Movement Disorders

6.1 Overview

[1] In this chapter, the methods developed in the previous chapters are applied to complete PET/FmT studies of 21 consecutive patients suspected of suffering from a variety of movement disorders. Graphical analyses were performed using the image-derived plasma (venous sinus) input function, as discussed in this thesis, and compared to results obtained using a reference tissue (cerebellum) input function. In addition, the potential of combining differences between caudate nucleus and putamen with left to right asymmetries in FmT uptake for the discrimination between different Parkinsonian syndromes was investigated. A decreased K_i in the putamen contralateral to the affected limbs supported the diagnosis of idiopathic Parkinson's disease (PD) in four patients. A lower K_i in the putamen bilaterally in two patients was considered to be indicative of a more advanced stage of PD, although other Parkinsonian syndromes can produce a similar pattern of striatal involvement. Since the remaining patients were found to have a uniform pattern of distribution similar to that seen in normals, the classification between normal and abnormal was based on a discriminant level set at upper limit of the 95% confidence interval around the mean putamen influx

[1] *This work was presented in part at the BrainPET'01 International Conference, Taipei (Taiwan), June 2001.*

constant of the probable PD group. Four of these fifteen patients had a putamen K_i that was below the discriminant level. The venous sinus input function classified 20 of the 21 patients studied in the same categories as the cerebellum input function. Using image-derived input functions, quantitative analyses of PET/F*m*T studies are feasible in a clinical setting and, in combination with striatal patterns of F*m*T uptake, the method provides useful diagnotic information in individual patients with movement disorders.

6.2 Introduction

Idiopathic Parkinson's disease (PD) is a debilitating neurodegenerative movement disorder with a *prevalence* (total number of cases with a disease at a given point in time) of 1% of the general population over 65 years of age (Frey, 2002) and an *incidence* (number of new cases with a disease during a given time interval) that increases with age. The typical presentation of the disease comprises a triad of cardinal symptoms: Rest tremor (4-6 Hz), bradykinesia (slowness of movement) and muscular rigidity. The symptoms appear on average around 55 years of age and the disease can progress for more than a decade before death occurs (Hoehn and Yahr, 1967). Since no systemic biochemical marker currently exists for PD, confirmation of the clinical diagnosis is made at autopsy if neuronal cell losses and Lewy body inclusions are detected in the pars compacta of the substantia nigra and other brainstem nuclei (Kish *et al*, 1988; Gibb and Lees, 1988). At the onset of the symptoms, destruction of 50% of nigral neurons has led to 80% depletion of dopamine levels in the striatum (Marsden, 1990). Even though PD was first described almost 200 years ago, the cause and the mechanisms of cell death are still unknown (Langston, 1998) and only symptomatic relief can currently be offered to PD patients. Initially proposed and tested 40 years ago (Birkmayer and Birkmayer, 1989), administration of L-DOPA remains the most effective treatment for PD (Lang and Lozano, 1998). With the progression of the disease however, patients become less responsive to L-DOPA therapy and develop dyskinesias (medication-induced motor side effects). As a lot of efforts are being spent into the development of neuroprotective (e.g. dopamine agonists (Whone *et al*, 2003)) and neurorestorative (e.g. glial derived neurotrophic factors (Gill *et al*, 2003)) treatments, it is important to accurately select patients to whom these treatments are most beneficial (Frey, 2002).

PET can assist in the diagnosis of PD by its ability to detect preclinical cases, to

differenciate PD from other movement disorders, and to follow patients over time objectively (Brooks, 1998; Shinotoh and Calne, 1995). In particular, PET has the ability to reveal characteristic patterns of striatal dopamine dysfunction that can distinguish PD from other Parkinsonian syndromes. PET studies with 6-[^{18}F]fluoro-L-DOPA (FDOPA) have shown reduced uptake in the putamen and to a lesser extent in the caudate nucleus of PD patients compared to normal controls (Brooks *et al*, 1990a,b; Kuwabara *et al*, 1995). In the early stages of PD, FDOPA uptake in the putamen is within the normal range on the side of the clinical symptoms, but is reduced by 30% on the opposite side (Morrish *et al*, 1995). Using discriminant function analysis, Burn *et al*(1994) showed that FDOPA/PET studies can correctly separate 90% of patients with progressive supranuclear palsy (PSP) and 60% of patients with multiple system atrophy (MSA) from patients with PD when the severity of involvement of the putamen relative to the caudate nucleus is taken into consideration. Patients with corticobasal degeneration (CBD) have reduced striatal FDOPA uptake on the side contralateral to their clinical symptoms but normal striatal uptake on the ipsilateral side (Brooks *et al*, 2000). The striatal FDOPA uptake is normal in PET images of patients with essential tremor (ET) (Brooks *et al*, 1992) and L-DOPA responsive dystonia (DRD) (Turjanski *et al*, 1993; Snow *et al*, 1993b). In late-onset dystonia (LOD), FDOPA uptake is lower in the putamen than in the caudate nucleus, but equal on either side (Turjanski *et al*, 1993).

F*m*T is a radiolabelled substrate for the enzyme aromatic L-amino acid decarboxylase (AADC) and can be used with PET to study dopamine terminal integrity in the striatum (Nahmias *et al*, 1995). F*m*T , unlike FDOPA, is not methylated into radiolabelled metabolite which crosses the blood brain barrier, and thus produces PET images with superior delineation of the striatum than FDOPA. In this chapter, caudate nucleus to putamen gradients in F*m*T uptake are combined with side to side asymmetries in an attempt to clarify the differential diagnosis of 21 patients presenting with atypical Parkinsonian symptoms. Five normal volunteers and one typical early Parkinsonian subject were also studied. Graphical analyses were carried out on six subregions of the striatum (left and right caudate nucleus, right and left, anterior and posterior putamina) using a plasma (venous sinus) input function, and the results were compared with those obtained using a reference tissue (cerebellum) input function. Patients having both a caudate to putamen influx constant ratio and a contralateral to ipsilateral putamen influx constant ratio significantly greater than one were considered to probably suffer from Parkinson's disease. A discriminant level

was set at the upper limit of the 95% confidence interval around the mean putamen influx constant of this group of patients. The discriminant level was then used to separate the remaining patients showing a uniform pattern of striatal F*m*T uptake into probably normal or abnormal.

6.2.1 Background

6.2.1.1 Clinical features of Parkinson's disease

A marked variability is observed in the presentation (the age and symtoms at onset, the relative prominence of the cardinal symptoms) and the progression (the rate and extent of the disability) of idiopathic Parkinson's disease, making the clinical diagnosis difficult. Hoehn and Yahr (1967) proposed the now well-established rating scale, summarized in **Table 6.1**, that grades PD patients in five stages based upon their level of clinical impairment. The Hoehn and Yahr rating scale (HY) highlights the natural history of untreated PD from asymmetric onset to complete incapacitation, as well as provides guidelines to define more homogeneous subgroups of patients. The median disease duration before reaching the different stages suggests that the progression of the motor disability is more rapid in the early stages (HY I to III) compared to the later stages of the disease (HY IV to V). Patients presenting predominantly with tremor seem to have a more favorable prognosis than those presenting with muscular rigidity or bradykinesia. Gender and age at onset have not been found to affect the prognosis of PD. The rate of progression of PD is thought to be closely related to the rate of depletion of nigral neurons, from which a latent phase has been predicted to preceed the appearance of the first clinical symptoms.

The clinical diagnosis of Parkinson's disease can also be complicated by the absence of one of the cardinal symptoms, and the presence of other symptoms such as early onset of gait instability, autonomic failure or dementia, that are the hallmarks of other movement disorders (Brooks, 2002) (see **Table 6.2**). Clinico-pathological studies have estimated the rate of false-positives to be 20% and that of false-negatives, 5-10% (Hugues *et al*, 1992) in cases with unknown etiology. Multiple system atrophy (10% of cases) and progressive supranuclear palsy (5% of cases) are the two diseases most frequently confounded with PD (Brooks, 1998). The clinical diagnosis of PD is further supported when the initial symptoms develop predominantly on one side (asymmetry) and the patient shows a good response to L-DOPA. However, patients with corticobasal degeneration also have asymmetrical symptoms

Table 6.1: *Hoehn and Yahr scale.*

Stage	Duration	Clinical impairment
I	3y	Unilateral involvement with minimal or no functional impairment
II	6y	Bilateral involvement without impairment of balance
III	7y	Impaired *righting reflexe* [a] restricting level of activities (mild to moderately incapacitated)
IV	9y	Walking and standing without assistance (markedly incapacitated)
V	14y	Confinement to bed or wheelchair unless aided

[a] Unsteadyness demonstrated by pushing the patient from standing equilibrium with the feet together and the eyes closed.

and patients with MSA initially respond well to L-DOPA treatment. PD patients have a better prognosis than those suffering from Parkinsonian syndromes, and although the efficacy of L-DOPA diminishes with the progression of PD, no treatment can currently be offered to those with MSA, PSP or CBD. Accurate differential diagnosis of PD does not only affect the management of patients, but also epidemiological studies and clinical trials.

6.2.1.2 Pathological findings in Parkinson's disease

The characteristic patterns of nigral cell loss in PD are different from that in normal aging (Fearnley and Lees, 1991). An exponential loss of nigral cells with a rate of 45% in the first decade of the disease is observed in patients with PD. The ventral parts of the pars compacta of the substantia nigra incurs greater losses (91% laterally and 71% medially) than the dorsal part (56%). The rate of nigral cell loss associated with normal aging is estimated to be about ten times slower, at a constant rate of 4.7% per decade. Regionally, the patterns are different from PD with the dorsal part being more affected (6.9%) than the ventral parts (5.4% in the medial part and 2.1% in the lateral part). The nigral cell losses result in subregional patterns of dopamine losses that are also different between PD and normal aging (Kish *et al*, 1988, 1992). Recall that the lateral ventral nigra projects to the dorsal putamen and the dorsal nigra to the caudate nucleus. In PD, the putamen is much more depleted of dopamine (2% of normal levels) than the caudate nucleus (19% of normal levels) (Kish *et al*, 1988). Within the putamen, the caudal and dorsal parts

Table 6.2: *Differential diagnosis between PD and Parkinsonian syndromes.*

Disease	[a]Clinical features	Pathological findings	Response to L-DOPA	Onset	Duration
PD	-rest tremor -muscular rigidity -bradykinesia * asymmetric onset	-non-uniform nigral cell loss -Lewy body neuronal inclusions	good response with late complications	55y	>10y
MSA	-Parkinsonian -intention tremor -gait disturbance with falls -autonomic and pyramidal * asymmetric onset	-striatal, nigral, brainstem, cerebellar and spinal cell loss -argyrophilic neuronal and glial inclusions	responsive at early stages	45y	9y
PSP	-Parkinsonian -gait instability with falls -supranuclear gaze problems -dysarthria and hypophonia -frontal lobe deficiencies * symmetric onset	-pallidal, nigral, brainstem and cerebellar cell loss -neurofibrillary tangle neuronal inclusions	mildly responsive	65y	6y
CBD	-Parkinsonian -limb apraxia -limb myoclonus -alien limb * asymmetric symptoms	-contralateral parietal lobe atrophy -thalamic, nigral and cerebellar cell loss -Lewy body and globsose tangle neuronal inclusions	poorly responsive	60y	similar to PSP
DRD	-Parkinsonian -lower limb dystonia	-genetic defect in TH gene	sustained response	<10y	normal life expectancy
ET	-postural tremor (4-9Hz)	unknown	none		

[a] PD: idiopathic Parkinson's disease; MSA: multiple system atrophy (includes Dry-Shager syndrome, striatonigral degeneration (SND), pure autonomic failure and olivopontocerebellar atrophy); PSP: progressive supranuclear palsy (also known as Steele-Richardson-Olszewski syndrome); DRD: DOPA-responsive dystonia; and ET: essential tremor.

are more affected by dopamine loss than the rostral and ventral parts, respectively. In contrast, the caudate nucleus and the putamen are equally depleted of dopamine (-60% from 14 to 92 years old) as a result of normal aging (Kish *et al*, 1992). Furthermore, the dopamine loss is similar in all subregions of the striatum.

The regional selectivity of nigral cell death and dopamine depletion is relatively specific to PD (Fearnley and Lees, 1991). In PSP, nigral cell losses are larger in the dorsal part (83%) and smaller in the lateral ventral part (81%), showing a more uniform pattern of cell losses compared with PD. In MSA, nigral cell losses are comparable to those detected in PD in the ventral parts (97% laterally and 76% medially) but greater in the dorsal part (76%). The involvement of the putamen is belived to account for the symptoms of bradykinesia and muscular rigidity, whereas greater involvement of the caudate nucleus could result in more cognitive dysfunction (Lang and Lozano, 1998).

In PD cases, Lewy bodies are detected in the surviving cells of the substantia nigra and other brainstem nuclei. *Lewy bodies* are neuronal inclusions formed of aggregated filaments shaped into a round body 5-25 μm in diameter surrounded by a pale ubiquitin-staining halo (Gibb and Lees, 1988). The role of Lewy body in the pathogenesis of PD remains unknown. It is found in some elderly individuals and rarely in other neurodegenerative disease. The prevalence of incidental Lewy body cases has been found to increase from 3.8% to 12.8% from the sixth to the ninth decades (Gibb and Lees, 1988), in parallel to the prevalence of PD. Lewy bodies thus provide a biochemical marker for PD.

6.3 Materials and Methods

6.3.1 Data Collection

Twenty-seven subjects underwent a two-hour PET study following an intravenous bolus injection of 110 to 185 MBq of FmT . Twenty-five subjects, four normal controls (four males aged from 25 to 54 years old) and 21 patients (11 males and 10 females aged from 23 to 76 years old) presenting with atypical Parkinsonian symptoms, were studied on an ECAT/ART (CTI/Siemens, Knoxville, TN, USA) over a two-year period. The patients were referred for a PET study at the McMaster University Medical Centre (Hamilton, Canada) by a number of neurologists requesting additional information to assist them in the diagnosis of these patients. The clinical characteristics of the individual patients are

presented in **Table 6.3**. One of the normal controls was studied on the ECAT/ART twice (identified as #2 and #3 in **Figure 6.4** and thereafter), two years apart, in order to estimate the reproducibility of the method. The other two subjects, one normal (47-year old man — subject #1) and one typical PD (60-year-old woman — subject #7) affected on the right side (Hoehn and Yahr stage I) were studied on an ECAT/EXACT3D (CTI/Siemens, Knoxville, TN, USA) at the Hammersmith Hospital (London, UK). The details of the data collected at the Hammersmith Hospital have already been reported in Chapter 3, but the clinical characteristics of the PD subject were included in **Table 6.3**.

All the images were acquired in 3D mode. The images were reconstructed using the 3D reprojection algorithm (Kinahan and Rogers, 1989) with the Colsher and ramp filters set at Nyquist frequency. The model-based scatter correction of Watson *et al*(1996) and an attenuation correction based on the single-photon transmission images (Yu and Nahmias, 1995) acquired prior to the injection of the radiotracer were applied to the emission images during reconstruction. In order to use image-derived input functions, a frame definition that accurately characterizes the early time course of the radiotracer in the blood was chosen (typically 2 frames at 10s per frame, 20 frames at 5s per frame, 4 frames at 180s per frame, and 21 frames at 300s per frame). Four to six discrete venous blood samples were drawn at increasing intervals during the scan and later processed for the determination of the haematocrit, the partition of FmT between plasma and erythrocytes and the radiolabelled metabolites of FmT .

6.3.2 Data Analyses

The *image-derived plasma input function* was obtained using the method validated in Chapter 3 and the population value for the superior sagittal sinus (SSS) determined in Chapter 4. Briefly, the time-course of the radioactivity concentration in the blood was derived by drawing circular regions of interest (ROI) (diameter=7.5mm) in the SSS visible on ten to fifteen contiguous planes of the reconstructed image of the first two minutes of the PET study. These ROIs were superimposed on the dynamic images and an *average* time-activity curve (TAC) was generated. The venous sinus TAC was corrected for partial volume and spillover using the method described in Chapter 3 (see equation (3.2)). For an SSS and ROI radius of 3.5mm each, the values of the recovery coefficient were calculated to be 0.42 and 0.54 for the ECAT/ART and ECAT/EXACT3D, respectively, using values

Table 6.3: *Clinical characteristics of subjects studied with PET/FmT .*

Subject	Gender[a]	Age (y)	Disease duration(y)	Rest tremor	Rigidity	Brady-kinesia	Atypical features[b]	Asym-metry[b]	Response[c] to L-DOPA	CT or MRI[d]
Idiopathic Parkinson's disease (PD)										
7	F	60	3	yes	yes	yes	none	R	good	N
8	M	58	8	yes	yes	yes	Restless leg syndrome, sleep disturbance, fatigue, headaches	R	not tested	N
9	M	43	3	yes	yes	not reported	L foot cramp, depression	L	poor	N
10	F	63	2.5	yes	yes	yes	Postural tremor	R	poor	n/a
11	F	47	3	no	yes	yes	Action tremor, toe clenching on R foot, anxiety and depression	R>L	good (DA-agonist)	N
12	F	45	1	yes	yes	yes	Multiple sclerosis, dystonia on R foot	R>L	good	No plaque in SN
13	M	70	7	yes	yes	yes	Bilateral action tremor, restricted extra-ocular mouvements	R, L>R	good initially	n/a
14	F	38	4.5	yes	yes	yes	Action tremor	R	not reported	N
15	M	53	4	yes	yes	yes	Postural, head and abdomen tremor, dystonia on R hand and foot, difficulty swallowing, cognitive impairments	R>L	good	n/a
16	M	44	2	no	no	no	Amyotrophic lateral sclerosis (ALS), weakness in limbs, difficulty swallowing, depression	R>L	not reported	n/a
17	F	76	1	yes	yes	yes	Falls, depression, cognitive impairments	R>L	not reported	n/a

Table 6.3: *...Continued*

Subject	Gender[a]	Age (y)	Disease duration(y)	Rest tremor	Rigidity	Brady-kinesia	Atypical features[b]	Asym-metry[b]	Response[c] to L-DOPA	CT or MRI[d]
Corticobasal degeneration (CBD)										
18	M	50	2	no	yes	yes	Action tremor	R	good	N
19	F	23	2	no	no	no	Dystonia on L foot and hand, slurred speech, difficulty swallowing	L	poor	N
20	F	71	1	no	yes	yes	Dystonia on R, action tremor, mild cognitive problems	R	not reported	N
21	F	33	1	no	yes	yes	Action tremor on R arm, spasticity on R limbs	R	not reported	N
22	M	55	3.5	yes	yes	yes	Action tremor on R arm	R>L	poor	N
Dystonia (D)										
23	M	46	1.5	no	no	no	Dystonia on R foot, (anatomical abnormality)	R	poor	n/a
24	M	68	3	no	yes	yes	Action tremor, decreased arm swing and stiff gait	L>R	good	n/a
Essential tremor (ET)										
25	F	44	1.5	yes	no	no	Action tremor	R	good	N
26	M	45	5	no	yes	yes	Action tremor, depression	L>R	not reported	n/a
Chorea (C)										
27	F	33	19	no	no	no	Generalized atypical dystonia, hemi-ballistic and choreoalletotic mouvements	R>L	poor	N
28	M	45	3	no	no	no	Choreoathetotic movements in limbs, restless leg syndrome	no	poor	N

[a] M: male; F: female; [b] L:left; R: right; [c] DA: dopamine; [d] N: normal; n/a: not available; SN: substantia nigra.

of 6.7mm and 5.0mm, respectively, for the spatial resolution of the tomographs at 5cm from the center of the field of view. The background ROI was drawn as an annulus around each SSS ROI in the occipital lobe. The noisy blood TAC was then fitted to the three-compartmental model of Feng *et al*(1993) as done in Chapter 3 and corrected for blood partition and metabolites using the blood model presented in Chapter 5. The *reference tissue input function* was derived by drawing on the reconstructed image of the second hour of the scan two elliptical ROIs (area=12.7cm^2) in the cerebellum (left and right lobes) on five contiguous planes. An *average* TAC was generated by overlaying these ROIs on the dynamic images.

Six elliptical ROIs (area=1.2cm^2) were drawn on the reconstructed image of the second hour of the scan using a brain atlas for reference: Two in the caudate nucleus (left and right) and four in the putamen (anterior and posterior, left and right). Relatively small ROIs were drawn in the striatum in order to limit the effects of partial volume (Yu *et al*, 1993). These ROIs were copied to four contiguous planes and *individual* TACs of each subregion of the striatum were generated from the dynamic images. An influx constant, reflecting the uptake of F*m*T in brain tissues which irreversibly trap the metabolized radiotracer, was calculated for each striatal TAC using multiple-time graphical analysis (Patlak and Blasberg, 1985) with the two different image-derived input functions. Using either input function, the transformed data corresponding to the time interval 20-120min were fitted to a straight line.

6.3.2.1 Comparison between input functions

The influx constant derived with reference tissue input function (K_{ir}) is related to the influx constant derived with a plasma input function (K_{ip}) by the inverse of the volume of distribution of the reference tissue (see **Appendix C.2**). The volume of distribution of the cerebellum (VD_r) was calculated from a Logan plot (Logan *et al*, 1990) using the venous sinus input function under the assumption that the uptake of F*m*T in the cerebellum can be modelled as a one-compartment two rate constant model (see **Appendix B.1**). The correlation between K_{ir} and K_{ip}, and between K_{ir} and K_{ip}/VD_r was determined from a linear least-squares regression.

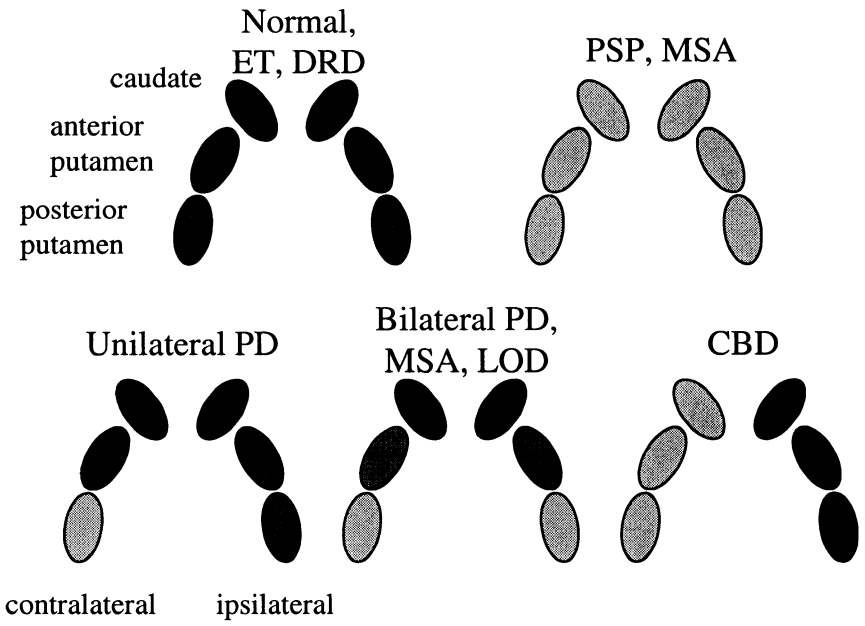

Figure 6.1: *Striatal patterns of distribution of FmT : Normal (***N***) (and essential tremor (***ET***) and DOPA-responsive dystonia (***DRD***)): cau/put and ipsi/contra ratios not different than 1, and K_i values within normal range; progressive supranuclear palsy (***PSP***) and multiple system atrophy (***MSA***): cau/put and ipsi/contra ratios not different than 1, and K_i values within PD range; unilateral Parkinson's disease (***PD***): contra cau/put>1 and ipsi/contra put>1; bilateral PD and MSA and late-onset dystonia (***LOD***): contra cau/put>1 and ipsi cau/put>1; corticobasal degeneration (***CBD***): ipsi/contra cau>1 and ipsi/contra put>1. Dark gray corresponds to normal FmT uptake; light gray to low FmT uptake. Contralateral refers to the side opposite of the affected limbs, ipsilateral, to the same side as the affected limbs.*

6.3.2.2 Within- and between-subject comparisons

The mean and standard deviation of the influx constant over all planes was calculated for each subregion of the striatum. The caudate to putamen ratios on the sides contralateral and ipsilateral to the affected limbs as well as the contralateral to ipsilateral ratios for the caudate nucleus and posterior putamen were calculated for each subject. To test if the ratios were significantly greater from unity (significance level set at 0.05), a one-tailed two-sample Student's t-test was applied to individual ratios. The patterns of distribution of FmT uptake in the striatum are illustrated in **Figure 6.1**. Patients with a contralateral caudate to putamen ratio and a contralateral to ipsilateral posterior putamen ratio greater than one were classified as unilateral PD. Patients with a contralateral and an ipsilateral caudate to putamen ratios greater than one were regarded as bilateral PD, although MSA and LOD can produce a similar pattern of striatal involvement. When the contralateral to ipsilateral ratio of both the posterior putamen and the caudate nucleus were greater than one, the patient was considered to have CBD. Subjects with equal involvement of all striatal subregions, as seen in PSP or MSA, could not be differentiated from normal subjects, since in both cases none of the ratios would be different from unity. In these cases, the classification between normal and abnormal was based on the absolute values of the posterior putamen influx constant compared to those of the probable PD patients (see below).

6.3.2.3 Within- and between-group comparisons

The ipsilateral and contralateral caudate nucleus influx constants in all subjects as well as the ipsilateral and contralateral posterior putamen influx constants in the normal controls and in the patients not showing left and right asymmetry were averaged. Three groups were formed: the first group (*normal*) comprised the five normal controls, the second group gathered the seven subjects classified as unilateral and bilateral PD (*non-uniform*), and the third group (*uniform*) was composed of the sixteen remaining subjects showing a uniform pattern of distribution of FmT . The mean and standard deviation of the caudate and putamen influx constants for the first two groups were calculated. Within each group, a two-tailed matched-pairs Student's t-test was used to detect significant differences between the caudate and putamen. A one-tailed two-sample Student's t-test was applied to determine if the contralateral putamen of the non-uniform group was significantly lower than that

of normal group. The upper limit of the 95% confidence interval around the mean putamen influx constant of the non-uniform group was chosen as the discriminant level that separates the normal and abnormal subgroups within the uniform group. These statistical analyses were applied to both K_{ir} and K_{ip}/VD_r. VD_r was also tested for group differences that could have potentially confounded the classification using a two-tailed two-sample Student's t-test.

6.4 Results

Typical examples of ROI-based blood and tissue TACs are shown in **Figures 6.2a)** and **b)**, respectively. Whereas the blood TACs extracted from images acquired on the ECAT/EXACT3D tomograph contain some undesirable noise (see **Figure 3.8**), those from the ECAT/ART tomograph are too noisy to be used as input functions without pre-smoothing. The whole putamen TACs acquired on the ECAT/ART are also noisier than the corresponding ones from the ECAT/EXACT3D (see **Figures 3.9**). The separation between the anterior and posterior parts of the putamen results in even noisier TACs, but reveals greater differences between the left and right sides of the posterior part of the putamen compared to those of the whole putamen. The transformation of these data into linearised plots are examplified in **Figures 6.3a)**, **b)** and **c)**. All parts of the putamen display an irreversible behavior as indicated by the non-zero slope of the plasma Patlak plots. The mostly reversible uptake in the cerebellum is verified in the plasma Patlak plot where its slope is close to zero, and in the Logan plot where its slope is of finite magnitude. As shown in the insert of **Figure 6.3b)**, the intercept does not coincide with the origin as one would expect if the cerebellum kinetics were described by a one-compartment two-rate constant model. The volume of distribution of the cerebellum as determined from all the data in the Logan plot is thus slightly underestimated. Nevertheless, the reference tissue Patlak plots are seen to become linear like the corresponding plasma Patlak plots.

6.4.1 Within- and Between-Subject Comparisons

Individual influx constant, K_{ir} and K_{ip}, values for each striatal subregions are plotted in **Figures 6.4a)** and **b)**, respectively. Individual ratios for the cerebellum input function are displayed in **Figures 6.5a)**, **b)**, **c)** and **d)**. In the five normal controls (#1, #2, #4, #5 and #6), all four ratios were not significantly greater than one, in accordance with

a)

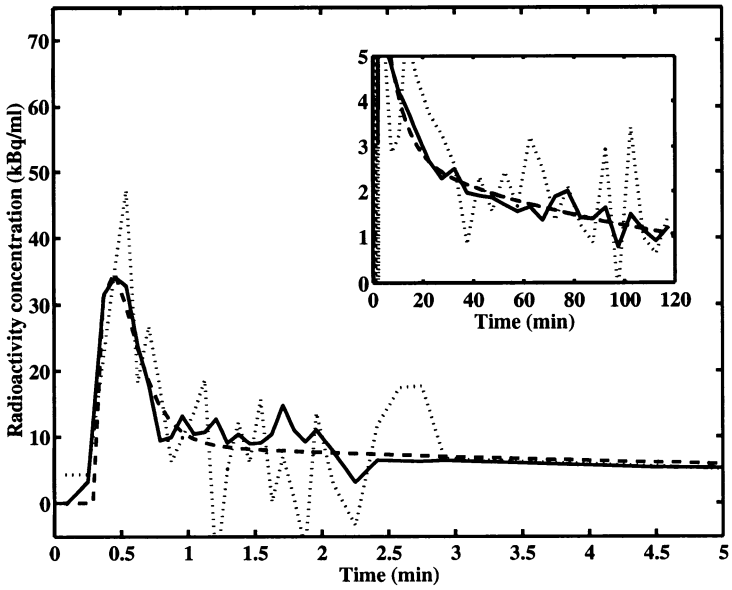

b)

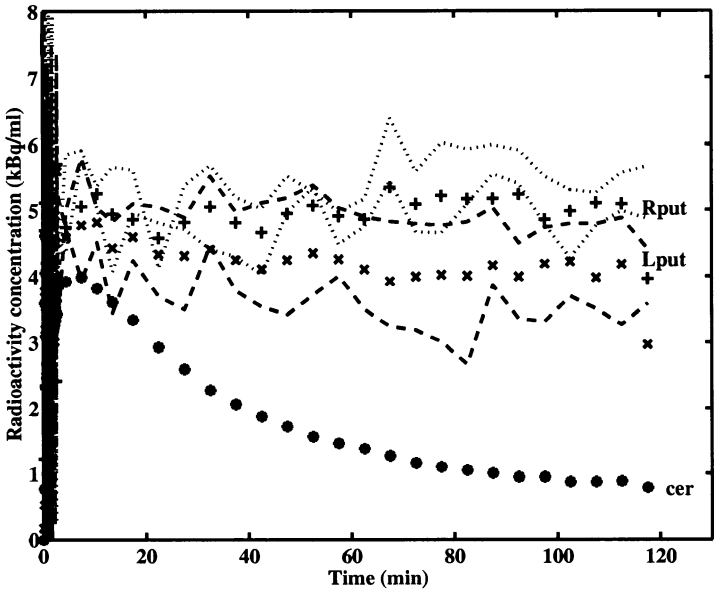

Figure 6.2: **a)** *Comparison of ROI-based blood TACs (from subject #10) corrected for partial volume and spillover: ·····single plane, ——average of several planes, and - - - -fitted to sum of exponentials. The tail and the shoulder of the curves are enlarged in the insert.* **b)** *Comparison of tissue TACs (from subject #10): ·····left anterior (top) and posterior (bottom) putamen; - - - -right anterior (top) and posterior (bottom) putamen; average of anterior and posterior putamen (+ left, × right); ∗ cerebellum.*

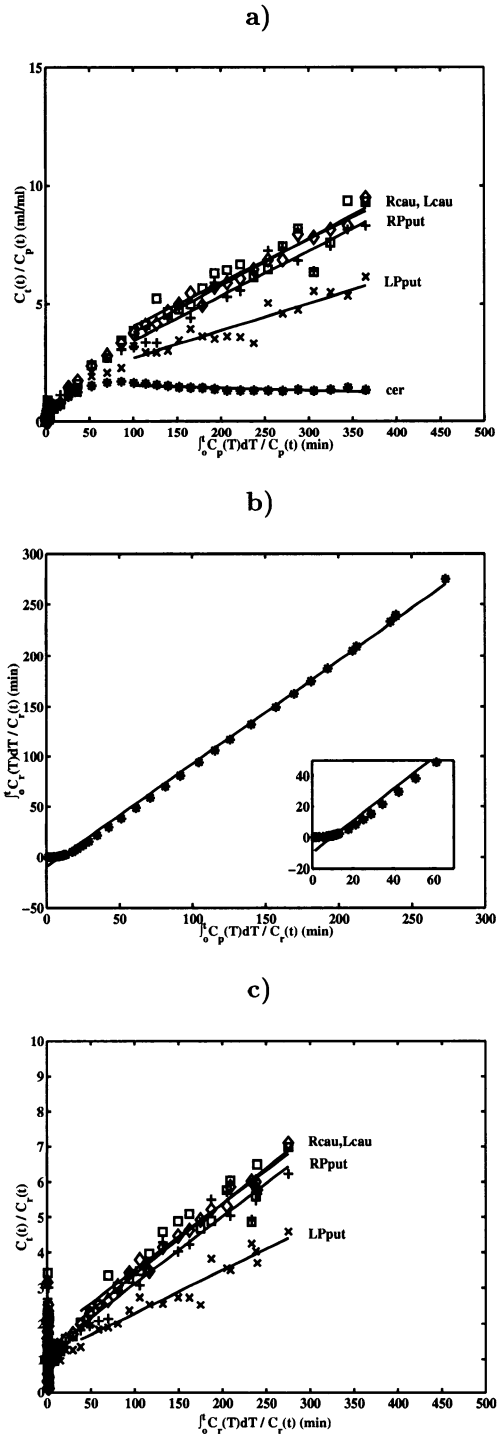

Figure 6.3: *Examples of linearised plots (from subject #10):* **a**) *Patlak plots using the image-derived plasma input function,* **b**) *Logan plot of the cerebellum using the image-derived plasma input function (with the origin of the plot enlarged in the insert), and* **c**) *Patlak plots using a reference tissue (cerebellum) input function (□ left caudate; + left posterior putamen; ◇ right caudate; × right posterior putamen; ∗ cerebellum).*

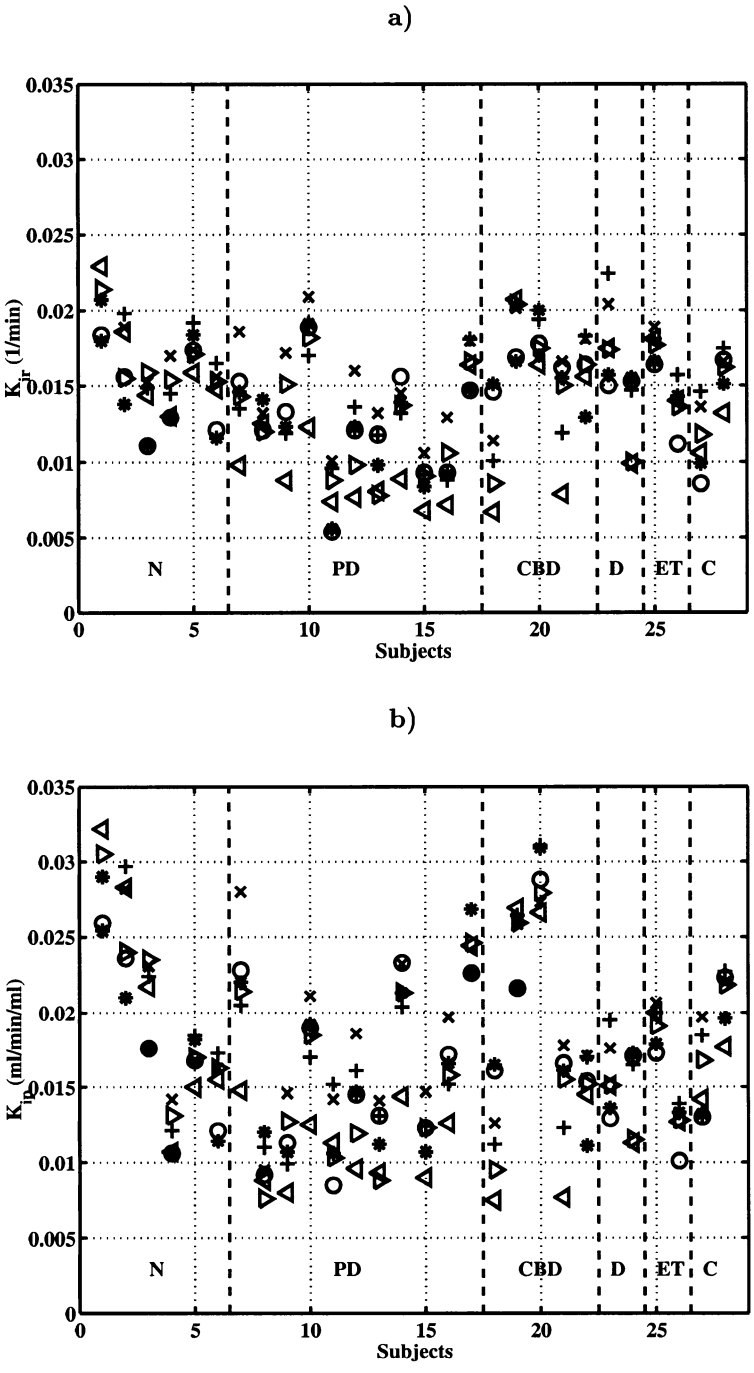

Figure 6.4: *Individual influx constants calculated using* **a**) *a cerebellar input function (K_{ir}) and* **b**) *an image-derived plasma input function (K_{ip}) for each striatal subregion:* $*$ *contralateral caudate nucleus;* $\circ$ *ipsilateral caudate nucleus;* $+$ *contralateral anterior putamen;* $\times$ *ipsilateral anterior putamen;* $\triangleleft$ *contralateral posterior putamen;* $\triangleright$ *ipsilateral posterior putamen (see* **Table 6.3** *for subjects identification). Contralateral refers to the side opposite of the affected limbs, ipsilateral, to the same side as the affected limbs.*

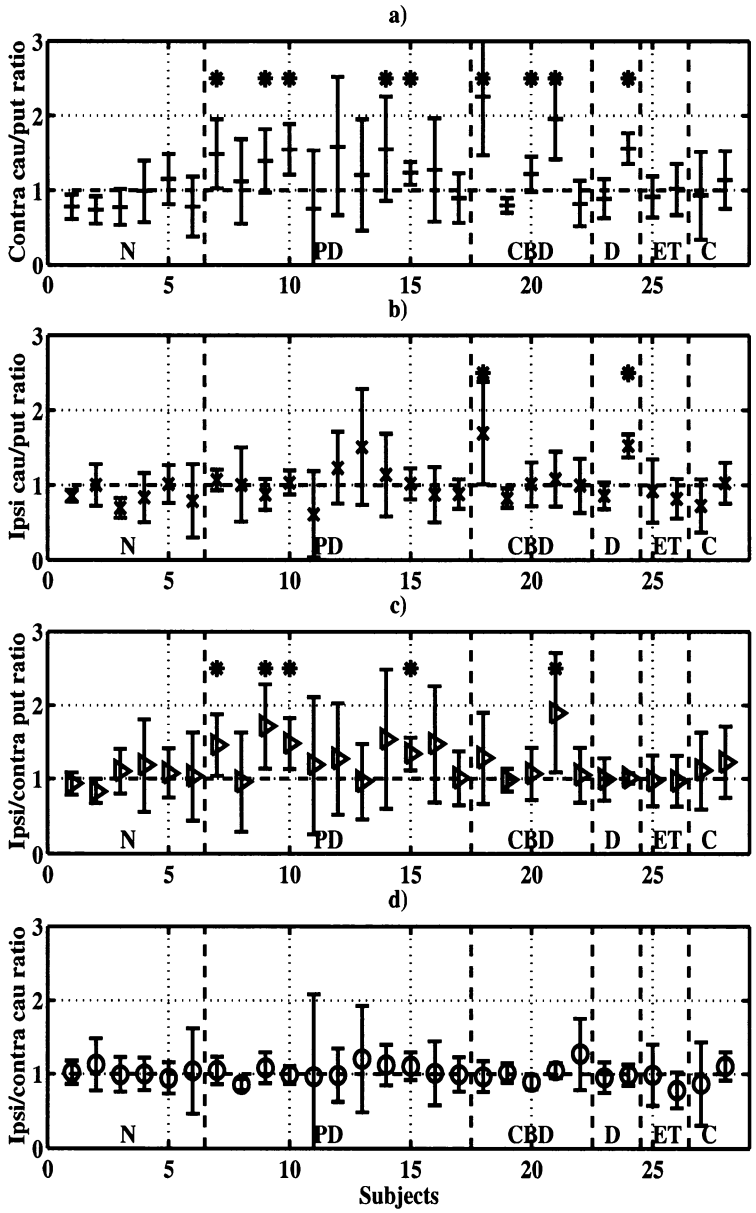

Figure 6.5: *Individual K_{ir} ratios:* **a**) *contralateral caudate/putamen;* **b**) *ipsilateral caudate/putamen;* **c**) *ipsilateral/contralateral putamen; and* **d**) *ipsilateral/contralateral caudate (see* **Table 6.3** *for subjects identification). Ratio values significantly greater than one (p-value<0.05) are indicated by an asterix. Contralateral refers to the side opposite of the affected limbs, ipsilateral, to the same side as the affected limbs. The errorbars correspond to the 95% confidence interval around the mean.*

the expectation of a uniform pattern of distribution of FmT . In the typical PD subject (#7), the contralateral caudate to putamen ratio and an ipsilateral to contralateral putamen ratio were both significantly greater than one. A non-uniform pattern of distribution can thus be considered as indicative of an abnormality in the presynaptic dopaminergic system. Among the ten patients referred to as having PD, three (#9, #10 and #15) had a contralateral caudate to putamen ratio and an ipsilateral to contralateral putamen ratio significantly greater than one, thus confirming the diagnosis of PD. The other seven patients had all four ratios not significantly different from one. Three of them (#8, #14 and #17) had a K_{ir} values above the discriminant level whereas the K_{ir} values of the other four (#11, #12, #13, and #16) were in the range of the probable PD patients.

One (#18) of the five patients referred as CBD had a contralateral and an ipsilateral caudate to putamen ratios greater than one, and another (#21) had a contralateral caudate to putamen ratio and an ipsilateral to contralateral putamen ratio significantly greater than one. These two patients are more likely to suffer from bilateral and unilateral PD than from CBD or MSA, respectively. In the other three patients (#19, #20 and #22), all four ratios were not significantly different than one and their influx constants were within the range of normal controls, giving evidence against CBD and PD. The patient referred as LOD (#23) had a uniform pattern of distribution and a K_{ir} value in the normal range, indicating that the cause of his dystonic foot is more likely to be anatomical than neurological. The patient referred as DRD (#24) had a pattern of distribution typical of bilateral PD rather than DRD. For the two patients referred to as ET (#25 and #26), the uniform pattern of distribution and the normal value of K_{ir} are pointing towards ET and away from PD. Both patients with chorea (#27 and #28) had a uniform distribution of FmT and a K_{ir} value above the discriminant level, showing normal basal ganglia dopamine metabolism. None of the 21 Parkinsonian patients studied is likely to have CBD since a contralateral to ipsilateral caudate nucleus ratio greater than one was not observed. The referring diagnosis and the pattern of distribution of FmT that was used to clarify the differential diagnosis are summarized in **Table 6.4**.

6.4.2 Comparison Between Input Functions

Figure 6.6a) illustrates that the range of absolute values of influx constants calculated with an image-derived plasma input function (K_{ip}) is wider than the range of

Table 6.4: *Differential diagnoses of atypical Parkinsonian patients based on striatal patterns of FmT uptake constants.*

Subject	Referring diagnosis [a]	FmT pattern [b]	
		K_{ir} (1/min)	K_{ip}/VD_r (1/min)
Idiopathic Parkinson's disease (PD)			
8	Early PD?	*normal*	*abnormal*
9	PD?	unilateral	unilateral
10	HemiPD-hemiatrophy vs. PD?	unilateral	unilateral
11	PD?	abnormal	abnormal
12	PD?	abnormal	*abnormal?*
13	PD?	abnormal	abnormal
14	Young-onset PD?	*normal?*	normal
15	PD vs. SND vs. PSP?	unilateral	unilateral
16	PD?	abnormal	*abnormal?*
17	PD?	normal	normal
Corticobasal degeneration (CBD)			
18	CBD vs. PD?	bilateral	bilateral
19	CBD vs. Young-onset PD?	normal	normal
20	CBD vs. hemidystonia?	normal	normal
21	CBD vs. MSA?	unilateral	unilateral
22	CBD?	normal	normal
Dystonia (D)			
23	Late-onset dystonia vs. Orthopaedic problem?	normal	normal
24	Dopa-responsive distonia vs. PD?	bilateral	bilateral
Essential tremor (ET)			
25	ET vs. PD?	normal	normal
26	ET vs. Early PD?	normal	normal
Chorea (C)			
27	Abnormal BG metabolism?	*normal?*	normal
28	?	normal	normal

[a] SND: striatonigral degeneration; PSP: progressive supranuclear palsy; MSA: multiple system atrophy; BG: basal ganglia.

[b] unilateral: contra cau/put>1 and ipsi/contra put>1;
bilateral: contra cau/put>1 and ipsi cau/put>1;
abnormal: all ratios are equal to 1, and K_i values are within PD range; or
normal: all ratios are equal to 1, and K_i values are within normal range.

a)

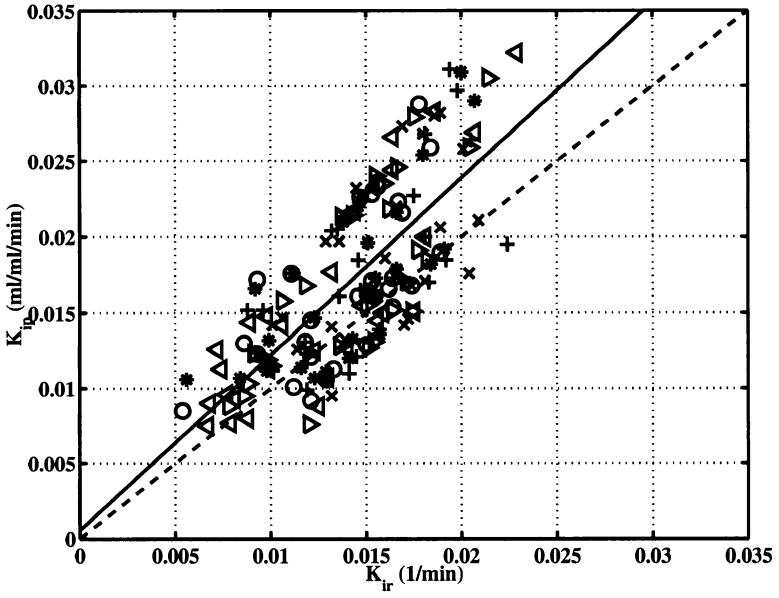

b)

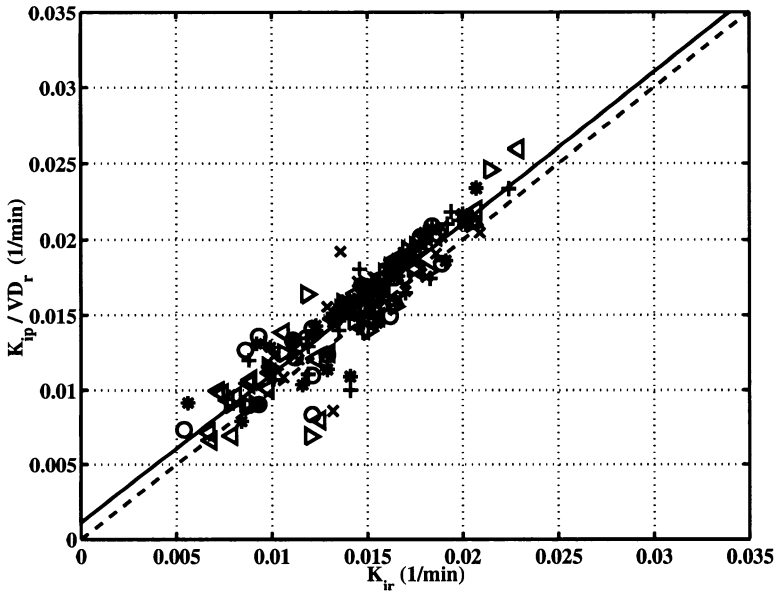

Figure 6.6: *Correlation between* **a)** K_{ip} *and* K_{ir} *and* **b)** K_{ip} *normalized to the volume of distribution of the cerebellum* (VD_r) *and* K_{ir}: $*$ *contralateral caudate nucleus;* $\circ$ *ipsilateral caudate nucleus;* $+$ *contralateral anterior putamen;* $\times$ *ipsilateral anterior putamen;* $\triangleleft$ *contralateral posterior putamen;* $\triangleright$ *ipsilateral posterior putamen;* —— *least-squares regression line, and* – – – *line of identity. Contralateral refers to the side opposite of the affected limbs, ipsilateral, to the same side as the affected limbs.*

influx constants calculated with a cerebellum input function (K_{ir}). Dividing K_{ip} by the volume of distribution of the cerebellum (VD_r) increases the R^2-value from 0.55 to 0.84. It also brings the best-fit lines closer to the line of identity, as shown in **Figure 6.6b)**. Both input functions produce the same patterns of distribution of FmT , when relative values of the influx constants are used. However, classification between normal and abnormal is different in one (#8) of the fifteen patients with a uniform pattern of distribution when the judgement is based on the absolute values of the influx constants.

6.4.3 Within- and Between-Group Comparisons

Scatter diagrams of K_{ir}, K_{ip}/VD_r and VD_r for the normal, non-uniform and uniform groups are presented in **Figures 6.7a)** and **b)**, and **6.8**, respectively. The mean and standard deviation of the influx constants for the normal and non-uniform groups are gathered in **Table 6.5**. For both K_{ir} and K_{ip}/VD_r, the caudate nucleus was not significantly different from the average posterior putamen in the normal group. In contrast, the contralateral posterior putamen was significantly different from the caudate nucleus in the non-uniform group ($p<0.001$ for both input functions). The influx constant of the contralateral anterior and posterior putamina, but not that of the caudate nucleus, was found to be significantly lower in the non-uniform group than in the normal group. However, the level of significance was stronger for the cerebellum input function ($p<0.002$) than for the venous sinus input function ($p<0.01$). The volume of distribution in the cerebellum was not significantly different ($p>0.40$) amongst groups. Based on the upper limit of the 95% confidence interval around the mean contralateral putamen influx constant values, the discriminant level was set at 0.0107 min^{-1} and 0.0113 min^{-1} for K_{ir} and K_{ip}/VD_r, respectively.

6.5 Discussion

The classification scheme used in the present work was based on the reported findings of FDOPA/PET studies (Brooks *et al*, 1990a,b; Kuwabara *et al*, 1995; Morrish *et al*, 1995; Burn *et al*, 1994; Brooks *et al*, 2000; Brooks *et al*, 1992; Turjanski *et al*, 1993 and Snow *et al*, 1993b). The patterns of distribution that were observed with FDOPA in various Parkinsonian syndromes have yet to be replicated with FmT in homogeneous groups of subjects presenting with the characteristic symptoms of each of the diseases. This study

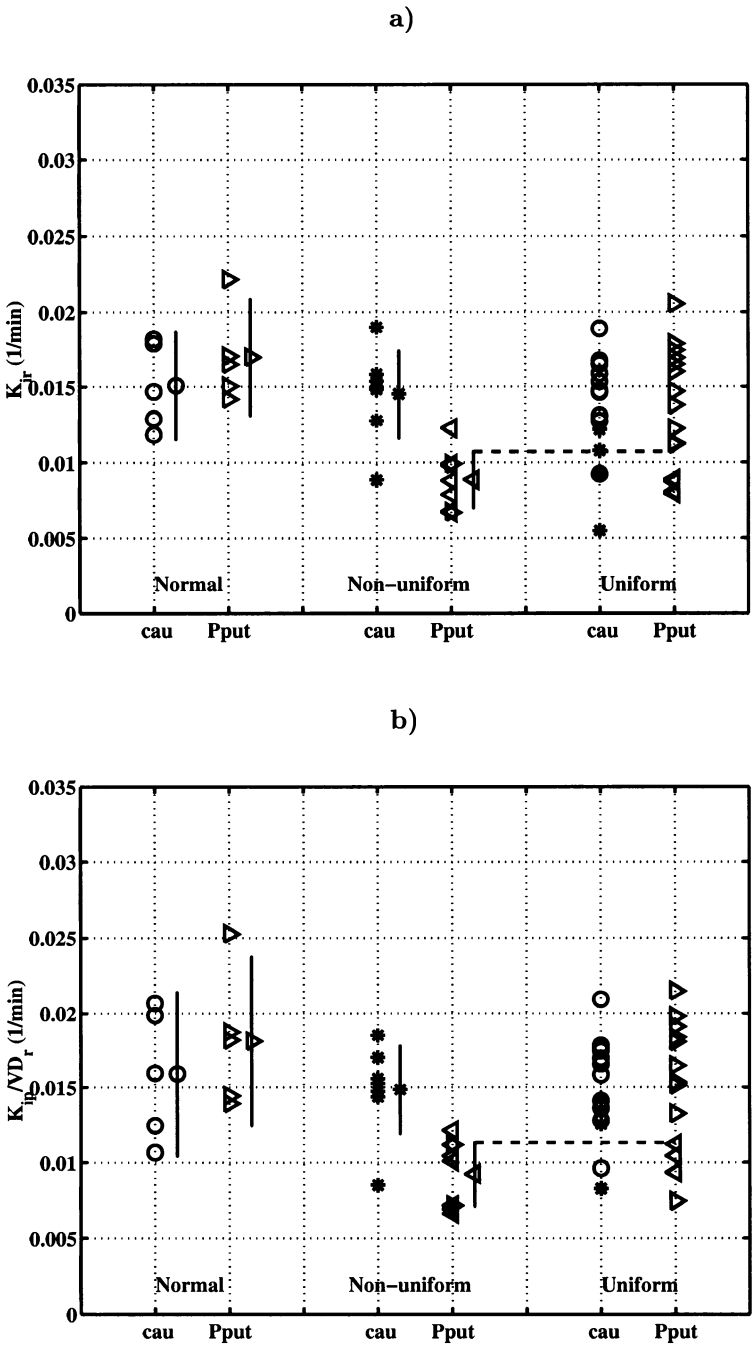

Figure 6.7: *Influx constants* **a**) K_{ir}, **b**) K_{ip} *normalized to the volume of distribution of the cerebellum* (VD_r) *grouped according to the pattern of striatal involvement: normal, non-uniform* (◁ *contralateral;* ▷ *ipsilateral), and uniform* (○, ▷ *probable normal;* ∗, ◁ *probable abnormal). Contralateral refers to the side opposite of the affected limbs, ipsilateral, to the same side as the affected limbs. The error bars correspond to the 95% confidence interval around the mean.*

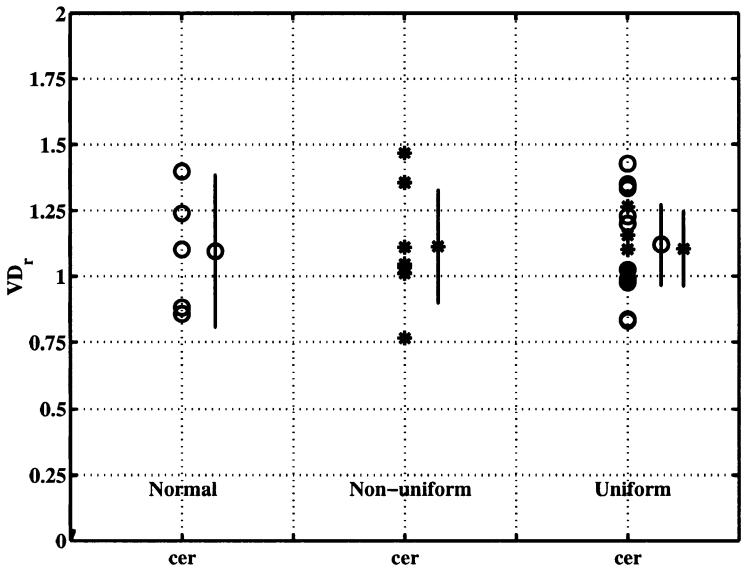

Figure 6.8: *Volumes of distribution of the cerebellum (VD_r) grouped according to the pattern of striatal involvement: normal, non-uniform, and uniform ($\circ$, probable normal; $*$, probable abnormal). The error bars correspond to the 95% confidence interval around the mean.*

Table 6.5: *Comparison of the FmT influx constants calculated using a cerebellum and a venous sinus input functions in the normal and probable PD groups.*

Tissue	K_{ir} (1/min) [a]		K_{ip}/VD_r (1/min) [a]	
	Normal (n=5)	Probable PD (n=7)	Normal (n=5)	Probable PD (n=7)
Caudate nucleus	0.0151±0.0029	0.0145±0.0031	0.0159±0.0044	0.0149±0.0032
Anterior putamen [b]	0.0180±0.0021[c]	0.0126±0.0027[c,e]	0.0190±0.0035[c]	0.0130±0.0028[c,e]
Posterior putamen [b]	0.0170±0.0031	0.0089±0.0020[c,d,e]	0.0181±0.0045	0.0092±0.0023[c,d,e]

[a] Mean ±standard deviation.

[b] The left and right putamina were averaged in the normal group;
the putamen contralateral to the affected side was considered in the probable PD group.

[c] The putamen is significantly different than caudate.

[d] The posterior putamen significantly different than anterior putamen.

[e] The probable PD group is significantly lower than normal group.

shows that the contralateral posterior putamen in the probable PD (non-uniform) group was 52% and 51% of the average posterior putamen of the normal group for K_{ir} and K_{ip}/VD_r, respectively. In addition, the probable PD group was found to have a caudate to putamen ratio of 1.6. These results compare well with the 45% and the 1.9 values published by Brooks *et al*(1990b) based on a Patlak analysis using the occipital lobe as the reference region. In contrast with FDOPA however, the quantitative analysis of the spatio-temporal distribution of F*m*T is not confounded by the undesirable contribution of radiolabelled peripheral metabolites that enter the brain.

The cohort of 21 patients were referred to the McMaster PET Centre to eliminate idiopathic PD as the possible disease underlying their atypical clinical symptoms. A decreased influx constant (K_i) in the posterior putamen contralateral to the affected limbs confirmed the diagnosis of PD in four patients. A lower K_i in the posterior putamen bilaterally in two patients was considered to be indicative of a more advanced stage of PD, since the differential diagnosis did not involve MSA or LOD. Of the remaining fifteen patients, four had a K_i in the posterior putamina that was below the discriminant level set at upper limit of the 95% confidence interval around the mean putamen influx constant of the probable PD group.

A 10% difference in both K_{ir} and K_{ip}/VD_r of the posterior putamen was observed between the two studies that were performed on the same normal control (#2 and #3). If the same uncertainty is attributed to the putamen influx constants of all patients, two patients (#14 and #27) would have a K_{ir} that falls below the discriminant level and two others (#12 and #16) would have a K_{ip}/VD_r above the discriminant level. In addition, the absolute value of the contralateral putamen K_{ir} of one of the probable PD (#10) is 15% higher than the discriminant level. Discrimination based on absolute values of the influx constants is expected to improve when more subjects, in particular normal controls, will be studied with PET/F*m*T .

The striatal patterns of F*m*T uptake can be summarized, as shown in **Figure 6.9**, in a plot of the contralateral caudate to putamen ratio vs. contralateral to ipsilateral putamen ratio in which the first quadrant is occupied by unilateral PD patients, the second one by bilateral PD patients, the third one by normals or patients with a uniform involvement of the striatum, and the fourth one would be filled by CBD patients. Allowing for uncertainties in these ratios, the dividing lines are set tentatively to subject #15, the one amongst the probable PD group having the smallest ratios. Based on that plot, the classification of

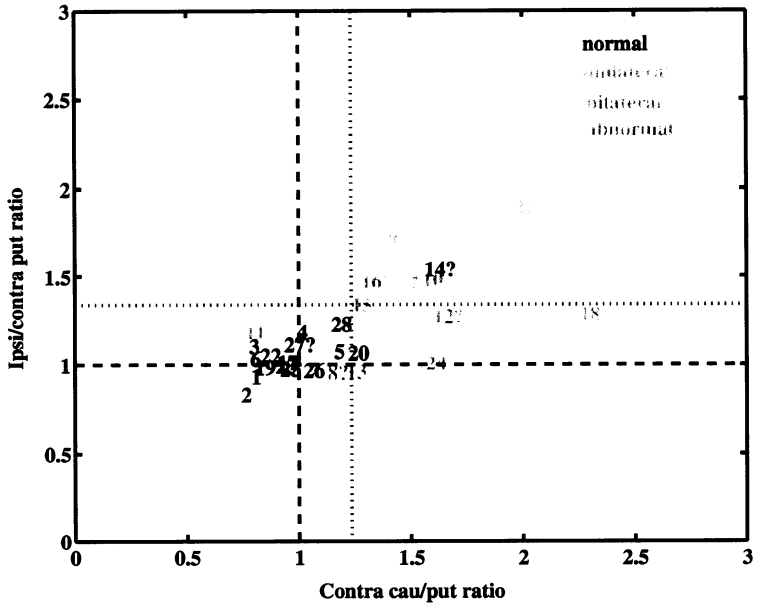

Figure 6.9: *Asymmetry plot: Contralateral caudate to putamen ratio vs. Contralateral to ipsilateral putamen ratio. The first quadrant is occupied by unilateral PD patients, the second one by bilateral PD patients, the third one by normals or patients with a uniform involvement of the striatum, and the fourth one would be filled by CBD patients. The dividing (dashed) lines were set tentatively to subject #15, the one amongst the probable PD group having the smallest ratios.*

patients #12, #14 and #16 in the uniform group is also questionable. The contralateral caudate to putamen ratio of patient #14 was significantly greater than one, but because of the large uncertainties in the ipsilateral to contralateral putamen ratio, this patient was not classified in the unilateral PD group. Large uncertainties in both the contralateral caudate to putamen ratio and the ipsilateral to contralateral putamen ratio of patients #12 and #16 render the distinction between the uniform and the unilateral PD groups difficult for these two patients. Patient #12 could even be categorised in the bilateral PD group, as further supported by the relatively large, but not significantly greater than one, ipsilateral caudate to putamen ratio. Patient #13, who was assigned to the uniform group because of the large uncertainties in the ipsilateral caudate to putamen ratio and the ipsilateral to contralateral putamen ratio, could also be re-classified to the bilateral PD group. Even though the contralateral caudate to putamen ratio and contralateral to ipsilateral putamen ratio are sufficient for the classification of subjects between uniform uptake, unilateral PD, bilateral PD and CBD, the other two ratios bring supplementary evidence which can be particularly helpful in borderline cases.

The overall method presented in this chapter requires 120min of continuous image acquisition and intermittent blood sampling. Over the two-year period that these 21 patients were studied, data on four more patients and one more normal volunteer were acquired but rejected due to severe head motion throughout the PET examination. Amongst the 21 patients retained for data analyses, two studies (#12 and #13) were stopped at 100min after which time the patients could no longer lie in the tomograph. Three further studies (#11, #25 and #27) were shortened to 100min, time at which sudden head motion was observed. The relatively large uncertainties in the influx constant and ratio values of patients #11, #12, #13 and #27 could at least in part be attributed to the shorter duration of the PET study. Owing to qualified staff shortage, metabolites analysis was not performed for one study on a normal volunteer (#2) and two studies on patients (#15 and #22). Using the blood model however, one was able to predict the parent fraction from the plasma to whole blood ratio for the first two studies, but one had to resort to the population curve for the third subject. The quality of the information that can be derived from careful analyses of the dynamic PET/FmT studies is in large part dependant on the quality and completeness of the data acquired, which in this patient population is not always easy to achieve.

The data analyses were carried out on tissue TACs derived from multiple ROIs

positioned on the integral PET image according to the pattern of distribution of F*m*T in normal volunteers. A more objective approach would have been to delineate the same parts of the striatum on a magnetic resonance (MR) image acquired on each individual and co-registered to the integral PET image of the same subject. Such an approach however was not feasible given the long waiting list for an MR examination at the McMaster University Medical Centre at the time when the studies were conducted. As a practical alternative, the size of the ROIs and their relative position on the PET images were standardised across subjects. This approach ensured that the same tissue volume would be sampled in each subject, thereby reducing the natural tendency towards focussing on high uptake areas, which in turn would have prevented the detection of mildly affected cases. Furthermore, the size of the ROIs was carefully selected so that the striatal F*m*T uptake would not be underestimated due to partial volume effects. The observation that the influx constant of the caudate nucleus is lower than that of the putamen in the normal volunteers (see **Table 6.5**) indicates that the uptake measured in caudate nucleus probably suffered slightly from partial volume effects. Transposing this finding to the patient population, some cases where the posterior putamen was mildly affected may have been missed.

The large between-subject variability observed in K_{ip} was reduced by dividing the influx constant by the volume of distribution of F*m*T in the cerebellum (VD_r). The influx constant depends on the rate of trapping as well as the amount of radiotracer delivered to the tissue of interest. Stout *et al*(2001) found that both K_{ip} and the volume of distribution of F*m*T in the striatum strongly depend on the plasma large neutral amino acids concentrations. They showed that correcting for this confounding variable reduces the variability in the K_{ip} estimates by half. Assuming that the volume of distribution of F*m*T in the cerebellum is representative of that of the striatum, the effect of dividing K_{ip} by VD_r is to reduce the dependence of the influx constant on F*m*T delivery to yield an index that is more closely related to the metabolism and retention of F*m*T in the striatum, and to the integrity of the presynaptic dopaminergic system.

Using the two image-derived input functions, 20 of the 21 patients studied with PET/F*m*T were classified in the same groups (normal, non-uniform and abnormally uniform). Even though both input functions are obtained non-invasively, the derivation of the cerebellum input function is simpler than that of the venous sinus input function. The venous sinus input function has the potential to become non-invasive if population values for the partition between plasma and erythrocytes and for peripheral metabolism are used,

as shown in chapter 5. However, only using the venous sinus input function can the validity of the reference region be tested amongst different populations (e.g. normal vs. disease) or treatment (e.g. baseline vs. drug). In patients suffering from either MSA, PSP or CBD, the cortical and/or cerebellar regions can be affected by the disease (see **Table 6.2**), thereby limiting the discrimination power of the reference tissue approaches. The venous sinus input function can also be used with compartmental analysis to obtain the individual rate constants for the delivery and trapping of F*m*T in brain tissues, as done in chapter 3.

6.6 Conclusion

For the 21 patients referred to the McMaster PET Centre for an F*m*T study, a diagnosis based on a clinical assessment was difficult to make, in part because most patients were in the early stages of their disease, in part because they were presenting with atypical confounding symptoms. F*m*T images, when analysed for the relative involvement of the caudate vs. the putamen and the ipsilateral vs. the contralateral sides of the striatum, supported the diagnosis of PD in three out of ten cases, did not support the diagnosis of CBD in all five cases, did not support both diagnoses of dystonia and supported the two diagnoses of ET. One suspected PD patient had normal F*m*T uptake in the striatum whereas abnormally low uniform F*m*T uptake was found in the striatum of another suspected PD patients. In the last five patients referred as PD, striatal F*m*T uptake could not clearly be categorized as normal or abnormal, nor could the pattern of distribution be definitively appraised due to the large uncertainties in their influx constants. Quantitative analyses of PET/F*m*T studies are feasible in a clinical setting using image-derived input functions and also provide useful diagnostic information in individual patients with movement disorders.

Chapter 7

Conclusion

7.1 Summary

In this thesis, a new method for the generation of an image-derived plasma input function for brain PET studies with the radiotracer FmT was developed, validated in phantom studies, and its usefulness assessed in a clinical population.

Cerebral blood vessels are small relative to the spatial resolution of current PET cameras. The biggest challenge faced in this thesis was the necessity to correct for partial volume and spillover with the restriction that none of the voxels in the PET images represented an accurate measurement of the radioactivity concentration in the blood, and this at all times following radiotracer injection. In order to limit the importance of the correction and the concomittant amplification of statistical noise, the superior sagittal sinus (SSS) was selected for having the largest calibre amongst the cerebral blood vessels.

The problem of partial volume and spillover correction was addressed in two steps. A region of interest (ROI) approach (Kessler al, 1984) was first investigated by assuming that the required anatomical information (blood vessel calibre and surrounding tissue geometry) and the tomograph characteristics (point spread function, PSF) were known. The correction was applied to all time frames because the difference between the blood and tissue radioactivity concentrations varies dramatically throughout the PET study (Wahl *et al*, 1999b). A direct comparison with arterial sampling on two subjects demonstrated that using the ROI-based input function introduced a small bias in the physiological parameters of interest which did not impede the discrimination power between a normal volunteer and an early Parkinsonian subject (Asselin *et al*, 2001). The statistical noise present in PET images was filtered out by first averaging the ROI-based blood time-activity curve (TAC)

over several planes and then by fitting the average blood TAC to a delayed sum of exponentials (Feng *et al*, 1993). This part of the work confirmed the feasibility of the preliminary method, but also revealed its limitations.

A voxel approach to partial volume and spillover correction (Aston *et al*, 2002) was then adopted which allowed the estimation of the blood vessel calibre from the PET image as well as the delineation of a non-uniform background region. The revised method was sucessfully tested in a phantom experiment where the diameter and the radioactivity concentration of syringes immersed in a water-filled cylindrical phantom were recovered to within 1 mm and 5%, respectively. Unfortunately, these results were not repeated upon the application of the method to subjects injected with 6-[^{18}F]fluoro-L-DOPA or [^{11}C]CO-labelled red blood cells for which the SSS calibre was systematically overestimated by 2-3 mm compared to measurements made on magnetic resonance venograms. This finding prevented the derivation of a blood TAC using the revised method. An error analysis demonstrated that the simplifying assumptions related to the anatomy of the blood vessel did not impede the applicability of the method to human subjects. It also highlighted that a major source of error in any method for partial volume and spillover correction comes from assuming a time-invariant and subject-independent PSF (Asselin *et al*, 2004). Even though the distortion of the PSF by head motion had previously been characterized (Green *et al*, 1994), its impact on methods of partial volume and spillover correction had not been realised.

The radioactivity concentration extracted from the PET images at the location of the SSS corresponds to the total radioactivity of all radiolabelled compounds present in cerebral venous blood at a given time point. Since the first pass extraction of F*m*T is small, the radioactivity profile of the venous blood in the SSS was assumed not to differ from that of arterial blood in the internal carotid arteries. However, F*m*T is substantially metabolised in peripheral organs and its partition between plasma and erythrocytes differs from that of its radiolabelled metabolites, both with time and at equilibrium (Nahmias *et al*, 2000). Taking advantage of these properties, a compartmental model which combines the blood partition ratio with the parent fraction in plasma was developed and used to transform the blood TAC into a plasma input function. By imposing consistency between the two datasets and increasing the number of degrees of freedom in the fitting procedure, the blood model was shown to improve the robustness of these corrections, particularly in cases where only a few unreliable measurements were available (Asselin *et al*, 2002c).

In order to clarify their differential diagnoses, certain patients presenting with atypical Parkinsonian symptoms were refered by different neurologists to the McMaster PET Centre for an F*m*T study. Presynaptic dopamine function is severely disturbed in Parkinson's disease with a pattern of striatal involvement that distinguishes it from other movement disorders. The scanning protocol of PET/F*m*T studies was altered as a consequence of the progress of the work in this thesis: Frames for the first 5min of the PET study were shortened for accurate definition of the blood peak following bolus injection; upon the discovery of the kinetics of the radiolabelled compounds in blood, samples were stored into an ice bath until processing; the routine measurement of haematocrit in individual patients was introduced; and after the development of the blood model and the extraction of the blood TAC from the PET images, the number of blood samples drawn and processed was dramatically reduced. For 21 of these patients in whom a complete dataset was acquired, graphical analyses were carried out on six subregions of the striatum using the image-derived plasma input function, and results were compared to those obtained using a cerebellar input function. The cerebellum is an imperfect reference region for F*m*T , and in particular for this patient population. The uptake of F*m*T in the cerebellum has been described by an irreversible compartment, a violation of the assumptions of the reference tissue models. It may also be affected in some Parkinsonian syndromes, reducing the detection power of the reference tissue influx constant for patients suffering from cerebellar atrophy. The image-derived plasma input function allowed the verification that the volume of distribution in the cerebellum was not reduced in the patient groups, with either a uniform or non-uniform pattern of F*m*T uptake, compared to the normal group. The classification of 20 of the 21 patients between the non-uniform, normally uniform and abnormally uniform groups was the same using either input function (Asselin *et al*, 2002a). The classification of five of these patients is however questionable due to the large uncertainties in their influx constants. The diagnostic information extracted from the PET images could be confirmed by following up these patients over time, clinically and/or with another PET/F*m*T study.

7.2 Future Work

At the start of this thesis, it was believed that the spatial resolution (transaxially 5-6mm) and the sensitivity (1-5%) of current PET cameras were adequate for the accurate quantification of the blood radioactivity concentration from the cerebral blood vessels im-

aged in dynamic PET studies. The preceeding chapters have shown that this goal could be partly achieved, requiring a considerable amount of image processing and providing with adequate results only in limited conditions. Since then, tomographs offering higher spatial resolution (transaxially <2.5mm) without compromising the sensitivity (>4%) have been developed with LSO detectors (Wienhard *et al*, 2002). As predicted in **Figure 3.5b)**, PET images acquired with this state-of-the-art tomograph should contain a number of voxels, at least in the largest cerebral blood vessels, which are not contaminated by partial volume effects. With the implementation of head motion correction methods (Bloomfield *et al*, 2003), the degradation of the spatial resolution frequently observed when studying human subjects should no longer be a limiting factor in the derivation of reliable time-activity curves from small brain regions.

These major technical improvements open up new possibilities. Partial volume and spillover correction could be bypassed by using factors analysis in dynamic structures (FADS) (Barber, 1980) for the extraction of pure blood TACs from brain PET studies. The feasibility of this approach has been demonstrated in PET/2-[^{18}F]fluoro-2-deoxy-D-glucose (FDG) studies of small monkey hearts (Wu al, 1996). When the left ventricle chamber was larger than twice the spatial resolution of the tomograph, the method could derive a blood TAC from the extreme *dixels* (voxel TACs). In monkeys with a smaller heart, the method required *a priori* information from a late blood sample in order to construct the true blood factor. As expressed many times already, the need for one blood sample is not desirable because of the necessity of cross-calibration between the tomograph and the blood detector, and the risks associated with drawing and processsing the blood sample. With the availability of uncontaminated blood dixels in images from the state-of-the-art tomograph, this additional constraint should not be required by the method. FADS, by defining functional rather than spatial ROIs, would include all relevant voxels in the derivation of the pure blood TAC, thereby providing the optimal signal-to-noise ratio. Alternatively, sophistication of the system matrix used in iterative reconstruction algorithms could eventually allow the partial volume and spillover correction to be performed on sinogram data in the reconstruction rather than in the PET image post-reconstruction.

A pure blood TAC extracted from the SSS can be used as an approximation for arterial blood only with radiotracers with a low extraction fraction, such as FmT . Extension of the method to radiotracers with a higher extraction fraction would require the derivation of a brain model for the artery-vein transfer function. Using the double-

indicator method, brain (well-mixed and non-mixed) models for the first pass extraction of radiolabelled substances have been developed with intracarotid injection (Knudsen *et al*, 1990a,b), and their use adapted for intravenous injection with arterial blood sampling for the definition of the non-bolus input function (Knudsen *et al*, 1994). Using the well-mixed model with the parameters for Na^+ and tyrosine as the reference and test substances repectively, Wahl *et al*(1999b) predicted the blood peak in the internal carotid artery from the blood peak measured in the SSS with FmT . These models however cannot be applied to the time course after recirculation of the radiotracer in the blood. Conducting experiments where the blood time course is measured in the radial artery and extracted from the SSS, an *ad hoc* model for the artery-vein transfer function could be derived, following appropriate corrections for delay and dispersion of the measured arterial blood (Iida *et al*, 1986). This approach would widen the applicability of the method to radiotracers with a moderate extraction fraction, those for which the time course in tissue and in venous blood carries different information. For radiotracers with a high extraction fraction, the high frequency information present in the arterial blood time course is likely to be non-recoverable from the venous blood time course. Furthermore, the radioactivity concentration in the venous blood will be much smaller than that in arterial blood — initially and later on depending on the backflux of the radiotracer — and highly dependent on cerebral blood flow.

The applicability of the blood model to other radiotracers is limited by the assumption of a bolus input. Under this assumption, the blood model can be used without the availability of the time course of total radioactivity concentration in the blood (blood input). However, several radiotracers have radiolabelled metabolites which are trapped in peripheral organs and released in the blood following a finite transit time. The compartmental model could be modified to allow for inputs to the parent and/or the metabolite plasma compartments. Using a bolus input to the parent plasma compartment as initial estimate, the evaluation of the blood model could be iterated, comparing the sum of the four compartments with the measured blood input after each evaluation. This modification of the blood model would also accommodate study protocols which make use of a slow bolus injection or an infusion.

Appendix A

Physical Characteristics of Two 3D Tomographs: ECAT/EXACT3D *versus* ECAT/ART

The expected increase in sensitivity by using PET tomographs in 3D mode instead of 2D mode has been verified experimentally by scanning the same phantoms in the ECAT 931 (CTI/Siemens, Knoxville, TN) tomograph with interplane septa in place and with interplane septa retracted (Townsend *et al*, 1989). Furthermode, when the acquisition time is adjusted such that the same number of events are detected in 2D and 3D modes with the ECAT 953B (CTI/Siemens, Knoxville, TN) tomograph, the data acquired in 3D mode were shown to be of comparable quantitative accuracy as those acquired in 2D mode (Sossi *et al*, 1998). This improvement in sensitivity without quantification loss can be exploited in a number of ways. For the same administered radioactive dose and acquisition time, the signal-to-noise ratio in the PET images can be greatly improved. This was the goal for developing the EXACT3D tomograph at the Cyclotron Unit of the Hammersmith Hospital where high-quality kinetic data are analysed to answer clinical research questions. Alternatively, the acquisition time can be reduced to the point where the image quality is maintained and the subject throughput increased. Without compromising image quality, the radioactive dose administered can be lowered in order to perform repeat scans on the same subjects. Another option is to decrease the number of detectors, hence decreasing the cost of the tomograph, and yet generate images of sufficient quality for clinical studies. It was for this last purpose that the Nuclear Medicine Department at the McMaster University Medical Centre purchased the ART tomograph.

A.1 The ECAT/EXACT3D

The EXACT3D is a 3D-only tomograph (Spinks *et al*, 2000). It is built with *high-resolution* BGO block detectors grooved into small eight by eight crystals, each measuring 4.39 mm×4.05 mm across and 30 mm deep. It is composed of six rings of 72 blocks, giving a long axial field of view of 23.4 cm. The reconstructed images thus contain 48 direct planes and 47 cross planes for a total of 95 slices. The ring diameter is 83 cm, allowing the subject aperture to be large enough for whole-body scans. The tomograph is shielded on either end of the FOV with 2.5 cm thick lead which extends for 8 mm inside the FOV. Additional lead shielding can be inserted to minimize the sensitivity to radioactivity arising from outside the field of view (Spinks *et al*, 1998). The data can be recorded in either sinogram or list modes. List mode acquisition provides a temporal resolution of milliseconds, efficient data storage, and the flexibility to rebin data post-acquisition. For the work presented in this thesis, the images are reconstructed using the 3D reprojection algorithm (Kinahan and Rogers, 1989) with a maximum ring difference of 40 ($\theta_{max} = 13.6°$) and a span of 9. Correction for random coincidences is performed on-line by subtracting the counts in the delayed coincidence time window set to 12 ns The model-based scatter correction of Watson *et al*(1996) was implemented. For attenuation correction, transmission scans are acquired in singles mode using a ^{137}Cs point source (150 MBq) that is wound into a helix through the axial field of view at a velocity of 1 m/s. The energy window is set to 350-650 keV and 500-800 keV for emission and transmission measurements, respectively.

A.2 The ECAT/ART

The ART is also a 3D-only tomograph (Bailey *et al*, 1997; Townsend *et al*, 1999). It consists of two detector arrays that are diametrically opposed to each other with an offset of 15°. Each detector array contains 33 *standard* BGO block detectors, eleven transaxially by three axially, and spans an arc of 83°. The axial field of view is 16.2 cm, about 2/3 of that of the ECAT3D. The *standard* BGO block detectors are cut into eight by eight crystals, each measuring 6.75 mm×6.75 mm across and 20 mm deep. The resulting crystals are larger in the transaxial dimensions than the ones of the high-resolution block detectors. The reconstructed images contain 47 slices, 24 direct planes and 23 cross planes. The ring diameter is 82 cm, similar to that of the ECAT3D tomograph. The detector arrays are

Table A.1: *Comparison of the performance of the ECAT/EXACT3D and ECAT/ART tomographs.*

Characteristics	EXACT3D[a]	ART[b]
Transaxial resolution (1 cm off-axis)	4.8 ±0.2 mm	6.4 ±0.1 mm
Axial resolution (on axis)	5.6 ±0.5mm	6.0 ±0.8mm
Scatter fraction	42%	34%
Sensitivity		
- cylindrical phantom	69 cps/Bq/ml	11.4 cps/Bq/ml[c]
- line source in air	5.8%	1.0%
Count rate (peak NEC)	11 kBq/ml (80MBq)	15 kBq/ml

[a] Data extracted from Spinks *et al*(2000).

[b] Data extracted from Bailey *et al*(1997).

[c] Not scatter corrected.

shielded on both sides with 2.5 cm thick lead that projects 8.5 cm into the FOV. The detector arrays and shielding rotate continuously over 360° at 30 rpm and their position is monitored by an optical encoder. The full set of 3D LORs can hence be collected and assigned to the correct sinogram locations. This speed of rotation limits the temporal resolution to 2 sec. The data are acquired in sinogram mode only and reconstructed using the 3D reprojection algorithm (Kinahan and Rogers, 1989) with a maximum ring difference of 17 ($\theta_{max} = 8.0°$) and a span of 7. Random coincidences are corrected for by subtracting counts in delayed coincidence time window set to 12 ns. As for the ECAT3D tomograph, the model-based scatter correction of Watson *et al*(1996) was implemented. The attenuation correction is done with a transmission scan acquired in singles mode using two collimated ^{137}Cs point sources (555 MBq), each fixed at the end of a detector array (Townsend *et al*, 1999). The transmission sources rotate along side with the detector arrays, and hence are only propelled axially. The energy window is set to the sames values as for the ECAT3D: 350-650 keV and 500-800 keV for emission and transmission measurements, respectively.

A.3 Comparison of Performance

Published results of the NEMA/SNM tests performed on the EXACT3D and ART tomographs are summarized in **Table A.1**. The EXACT3D tomograph generates images

with a higher spatial resolution, both transaxially and axially, than the ART tomograph. This is achieved by reducing the crystal face dimensions. However, the smaller crystals suffer from poorer geometric detection efficiency. The noise in the corresponding LORs increases and propagates to voxel values in the reconstructed images. Adding rings of block detectors overcomes the increase in noise by increasing the number of LORs, thereby introducing more redundancy in the 3D dataset. The main intention behind doubling the number of rings however was to maximize the sensitivity of the EXACT3D tomograph, which is about six times greater than that of the ART tomograph. As a result, the EXACT3D produces images with less variance than the ART. The EXACT3D is also more sensitive to scatter events as reflected by its larger scatter fraction compared to the ART. The quantitative accuracy of the EXACT3D images thus depends even more than the ART images on the accuracy of the scatter correction method. The higher sensitivity of the EXACT3D imposes a more stringent limit than the ART on the radiactive dose when high desintegration rates are being measured. As depicted in **Figure A.1**, the uniformity of the EXACT3D is slightly worse than that of the ART, the former being just above 10% and the latter just below 10%, provided that the ten extreme planes on either side are excluded from the image analyses. Overall, the EXACT3D is a superior tomograph than the ART for imaging small objects containing low radioactivity concentrations.

a)

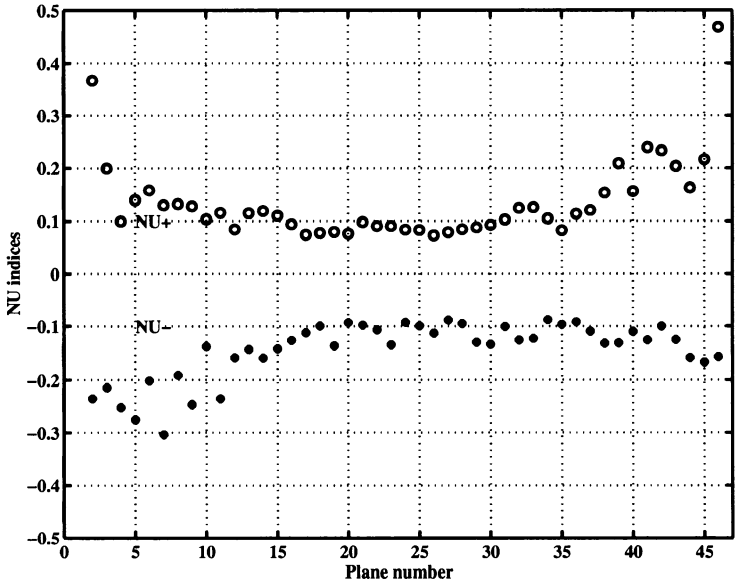

b)

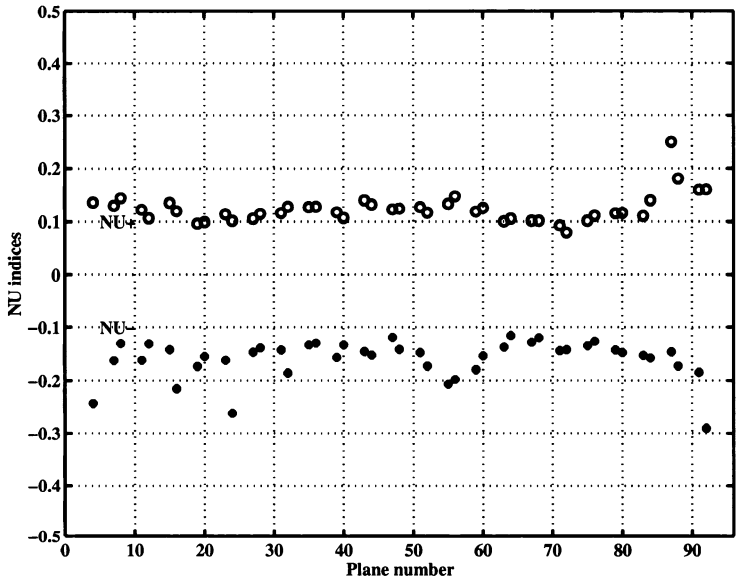

Figure A.1: *Results of NEMA/SNM uniformity test for* **a)** *the ECAT/ART and* **b)** *the ECAT/EXACT3D tomographs.*

Appendix B

Catalog of Solutions to Compartmental Models with a Plasma Input Function

B.1 One-compartment two-rate constant model

This model is typically used for reference tissue, i.e. tissue in which no specific binding or metabolism of the radiotracer occurs.

Formulation

$$\frac{dC_t}{dt} = -k_2 C_t(t) + K_1 C_p(t), \tag{B.1}$$

where $C_p(t)$ is the concentration of the radiotracer in plasma and K_1, the fraction of the plasma concentration that enters the first compartment per unit time. The units of K_1 are [(ml of tissue)(ml of plasma)$^{-1}$min^{-1}] so that the product $K_1 C_p(t)$ gives the rate of influx of the radiotracer to the first compartment, the input function.

Operational Equation

Direct integration of the homogeneous differential equation yields

$$C_t(t) = C_t(0) \exp -k_2 t. \tag{B.2}$$

Solving for the initial condition $C_t(0) = 1$,

$$C_t(t) = \exp(-k_2 t). \tag{B.3}$$

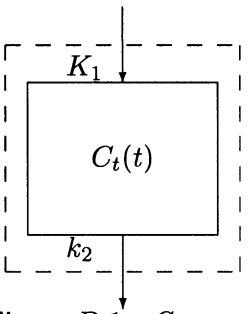

Figure B.1: *Compartmental model describing the uptake of the radiotracer in the target tissue ($C_t(t)$): K_1 is the rate constant for the influx from the plasma to the tissue while k_2 is the rate constant for the backflux from the tissue to the plasma.*

Convolving with the input function yields

$$y(t) = \exp(-k_2 t) \otimes K_1 C_p(t). \tag{B.4}$$

Volume of Distribution

After steady state has been reached,

$$\frac{dC_t}{dt} = 0 \;\Rightarrow\; k_2 C_t(t) = K_1 C_p(t)$$
$$VD = \frac{C_t(t)}{C_p(t)} = \frac{K_1}{k_2}. \tag{B.5}$$

Linearisation

Integrating equation (B.1) with $C_t(0) = 0$,

$$C_t(t) = K_1 \int C_p(t)dt - k_2 \int C_t(t)dt \tag{B.6}$$

Dividing each term by $C_t(t)$ and rearranging,

$$1 = K_1 \frac{\int C_p(t)dt}{C_t(t)} - k_2 \frac{\int C_t(t)dt}{C_t(t)} \tag{B.7}$$

$$\frac{\int C_t(t)dt}{C_t(t)} = \frac{K_1}{k_2} \frac{\int C_p(t)dt}{C_t(t)} - \frac{1}{k_2}. \tag{B.8}$$

A Logan plot of $\frac{\int_0^t C_t(T)dT}{C_t(t)}$ vs. $\frac{\int_0^t C_p(T)dT}{C_t(t)}$ will give at all times a straight line with a slope of $VD = \frac{K_1}{k_2}$ and a negative y-intercept of $-\frac{1}{k_2}$.

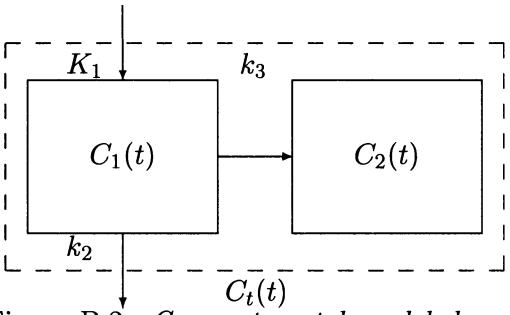

Figure B.2: *Compartmental model describing the uptake of the radiotracer in the target tissue ($C_t(t)$): K_1 is the rate constant for the influx from the plasma to the tissue while k_2 is the rate constant for the backflux from the tissue to the plasma; and k_3 is the rate constant representing the metabolism of the parent radiotracer in the tissue. The metabolites are assumed to be trapped in the tissue for the duration of the study.*

B.2 Two-compartment three-rate constant model

This is the simplest model that can describe trapping of the radiotracer in a tissue. Both compartments have the same volume, allowing for the differential equations to be written in terms of concentrations.

Formulation

$$\frac{dC_1}{dt} = -(k_2 + k_3)C_1(t) + K_1 C_p(t) \tag{B.9a}$$

$$\frac{dC_2}{dt} = k_3 C_1(t) \tag{B.9b}$$

Operational Equation

Rewriting equations (B.9a) and (B.9b) in matrix form,

$$\begin{pmatrix} \dot{C}_1 \\ \dot{C}_2 \end{pmatrix} = \begin{pmatrix} -k_2 - k_3 & 0 \\ k_3 & 0 \end{pmatrix} \begin{pmatrix} C_1 \\ C_2 \end{pmatrix} + \begin{pmatrix} K_1 C_p(t) \\ 0 \end{pmatrix}. \tag{B.10}$$

The roots of the characteristic polynomial $\lambda(k_2 + k_3 + \lambda) = 0$ correspond to the system eigenvalues $\lambda_1 = 0$ and $\lambda_2 = -(k_2 + k_3)$. The homogeneous solution to equation (B.10) can then be found from the system eigenvectors:

$$\begin{pmatrix} C_1 \\ C_2 \end{pmatrix} = c_1 \begin{pmatrix} 0 \\ 1 \end{pmatrix} + c_2 \begin{pmatrix} 1 \\ \frac{-k_3}{k_2+k_3} \end{pmatrix} \exp\big(-(k_2 + k_3)t\big). \tag{B.11}$$

Incorporating the initial conditions $C_1(0) = 1$ and $C_2(0) = 0$, equation (B.11) becomes

$$C_1(t) = \exp\big(-(k_2 + k_3)t\big) \tag{B.12a}$$

$$C_2(t) = \left(\frac{k_3}{k_2 + k_3}\right)\Big[1 - \exp\big(-(k_2 + k_3)t\big)\Big]. \tag{B.12b}$$

The total concentration in the tissue is then found to be

$$\begin{aligned} C_t(t) &= C_1(t) + C_2(t) \\ &= \left(\frac{1}{k_2 + k_3}\right)\Big[k_3 + k_2 \exp\big(-(k_2 + k_3)t\big)\Big], \end{aligned} \tag{B.13}$$

which can finally be convolved with the input function to yield the solution to the non-homogeneous equation:

$$y(t) = \left(\frac{1}{k_2 + k_3}\right)\Big[k_3 + k_2 \exp\big(-(k_2 + k_3)t\big)\Big] \otimes K_1 C_p(t). \tag{B.14}$$

Volume of Distribution

Under steady-state conditions, the distribution volume of the first compartment is given by

$$\begin{aligned} \frac{dC_1}{dt} = 0 \;\Rightarrow\; K_1 C_p(t) &= (k_2 + k_3) C_1(t) \\ VD_1 = \frac{C_1(t)}{C_p(t)} &= \frac{K_1}{k_2 + k_3}. \end{aligned} \tag{B.15}$$

Linearisation

Integrating equations (B.9a) and (B.9b) with $C_1(0) = C_2(0) = 0$,

$$C_1(t) = K_1 \int C_p(t)dt - (k_2 + k_3) \int C_1(t)dt \tag{B.16a}$$

$$C_2(t) = k_3 \int C_1(t)dt \;\Rightarrow\; \int C_1(t)dt = \frac{1}{k_3} C_2(t). \tag{B.16b}$$

Inserting equation (B.16b) into equation (B.16a) and isolating $C_2(t)$,

$$C_2(t) = \frac{K_1 k_3}{k_2 + k_3} \int C_p(t)dt - \frac{k_3}{k_2 + k_3} C_1(t). \tag{B.17}$$

Adding $C_1(t)$ to the above expression for $C_2(t)$ and dividing the sum by $C_p(t)$,

$$\frac{C_1(t) + C_2(t)}{C_p(t)} = \left(\frac{K_1 k_3}{k_2 + k_3}\right) \frac{\int C_p(t)dt}{C_p(t)} + \left(\frac{k_2}{k_2 + k_3}\right) \frac{C_1(t)}{C_p(t)}. \tag{B.18}$$

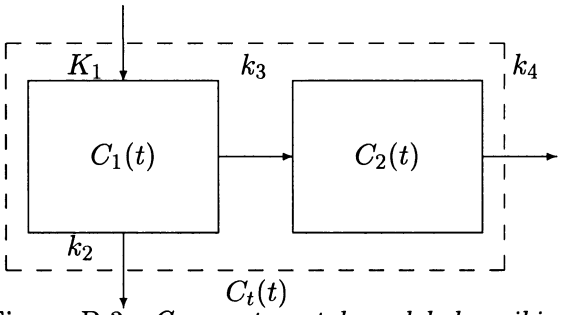

Figure B.3: *Compartmental model describing the uptake of the radiotracer in the target tissue ($C_t(t)$): K_1 is the rate constant for the influx from the plasma to the tissue while k_2 is the rate constant for the backflux from the tissue to the plasma; k_3 is the rate constant representing the metabolism of the parent radiotracer in the tissue; and k_4 is the rate constant for the outflux of the metabolites from the tissue.*

After a time t*, the first compartment (C_1) will be in effective steady state with the plasma (C_p), such that

$$\frac{C_1(t > t^*)}{C_p(t > t^*)} = VD_1 = \frac{K_1}{k_2 + k_3}. \tag{B.19}$$

Equation (B.18) therefore becomes

$$\frac{C_t(t)}{C_p(t)} = \left(\frac{K_1}{k_2 + k_3}\right) k_3 \frac{\int_0^t C_p(T)dT}{C_p(t)} + \frac{K_1 k_2}{(k_2 + k_3)^2}. \tag{B.20}$$

A Patlak plot of $\frac{C_t(t)}{C_p(t)}$ vs. $\frac{\int_0^t C_p(T)dT}{C_p(t)}$ will approach a straight line with a slope of VD_1k_3 and a positive y-intercept of $\frac{K_1k_2}{(k_2+k_3)^2}$ for all times t>t*.

B.3 Two-compartment four-rate constant irreversible model

The previous model is modified here to include a leak from the irreversible compartment ($C_2(t)$) to the exterior environment.

Formulation

$$\frac{dC_1}{dt} = -(k_2 + k_3)C_1(t) + K_1C_p(t) \tag{B.21a}$$

$$\frac{dC_2}{dt} = k_3C_1(t) - k_4C_2(t) \tag{B.21b}$$

Operational Equation

Rewriting equations (B.21a) and (B.21b) in matrix form,

$$\begin{pmatrix}\dot{C}_1\\ \dot{C}_2\end{pmatrix} = \begin{pmatrix}-k_2-k_3 & 0\\ k_3 & -k_4\end{pmatrix}\begin{pmatrix}C_1\\ C_2\end{pmatrix} + \begin{pmatrix}K_1C_p(t)\\ 0\end{pmatrix}. \tag{B.22}$$

The roots of the characteristic polynomial $(k_4+\lambda)(k_2+k_3+\lambda)=0$ correspond to the system eigenvalues $\lambda_1=-k_4$ and $\lambda_2=-(k_2+k_3)$. The homogeneous solution to equation (B.22) can then be found from the system eigenvectors:

$$\begin{pmatrix}C_1\\ C_2\end{pmatrix} = c_1\begin{pmatrix}0\\ 1\end{pmatrix}\exp\left(-k_4t\right) + c_2\begin{pmatrix}1\\ \frac{-k_3}{k_2+k_3-k_4}\end{pmatrix}\exp\big(-(k_2+k_3)t\big). \tag{B.23}$$

Incorporating the initial conditions $C_1(0)=1$ and $C_2(0)=0$, equation (B.23) becomes

$$C_1(t) = \exp\big(-(k_2+k_3)t\big) \tag{B.24a}$$

$$C_2(t) = \left(\frac{k_3}{k_2+k_3-k_4}\right)\Big[\exp\left(-k_4t\right) - \exp\left(-(k_2+k_3)t\right)\Big]. \tag{B.24b}$$

The total concentration in the tissue is then found to be

$$\begin{aligned} C_t(t) &= C_1(t) + C_2(t)\\ &= \left(\frac{1}{k_2+k_3-k_4}\right)\Big[k_3\exp\left(-k_4t\right) + (k_2-k_4)\exp\big(-(k_2+k_3)t\big)\Big], \end{aligned} \tag{B.25}$$

which can finally be convolved with the input function to yield the solution to the non-homogeneous equation:

$$y(t) = \left(\frac{1}{k_2+k_3-k_4}\right)\Big[k_3\exp\left(-k_4t\right) + (k_2-k_4)\exp\big(-(k_2+k_3)t\big)\Big] \otimes K_1C_p(t). \tag{B.26}$$

It is important to note that the solution to this model is not unique. Redefining the rate constants as

$$k_2' = k_2 \tag{B.27a}$$

$$k_3' = k_4 - k_2 \tag{B.27b}$$

$$k_4' = k_2 + k_3 \tag{B.27c}$$

simply leads to an exchange of the exponential terms (the A's and λ's are inverted):

$$y(t) = \left(\frac{1}{k_4'-k_3'-k_2'}\right)\Big[(k_4'-k_2')\exp\left(-(k_3'+k_2')t\right) - k_3'\exp\big(-k_4't\big)\Big] \otimes K_1C_p(t). \tag{B.28}$$

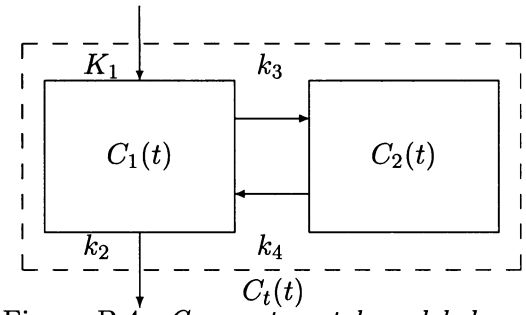

Figure B.4: *Compartmental model describing the uptake of the radiotracer in the target tissue ($C_t(t)$): K_1 is the rate constant for the influx from the plasma to the tissue while k_2 is the rate constant for the backflux from the tissue to the plasma; k_3 and k_4 represent the rate constants of association and disassociation, respectively, of the radiotracer to and from the receptors in the tissue.*

This means that the response of the total system remains the same with either combination of parameters despite the fact that the contribution of the two compartments to the total system response has changed. In practice, the ambiguity can be resolved by either measuring each compartment individually or by adding *a priori* information.

B.4 Two-compartment four-rate constant reversible model

This model describes the reversible binding or metabolism of the radiotracer following its delivery to a tissue. The differential equations can again be written in terms of concentrations since the radiotracer remains in the same volume.

Formulation

$$\frac{dC_1}{dt} = -(k_2 + k_3)C_1(t) + k_4 C_2(t) + K_1 C_p(t) \tag{B.29a}$$

$$\frac{dC_2}{dt} = k_3 C_1(t) - k_4 C_2(t) \tag{B.29b}$$

Operational Equation

Rewriting equations (B.29a) and (B.29b) in matrix form,

$$\begin{pmatrix} \dot{C}_1 \\ \dot{C}_2 \end{pmatrix} = \begin{pmatrix} -k_2 - k_3 & k_4 \\ k_3 & -k_4 \end{pmatrix} \begin{pmatrix} C_1 \\ C_2 \end{pmatrix} + \begin{pmatrix} K_1 C_p(t) \\ 0 \end{pmatrix}. \tag{B.30}$$

The roots of the characteristic polynomial $\lambda^2 + (k_2 + k_3 + k_4)\lambda + k_2k_4 = 0$ correspond to the system eigenvalues:

$$\lambda_1 = -\frac{1}{2}(k_2 + k_3 + k_4) + \frac{1}{2}\sqrt{(k_2 + k_3 + k_4)^2 - 4k_2k_4} \tag{B.31a}$$

$$\lambda_2 = -\frac{1}{2}(k_2 + k_3 + k_4) - \frac{1}{2}\sqrt{(k_2 + k_3 + k_4)^2 - 4k_2k_4}. \tag{B.31b}$$

The homogeneous solution to equation (B.30) can then be found from the system eigenvectors:

$$\begin{pmatrix} C_1 \\ C_2 \end{pmatrix} = c_1 \begin{pmatrix} \frac{\lambda_1}{\lambda_1 + k_2} \\ -1 \end{pmatrix} \exp(\lambda_1 t) + c_2 \begin{pmatrix} \frac{\lambda_2}{\lambda_2 + k_2} \\ -1 \end{pmatrix} \exp(\lambda_2 t). \tag{B.32}$$

Incorporating the initial conditions $C_1(0) = 1$ and $C_2(0) = 0$, equation (B.32) becomes

$$C_1(t) = \frac{1}{\lambda_1 - \lambda_2}[(\lambda_1 + k_4)\exp(\lambda_1 t) - (\lambda_2 + k_4)\exp(\lambda_2 t)] \tag{B.33a}$$

$$C_2(t) = \frac{k_3}{\lambda_1 - \lambda_2}[\exp(\lambda_1 t) - \exp(\lambda_2 t)], \tag{B.33b}$$

after using $\lambda_1\lambda_2 = k_2k_4$ and $\lambda_1 + \lambda_2 = -(k_2 + k_3 + k_4)$. The total concentration in the tissue is then found to be

$$\begin{aligned} C_t(t) &= C_1(t) + C_2(t) \\ &= \frac{1}{\lambda_1 - \lambda_2}[(\lambda_1 + k_3 + k_4)\exp(\lambda_1 t) - (\lambda_2 + k_3 + k_4)\exp(\lambda_2 t)], \end{aligned} \tag{B.34}$$

which can finally be convolved with the input function to yield the solution to the non-homogeneous equation:

$$y(t) = \frac{1}{\lambda_1 - \lambda_2}[(\lambda_1 + k_3 + k_4)\exp(\lambda_1 t) - (\lambda_2 + k_3 + k_4)\exp(\lambda_2 t)] \otimes K_1C_p(t). \tag{B.35}$$

Volume of Distribution

Under steady-state conditions, the distribution volumes of each compartment and of the total compartmental system are given by

$$\frac{dC_1}{dt} = 0 \;\Rightarrow\; K_1C_p(t) = (k_2 + k_3)C_1(t) - k_4C_2(t) \tag{B.36a}$$

$$\frac{dC_2}{dt} = 0 \;\Rightarrow\; k_3C_1(t) = k_4C_2(t) \tag{B.36b}$$

$$VD_1 = \frac{C_1(t)}{C_p(t)} = \frac{K_1}{k_2} \tag{B.37}$$

$$VD_2 = \frac{C_2(t)}{C_p(t)} = \frac{k_3}{k_4}\frac{C_1(t)}{C_p(t)} = \frac{k_3}{k_4}\frac{K_1}{k_2} \tag{B.38}$$

$$VD = \frac{C_1(t) + C_2(t)}{C_p(t)} = \frac{K_1}{k_2}\left(1 + \frac{k_3}{k_4}\right). \tag{B.39}$$

Linearisation

Integrating equations (B.29a) and (B.29b) with $C_1(0) = C_2(0) = 0$,

$$C_1(t) = K_1 \int C_p(t)dt - (k_2 + k_3) \int C_1(t)dt + k_4 \int C_2(t)dt \tag{B.40a}$$

$$C_2(t) = k_3 \int C_1(t)dt - k_4 \int C_2(t)dt. \tag{B.40b}$$

Isolating $\int C_2(t)dt$ from equation (B.40b),

$$\int C_2(t)dt = \frac{k_3}{k_4} \int C_1(t)dt - \frac{1}{k_4}C_2(t). \tag{B.41}$$

Inserting it into equation (B.40a),

$$C_1(t) = K_1 \int C_p(t)dt - k_2 \int C_1(t)dt - C_2(t). \tag{B.42}$$

Isolating $\int C_1(t)dt$ from equation (B.42),

$$\int C_1(t)dt = \frac{K_1}{k_2} \int C_p(t)dt - \frac{1}{k_2}[C_1(t) + C_2(t)]. \tag{B.43}$$

Inserting it into equation (B.41),

$$\int C_2(t)dt = \frac{K_1}{k_2}\frac{k_3}{k_4} \int C_p(t)dt - \frac{k_3}{k_2k_4}[C_1(t) + C_2(t)] - \frac{1}{k_4}C_2(t). \tag{B.44}$$

Adding equations (B.43) and (B.44),

$$\int C_1(t)dt + \int C_2(t)dt = \frac{K_1}{k_2}\left(1 + \frac{k_3}{k_4}\right) \int C_p(t)dt - \frac{k_3 - k_4}{k_2k_4}[C_1(t) + C_2(t)] - \frac{1}{k_4}C_2(t). \tag{B.45}$$

Dividing the last equation by the sum $C_1(t) + C_2(t)$,

$$\frac{\int C_1(t)dt + \int C_2(t)dt}{C_1(t) + C_2(t)} = \frac{K_1}{k_2}\left(1 + \frac{k_3}{k_4}\right)\frac{\int C_p(t)dt}{C_1(t) + C_2(t)} - \frac{k_3 - k_4}{k_2k_4} - \frac{1}{k_4}\frac{C_2(t)}{C_1(t) + C_2(t)}. \tag{B.46}$$

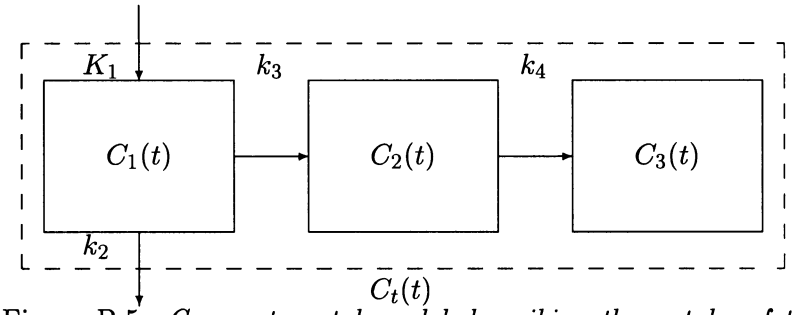

Figure B.5: *Compartmental model describing the uptake of the radiotracer in the target tissue ($C_t(t)$): K_1 is the rate constant for the influx from the plasma to the tissue while k_2 is the rate constant for the backflux from the tissue to the plasma; k_3 is the rate constant representing the metabolism of the parent radiotracer into its first metabolite in the tissue; and k_4 is the rate constant representing the metabolism of the first metabolite into the second metabolite in the tissue. The metabolites are assumed to be trapped in the tissue for the duration of the study.*

After a time t*, the two compartments (C_1 and C_2) will have reached effective steady state with the plasma (C_p) such that

$$\frac{C_2(t > t^*)}{C_1(t > t^*) + C_2(t > t^*)} = \frac{VD_2}{VD} = \frac{k_3}{k_3 + k_4}. \tag{B.47}$$

Equation(B.46) therefore becomes

$$\frac{\int_0^t C_t(T)dT}{C_t(t)} = \frac{K_1}{k_2}\left(1 + \frac{k_3}{k_4}\right)\frac{\int_0^t C_p(T)dT}{C_t(t)} - \frac{1}{k_4}\left[\frac{k_3 + k_4}{k_2} + \frac{k_3}{k_3 + k_4}\right]. \tag{B.48}$$

A Logan plot of $\frac{\int_0^t C_t(T)dT}{C_t(t)}$ vs. $\frac{\int_0^t C_p(T)dT}{C_t(t)}$ will approach a straight line with a slope of $VD = \frac{K_1}{k_2}\left(1 + \frac{k_3}{k_4}\right)$ and a negative y-intercept for all times t>t*.

B.5 Three-compartment four-rate constant model

An additional compartment is inserted between the first and the irreversible compartments to include an intermediate step in the pathway of the radiotracer prior its trapping in a tissue. Again, the differential equations can be written in terms of concentrations.

Formulation

$$\frac{dC_1}{dt} = -(k_2 + k_3)C_1(t) + K_1C_p(t) \tag{B.49a}$$

$$\frac{dC_2}{dt} = k_3C_1(t) - k_4C_2(t) \tag{B.49b}$$

$$\frac{dC_3}{dt} = k_4C_2(t) \tag{B.49c}$$

Operational Equation

Rewriting equations (B.49a), (B.49b) and (B.49c) in matrix form,

$$\begin{pmatrix} \dot{C}_1 \\ \dot{C}_2 \\ \dot{C}_3 \end{pmatrix} = \begin{pmatrix} -k_2 - k_3 & 0 & 0 \\ k_3 & -k_4 & 0 \\ 0 & k_4 & 0 \end{pmatrix} \begin{pmatrix} C_1 \\ C_2 \\ C_3 \end{pmatrix} + \begin{pmatrix} K_1C_p(t) \\ 0 \\ 0 \end{pmatrix}. \tag{B.50}$$

The roots of the characteristic polynomial $-(k_2 + k_3 + \lambda)(k_4 + \lambda)\lambda = 0$ correspond to the system eigenvalues $\lambda_1 = 0$, $\lambda_2 = -k_4$ and $\lambda_3 = -(k_2 + k_3)$. The homogeneous solution to equation (B.50) can then be found from the system eigenvectors:

$$\begin{pmatrix} C_1 \\ C_2 \\ C_3 \end{pmatrix} = c_1 \begin{pmatrix} 0 \\ 0 \\ 1 \end{pmatrix} + c_2 \begin{pmatrix} 0 \\ 1 \\ -1 \end{pmatrix} \exp(-k_4t) + c_3 \begin{pmatrix} 1 \\ \frac{-k_3}{k_2+k_3-k_4} \\ \frac{k_3k_5}{(k_2+k_3)(k_2+k_3-k_4)} \end{pmatrix} \exp(-(k_2 + k_3)t). \tag{B.51}$$

Incorporating the initial conditions $C_1(0) = 1$, $C_2(0) = 0$ and $C_3(0) = 0$, equation (B.51) becomes

$$C_1(t) = \exp(-(k_2 + k_3)t) \tag{B.52a}$$

$$C_2(t) = \frac{k_3}{k_2 + k_3 - k_4}[\exp(-k_4t) - \exp(-(k_2 + k_3)t)] \tag{B.52b}$$

$$\begin{aligned} C_3(t) = {} & \frac{k_3}{k_2 + k_3} - \frac{k_3}{k_2 + k_3 - k_4} \exp(-k_4t) \\ & + \frac{k_3k_5}{(k_2 + k_3)(k_2 + k_3 - k_4)} \exp(-(k_2 + k_3)t). \end{aligned} \tag{B.52c}$$

The total concentration in the tissue is then found to be

$$\begin{aligned} C_t(t) &= C_1(t) + C_2(t) + C_3(t) \\ &= \frac{1}{k_2 + k_3}[k_3 + k_2 \exp(-(k_2 + k_3)t)], \end{aligned} \tag{B.53}$$

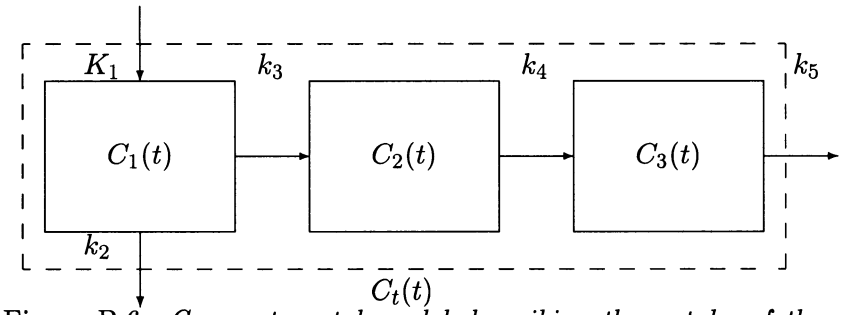

Figure B.6: *Compartmental model describing the uptake of the radiotracer in the target tissue ($C_t(t)$): K_1 is the rate constant for the influx from the plasma to the tissue while k_2 is the rate constant for the backflux from the tissue to the plasma; k_3 is the rate constant representing the metabolism of the parent radiotracer into its first metabolite in the tissue; k_4 is the rate constant representing the metabolism of the first metabolite into the second metabolite in the tissue; and k_5 is the rate constant for the outflux of the metabolites from the tissue.*

which can finally be convolved with the input function to yield the solution to the non-homogeneous equation:

$$y(t) = \frac{1}{k_2 + k_3}[k_3 + k_2 \exp\left(-(k_2 + k_3)t\right)] \otimes K_1 C_p(t). \tag{B.54}$$

Notice that equations (B.53) and (B.54) are identical to equations (B.13) and (B.14), respectively. This implies that three-compartment four-rate constant model and the two-compartment three-rate constant model cannot be distinguished from the measurement of the total concentration in the system, unless one or more of the compartments are measured individually. Furthermore, the rate constant describing the efflux from the first compartment (k_3) can be determined, but not that from the middle compartment (k_4).

B.6 Three-compartment five-rate constant model

The radiotracer is now allowed to leak from the irreversible compartment ($C_3(t)$) to the exterior environment.

Formulation

$$\frac{dC_1}{dt} = -(k_2 + k_3)C_1(t) + K_1C_p(t) \tag{B.55a}$$

$$\frac{dC_2}{dt} = k_3C_1(t) - k_4C_2(t) \tag{B.55b}$$

$$\frac{dC_3}{dt} = k_4C_2(t) - k_5C_3(t) \tag{B.55c}$$

Operational Equation

Rewriting equations (B.55a), (B.55b) and (B.55c) in matrix form,

$$\begin{pmatrix} \dot{C}_1 \\ \dot{C}_2 \\ \dot{C}_3 \end{pmatrix} = \begin{pmatrix} -k_2 - k_3 & 0 & 0 \\ k_3 & -k_4 & 0 \\ 0 & k_4 & -k_5 \end{pmatrix} \begin{pmatrix} C_1 \\ C_2 \\ C_3 \end{pmatrix} + \begin{pmatrix} K_1C_p(t) \\ 0 \\ 0 \end{pmatrix}. \tag{B.56}$$

The roots of the characteristic polynomial $-(k_2 + k_3 + \lambda)(k_4 + \lambda)(\lambda + k_5) = 0$ correspond to the system eigenvalues $\lambda_1 = -k_5$, $\lambda_2 = -k_4$ and $\lambda_3 = -(k_2 + k_3)$. The homogeneous solution to equation (B.56) can then be found from the system eigenvectors:

$$\begin{aligned} \begin{pmatrix} C_1 \\ C_2 \\ C_3 \end{pmatrix} = c_1 \begin{pmatrix} 0 \\ 0 \\ 1 \end{pmatrix} \exp(-k_5t) + c_2 \begin{pmatrix} 0 \\ 1 \\ \frac{-k_5}{k_4-k_5} \end{pmatrix} \exp(-k_4t) \\ + c_3 \begin{pmatrix} 1 \\ \frac{-k_3}{k_2+k_3-k_4} \\ \frac{k_3k_5}{(k_2+k_3-k_5)(k_2+k_3-k_4)} \end{pmatrix} \exp(-(k_2 + k_3)t). \end{aligned} \tag{B.57}$$

Incorporating the initial conditions $C_1(0) = 1$, $C_2(0) = 0$ and $C_3(0) = 0$, equation (B.57) becomes

$$C_1(t) = \exp(-(k_2 + k_3)t) \tag{B.58a}$$

$$C_2(t) = \frac{k_3}{k_2 + k_3 - k_4}[\exp(-k_4t) - \exp(-(k_2 + k_3)t)] \tag{B.58b}$$

$$\begin{aligned} C_3(t) = \frac{k_3k_4}{(k_4 - k_5)(k_2 + k_3 - k_5)} \exp(-k_5t) - \frac{k_3k_4}{(k_4 - k_5)(k_2 + k_3 - k_4)} \exp(-k_4t) \\ + \frac{k_3k_4}{(k_2 + k_3 - k_5)(k_2 + k_3 - k_4)} \exp(-(k_2 + k_3)t). \end{aligned} \tag{B.58c}$$

The total concentration in the tissue is then found to be

$$\begin{aligned} C_t(t) &= C_1(t) + C_2(t) + C_3(t) \\ &= \frac{k_3k_4}{(k_4 - k_5)(k_2 + k_3 - k_5)} \exp(-k_5t) - \frac{k_3k_5}{(k_4 - k_5)(k_2 + k_3 - k_4)} \exp(-k_4t) \\ &+ \frac{(k_2 + k_3 - k_4 - k_5)k_2 + k_4k_5}{(k_2 + k_3 - k_5)(k_2 + k_3 - k_4)} \exp(-(k_2 + k_3)t), \end{aligned} \tag{B.59}$$

which can finally be convolved with the input function to yield the solution to the non-homogeneous equation:

$$y(t) = \left[\frac{k_3 k_4}{(k_4 - k_5)(k_2 + k_3 - k_5)} \exp(-k_5 t) - \frac{k_3 k_5}{(k_4 - k_5)(k_2 + k_3 - k_4)} \exp(-k_4 t) + \frac{(k_2 + k_3 - k_4 - k_5)k_2 + k_4 k_5}{(k_2 + k_3 - k_5)(k_2 + k_3 - k_4)} \exp(-(k_2 + k_3)t) \right] \otimes K_1 C_p(t). \tag{B.60}$$

Appendix C

Catalog of Solutions to Compartmental Models with a Reference Tissue Input Function

C.1 Two-compartment four-rate constant reversible target tissue with a reversible reference tissue model

Formulation

In the target tissue:

$$\frac{dC_1}{dt} = -(k_2 + k_3)C_1(t) + k_4 C_2(t) + K_1 C_p(t) \tag{C.1a}$$

$$\frac{dC_2}{dt} = k_3 C_1(t) - k_4 C_2(t) \tag{C.1b}$$

In the reference tissue:

$$\frac{dC_r}{dt} = -k_2' C_r(t) + K_1' C_p(t) \tag{C.2}$$

Operational Equation

Replacing in equation (2.57) the expressions for the A_i and λ_i given in equation (B.34),

$$\begin{aligned} y(t) = R_1 C_r(t) + R_1 C_r(t) \otimes \Bigg[& \frac{(\lambda_1 + k_3 + k_4)(\frac{k_2'}{R_1} + \lambda_1)}{\lambda_1 - \lambda_2} \exp(\lambda_1 t) \\ & - \frac{(\lambda_2 + k_3 + k_4)(\frac{k_2'}{R_1} + \lambda_2)}{\lambda_1 - \lambda_2} \exp(\lambda_2 t) \Bigg], \end{aligned} \tag{C.3}$$

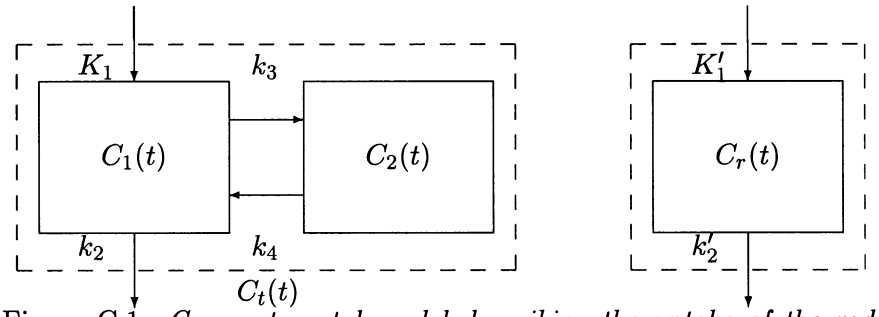

Figure C.1: *Compartmental model describing the uptake of the radiotracer in the target tissue ($C_t(t)$) relative to that in a reference tissue ($C_r(t)$): K_1 is the rate constant for the influx from the plasma to the target tissue while k_2 is the rate constant for the backflux from the target tissue to the plasma; k_3 and k_4 represent the rate constants of association and disassociation, respectively, of the radiotracer to and from the receptors in the reference tissue; K_1' is the rate constant for the influx from the plasma to the reference tissue while k_2' is the rate constant for the backflux from the reference tissue to the plasma.*

where $R_1 = K_1/K_1'$.

Alternatively, one can derive equation (C.3) from equations (C.1a), (C.1b) and (C.2) using the Laplace transform $\mathcal{L}\{\dot{C}(t)\} = s\mathcal{L}\{C(t)\} - C(0)$ and the inverse Laplace transform $\mathcal{L}^{-1}\{\frac{1}{s-k}\} = exp^{kt}$ with the identity $K_1/k_2 = K_1'/k_2'$ and the equivalence

$$\frac{s^2}{(s-\lambda_1)(s-\lambda_2)} = \frac{(s-\lambda_1)(s-\lambda_2)}{(s-\lambda_1)(s-\lambda_2)} + \frac{s(\lambda_1+\lambda_2)-\lambda_1\lambda_2}{(s-\lambda_1)(s-\lambda_2)}, \tag{C.4}$$

where s is the variable in Laplace space. Using Laplace transforms, coupled differential equations with constant coefficients are transformed into a system of linear algebraic equations which can be solved more easily. In particular, this approach simplifies the expression of the plasma input function as a function of the concentration in the reference tissue since the deconvolution operation in time space becomes a division in Laplace space.

Linearisation

Integrating equations (C.2) with $C_r(0) = 0$,

$$C_r(t) = K_1' \int C_p(t)dt - k_2' \int C_r(t)dt. \tag{C.5}$$

Expressing $\int C_p(t)dt$ in terms of $C_r(t)$ using equation (C.5),

$$\int C_p(t)dt = \frac{1}{K_1'}C_r(t) + \frac{k_2'}{K_1'}\int C_r(t)dt. \tag{C.6}$$

Inserting equation (C.6) into equation (B.48) and rearranging,

$$\frac{\int_0^t C_t(T)dT}{C_t(t)} = \frac{K_1}{k_2}\left(1+\frac{k_3}{k_4}\right)\frac{k_2'}{K_1'}\frac{\int_0^t C_r(T)dT + \frac{1}{k_2'}C_r(t)}{C_t(t)} - \frac{1}{k_4}\left[\frac{k_3+k_4}{k_2} + \frac{k_3}{k_3+k_4}\right]. \tag{C.7}$$

A Logan plot of $\frac{\int_0^t C_t(T)dT}{C_t(t)}$ vs. $\frac{\int_0^t C_r(T)dT}{C_t(t)}$ — assuming a fast washout from the reference tissue or a large k_2' — will approach a straight line with a slope of $\frac{VD_t}{VD_r}$ and a negative y-intercept for all times t>t*.

C.2 Two-compartment three-rate constant target tissue with a reversible reference tissue model

Formulation

In the target tissue:

$$\frac{dC_1}{dt} = -(k_2+k_3)C_1(t) + K_1C_p(t) \tag{C.8a}$$

$$\frac{dC_2}{dt} = k_3C_1(t) \tag{C.8b}$$

In the reference tissue:

$$\frac{dC_r}{dt} = -k_2'C_r(t) + K_1'C_p(t) \tag{C.9}$$

Operational Equation

The total concentration in the target tissue can be found by simply setting $k_4 = 0$ in equations (C.3), (B.31a) and (B.31b):

$$y(t) = R_1C_r(t) + R_1C_r(t)\left[\frac{k_3}{k_2+k_3}\left(\frac{k_2'}{R_1}\right) + \frac{k_2}{k_2+k_3}\left(\frac{k_2'}{R_1} - k_2 - k_3\right)\exp\left(-(k_2+k_3)t\right)\right]. \tag{C.10}$$

Linearisation

Inserting the equation (C.6) into equation (B.17) and rearranging,

$$C_2(t) = \frac{K_1}{K_1'}\frac{k_2'k_3}{k_2+k_3}\int C_r(t)dt - \frac{k_3}{k_2+k_3}C_1(t) + \frac{K_1}{K_1'}\frac{k_3}{k_2+k_3}C_r(t). \tag{C.11}$$

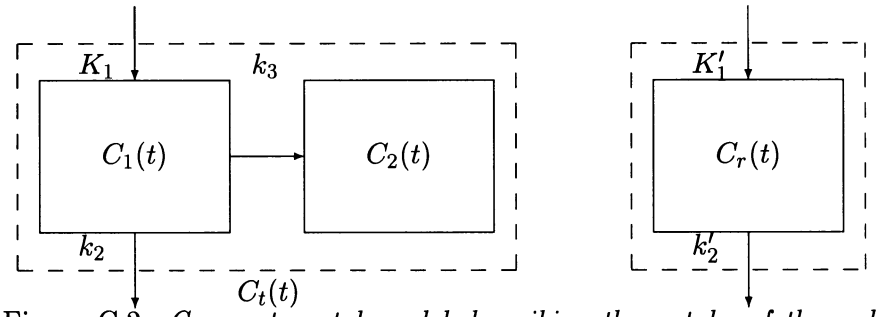

Figure C.2: *Compartmental model describing the uptake of the radiotracer in the target tissue ($C_t(t)$) relative to that in a reference tissue ($C_r(t)$): K_1 is the rate constant for the influx from the plasma to the target tissue while k_2 is the rate constant for the backflux from the target tissue to the plasma; and k_3 is the rate constant representing the metabolism of the parent radiotracer in the target tissue; K_1' is the rate constant for the influx from the plasma to the reference tissue while k_2' is the rate constant for the backflux from the reference tissue to the plasma. The metabolites are assumed to be trapped in the target tissue for the duration of the study.*

Adding $C_1(t)$ to the above expression of $C_2(t)$ and dividing the sum by $C_r(t)$,

$$\frac{C_1(t)+C_2(t)}{C_r(t)} = \frac{K_1}{K_1'}\frac{k_2'k_3}{k_2+k_3}\frac{\int C_r(t)dt}{C_r(t)} + \frac{k_2}{k_2+k_3}\frac{C_1(t)}{C_r(t)} + \frac{K_1}{K_1'}\frac{k_3}{k_2+k_3}. \tag{C.12}$$

After a time t*, effective steady state is reached between the first compartment of the target tissue (C_1) and the plasma (C_p) and also between the reference tissue and the plasma such that

$$\frac{C_1(t>t^*)}{C_p(t>t^*)} = VD_1 = \frac{K_1}{k_2+k_3} \tag{C.13}$$

$$\frac{C_r(t>t^*)}{C_p(t>t^*)} = VD_r = \frac{K_1'}{k_2'} \tag{C.14}$$

$$\Rightarrow \frac{C_1(t>t^*)}{C_r(t>t^*)} = \frac{K_1}{k_2+k_3}\frac{k_2'}{K_1'}. \tag{C.15}$$

Replacing $\frac{C_1(t>t^*)}{C_r(t>t^*)}$ into equation (C.12)

$$\frac{C_t(t)}{C_r(t)} = \left(\frac{K_1}{k_2+k_3}\right)\left(\frac{k_2'}{K_1'}\right)k_3\frac{\int C_r(t)dt}{C_r(t)} + \left[\frac{k_2}{k_2+k_3}\left(\frac{K_1}{k_2+k_3}\frac{k_2'}{K_1'}\right) + \frac{K_1}{K_1'}\frac{k_3}{k_2+k_3}\right]. \tag{C.16}$$

A Patlak plot of $\frac{C_t(t)}{C_r(t)}$ vs. $\frac{\int_0^t C_r(T)dT}{C_r(t)}$ will approach a straight line with a slope of $\frac{VD_1}{VD_r}k_3$ and a positive y-intercept for all times t>t*.

Appendix D

Catalog of Solutions to Compartmental Models for the *In Vitro* Metabolism and Partitioning of a Radiotracer in Blood

D.1 General case: Two-compartment two-parameter blood model

This model was developed to describe the *in vitro* equilibration of a radiotracer between plasma and erythrocytes [1] .

Formulation

Following its introduction into a blood sample, a radiotracer is exchanged bilaterally between plasma and erythrocytes. The volume V_e of the erythrocytes compartment is set to the haematocrit H, and the volume V_p of the plasma compartment to (1-H), such that the volume of whole blood is equal to unity. The concentration in whole blood C_w (in kBq/ml of whole blood) can then be infered from the concentrations in erythrocytes C_e (in kBq/ml of erythrocytes) and in plasma C_p (in kBq/ml of plasma) using

$$C_w = HC_e + (1 - H)C_p. \tag{D.1}$$

The exchange of a radiotracer between plasma and erythrocytes is modelled by two rate constants, k_1 and k_2, where k_1 and k_2 represent the rate constants of influx and backflux to

[1] *This work has been published in the journal* J. Nucl. Med. (2000) **41**: 1636-41.

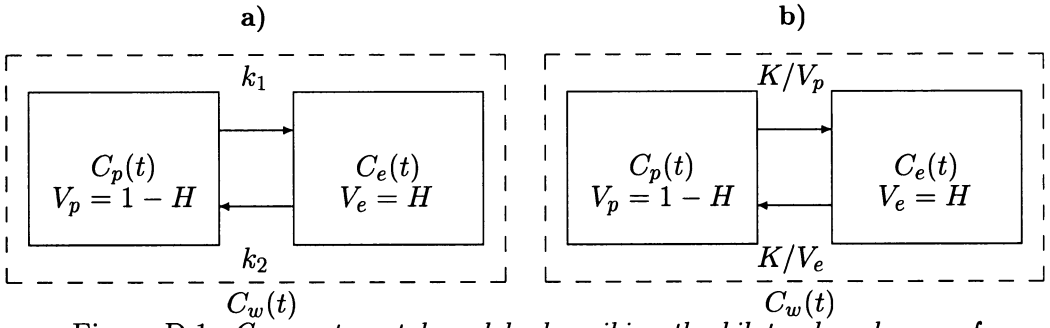

Figure D.1: *Compartmental models describing the bilateral exchange of a radiotracer between plasma (C_p) and erythrocytes (C_e) in whole blood (C_w):* **a)** *when the influx from plasma to erythrocytes $V_p k_1$ is different from the backflux from erythrocytes to plasma $V_e k_2$, and* **b)** *when the influx and backflux are equal, i.e. $V_p k_1 = V_e k_2 = K$.*

and from the erythrocytes. Under the assumptions of linearity and stationarity, the rates of change of the concentration in each compartment are given by

$$V_p \frac{dC_p}{dt} = -k_1 V_p C_p(t) + k_2 V_e C_e(t) \tag{D.2a}$$

$$V_e \frac{dC_e}{dt} = k_1 V_p C_p(t) - k_2 V_e C_e(t). \tag{D.2b}$$

This model assumes that the radiotracer is not metabolised in either compartments.

Operational Equations

Rewriting equations (D.2a) and (D.2b) in matrix form,

$$\begin{pmatrix} \dot{C}_p \\ \dot{C}_e \end{pmatrix} = \begin{pmatrix} -k_1 & \left(\frac{V_e}{V_p}\right) k_2 \\ \left(\frac{V_p}{V_e}\right) k_1 & -k_2 \end{pmatrix} \begin{pmatrix} C_p \\ C_e \end{pmatrix}. \tag{D.3}$$

The roots of the characteristic polynomial $(k_1 + \lambda)(k_2 + \lambda) - k_1 k_2 = 0$ correspond to the system eigenvalues $\lambda_1 = 0$ and $\lambda_2 = -(k_1 + k_2)$. Equation (D.3) can then be solved in terms of the system eigenvectors:

$$\begin{pmatrix} C_p \\ C_e \end{pmatrix} = c_1 \begin{pmatrix} \frac{V_e}{V_p} \\ \frac{k_1}{k_2} \end{pmatrix} + c_2 \begin{pmatrix} \frac{V_e}{V_p} \\ -1 \end{pmatrix} \exp\big(-(k_1 + k_2)t\big). \tag{D.4}$$

Assuming that initially, the radiotracer is found solely in plasma, i.e. $C_p(0) = 1/V_p$ and $C_e(0) = 0$, equation (D.4) becomes

$$C_p(t) = \left(\frac{1}{V_p}\right)\left(\frac{1}{k_1 + k_2}\right)\Big[k_2 + k_1 \exp\big(-(k_1 + k_2)t\big)\Big] \tag{D.5a}$$

$$C_e(t) = \left(\frac{1}{V_e}\right)\left(\frac{k_1}{k_1 + k_2}\right)\Big[1 - \exp\big(-(k_1 + k_2)t\big)\Big]. \tag{D.5b}$$

The ratio of the erythrocytes concentration over the plasma concentration is then simply given by

$$\frac{C_e(t)}{C_p(t)} = \left(\frac{V_p}{V_e}\right) \frac{k_1\left[1 - \exp\left(-(k_1 + k_2)t\right)\right]}{k_2 + k_1 \exp\left(-(k_1 + k_2)t\right)}. \tag{D.6}$$

Volume of Distribution
Under steady-state conditions,

$$\frac{dC_p}{dt} = \frac{dC_e}{dt} = 0 \;\Rightarrow\; k_1 V_p C_p(t) = k_2 V_e C_e(t)$$

$$VD = \frac{C_e(t)}{C_p(t)} = \left(\frac{V_p}{V_e}\right)\left(\frac{k_1}{k_2}\right). \tag{D.7}$$

D.2 Special Case: Two-compartment one-parameter blood model

The model can be simplified in the case where the influx of the radiotracer from the plasma to the erythrocytes is equal to the backflux from the erythrocytes to the plasma, i.e.

$$V_p k_1 = V_e k_2 = K. \tag{D.8}$$

Equations (D.5a), (D.5b), (D.6), and (D.7) then become

$$C_p(t) = 1 + \left(\frac{V_e}{V_p}\right) \exp\left(-\frac{K}{V_e V_p} t\right) \tag{D.9a}$$

$$C_e(t) = 1 - exp\left(-\frac{K}{V_e V_p} t\right) \tag{D.9b}$$

$$\frac{C_e(t)}{C_p(t)} = \frac{1 - exp\left(-\frac{K}{V_e V_p} t\right)}{1 + \left(\frac{V_e}{V_p}\right) \exp\left(-\frac{K}{V_e V_p} t\right)} \tag{D.10}$$

$$VD = 1. \tag{D.11}$$

Bibliography

Andrews B.T., Dujovny M., Mirchandani H.G. and Ausman J.I. (1989) *Microsurgical Anatomy of the Venous Drainage into the Superior Sagittal Sinus* Neurosurgery **24**: 514-20.

Asburner J., Haslam J., Taylor C., Cunningham V.J. and Jones T. (1996) *A Cluster Analysis Approach for the Characterization of Dynamic PET Data* Quantification of Brain Function using PET Eds R. Myers, V. Cunningham, D. Bailey and T. Jones (San Diego: Academic Press) pp.301-06.

Asselin M.-C., Cunningham V.J., Amano S., Gunn R.N. and Nahmias C. (2004) *Parametrically Defined Cerebral Blood Vessels as Non-Invasive Blood Input Functions for Brain PET Studies* Phys. Med. Biol. **49**: 1033-54.

Asselin M.-C., Amano S., Chirakal R., Thompson M. and Nahmias C. (2002a) *Patterns of Distribution of [^{18}F]6-Fluoro-L-m-Tyrosine in PET Images of Patients with Movement Disorders* Brain Imaging Using PET Eds M. Senda, Y. Kimura and P. Herscovitch (San Diego: Academic Press) pp.291-301.

Asselin M.-C., Amano S., Cunningham V.J., Gunn R.N. and Nahmias C. (2002b) *Parametric Definition of ROIs to Recover the Calibre of Cerebral Blood Vessels Directly from PET Images* Brain Imaging Using PET Eds M. Senda, Y. Kimura and P. Herscovitch (San Diego: Academic Press) pp.139-45.

Asselin M.-C., Wahl L.M., Cunningham V.J., Amano S. and Nahmias C. (2002c) *In vivo metabolism and partitioning of 6-[^{18}F]fluoro-L-meta-tyrosine in whole blood: a unified compartmental model* Phys. Med. Biol. **47**: 1961-77.

Asselin M.-C., Cunningham V.J., Turjanski N., Wahl L.M., Bloomfield P.M., Gunn R.N. and Nahmias C. (2001) *Venous Sinuses vs On-Line Arterial Sampling as Input Functions in PET* Physiological Imaging of the Brain with PET Eds A. Gjedde, S.B. Hansen, G.M. Knudsen and O.B. Paulson (San Diego: Academic Press) pp.73-81.

Aston J.A.D., Cunningham V.J., Asselin M.-C., Hammers A., Evans A.C. and Gunn R.N. (2002) *Positron Emission Tomography Partial Volume Correction: Estimation and Algorithms* J. Cereb. Blood Flow Metab. **22**: 1019-34.

Badawi R.D. and Marsden P.K. (1999) *Developments in component-based normalization for 3D PET* Phys. Med. Biol. **44**: 571-94.

Bailey D.L., Young H., Bloomfield P.M., Meikle S.R., Glass D., Myers M.J., Spinks T.J., Watson C.C., Luk P., Peters A.M. and Jones T. (1997) *ECAT ART - a continuously rotating PET camera: performance characteristics, initial clinical studies, and installation considerations in a nuclear medicine department* Eur. J. Nucl. Med. **4**: 6-15.

Bailey D.L., Townsend D.W., Kinahan P.E., Grootoonk S. and Jones T. (1996) *An Investigation of Factors Affecting Detector and Geometric Correction in Normalisation of 3D PET Data* IEEE Trans. Nucl. Sci. **43**: 3300-07.

Barber D.C. (1980) *The use of principal components in the quantitative analysis of gamma camera dynamic studies* Phys. Med. Biol. **25**: 283-92.

Barrio J.R., Huang S.C. and Phelps M.E. (1997) *Biological Imaging and the Molecular Basis of Dopamine Disease* Biochem. Pharmacol. **54**: 341-48.

Barrio J.R., Huang S.-C., Yu D.-C., Melega W.P., Quintana J., Cherry S.R., Jacobson A., Namavari M., Satyamurthy N. and Phelps M.E. (1996) *Radiofluorinated* L-*m-Tyrosines: New In-Vivo Probes for Central Dopamine Biochemistry* J. Cereb. Blood Flow Metab. **16**: 667-78.

Barrio J.R., Huang S.C., Melaga W.P., Yu D.C., Hoffman J.M., Schneider J.S., Satyamurthy N., Mazziotta J.C., and Phelps M.E. (1990) *6-[^{18}F]Fluoro-L-DOPA Probes Dopamine Turnover Rates in Central Dopaminergic Structures* J. Neurosci. Res. **27**: 487-93.

Bendriem B. and Townsend D.W. (1998) The Theory and Practice of 3D PET (Dordrecht: Kluwer Academic Publushers) 167p.

Birkmayer W. and Birkmayer J.G.D. (1989) *The* L-*Dopa Story* Parkinsonism and Aging Eds D.B. Calne *et al*(New York: Raven Press Ltd) pp.1-7.

Bloomfield P.M., Spinks T.J., Reed J., Schnorr L., Westrip A.M., Livieratos L., Ful-

ton R. and Jones T. (2003) *The design and implementation of a motion correction scheme for neurological PET* Phys. Med. Biol. **48**: 959-78.

Brooks D.J. (2002) *Diagnosis and Management of Atypical Parkinsonian Syndromes* J. Neurol. Neurosurg. Psychiatry **72** (Suppl. I): i10-16.

Brooks D.J. (2000) *Functional Imaging Studies in Corticobasal Degeneration* Adv. Neurol. **82**: 209-15.

Brooks D.J. (1998) *The Early Diagnosis of Parkinson's Disease* Ann. Neurol. (Suppl.1) **44**: S10-18.

Brooks D.J., Playford E.D., Ibanez V., Sawle G.V., Thompson P.D., Findley L.J. and Marsden C.D. (1992) *Isolated tremor and disruption of the nigrostriatal dopaminergic system: An ^{18}F-dopa study* Neurology **42**: 1554-60.

Brooks D.J., Salmon E.P., Mathias C.J., Quinn N., Leenders K.L., Bannister R., Marsden C.D. and Frackowiak R.S.J. (1990a) *The relationship between locomotor disability, autonomic dysfunction, and the integrity of the striatal dopaminergic system in patients with multiple system atrophy, pure autonomic failure, and Parkinson's disease, studied with PET* Brain **113**: 1539-52.

Brooks D.J., Ibanez V., Sawle G.V., Quinn N., Lees A.J., Mathias C.J., Bannister R., Marsden C.D. and Frackowiak R.S.J. (1990b) *Differing Patterns of Striatal ^{18}F-Dopa Uptake in Parkinson's Disease, Multiple System Atrophy, and Progressive Supranuclear Palsy* Ann. Neurol. **28**: 547-55.

Brown W.D., DeJesus O.T., Pyzalski R.W., Malischke L., Roberts A.D., Shelton S.E., Uno H., Houser W.D., Nickles R.J. and Holden J.E. (1999) *Localization of Trapping of 6-[^{18}F]fluoro-L-m-tyrosine, an Aromatic L-Amino Acid Decarboxylase Tracer for PET* Synapse **34**: 111-23.

Burn D.J., Sawle G.V. and Brooks D.J. (1994) *Differential diagnosis of Parkinson's disease, multiple system atrophy, and Steele-Richardson-Olszewski syndrome: discriminant analysis of striatal ^{18}F-dopa PET data* J. Neurol. Neurosurg. Psychiatry **57**: 278-84.

Burns R.S., Chiueh C.C., Markey S.P., Ebert M.H., Jacobowitz D.M. and Kopin I.J. (1983) *A primate model of parkinsonism: Selective destruction of dopaminergic neurons in the pars compacta of the substantia nigra by N-methyl-4-phenyl-1,2,3,6-*

tetrahydropyridine Proc. Natl Acad. Sci. USA **80**: 4546-50.

Carson R.E., Breier A., de Bartolomeis A., Saunders R.C., Su T.P., Schmall B., Der M.G., Pickar D. and Eckelman W.C. (1997) *Quantification of amphetamine-induced changes in [^{11}C]raclopride binding with continuous infusion* J. Cereb. Blood Flow Metab. **17**: 437-47.

Carson R.E., Channing M.A., Blasberg R.G., Dunn B.B., Cohen R.M., Rice K.C. and Herscovitch P. (1993) *Comparison of Bolus and Infusion Methods for Receptor Quantitation: Application to [^{18}F]Cyclofoxy and Positron Emission Tomography* J. Cereb. Blood Flow Metab. **13**: 24-42.

Carson, R.E. (1991) *Precision and Accuracy Considerations of Physiological Quantitation in PET* J. Cereb. Blood Flow Metab. **11**: A45-50.

Casey M.E. and Nutt R. (1986) *A multicrystal two dimensional BGO detector system for positron emission tomography* IEEE Trans. Nucl. Sci. **33**: 460-63.

Casey M.E. and Hoffman E.J. (1986) *Quantitation in Positron Emission Computed Tomography: 7. A Technique to Reduce Noise in Accidental Coincidence Measurements and Coincidence Efficiency Calibration* J. Comput. Assist. Tomogr. **10**: 845-50.

Chen C.-H., Muzic R.F. Jr, Nelson A.D. and Adler L.P. (1999) *Simultaneous Recovery of Size and Radioactivity Concentration of Small Spheroids with PET Data* J. Nucl. Med. **40**: 118-30.

Chen K., Bandy D., Reiman E., Huang S.-C., Lawson M., Feng D., Yun L.-S. and Palant A. (1998) *Noninvasive Quantification of the Cerebral Metabolic Rate for Glucose Using Positron Emission Tomography, ^{18}F-Fluoro-Deoxyglucose, the Patlak Method, and an Image-Derived Input Function* J. Cereb. Blood Flow Metab. **18**: 716-23.

Chirakal R., Schrobilgen G.J., Firnau G. and Garnett S. (1991) *Synthesis of ^{18}F Labelled Fluoro-m-tyrosine, Fluoro-m-tyramine and Fluoro-3-hydroxyphenylacetic Acid* Appl. Radiat. Isot. **42**: 113-9.

Cho Z.H. and Farukhi M.R. (1977) *Bismuth Germanate as Potential Scintillation Detector in Positron Cameras* J. Nucl. Med. **18**: 840-44.

Cobelli C. and DiStefano J.J. III (1980) *Parameter and structural identifiability con-*

cepts and ambiguities: a critical review and analysis Am. J. Physiol. **239**: R7-24.

Colsher J.G. (1980) *Fully three-dimensional positron emission tomography* Phys. Med. Biol. **25**: 103-15.

Correia J. (1992) *A Bloody Future for Clinical PET?* J. Nucl. Med. **32**: 620-2.

Cumming P. and Gjedde A. (1998) *Compartmental Analysis of Dopa Decarboxylation in Living Brain From Dynamic Positron Emission Tomograms* Synapse **29**: 37-61.

Cunningham V.J. and Lammertsma A.A. (1994) *Radioligand Studies in Brain: Kinetic Analysis of PET Data* Med. Chem. Res. **5**:79-96.

Cunningham V.J., Hume S.P., Price G.R., Ahier R.G., Cremer J.E., and Jones A.K.P. (1991) *Compartmental Analysis of Diprenorphine Binding to Opiate Receptors in the Rat In Vivo and Its Comparison with Equilibrium Data In Vitro* J. Cereb. Blood Flow Metab. **11**: 1-9.

Curé J.K., van Tassel P. and Smith T. (1994) *Normal and Variant Anatomy of the Dural Venous Sinuses* Semimars in Ultrasound, CT, and MRI **15**: 499-519.

Daube-Witherspoon M.E., Karp J.S., Casey M.E., DiFilippo F.P., Hines H., Muehllehner G., Simcic V., Stearns C.W., Adam L.-E., Kohlmyer S., and Sossi V. (2002) *PET Performance Measurements Using the NEMA NU-2-2001 Standard* J. Nucl. Med. **43**: 1398-1409.

Daube-Witherspoon M.E. and Muehllehner G. (1987) *Treatment of Axial Data in Three-Dimensional PET* J. Nucl. Med. **28**: 1717-24.

Defrise M., Kinahan P.E., Townsend D.W., Michel C., Sibomana M. and Newport D.F. (1997) *Exact and Approximate Rebinning Algorithms for 3-D PET Data* IEEE Trans. Med. Imag. **16**: 145-58.

Defrise M. (1995) *A factorization method for the 3D x-ray transform* Inverse Problems **11**: 983-94.

Defrise M., Townsend D. and Geissbuhler A. (1990) *Implementation of three-dimensional image reconstruction for multi-ring positron tomograph* Phys. Med. Biol. **35**: 1361-72.

DeJesus O.T. (2003) *Positron-Labelled DOPA Analogs to Image Dopamine Terminals* Drug Develop. Res. **59**: 249-60.

DeJesus O.T., Endres C.J., Shelton S.E., Nickles R.J., and Holden J.E. (2001) *Noninvasive Assessment of Aromatic* L-*Amino Acid Decarboxylase Activity in Aging Rhesus Monkey Brain In Vivo* Synapse **39**: 58-63.

DeJesus O.T., Endres C.J., Shelton S.E., Nickles R.J. and Holden J.E. (1997) *Evaluation of Fluorinated m-Tyrosine Analogs as PET Imaging Agents of Dopamine Nerve Terminals: Comparison with 6-Fluorodopa* J. Nucl. Med. **38**: 630-36.

DeJesus O.T. and Mukherjee J. (1988) *Radiobrominated meta-tyrosine analog as a potential CNS L-DOPA PET tracer* Biochem. Biophys. Res. Commun. **150**: 1027-31.

deKemp R.A. and Nahmias C. (1994) *Attenuation correction in PET using single photon transmission measurement* Med. Phys. **21** : 771-78.

Dhawan V., Ishikawa T., Patlak C., Chaly T., Robeson W., Belakhlef A., Margouleff C., Mandel F. and Eidelberg D. (1996) *Combined FDOPA and 3OMFD PET Studies in Parkinson's Disease* J. Nucl. Med. **37**: 209-16.

Dhawan V., Takikawa S., Robeson W., Spetsieris P., Chaly T., Dahl R., Zanzi I., Bandyopadhyay D., Margouleff D. and Eidelberg D. (1994) *Quantitative brain FDG/PET studies using dynamic aortic imaging* Phys. Med. Biol. **39**: 1475-87.

Di Bella E.V.R., Clackdoyle R. and Gullberg G.T. (1999) *Blind estimation of compartmental model parameters* Phys. Med. Biol. **44**: 765-80.

DiStefano J.J. III and Landaw E.M. (1984) *Multiexponential, multicompartmental, and noncompartmental modeling. I. Methodological limitations and physiological interpretations* Am. J. Physiol. **246**: R651-64.

Doudet D.J., Chan G.L.-Y., Jivan S., DeJesus O.T., McGeer E.G., English C., Ruth T.J. and Holden J.E. (1999) *Evaluation of Dopaminergic Presynaptic Integrity: 6-[^{18}F]Fluoro-*L*-Dopa Versus 6-[^{18}F]Fluoro-*L*-m-Tyrosine* J. Cereb. Blood Flow Metab. **19**: 278-87.

Doudet D.J., Aigner T.G., McLellan C.A. and Cohen R.M. (1992) *Positron Emission Tomography With ^{18}F-DOPA: Interpretation and Biological Correlates in Nonhuman Primates* Psych. Res.: Neuroimag. **45**: 153-68.

Doudet D.J., McLellan C.A., Carson R., Adams H.R., Miyake H., Aigner T.G., Finn R.T. and Cohen R.M. (1991) *Distribution and Kinetics of 3-O-Methyl-6-[^{18}F]fluoro-L-DOPA in the Rhesus Monkey Brain* J. Cereb. Blood Flow Metab. **11**: 726-34.

Eberling J.L., Pivirotto P., Bringas J. and Bankiewicz K.S. (2000) *Tremor is Associated with PET Measures of Nigrostriatal Dopamine Function in MPTP-Lesioned Monkeys* Exp. Neurol. **165**: 342-46.

Endres C.J., Swaminathan S., DeJesus O.T., Sievert M., Ruoho A.E., Murali D., Rommelfanger S.G. and Holden J.E. (1997) *Affinities of dopamine analogs for monoamine granular and plasma membrane transporters: Implications for PET dopamine studies* Life Sci. **60**: 2399-2406.

Eriksson L. and Kanno I. (1991) *Blood sampling devices and measurements* Med. Prog. Technol. **17**: 249-57.

Erlandsson K., Esser P.D., Strand S.-E. and van Heertum R.L. (1994) *3D reconstruction for multi-ring PET scanner by single-slice rebinning and axial deconvolution* Phys. Med. Biol. **39**: 619-29.

Fearnley J.M. and Lees A.J. (1991) *Ageing and Parkinson's Disease: Substantia nigra regional electivity* Brain **114**: 2283-2301.

Feng D., Huang S.-C. and Wang X. (1993) *Models for computer simulation studies of input functions for tracer kinetic modelling with positron emission tomography* Int. J. Biomed. Comput. **32**: 95-110.

Firnau G., Chirakal R., Wahl L., Chen J.J., Murthy D., Nahmias C. and Garnett S.E. (1995) *New PET tracers for cerebral dopamine: Should 6-[^{18}F]Fluoro-L-dopa be replaced?* Chemists' Views of Imaging Centers Ed. A.M. Emran (New York: Plenum Press) pp.237-47.

Firnau G., Sood S., Chirakal R., Nahmias C. and Garnett E.S. (1988) *Metabolites of 6-[^{18}F]Fluoro-L-Dopa in Human Blood* J. Nucl. Med. **29**: 363-69.

Frey K.A. (2002) *Can SPET imaging of dopamine uptake sites replace PET imaging in Parkinson's disease? - Against* Eur. J. Nucl. Med. **29**: 715-17.

Garnett E.S., Firnau G. and Nahmias C. (1983) *Dopamine visualized in the basal*

ganglia of living man Nature **305**: 137-38.

Germano G., Chen B.C., Huang S.-C., Gambhir S.S., Hoffman E.J. and Phelps M.E. (1992) *Use of the Abdominal Aorta for Arterial Input Function Determination in Hepatic and Renal PET Studies* J. Nucl. Med. **33**: 613-20.

Gibb W.R.G. and Lees A.J. (1988) *The relevance of the Lewy body to the pathenogenesis of idiopathic Parkinson's disease* J. Neurol. Neurosurg. Psychiatry **51**: 745-52.

Gill S.S., Patel N.K., Hotton G.R., O'Sullivan K., McCarter R., Bunnage M., Brooks D.J., Svendsen C.N. and Heywood P. (2003) *Direct brain infusion of glial cell line-derived neurotrophic factor in Parkinson disease* Nature Medicine **9**: 589-95.

Gjedde A., Reith J., Dyve S., Léger G., Guttman M., Diskic M., Evans A. and Kuwabara H. (1991) *Dopa decarboxylase activity of the living human brain* Proc. Natl Acad. Sci. USA **88**: 2721-25.

Godfrey K. (1983) Compartmental Models and Their Application (London: Academic Press) ?p.

Green M.V., Seidel J., Stein S.D., Tedder T.E., Kempner K.M., Kertzman C. and Zeffiro T.A. (1994) *Head Movement in Normal Subjects During Simulated PET Brain Imaging with and without Head Restraint* J. Nucl. Med. **35**:1538-46.

Grootoonk S., Spinks T.J., Sashin D., Spyrou N.M. and Jones T. (1996) *Correction for scatter in 3D brain PET using a dual energy window method* Phys. Med. Biol. **41**: 2757-74.

Gunn R.N., Gunn S.R. and Cunningham V.J. (2001) *Positron Emission Tomography Compartmental Models* J. Cereb. Blood Flow Metab. **21**: 635-52.

Gunn R.N., Ranicar A., Yap J.T., Wells P., Osman S., Jones T. and Cunningham V.J. (2000) *On-Line Measurement of Exhaled [^{11}C]CO_2 During PET* J. Nucl. Med. **41**: 605-11.

Gunn R.N., Sargent P.A., Bench C.J., Rabiner E.A., Osman S., Pike V.W., Hume S.P., Grasby P.M. and Lammertsma A.A. (1998) *Tracer Kinetic Modeling of the 5-HT_{1A} Receptor Ligand [carbonyl-^{11}C]WAY-100635 for PET* NeuroImage **8**: 426-440.

Gunn R.N., Lammertsma A.A., Hume S.P. and Cunningham V.J. (1997) *Paramet-*

ric Imaging of Ligand-Receptor Binding in PET Using a Simplified Reference Region Model Neuroimage **6**: 279-87.

Hadjiconstantinou M., Wemlinger T.A., Sylvia C.P., Hubble J.P., and Neff N.H. (1993) *Aromatic* L-*Amino Acid Decarboxylase Activity of Mouse Striatum Is Modulated via Dopamine Receptors* J. Neurochem. **60**: 2175-80.

Hagenfeldt L. and Arvidsson A. (1980) *The distribution of amino acids between plasma and erythrocytes* Clin. Chim. Acta **100**: 133-41.

Hoehn M. and Yahr M.D. (1967) *Parkinsonism: onset, progression and mortality* Neurology **17**: 427-42.

Hoffman E.J., Guerrero T.M., Germano G., Digby W.M. and Dahlbom M. (1989) *PET system calibrations and corrections for quantitative and spatially accurate images* IEEE Trans. Nucl. Sci. **36**: 1108-12.

Hoffman E.J., Huang S.-C., Phelps M.E. and Kuhl D.E. (1981) *Quantification in Positron Emission Computed Tomography: 4. Effect of Accidental Coincidences* J. Comput. Assist. Tomogr. **5**: 391-400.

Hoffman E.J., Huang S.-C. and Phelps M.E. (1979) *Quantitation in Positron Emission Computed Tomography: 1. Effect of Object Size* J. Comput. Assist. Tomogr. **3**: 299-308.

Holden J.E., Doudet D., Endres C.J., Chan G.L.-Y., Morrison K.S., Vingerhoets F.J.G., Snow B.J., Pate B.D., Sossi V., Buckley K.R. and Ruth T.J. (1997) *Graphical Analysis of 6-Fluoro-L-Dopa Trapping: Effect of Inhibition of Cathecol-O-Methytransferase* J. Nucl. Med. **38**: 1568-74.

Hoshi H., Kuwubara H., Léger G., Cumming P., Guttman M. and Gjedde A. (1993) *6-[^{18}F]fluoro-*L*-DOPA Metabolism in Living Human Brain: A Comparison of Six Analytical Methods* J. Cereb. Blood Flow Metab. **13**: 57-69.

Huang S.-C., Stout D.B., Yee R.E., Satyamurthy N. and Barrio J.R. (1998) *Distribution Volume of Radiolabeled Large Neutral Amino acids in Brain Tissue* J. Cereb. Blood Flow Metab. **18**: 1288-93.

Huang S.-C., Yu D.-C., Barrio J.R., Grafton S., Melega W.P., Hoffman J.M., Satyamurthy N., Mazziotta J.C. and Phelps M.E. (1991a) *Kinetics and Modeling*

of L-*6-[*^{18}*F]Fluoro-DOPA in Human Positron Emission Tomographic Studies* J. Cereb. Blood Flow Metab. **11**: 898-913.

Huang S.C., Barrio J.R., Yu D.C., Chen B., Grafton S., Melega W.P., Hoffman J.M., Satyamurthy N., Mazziotta J.C. and Phelps M.E. (1991b) *Modelling approach for separating blood time-activity curves in positron emission tomograpic studies* Phys. Med. Biol. **36**: 749-61.

Huang S.-C., Hoffman E.J., Phelps M.E. and Kuhl D.E. (1979) *Quantification in Positron Emission Computed Tomography: 2. Effect of Inaccurate Attenuation Correction* J. Comput. Assist. Tomogr. **3**: 804-14.

Hughes A.J., Ben-Shlomo Y., Daniel S.E. and Lees A.J. (1992) *What features improve the accuracy of clinical diagnosis in Parkinson's Disease* Neurology **42**: 1142-46.

Hume S.P., Myers R., Bloomfield P.M., Opacka-Juffry J., Cremer J.E., Ahier R.G., Luthra S.K., Brooks D.J. and Lammertsma A.A. (1992) *Quantitation of Carbon-11-Labeled Raclopride in Rat Striatum Using Positron Emission Tomography* Synapse **12**: 47-54.

Iida H., Miura S., Shoji Y., Ogawa T., Kado H., Narita Y., Hatazawa J., Eberl S., Kanno I. and Uemura K. (1998) *Noninvasive Quantification of Cerebral Blood Flow Using Oxygen-15-Water and Dual-PET System* J. Nucl. Med. **39**: 1789-98.

Iida H., Jones T. and Miura S. (1993) *Modeling Approach to Eliminate the Need to Separate Arterial Plasma in Oxygen-15 Inhalation Positron Emission Tomography* J. Nucl. Med. **34**: 1333-40.

Iida H., Rhodes C.G., de Silva R., Araujo L.I., Bloomfield P.M., Lammertsma A.A. and Jones T. (1992) *Use of the Left Ventricular Time-Activity Curve as a Noninvasive Input Function in Dynamic Oxygen-15-Water Positron Emission Tomography* J. Nucl. Med. **33**: 1669-77.

Iida H., Kanno I., Miura S., Murakami M., Takahashi K., and Uemura K. (1986) *Error Analysis of a Quantitative Cerebral Blood Flow Measurement Using* $H_2^{15}O$ *Autoradiography and Positron Emission Tomography, With Respect to the Dispersion of the Input Function* J. Cereb. Blood Flow Metab. **6**: 536-45.

Ishikawa T., Dhawan V., Chaly T., Margouleff C., Robeson W., Dahl R., Mandel F., Spetsieris P. and Eidelberg D. (1996) *Clinical Significance of Striatal DOPA*

Decarboxylase Activity in Parkinson's Disease J. Nucl. Med. **37**: 216-22.

Jacquez J.A. (1988) Compartmental Analysis in Biology and Medicine Second edition (Ann Arbor: The University of Michigan Press) ?p.

Jordan S., Bankiewicz K.S., Eberling J.L., VanBrocklin H.F., O'Neil J.P. and Jagust W.J. (1998) *An In Vivo Microdialysis Study of Striatal 6-[^{18}F]Fluoro-L-m-Tyrosine Metabolism* Neurochem. Res. **23**: 513-17.

Jordan S., Eberling J.L., Bankiewicz K.S., Rosenberg D., Coxson P.G., VanBrocklin H.F., O'Neil J.P., Emborg M.E. and Jagust W.J. (1997) *6-[^{18}F]Fluoro-*L*-m-tyrosine: metabolism, positron emission tomography kinetics, and 1-methyl-4-phenyl-1,2,3,6-tetrahydropyridine lesions in primates* Brain Res. **750**: 264-76.

Karp J.S. (2002) *Is LSO the future of PET? - Against* Eur. J. Nucl. Med. **29**: 1525-28.

Karp J.S., Muehllehner G., Qu H., and Yan X.-H. (1995) *Singles transmission in volume-imaging PET with a ^{137}Cs source* Phys. Med. Biol. **40**: 929-44.

Karp J.S., Daube-Witherspoon M.E., Hoffman E.J., Lewellen T.K., Links J.M., Wong W.-H., Hichwa R.D., Casey M.E., Colsher J.G., Hitchens R.E., Muehllehner G. and Stoub E.W. (1991) *Performance Standards in Positron Emission Tomography* J. Nucl. Med. **32**: 2342-50.

Kessler R.M., Ellis J.R. and Eden M. (1984) *Analysis of Emission Tomographic Scan Data: Limitations Imposed by Resolution and Background* J. Comput. Assist. Tomogr. **8**: 514-22.

Kiebel S.J., Ashburner J., Poline J.-B. and Friston K.J. (1997) *MRI and PET Coregistration - A Cross Validation of Statistical Parametric Mapping and Automated Image Registration* Neuroimage **5**: 271-9.

Kinahan P.E. and Rogers J.G. (1989) *Analytic 3D image reconstruction using all detected events* IEEE Trans. Nucl. Sci. **36**: 964-68.

Kish S.J., Shannak K., Rajput A., Deck J.H.N. and Hornykiewicz O. (1992) *Aging Produces a Specific Pattern of Striatal Dopamine Loss: Implications for the Etiology of Idiopathic Parkinson's Disease* J. Neurochem. **58**: 642-48.

Kish S.J., Shannak K. and Hornykiewicz O. (1988) *Uneven pattern of dopamine loss in the striatum of patients with idiopathic Parkinson's disease* New Engl. J. Med. **318**: 876-80.

Knoll G.F. (1989) Radiation detection and measurement (Second edition) (New York: John Wiley & Sons) 754p.

Knudsen G.M., Pettigrew K.D., Patlak C.S. and Paulson O.B. (1994) *Blood-brain barrier permeability measurements by double-indicator method using intravenous injections* Am. J. Physiol. **266**: H987-99.

Knudsen G.M., Pettigrew K.D., Patlak C.S., Hertz M.M., and Paulson O.B. (1990a) *Asymmetrical Transport of Amino Acids Across the Blood-Brain Barrier in Humans* J. Cereb. Blood Flow Metab. **10**: 698-706.

Knudsen G.M., Pettigrew K.D., Paulson O.B., Hertz M.M., and Patlak C.S. (1990b) *Kinetic Analysis of BLood-Brain Barrier Transport of* D-*Glucose in Man: Quantitative Evaluation in the Presence of Tracer Backflux and Capillary Heterogeneity* Microvasc. Res. **39**: 28-49.

Koeppe R.A., Holden J.E., Polcyn R.E., Nickles R.J., Hutchins G.D. and Weese J.L. (1985) *Quantitation of Local Cerebral Blood Flow and Partition Coefficient Without Arterial Sampling: Theory and Validation* J. Cereb. Blood Flow Metab. **5**: 214-23.

Kuwabara H., Cumming P., Yasuhara Y., Léger G.C., Guttman M., Diksic M., Evans A.C. and Gjedde A. (1995) *Regional Striatal DOPA Transport and Decarboxylase Activity in Parkinson's Disease* J. Nucl. Med. **36**: 1226-31.

Kuwabara H., Cumming P., Reith J., Léger G., Diksic M., Evans A.C. and Gjedde A. (1993) *Human Striatal* L-*DOPA Decarboxylase Activity Estimated In Vivo Using 6-[*^{18}*F]fluoro-DOPA and Positron Emission Tomography: Error Analysis and Application to Normal Subjects* J. Cereb. Blood Flow Metab. **13**: 43-56.

Labbé C., Froment J.C., Kennedy A., Ashburner J. and Cinotti L. (1996) *Positron Emission Tomography Metabolic Data Corrected for Cortical Atrophy Using Magnetic Resonance Imaging* Alzheimer Disease and Assocociated Disorders **10**: 141-70.

Lammertsma A.A., Bench C.J., Hume S.P., Osman S., Gunn K., Brooks D.J. and Frackowiak R.S.J. (1996) *Comparison of Methods for the Analysis of Clinical [*^{11}*C]Raclopride Studies* J. Cereb. Blood Flow Metab. **16**: 42-52.

Lammertsma A.A. and Hume S.P. (1996) *Simplified Reference Tissue Model for PET Receptor Studies* Neuroimage **4**: 153-58.

Lammertsma A.A., Hume S.P., Bench C.J., Luthra S.K., Osman S. and Jones T. (1993) *Measurement of monoamine oxydase B activity using* L-[^{11}*C]deprenyl: inclusion of compartmental analysis of plasma metabolites and a new model not requiring measurement of plasma metabolites* Quantification of Brain Function: Tracer Kinetics and Image Analysis in Brain PET Eds K. Uemura, T. Jones, N.A. Lassen and I. Kanno (Tokyo: Excerpta Medica) pp.313-8.

Landaw E.M. and DiStefano J.J. III (1984) *Multiexponential, multicompartmental, and noncompartmental modeling. II. Data analysis and statistical considerations* Am. J. Physiol. **246**: R665-77.

Lang A.E. and Lozano A.M. (1998) *Parkinson's Disease* New Engl. J. Med. **339**: 1044-53, 1130-43.

Langstron J.W. (1998) *Epidemiology Versus Genetics in Parkinson's Disease: Progress in Resolving an Age-old Debate* Ann. Neurol. (Suppl.1) **44**: S45-52.

Laverman P., Boerman O.C., Corstens F.H.M., and Oyen W.J.G. (2002) *Fluorinated amino acids for tumor imaging with positron emission tomography* Eur. J. Nucl. Med. **29**: 681-90.

Lee C.S., Samii A., Sossi V., Ruth T.J., Schulzer M., Holden J.E., Wudel J., Pal P.K., de la Fuente-Fernandez R., Calne D.B., and Stoessl S.J. (2000) *In Vivo Positron Emission Tomographic Evidence for Compensatory Changes in Presynaptic Dopaminergic Nerve Terminals in Parkinson's Disease* Ann. Neurol. **47**: 493-503.

Leenders K.L., Blasberg R., Emert F., van den Hoff J., Koeppe R.A., Lammertsma A.A., Maguire R.P., and Mueller-Schauenburg W. (1997) PET Pharmacokinetic Course Manual (Villigen: Paul Scherrer Institut) 99p.

Leenders K.L., Poewe W.H., Palmer A.J., Brenton D.P. and Frackowiak S.J. (1986) *Inhibition of* L-[^{18}*F]Fluorodopa Uptake into Human Brain by Amino Acids Demonstrated by Positron Emission Tomography* Ann. Neurol. **20**: 258-62.

Lewitt R.M., Muehllehner G. and Karp S. (1994) *Three-dimensional image reconstruction*

for PET by multi-slice rebinning and axial image filtering Phys. Med. Biol. **39**: 321-39.

Litton J.-E. (1997) *Input Function in PET Brain Studies Using MR-Defined Arteries* J. Comput. Assist. Tomogr. **21**: 907-9.

Liu X., Defrise M., Michel C., Sibomana M., Comtat C., Kinahan P. and Townsend D. (1999) *Exact Rebinning Methods for Three-Dimensional PET* IEEE Trans. Med. Imag. **18**: 657-64.

Logan J., Fowler J.S., Volkow N.D., Wang G.-J., Ding Y.-S. and Alexoff D.L. (1996) *Distribution Volume Ratios Without Blood Sampling from Graphical Analysis of PET Data* J. Cereb. Blood Flow Metab. **16**: 834-40.

Logan J., Fowler J.S., Volkow N.D., Wolf A.P., Dewey S.L., Schlyer D.J., MacGregor R.R., Hitzemann R., Bendriem B., Gatley S.J. and Christman D.R. (1990) *Graphical Analysis of Reversible Radioligand Binding from Time-Activity Measurements Applied to [N-^{11}C-methyl]-(−)-Cocaine PET Studies in Human Subjects* J. Cereb. Blood Flow Metab. **10**: 740-47.

Ludziejewski T., Moszyńska K. and Wolski D. (1995) *Advantages and Limitations of LSO Scintillator in Nuclear Physics Experiments* IEEE Trans. Nucl. Sci. **42**: 328-36.

Luthra S.K., Osman S., Turton D.R., Vaja V., Dowsett K. and Brady F. (1993) *An automated system based on solid phase extraction and HPLC for the routine determination in plasma of unchanged [^{11}C]-L-deprenyl, [^{11}C]diprenorphine, [^{11}C]flumazenil, [^{11}C]raclopride and [^{11}C]Scherring 23390* J. Labelled Compd Rad. **32**: 518-20.

Martin W.R.W., Palmer M.R., Patlak C.S. and Calne D.B. (1989) *Nigrostriatal Function in Humans Studied with Positron Emission Tomography* Ann. Neurol. **6**: 535-42.

Marsden C.D. (1990) *Parkinson's disease* (review) The Lancet **335**: 948-52.

McGeer P.L., Itagaki S., Akiyama H. and McGeer E.G. (1988) *Rate of Cell Death in Parkisonism Indicates Active Neuropathological Process* Ann. Neurol. **24**: 574-76.

McGeer P.L., Eccles J.C., and McGeer E.G. (1987) Molecular Neurobiology of the Mammalian Brain (Second edition) (New York: Plenum Press) 774p.

McGeer P.L., McGeer E.G. and Suzuki J.S. (1977) *Aging and Extrapyramidal Func-*

tion Arch. Neurol. **34**: 33-35.

McLellan C.A., Doudet D.J., Brucke T., Aigner T.G. and Cohen R.M. (1991) *New Rapid Analysis Method Demonstrates Differences in 6-[^{18}F]Fluoro-L-dopa Plasma Input Curves With and Without Carbidopa and in Hemi-MPTP Lesioned Monkeys* Appl. Radiat. Isot. **42**: 847-54.

Melega W.P., Scott T.G., Huang S.-C., Satyamurthy N., Phelps M.E. and Barrio J.R. (1991) *L-6-[^{18}F]Fluoro-DOPA Metabolism in Monkeys and Humans: Biochemical Parameters for the Formulation of Tracer Kinetic Models with Positron Emission Tomography* J. Cereb. Blood Flow Metab. **11**: 890-97.

Melega W.P., Hoffman J.M., Luxen A., Nissenson C.H.K., Phelps M.E. and Barrio J.R. (1990) *The effects of carbidopa on the metabolism of 6-[^{18}F]fluoro-L-DOPA in rats, monkeys and humans* Life Sci. **47**: 149-57.

Melega W.P., Perlmutter M.M., Luxen A., Nissenson C.H.K., Grafton S.T., Huang S.-C., Phelps M.E. and Barrio J.R. (1989) *4-[^{18}F]Fluoro-L-m-Tyrosine: An L-3,4-Dihydroxyphenylalanine Analog for Probing Presynaptic Dopaminergic Function with Positron Emission Tomography* J. Neurochem. **53**: 311-14.

Moisan C., Rogers J.G. and Douglas J.L. (1997) *A Count Rate Model for PET and its Application to an LSO HR PLUS Scanner* IEEE Trans. Nucl. Sci. **44**: 1219-24.

Morrish P.K., Sawle G.V. and Brooks D.J. (1995) *Clinical and [^{18}F]dopa PET findings in early Parkinson's disease* J. Neurol. Neurosurg. Psychiatry **59**: 597-600.

Meyer E. (1989) *Simultaneous Correction for Tracer Arrival Delay and Dispersion in CBF Measurements by the $H_2^{15}O$ Autoradiographic Method and Dynamic PET* J. Nucl. Med. **30**: 1069-78.

Nahmias C., Wahl L.M., Amano S., Asselin M.-C. and Chirakal R. (2000) *Equilibration of 6-[^{18}F]Fluoro-L-m-Tyrosine Between Plasma and Erythrocytes* J. Nucl. Med. **41**: 1636-41.

Nahmias C., Wahl L., Chirakal R., Firnau G. and Garnett S.E. (1995) *A Probe for Intracerebral Aromatic Amino-Acid Decarboxylase Activity: Distribution and Kinetics of [^{18}F]6-fluoro-L-m-Tyrosine in the Human Brain* Mov. Dis. **10**: 298-304.

Nelson A.D., Miraldi F., Muzic R.F. Jr, Leisure G.P. and Semple W.E. (1993) *Non-*

invasive Arterial Monitor for Quantitative Oxygen-15-Water Blood Flow Studies J. Nucl. Med. **34**: 1000-06.

Norwich K.H. (1997) *Noncompartmental Models of Whole-Body Clearance of Tracers: A Review* Ann. Biomed. Eng. **25**: 421-39.

Nutt R. (2002) *Is LSO the future of PET? - For* Eur. J. Nucl. Med. **29**: 1523-25.

Ollinger J.M. and Fessler J.A. (1997) *Positron-Emission Tomography* IEEE Signal Proc. Mag. **14**: 43-55.

Ollinger J.M. (1996) *Model-based scatter correction for fully 3D PET* Phys. Med. Biol. **41**: 153-76.

Ollinger J.M. (1995) *Detector Efficiency and Compton Scatter in Fully 3D PET* IEEE Trans. Nucl. Sci. **42** (1995): 1168-73.

Opacka-Juffry J. and Brooks D.J. (1995) *L-Dihydroxyphenylalanine and Its Decarboxylase: New Ideas on their Regulatory Roles* Mouv. Dis. **10**: 241-49.

Pages L., Bertel E., Joffre H. and Sklavenitis L. (1972) *Energy loss, range, and bremsstrahlung yield for 10-keV to 100-MeV electrons in various elements and chemical compounds* Atomic Data **4**: 1-127.

Pajevic S., Daube-Witherspoon M.E., Bacharach S.L. and Carson R.E. (1998) *Noise Characteristics of 3-D and 2-D PET images* IEEE Trans. Med. Imag. **17**: 9-23.

Pate B.D., Kawamata T., Yamada T., McGeer E.G., Hewitt K.A., Snow B.J., Ruth T.J. and Calne D.B. (1993) *Correlation of Striatal Fluorodopa Uptake in the MPTP Monkey with Dopaminergic Indices* Ann. Neurol. **34**: 331-38.

Patlak C.S. and Blasberg R.G. (1985) *Graphical Evaluation of Blood-to-Brain Transfer Constants from Multiple-Time Uptake Data. Generalizations* J. Cereb. Blood Flow Metab. **5**: 584-90.

Patlak C.S., Blasberg R.G. and Fenstermacher J.D. (1983) *Graphical Evaluation of Blood-to-Brain Transfer Constants from Multiple-Time Uptake Data* J. Cereb. Blood Flow Metab. **3**: 1-7.

Patlak C.S., Blasberg R.G. and Fenstermacher J.D. (1981) *Derivation of Equations*

for the Steady-State Reaction Velocity of a Substance Based on the Use of a Second Substance J. Cereb. Blood Flow Metab. **1**: 129-31.

Perese D.A., Ulman J., Viola J., Ewing S.E., and Bankiewicz K.S. (1989) *A 6-hydroxydopamine-induced selective parkinsonian rat model* Brain Res. **494**: 285-93.

Phelps M.E., Huang S.C., Hoffman E.J., Selin C., Sokoloff L. and Kuhl D.E. (1979) *Tomographic Measurement of Local Cerebral Glucose Metabolic Rate in Humans with (F-18)2-Fluoro-2-Deoxy-*D*-Glucose: Validation of a Method* Ann. Neurol. **6**: 371-88.

Pike V.W. (1993) *Positron-emitting radioligands for studies in vivo — probes for human psychopharmacology* J. Psychopharmacol. **7**: 139-58.

Poole R.C. and Halestrap A.P. (1993) *Transport of lactate and other monocarboxylates across mammalian plasma membranes* Am. J. Physiol. **264**: C761-82.

Ranicar A.S.O., Williams C.W., Schnorr L., Clark J.C., Rhodes C.G., Bloomfield P.M. and Jones T. (1991) *The on-line monitoring of continuously withdrawn arterial blood during PET studies using a single BGO/photomultiplier assembly and non-stick tubing* Med. Progr.Tech. **17**: 259-64.

Reith J., Dyve S., Kuwabara H., Guttman M., Diksic M., and Gjedde A. (1990) *Blood-brain transfer and metabolism of 6-[^{18}F]fluoro-L-DOPA in rat* J. Cereb. Blood Flow Metab. **10**: 707-19.

Rousset O.G., Ma Y. and Evans A.C. (1998) *Correction for Partial Volume Effects in PET: Principle and Validation* J. Nucl. Med. **39**: 904-11.

Schmidt K., Lucignani G., Moresco R.M., Rizzo G., Gilardi M.C., Messa C., Colombo F., Fazio F. and Sokoloff L. (1992) *Errors Introduced by Tissue Heterogeneity in Estimation of Local Cerebral Glucose Utilization with Current Kinetic Models of the [18F]Fluorodeoxyglucose Method* J. Cereb. Blood Flow Metab. **12**: 823-34.

Schmidt K., Mies G. and Sokoloff L. (1991) *Model of kinetic behavior of deoxyglucose in heterogeneous tissues in brain: a reinterpretation of the significance of parameters fitted to homogeneous tissue models* J. Cereb. Blood Flow Metab. **11**: 10-24.

Shinotoh H. and Calne D.B. (1995) *The Use of PET in Parkinson's Disease* Brain Cogn. **28**: 297-310.

Shoghi-Jadid, K., Huang S.-C., Stout D.B., Yee R.E., Yeh E.L., Farahani K.F., Satyamurthy N., Phelps M.E. and Barrio J.R. (2000) *Striatal Kinetic Modeling of FDOPA With a Cerebellar-derived Constraint on the Distribution Volume of 3OMFD: A PET Investigation Using Non-Human Primates* J. Cereb. Blood Flow Metab. **20**: 1134-48.

Slogoff S., Keats A.S. and Arlund C. (1983) *On the Safety of Radial Artery Cannulation* Anesthesiology **59**: 42-7.

Snow B.J., Vingerhoets F.J.G., Langston J.W., Tetrud J.W., Sossi V., and Calne D.B. (2000) *Pattern of dopaminergic loss in the striatum of humans with MPTP induced parkinsonism* J. Neurol. Neurosurg. Psychiatry **68**: 313-16.

Snow B.J., Tooyama I., McGeer E.G., Yamada T., Calne D.B., Takahashi H. and Kimura H. (1993a) *Human Positron Emission Tomographic [^{18}F]Fluorodopa Studies Correlate with Dopamine Cell Counts and Levels* Ann. Neurol. **34**: 324-30.

Snow B.J., Nygaard T.G., Takahashi H. and Calne D.B. (1993b) *Positron Emission Tomographic Studies of Dopa-responsive Dystonia and Early-Onset Idiopathic Parkinsonism* Ann. Neurol. **34**: 733-38.

Sossi V., Oakes T.R. and Ruth T.R. (1998) *A phantom study evaluating the quantitative aspect of 3D PET imaging of the brain* Phys. Med. Biol. **43**: 2615-30.

Spinks T.J., Jones T., Bloomfield P.M., Bailey D.L., Miller M., Hogg D., Jones W.F., Vaigneur K., Reed J., Young J., Newport D., Moyers C., Casey M.E. and Nutt R. (2000) *Physical Characteristics of the ECAT EXACT3D positron tomograph* Phys. Med. Biol. **45**: 2601-18.

Spinks T.J., Miller M.P., Bailey D.L., Bloomfield P.M., Livieratos L. and Jones T. (1998) *The effect of activity outside the direct field of view in a 3D-only whole-body positron tomograph* Phys. Med. Biol. **43** : 895-904.

Stout D.B., Huang S.-C., Yee R.E., Namavari M., Satyamurthy N., Shoghi-Jadid K., and Barrio J.R. (2001) *6-[^{18}F]Fluoro-m-tyrosine and 6-[^{18}F]Fluoro-L-dopa Kinetic Estimate Correlations with Plasma LNAA Concentrations* Physiological Imaging of the Brain with PET Eds A. Gjedde, S.B. Hansen, G.M. Knudsen and O.B. Paulson (San Diego: Academic Press) pp. 193-95.

Stout D.B., Huang S.-C., Melega W.P., Raleigh M.J., Phelps M.E. and Barrio J.R. (1998) *Effects of Large Neutral Amino Acid Concentrations on 6-[F-18]Fluoro-L-DOPA Kinetics* J. Cereb. Blood Flow Metab. **18**: 43-51.

Strother S.C., Casey M.E. and Hoffman E.J. (1990) *Measuring PET Scanner Sensitivity: Relating Countrates to Image Signal-to-Noise Ratios using Noise Equivalent Counts* IEEE Trans. Nucl. Sci. **37**: 783-88.

Strul D. and Bendriem B. (1999) *Robustness of Anatomically Guided Pixel-by-Pixel Algorithms for Partial Volume Effect Correction in Positron Emission Tomography* J. Cereb. Blood Flow Metab. **19**: 547-59.

Takikawa S., Dhawan V., Chaly T., Robeson W., Dahl R., Zanzi I., Mandel F., Spetsieris P. and Eidelberg D. (1994) *Input Functions for 6-[Fluorine-18]Fluorodopa Quantitation in Parkinsonism: Comparative Studies and Clinical Correlations* J. Nucl. Med. **35**: 955-63.

Takikawa S., Dhawan V., Spetsieris P., Robeson W., Chaly T., Dahl R., Margouleff D. and Eidelberg D. (1993) *Noninvasive Quantitative Fluorodeoxyglucose PET Studies with an Estimated Input Function Derived from a Population-based Arterial Blood Curve* Radiology **188**: 131-6.

Townsend D.W., Beyer T., Jerin J., Watson C.C., Young J. and Nutt R. (1999) *The ECAT ART Scanner for Positron Emission Tomography: 1. Improvements in Performance Characteristics* Clin. Pos. Imag. **2**: 5-15.

Townsend D.W., Spinks T., Jones T., Geissbühler A., Defrise M., Gilardi M.C. and Heather J. (1989) *Three dimensional reconstruction of PET data from a multi-ring camera* IEEE Trans. Nucl. Sci. **36** : 1056-65.

Tsuruda J., Saloner D. and Norman D. (1992) *Artefacts Associated with MR Neuroangiography* Am. J. Neuroradiol. **13**: 1411-22.

Tunnicliff G. (1994) *Amino acid transport by human erythrocyte membranes* Comp. Biochem. Physiol. **108A**: 471-8.

Turjanski N., Bhatia K., Burn D.J., Sawle G.V., Marsden C.D. and Brooks D.J. (1993) *Comparison of striatal ^{18}F-dopa uptake in adult-onset dystonia-parkinsonism, Parkinson's disease, and dopa-responsive dystonia* Neurology **43**: 1563-68.

Vingerhoets F.J.G., Schulzer M., Ruth T.J., Holden J.E. and Snow B.J. (1996) *Reproducibility and Discriminating Ability of Fluorine-18-6-Fluoro-L-Dopa PET in Parkinson's Disease* J. Nucl. Med. **37**: 421-26.

Vingethoets F.J.G., Snow B.J., Tetrud J.W., Langston J.W., Schulzer M. and Calne D.B. (1994b) *Positron Emission Tomographic Evidence for Progression of Human MPTP-induced Dopaminergic Lesions* Ann. Neurol. **36**: 765-770.

Vingerhoets F.J.G., Snow B.J., Schulzer M., Morrison S., Ruth T.J., Holden J.E., Cooper S. and Calne D.B. (1994a) *Reproducibility of Fluorine-18-6-Fluorodopa Positron Emission Tomography in Normal Human Subjects* J. Nucl. Med. **35**: 18-24.

Voet D and Voet J.G. (1995) Biochemistry (Second edition) Toronto: John Wiley & Sons) 1361p.

Volkow N.D., Fowler J.S., Gatley S.J., Logan J., Wang G.-J., Ding Y.-S., and Dewey S. (1996) *PET Evaluation of the Dopamine System of the Human Brain* J. Nucl. Med. **37**: 1242-56.

Wahl L.M., Chen J.J., Thompson M., Chirakal R. and Nahmias C.(1999a) *The time course of metabolites in human plasma after 6-[^{18}F]fluoro-L-m-tyrosine administration* Eur. J. Nucl. Med. **26**: 1407-12.

Wahl L.M., Asselin M.-C. and Nahmias C. (1999b) *Regions of Interest in the Venous Sinuses as Input Functions for Quantitative PET* J. Nucl. Med. **40**: 1666-75.

Wahl L. and Nahmias C. (1996a) *Modeling of Fluorine-18-6-L-Dopa in Humans* J. Nucl. Med. **37**: 432-37.

Wahl L. and Nahmias C. (1996b) *Quantification of dopamine metabolism in man: a mathematically justifiable approach* Phys. Med. Biol. **41**: 963-78.

Wahl L., Chirakal R., Firnau G., Garnett E.S. and Nahmias C. (1994) *The Distribution and Kinetics of [^{18}F]6-Fluoro-3-O-methyl-L-dopa in the Human Brain* J. Cereb. Blood Flow Metab. **14**: 664-70.

Watabe H., Channing M.A., Riddell C., Jousse F., Libutti S.K., Carrasquillo J.A., Bacharach S.L. and Carson R.E. (2001) *Noninvasive Estimation of the Aorta Input Function for Measurement of Tumor Blood Flow with [^{15}O]Water* IEEE Trans. Med. Imag. **20**: 164-74.

Watson C.C. (2000) *New, Faster, Image-Based Scatter Correction for 3D PET* IEEE Trans. Nucl. Sci. **47**: 1587-94.

Watson C.C., Newport D., Casey M.E., deKemp R.A., Beanlands R.S. and Schmand M. (1997) *Evaluation of Simulation-Based Scatter Correction for 3D PET Cardiac Imaging* IEEE Trans. Med. Imag. **44**: 90-5.

Watson C.C., Newport D. and Casey M.E. (1996) *A single scatter simulation technique for scatter correction in 3D PET* Three-Dimensional Image Reconstruction in Radiation and Nuclear Medicine Eds P. Grangeat and J.-L. Amans (Dordrecht: Kluwer Academic Publishers) pp 255-68.

Whone A.L., Watts R.L., Stoessl A.J., Davis M., Reske S., Nahmias C., Lang A.E., Rascol O., Ribeiro M.J., Remy P., Poewe W.H., Hauser R.A., and Brooks D.J. (2003) *Slower Progression of Parkinson's Disease with Ropinorole versus Levodopa: The REAL-PET Study* Ann. Neurol. **54**: 93-101.

Widmer J., Gaillard J.-M. and Tissot R. (1986) L-*Tyrosine and* L-*Tryptophan Transport in Red Blood Cells in Normal Subjects* Neuropsychobiology **15**: 7-12.

Wienhard K., Schmand M., Casey M.E., Baker K., Bao J., Eriksson L., Jones W.F., Knoess C., Lenox M., Lercher M., Luk P., Michel C., Reed J.H., Richerzhagen N., Treffert J., Vollmar S., Young J.W., Heiss W.D., and Nutt R. (2002) *The ECAT HRRT: Performance and First Clinical Application of the New High Resolution Research Tomograph* IEEE Trans. Nucl. Sci. **49** (1): 104-10.

Wong D.F., Gjedde A. and Wagner H.N. Jr. (1986) *Quantification of neurotransmitters in the living human brain: I. Irreversible binding of ligands* J. Cereb. Blood Flow Metab. **6**: 137-46.

Wu H.-M., Huang S.-C., Allada V., Wolfenden P.J., Schelbert H.R., Phelps M.E. and Hoh C.K. (1996) *Derivation of Input Function from FDG-PET Studies in Small Hearts* J. Nucl. Med. **37**: 717-22.

Xu M., Luk W.K., Cutler P.D. and Digby W.M. (1994) *Local threshold for segmented attenuation correction of PET imaging of the thorax* IEEE Trans. Nucl. Sci. **41**: 1532-37.

Yu D.-C., Huang S.-C., Barrio J.R. and Phelps M.E. (1995) *The assessment of the non-equilibrium effect in the 'Patlak analysis' of Fdopa PET studies* Phys. Med. Biol.

40: 1243-54.

Yu D.-C., Huang S.-C., Grafton S.T., Melega W.P., Barrio J.R., Mazziotta J.C. and Phelps M.E. (1993) *Methods for Improving Quantitation of Putamen Uptake Constant of FDOPA in PET Studies* J. Nucl. Med. **34**: 679-88.

Yu S.K. and Nahmias C. (1995) *Single-photon transmission measurements in positron tomography using* ^{137}Cs Phys. Med. Biol. **40**: 1255-66.

Zierler K. (1981) *A critique of compartmental analysis* Ann. Rev. Biophys. Bioeng. **10**: 531-62.

Zhu M.Y., Juorio A.V., Paterson I.A., and Boulton A.A. (1992) Regulation of Aromatic L-Amino Acid Decarboxylase by Dopamine Receptors in the Rat Brain J. Neurochem. **58**: 636-41.